



Commission of the European Communities



# ULTRASONIC TISSUE CHARACTERIZATION AND ECHOGRAPHIC IMAGING 6

Proceedings of the sixth European Communities workshop  
23–25 November 1986  
Paris, France



Report

EUR 10931 EN



Commission of the European Communities

# **ULTRASONIC TISSUE CHARACTERIZATION AND ECHOGRAPHIC IMAGING 6**

**Proceedings of the sixth European Communities workshop  
23–25 November 1986  
Paris, France**

Edited by:

**J.M. Thyssen,<sup>1</sup> G. Berger<sup>2</sup>**

<sup>1</sup> University of Nijmegen  
Faculty of Medicine  
The Netherlands 6500 HB Nijmegen

<sup>2</sup> Laboratoire de biophysique  
Centre hospitalier universitaire  
Cochin — Port Royal  
24, rue du Faubourg-St-Jacques  
F-75674 Paris

Directorate-General  
Science, Research and Development

1987

EUR 10931 EN

**Published by the  
COMMISSION OF THE EUROPEAN COMMUNITIES  
Directorate-General  
Telecommunications, Information Industries and Innovation  
Bâtiment Jean Monnet  
LUXEMBOURG**

**LEGAL NOTICE**

Neither the Commission of the European Communities nor any person acting on behalf of the Commission is responsible for the use which might be made of the following information

Cataloguing data can be found at the end of this publication

Luxembourg: Office for Official Publications of the European Communities, 1987

ISBN 92-825-7623-X

Catalogue number: CD-NA-10931-EN-C

© ECSC-EEC-EAEC, Brussels · Luxembourg, 1987

*Printed in Belgium*

## FOREWORD

The sixth Workshop on Ultrasonic Tissue Characterization and Echographic Imaging was organized under grant nr. MR-024-NL from the Directorate General for Science, Research Development of the European Commission. The aim of this Workshop was to offer the participating Local Research Groups the opportunity to expose the state of the art of their ongoing research programs and to discuss the running cooperative activities.

The schedule of the Workshop consisted of three days devoted to plenary sessions on the following topics: Tomography, Texture, Scattering, Attenuation and Tissue Movement. The schedule furthermore contained Discussion sessions at which work in progress was presented and discussed.

In this volume the order of the schedule of the Workshop has been maintained and in addition to the texts of the lectures presented in plenary sessions also some manuscripts from discussion sessions have been added. The very interesting tutorials which were presented by our guests from the USA: J.F. Greenleaf (Rochester, MN) and B.S. Garra (Bethesda, MD) may be specially mentioned. They not only presented an excellent lecture, but they participated actively in the discussions and sessions as well. Therefore, their presence greatly contributed to the success of this Workshop.

The Project Management Group and the Participants are very much indebted to Mrs. G. Berger, Ph.D., M.D. (Paris) who efficiently organized the Workshop.



## CONTENTS

	<u>Page</u>
Foreword	III
List of participants	IX
Institutes (+addresses) participating in the Concerted Action Programme	XI
 LECTURES AT WORKSHOP	
<u>Session (1) TOMOGRAPHY</u> , (chairmen J.M. Thijssen, H. Ermert)	1
 <u>Greenleaf</u> , J.F. (Rochester, MN) <u>Tutorial paper</u> : Tissue characterization by computed tomography	 3
<u>Hermens</u> , A., Cheriff, S., Demoment, Gk., Guglielmi, J.P. (Paris) High definition reflection mode tomography.	15
<u>Van Hoorn</u> , W., Berkhout, A.J. (Delft) The Delft acoustic microscope and synthetic focusing.	23
 <u>Session (2) TEXTURE</u> , (chairmen D. Nassiri, D. Nicholas)	
 <u>Zuna</u> , I., Volk, J., Walz, M., Lorenz, A., Naves, W., Raeth, U., Schlaps, D. (Heidelberg) TC-system influence on the B-mode image features.	 35
<u>Oosterveld</u> , B.J., Thijssen, J.M., Hartman, P., Rosenbusch, G. (Nijmegen). Preprocessing and texture analysis of in-vivo B-mode echograms.	43

<u>Casini</u> , A., Lotti, F., Bernardi, P., Laatanzi, F., Picano, E. (Florence, Pisa) First and second order statistics for atherosclerosis detection.	51
<u>Nicholas</u> , D., Bamber, M., Nassiri, D. (Norwich, London). B-scan texture as an indicator of diffuse liver disease.	61
<u>Iracá</u> , D., Landini, L. (Pisa) Application of signal restoration techniques to B-scan images.	67
<u>Biagi</u> , E., Calzolari, M., Castellini, G., Grimaldi, A., Masotti, L., Rocchi, S. (Florence) Data acquisition systems and their applications to tissue characterization.	73
<u>Session (3) ATTENUATION I</u> (chairman U. Raeth)	85
<u>Garra</u> , B.S. Shawker, T.H., Insana, M.F., Wagner, R.F. (Bethesda, MD) <u>Tutorial paper</u> : In vivo attenuation measurement methods and clinical relevance.	87
<u>Berger</u> , G., Laugier, P., Fink, M., Perrin, J. (Paris) Attenuation as an additive clinical indicator.	101
<u>Nicholas</u> , D. (Norwich) In-vivo attenuation for small tissue volumes.	113
<u>Romijn</u> , R.L., Oosterveld, B.J., Thijssen, J.M. (Nijmegen) Attenuation and scattering of ultrasound in intra-ocular tumours.	117
<u>Session (4) ATTENUATION II</u> (Chairmen K.M. Irion, H.G. Trier)	125
<u>Chivers</u> , R.C. (Guildford) The relation of coherent and incoherent scattering to measurements of attenuation and scattering in tissue.	127
<u>Duck</u> , F.A., Starritt, H.C. (Bath) Non-linear losses in the measurement of attenuation.	137
<u>Teo</u> , T.J., Chapelon, J.Y., Cathignol, D., Rud, J.M. (Lyon, Philadelphia). Attenuation in Doppler measurement.	145



<u>Costa</u> , E.T., Hoddinott, J.C., Leeman, S. Attenuation without diffraction correction? Experimental results.	155
<u>Nauth</u> , P., Schmidt, N., Loch, E.G., Von Seelen, W. (Wiesbaden). Attenuation and frequency imaging.	163
<u>Session (5) BACKSCATTERING</u> (chairman G. Berger)	169
<u>Vieli</u> , A., Basler, S. Lunkenheimer, P.P. (Zürich, Münster) Immediate effect of myocardial infarction on the histogram of the ultrasonic echo amplitude.	171
<u>Cherif</u> , S., Herment, A., Dumée, Ph., Péronneau, P. (Paris). Introduction to signal restoration for fibrous tissue characterization	179
<u>Mazzeo</u> , V., Golfletto, W., kRavalli, L., Galli, G., Perri, P., Rossi, A. (Ferrara). Comparison between the results of tissue analysis by means of power spectra and the histological structure of choroidal malanomas.	187
Index of keywords.	201



## List of participants

Adach, J.	Guildford	United Kingdom
Berger, G.	Paris	France
Cancre, F.	Paris	France
Casini, A.	Florence	Italy
Castellini, G.	Florence	Italy
Chapelon, J.	Lyon	France
Cherif, S.	Paris	France
Chivers, R.C.	Guildford	United Kingdom
Costa, E.T.	London	United Kingdom
Cook-Martin, D.	Sutton	United Kingdom
Duck, F.	Bath	United Kingdom
Erment, H.	Erlangen	Germany
Faust, U.	Stuttgart	Germany
Fink, M.	Paris	France
Fredfeldt, K.E.	Copenhagen	Denmark
Herment, A.	Paris	France
Iracà, D.	Pisa	Italy
Jensen, J.A.	Copenhagen	Denmark
Joseph, A.E.A.	London	United Kingdom
Landini, L.	Pisa	Italy
Lang, M.	Erlangen	Germany
Larsen, J.K.	Copenhagen	Denmark
Laugier, P.	Paris	France
Leeman, S.	London	United Kingdom
Mazzeo, V.	Ferrara	Italy
Mensah, S.	Marseille	France
Nassiri, D.K.	London	United Kingdom

Nauth, P.	Wiesbaden	Germany
Nicholas, D.	Norwich	United Kingdom
Nussli, B.	Stuttgart	Germany
Oosterveld, B.J.	Nijmegen	The Netherlands
Raeth, U.	Heidelberg	Germany
Rocchi, S.	Florence	Italy
Romijn, R.L.	Nijmegen	The Netherlands
Rühlmann, J.	Bonn	Germany
Solli, G.	Eindhoven	The Netherlands
Stapper, T.	Eindhoven	The Netherlands
Starritt, M.	Bath	United Kingdom
Teo, T.J.	Philadelphia/Lyon	USA
Thijssen, J.M.	Nijmegen	The Netherlands
Trier, H.G.	Bonn	Germany
Tristam, M.	Sutton	United Kingdom
Van Hoorn, W.	Delft	The Netherlands
Vieli, A.	Zürich	Switzerland
Zuna, I.	Heidelberg	Germany

Invited speakers

B.S. Garra	Bethesda MD	USA
J. Greenleaf	Rochester MN	USA

## Participating Institutes

### Belgium

S. Levi, M.D., J.P. Hermand; Université Libre de Bruxelles, Hôpital  
Universitaire Brugmann, Dept. de Gynaecologie-Obstetric, Service  
d'Ultrasonographie, Fondation Freserh, B-1020 Bruxelles, tel. 3224784870

### Denmark

K.E. Fredfeldt, J.K. Larsen, H.H. Holm; Ultrasonic Lab. Dept. of Urology,  
Herlev Hospital, Univ. Copenhagen, DK-2700 Herlev, tel. 452942733.

### France

G. Berger, M.D., J. Perrin; Laboratoire de Biophysique, ERA 498, CHU  
Cochin Port Royal, Paris 14<sup>e</sup>, tel. 3313201240 (361).

M. Fink; Groupe de Physique des Solides de l'Ecole Normale Supérieure.  
Univ. Paris 7. Tour 23. 2 Place Jussieu, 75221 Paris, Cedex 05.

A. Herment; I.D.C.V. CNRS ERA 785, Hôpital Broussais, 96, Rue Didot, 75014  
Paris, tel. 3315423793.

J.P. Lefebvre; C.N.R.S., Laboratoire de Mécanique et d'Acoustique-B.P. 71,  
31, Chemin Joseph Aiguier 13277, Marseille cedex 9, tel. 3391719042  
(488).

D. Catignol, J. Jossinet, J.Y. Chapelon; Institut National de la Santé et  
de la Recherche Médicale. 18, Avenue Doyca Lépine, 69500 Bron, tel.  
3378542784.

### West Germany

H.G. Trier, M.D.; Abteilung für Augenheilkunde der Universität Bonn,  
Abbestraße 2, D-5300 Bonn Venusberg, tel. 492282803696.

U. Faust; Institut für Biomedizinische Technik, AzenbergstraBe 18, D-7000 Stuttgart 1, tel. 4971120732144.

W. Buschmann, M.D., W. Haigis; Univ. Klinik für Augenranke, Josef SchneiderstraBe 11, D-8700 Würzburg, tel. 499312021454.

D. Harder, W. Döler; Institut für Med. Physik der Universität, GosslerstraBe 10, D-3400 Göttingen, tel.

H. Ermert et al.; Institut für Hochfrequenztechnik, Universität Erlangen-Nürnberg, CauerstraBe 9, D-8520 Erlangen, tel. 499313185-7227.

N. Stein; Deutsche Klinik für Diagnostik, Postfach 2149, D-6200 Wiesbaden, tel. 496121577-376.

U. Raeth, M.D., I. Zuna; Institut F. Nuklear Medizin, Deutsches Krebsforschungszenter, DKFZ, 6900 Heidelberg, tel. 496221484581.

### Italy

V. Mazzeo, M.D., W. Golfetto; Clinica Oculistica di Universita di Ferrara, Corso Giovecca, Ferrara, tel. 3953236359.

L. Masotti, G. Castellini, et al.; Istituto di Elettronica, Facultad di Ingegneria, Università degli Studi di Firenze, Firenze, tel. 39554796277 (271).

L. Landini, E. Picano, A. Distance; Centro per l'Automatica "E. Piaggio", Faculty of Engineering, Pisa, C.N.R. Institute of Clinical Physiology at the University of Pisa and Institute of 1<sup>st</sup> Medical Pathology of the University of Pisa, Pisa, tel. 395047231.

P. Sirotti; Dept. of Electrotechnology, Electronics, and Informatics. Università degli studi, Via A. Valerio 10, 34127 Treiste, tel. 3940574044.

### The Netherlands

A.J. Berkhout, W. van Hoorn; Afd. Technische Natuurkunde, Technische Hogeschool Delft, Lorentzweg 1, Delft, tel. 311578529.

J.M. Thijssen, B.J. Oosterveld, L. Romijn; Afd. Oogheelkunde, Biofysisch Laboratorium, Philips van Leydenlaan 15, 6500 HB Nijmegen, tel. 3180514447.

J.C. Somer, T.J.M. Jeurens; Biomedisch Centrum, Rijksuniversiteit Limburg, Beeldsnijdersdreef 101, 6216 EA Maastricht, tel. 3143888888.

M. Stapper, G. Sollie; Department of Biomedical Electrotechnical Engineering, Technical University, P.P. Box 513, Eindhoven, Tel. 3140473288

### United Kingdom

S. Leeman, D. Seggie, M. Doherty, M. Monagan; King's College, School of Medicine and Dentistry, Department of Medical Engineering and Physics, Dulwich Hospital, East Dulwich Grove, London SE 22 8 PT, tel. 4416933377, ext. 3074.

J.C. Bamber, M. Tristram, D.O. Cosgrove, M.D.; Physics Department + Department of Nuclear Medicine, Sutton, Surrey, tel. 4416438901.

W.I. Pryce, D. Morris; Northern General Hospital, Herries Road, Sheffield S5 7AU, tel. 44742387253.

R.C. Chivers, J.D. Aindow, R.A. Bacon; Physics Department, University of Surrey, Guildford, Surrey, tel. 44483571281-531.

D. Nicholas; Dept. of Medical Physics, Norfolk and Norwich Hospital, Brunswick Road, Norwich, NR1 3SR, tel. 44628377

D.K. Nassiri, A.E.A. Joseph, M.D.; Dept. of Medical Physics, St George's Hospital, Blackshaw Road, London SW17 0QT, tel. 4416721255 ext. 5090.

## Affiliated Research Groups

### Austria

N. Leitgeb, S. Schuy; Institut für Elektro- und Biomedizinische Technik,  
Technische Universität, A-8010 Graz, tel. 31677511/7390.

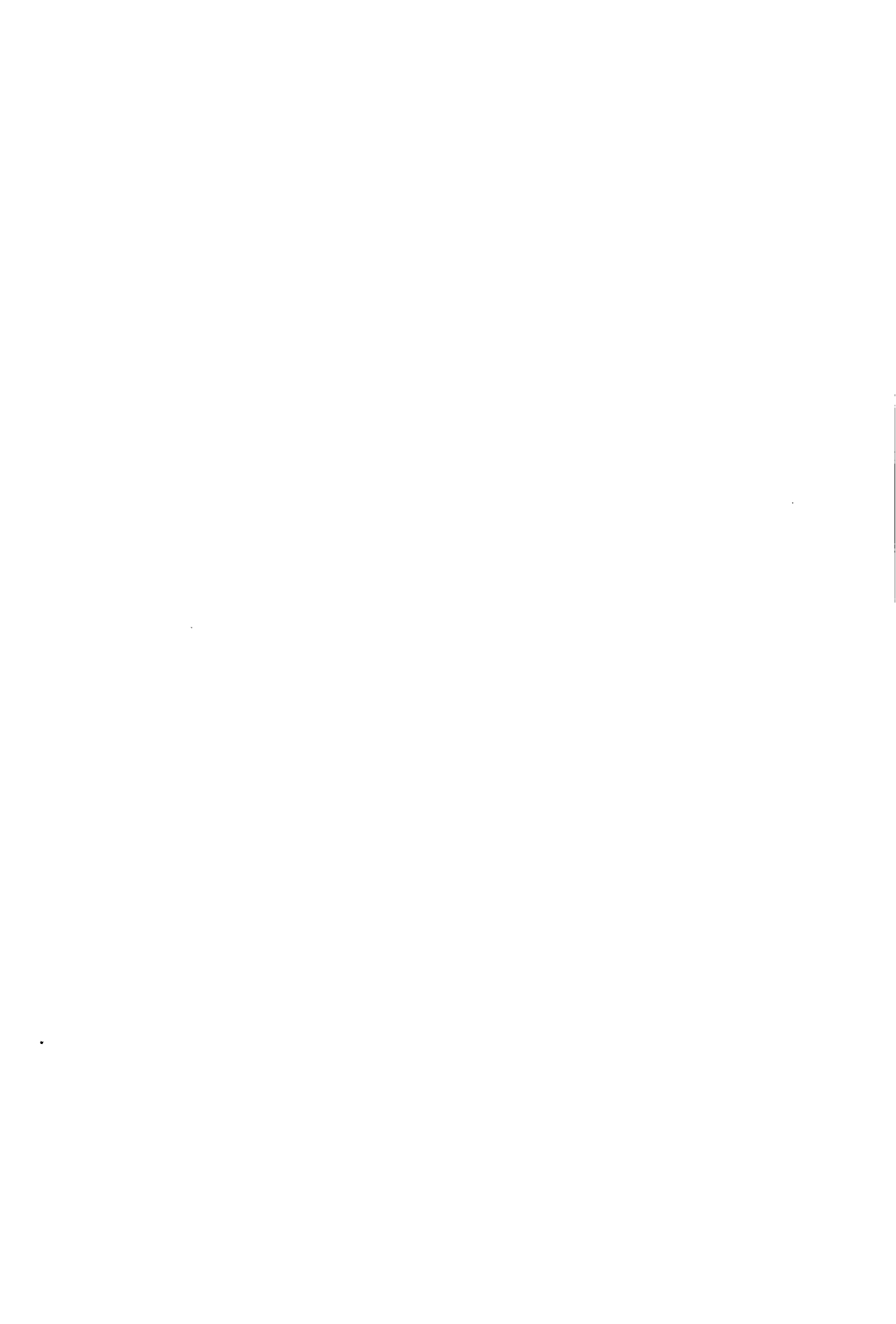
### Switzerland

A. Vieli e.a.; Institut f. Biomedizinische Technik, ETH und Universität,  
CH-8092 Zürich, tel. 4112564565.



Session 1 - TOMOGRAPHY

Chairmen : J.M. Thijssen, H. Ermert



# TISSUE CHARACTERIZATION BY COMPUTED TOMOGRAPHY

J. F. Greenleaf

Biodynamics Research Unit, Department of  
Physiology and Biophysics, Mayo Clinic/Foundation,  
Rochester, MN 55905 U.S.A.

Ultrasonic computer-assisted tomography (UCAT) can be used for a wide range of tissue characterization problems. Examples are given for the use of UCAT in measuring speed, attenuation, absorption, and scattering in the transmission mode. In the reflection mode, examples are given for measuring backscatter and Doppler flow velocity. *In vitro* studies in excised tissues are described as well as results for *in vivo* clinical studies for the detection of breast cancer.

Key words: Ultrasonic tomography; reconstruction; transmission, Doppler.

## INTRODUCTION

An objective of diagnostic imaging with ultrasound is to obtain images of mechanical properties of biologic tissue that are sensitive to disease processes. One of the goals of the biomedical ultrasound imaging community has been to obtain images of material properties that are related quantitatively to the intrinsic property of tissues such as speed, attenuation, absorption, or scattering cross section. These goals have resulted in many attempts to relate intrinsic properties of elastic materials to measurable extrinsic properties such as pressure, temperature, or particle velocity of the scattered wave [Carson et al., 1977; Glover and Sharp, 1977; Goss et al., 1978; Greenleaf, 1981]. However, it is true that in almost no other area of biomedical imaging in medicine are quantitative values used for evaluating the state of tissues. For example, it is not CT numbers but rather morphologic characteristics of the CT images that are used for detecting alterations from normal. Certainly pathologists evaluating histologic tissue slides use virtually no quantitative measurements of optical spectra or optical density of the tissue slides but rather, they use morphologic and stereo metric evaluations of the images to select tissue state [Sandritter and Thomas, 1979].

The most widely used ultrasonic imaging technique is that of the simple B-scan. Real-time B-scans are obtained with mechanical or phased array sector and phased array linear scanners and the resulting images are seldom analyzed quantitatively. Thus, regions of tissue or volumes of tissue are evaluated by visual study of a sequence of two-dimensional images. Computed tomography provides the capability of automatically obtaining a set of images for evaluation either in true three-dimensional geometry or its projection or stereo projection as two-dimensional images [Greenleaf, 1982; Greenleaf et al., 1985]. In addition, many properties of the tissue can be imaged using computed tomography and the instrument can be designed to automatically obtain data in a manner independent of the technical skill of the operator. The purpose of this paper is to describe the wide range of images that can be obtained by ultrasonic computer-assisted tomography and to provide examples of their use in evaluating biomedical tissue states and functions. The paper consists of a number of

(187 Regions; 18 Patients, 29-68 Years)

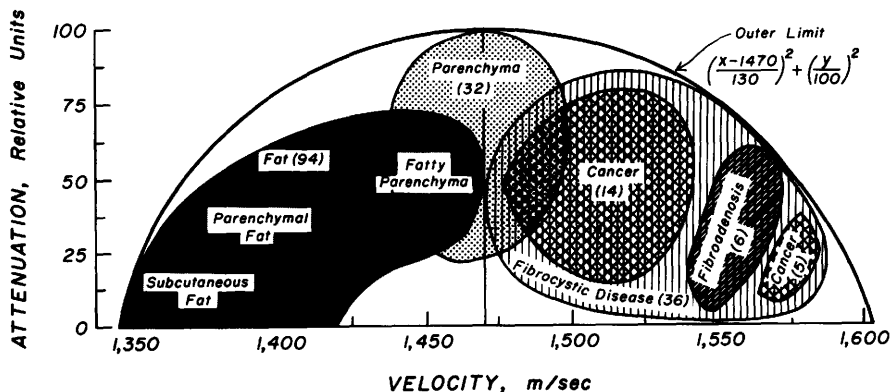


Fig. 1 Distribution of speed and relative attenuation for various tissues found in human breasts. Ultrasonic computer-assisted tomography was used to identify tissues and measure speed and attenuation in regions of tissues within human breasts. It was found that speed of sound separates the tissues better than attenuation but that there is a great deal of overlap among fibrocystic disease, cancer, and fibroadenoma on this two-dimensional plane. (Reproduced with permission from Greenleaf, J. F., and Bahn, R. C., *IEEE Transactions on Biomedical Engineering BME-28*, 177-185 (1981))



1/27

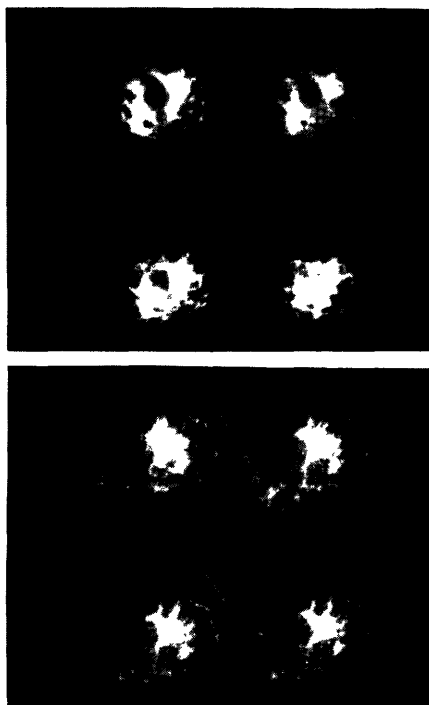
Fig. 2 Ultrasonic computer-assisted tomograms through the breast of a patient with a 3 cm grade 4 infiltrating ductal carcinoma in the upper right inner quadrant. In fatty breasts ultrasonic computer-assisted tomography is very useful for detecting tumors and diagnosing their type. However, it was found in dense breasts that computer-assisted tomography was not capable of detecting or diagnosing cancer with adequate sensitivity and specificity. (Reproduced with permission from Greenleaf, J. F., et al., in *Acoustical Imaging*, E. A. Ash and C. R. Hill, eds., 12, pp. 579-587 (1982))

examples, without extensive derivation of the theory, in order to provide a quick overview of the range and robust nature of computed tomography applications. The term 'tomography' means slice imaging and thus computed tomography will be used in this paper to describe any computer-assisted imaging of slices obtained either in transmission or reflection mode scans.

### Computed Tomography Applications

Ultrasonic computer-assisted tomography has been used to evaluate the characteristics of tissues in breasts. In figure 1, for example, the distribution of means of ultrasonic attenuation and velocity were obtained in a set of 18 patients, aged from 29 to 68 years, using ultrasonic computer-assisted tomography [Greenleaf et al., 1985; Robinson and Greenleaf, 1985]. In fatty breasts it was found that the material characteristics measured by computed ultrasound could distinguish cancer from other abnormal lesions in fatty breasts. Images of breast cancer in fatty breasts were constructed using transmission ultrasonic computed tomography in which speed and attenuation were used to evaluate the region of cancer (Fig. 2). Evaluation of these techniques in a wide range of patients has resulted in disappointing results [Schreiman et al., 1984]. UCAT has been recently further developed to obtain backscatter images of human breasts to decrease the effects of speckle. Sixty view backscatter tomograms have been obtained in breasts of patients (Fig. 3). The method is currently being evaluated for efficacy in detecting breast cancer.

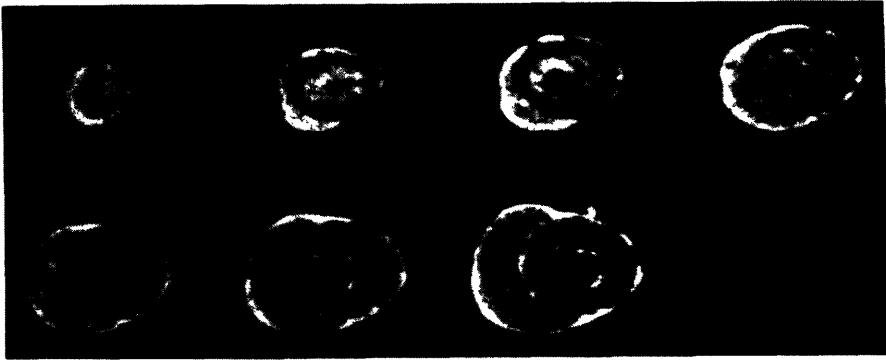
Fig. 3 Ultrasonic computer-assisted tomograms of backscatter. B-scans were compounded from sixty views around the breast obtaining these high-resolution images of the human female breast. Cooper's ligaments, parenchyma, and fatty inclusions and cysts can be seen in these images. Such computed backscatter images may be useful for detecting breast cancer in dense breasts. (reproduced with permission from Greenleaf, J. F., and Ylitalo, Y., Doppler tomography, 1986 *Ultrasonics Symposium Proceedings*, November 17-19, 1986, Williamsburg, VA (In Press))



05/85/JEG

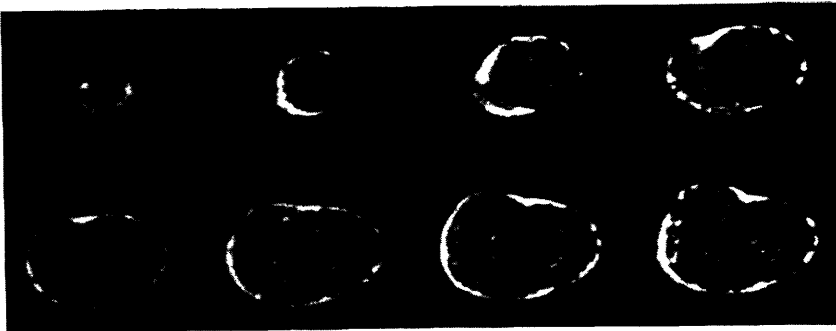
Ultrasonic computer-assisted tomography can also be used to study the distribution of ischemia in experimental models of coronary infarction. In a study in which dogs were used to evaluate the effects of regional myocardial ischemia on ultrasound images, the hearts were excised from the animal after varying periods of ischemia and multiple transverse ultrasonic computer-assisted

COMPOUND ECHO IMAGE - ISCHEMIC CANINE HEART



02/85/KC

COMPOUND ECHO IMAGE - NORMAL CANINE HEART



02/85/KC

Fig. 4 Ultrasonic computer-assisted tomography has been used to evaluate distributions of ischemia within canine hearts. The normal canine heart shown in the upper panel was scanned *in vitro* less than thirty minutes after removal from the live animal. The ischemic canine heart (lower panel) was scanned after fifteen minutes of regional ischemia produced by ligation of the LAD artery, the resulting tomograms illustrate distributions of ischemia with good resolution. (Reproduced with permission from Chandrasekaran, K., et al., *Ultrasound in Medicine and Biology* 12, pp. 784-793 (1986))

tomograms were obtained of the heart. As shown in figure 4, it was found that the regional distribution of ischemia resulted in edema that could be visualized using ultrasonic computer-assisted tomographic methods of imaging the *in vitro* heart [Chandrasekaran et al., 1986]. This study indicated, that given appropriate compounding, that is, appropriate methods for decreasing speckle, high-resolution images of the regional distribution of ischemia in the heart may be possible. Experimental measurements from computed tomograms of speed, attenuation, and backscatter, shown in figure 5, indicate that ischemic regions are associated with increased backscatter, decreased attenuation and decreased ultrasonic speed.

We have recently developed techniques for obtaining new images of scatter and absorption that are derived from original tomograms of speed and attenuation [Sehgal and Greenleaf, 1985]. Using the mean difference in acoustic speed to calculate probable scattering strengths and subtracting these values from the attenuation image, measures of absorption were estimated. Figure 6 illustrates in the upper panel, the original speed and attenuation tomograms and, in the lower panel, the derived scatter and absorption tomograms. The new absorption images have what appears to be more information than the original images. Whether these images can be used for aiding diagnosis with computed tomography is yet to be determined.

One of the ways nonlinearity manifests itself is by generating sum and difference frequencies when ultrasonic waves of two frequencies are propagated in the same direction. Ultrasonic computed tomography can be used to produce a nonlinear image by using a measurement of the amplitude of the resulting difference frequency that is proportional to the nonlinearity, among other things, of the intervening tissue. The difference frequency is used since it is lower and therefore undergoes less attenuation than the sum frequency. Although the difference frequency signal is a function of nonlinear parameters in addition to sound speed, spreading of the secondary field due to diffraction and attenuation of the primary and secondary fields, it is possible to obtain an image using this technique [Sehgal and Greenleaf, 1985] (Fig. 7). Although the resulting nonlinear image is contaminated with attenuation and refraction, probably to a greater degree than typical tomography, the two images (nonlinearity and backscatter) provide different types of information primarily because they represent different properties of the medium. Perhaps the nonlinear methods can obtain information about tissues that is complimentary to the backscatter or speed or attenuation images.

A completely new type of computed tomography has recently been developed that can be termed Doppler tomography [Greenleaf and Ylitalo, 1986]. It has been shown previously that cancer may have different Doppler characteristics from other tissues and vessels and thus Doppler interrogation of tissues could be used to distinguish between cancer and normal tissue [Burns et al., 1983]. Other investigators have attempted to characterize cancers in the breast by utilizing single probes, usually handheld, in which Doppler shift in one breast has been compared to Doppler shift in the same region on the contralateral breast [Wells et al., 1977; Burns et al., 1983]. Computed ultrasonic tomography may provide a capability for automatically obtaining distributions of Doppler shifts within planes through the breast, perhaps allowing automated surveying of breasts. We have modified our previously developed computed tomography instrument for obtaining Doppler signals to be used for computed tomographic reconstruction of distributions of Doppler shifts with the breast. Figure 8 illustrates the geometry of the Doppler tomography experiment and figure 9 illustrates Doppler tomograms through a phantom with flow and without flow. It is clear that distributions of flow can be imaged using Doppler tomography in the reflection mode and that although there is some clutter due to high-amplitude signals caused by fixed targets, adequate Doppler images have been obtained illustrating a potential for automated Doppler analysis of breast disease.

**MEAN GRAY LEVEL DIFFERENCE: CONTROL GROUP & NORMAL REGION OF ISCHEMIC GROUP ( $\Delta C$ ); ISCHEMIC REGION & NORMAL REGION OF ISCHEMIC GROUP ( $\Delta I$ ) FOR BACKSCATTER, ATTENUATION AND SPEED**

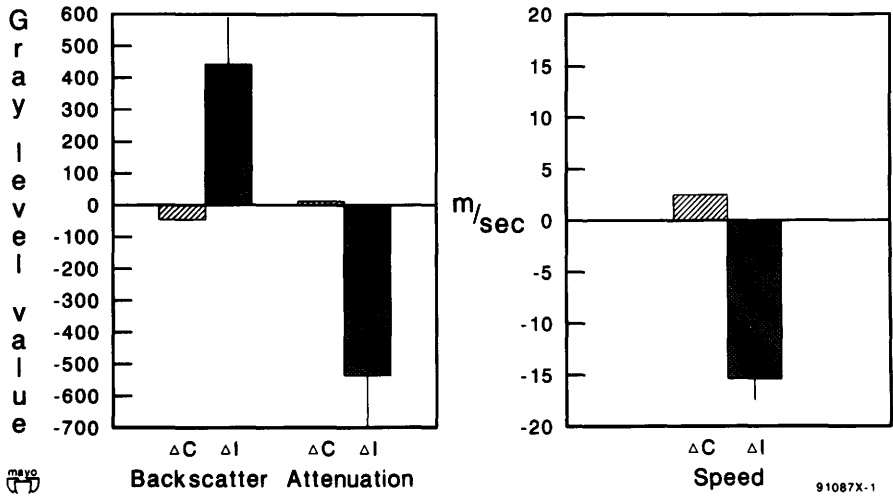


**Fig. 5** Changes in backscatter, attenuation and speed in hearts due to ischemia. Data are calculated from images such as those in figure 4 taken of hearts with and without ischemia. These types of data, obtained from a variety of experiments, can lead to understanding effects of various dysfunctions on ultrasonic tissue parameters.

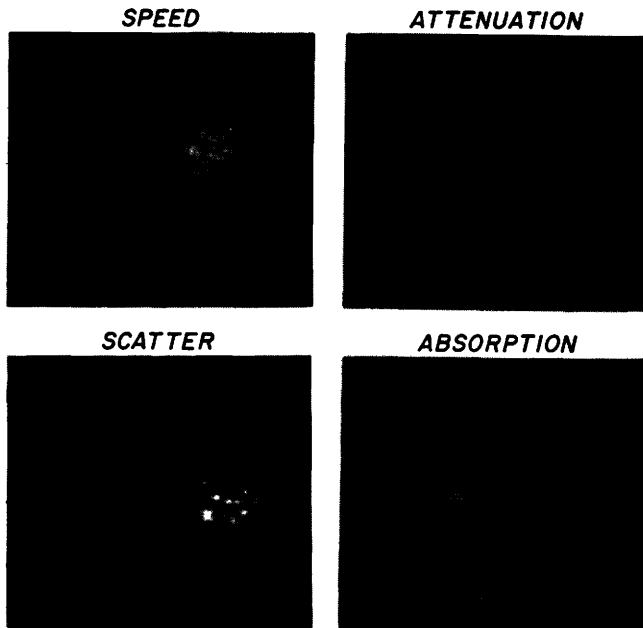


**Fig. 6** Computer-assisted tomograms of speed and attenuation, upper panel, obtained from an excised breast. From these two images scatter and absorption have been calculated and are shown in the lower two panels.



Advanced computed tomography imaging has been attempted by several investigators [Mueller, 1980; Kaveh et al., 1981; Devaney, 1982; Greenleaf And Chu, 1984]. The advanced imaging techniques are an attempt at conducting ultrasonic computed tomography in which a wave equation is used as a descriptor of wave propagation rather than the straight line approximation. When used in the transmission mode, diffraction tomography may be capable of providing quantitative images of speed and absorption and therefore could complement qualitative backscatter images obtained by B-scan methods or by backscatter compound tomography methods. We have recently obtained very good reconstructions using the Born approximation and diffraction tomography reconstruction methods. Shown in figure 10 is a diffraction tomographic reconstruction of the real and imaginary parts of the image obtained by using the Born inverse scattering approximation. The object, a breast phantom produced by Ernie Madson of the University of Wisconsin, was scanned using plane wave insonification and the resulting scattered signal was measured and used to accomplish the inversion shown here in a manner described in [Robinson and Greenleaf, 1985]. The resulting image is not quantitative in the sense that pixel values represent real or imaginary values of the refraction index, however, the image is faithful in reproducing the distribution of scatterers within the phantom at the right position and at the right size. Thus, although this is a qualitative image, the effects of diffraction and refraction have been decreased relative to straight line methods.

## CONCLUSION

Ultrasonic computer-assisted tomography can be used for the following activities:

1. Experimental tissue evaluation in which computed tomography on excised or live tissues can be used for measuring distributions of speed, attenuation, backscatter and Doppler flow.
2. Clinical evaluations of breast in the transmission mode for attenuation and speed and in the reflection mode for backscatter and Doppler images. However, it is unclear to this date whether ultrasonic computer-assisted tomography in the breast can compete with or complement the x-ray mammogram as a screening or as a diagnosing modality.
3. Theoretical scattering studies in which scattering caused by models or tissues can be evaluated and studied using inverse scattering theory developed for ultrasonic computer-assisted tomography.

## ACKNOWLEDGMENTS

The author thanks E. C. Quarve for secretarial assistance and S. D. Orwoll for graphics.

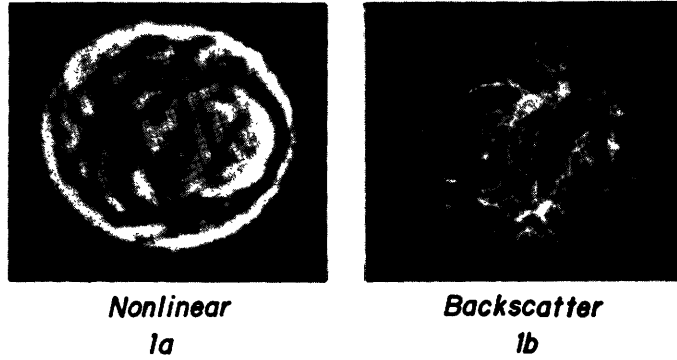
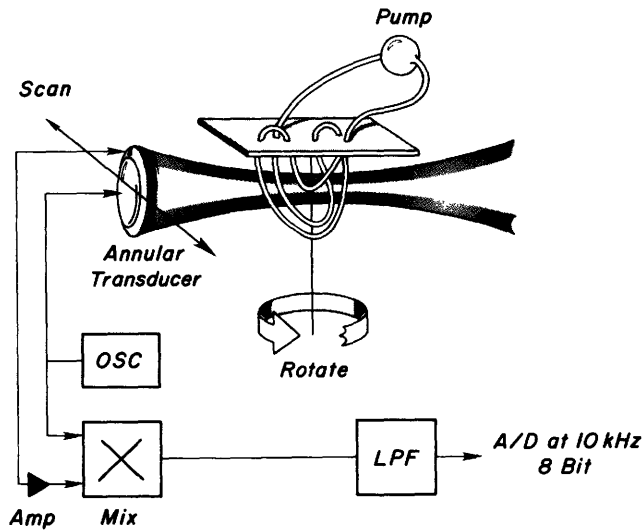


Fig. 7 A difference frequency ultrasonic computer-assisted tomogram of the nonlinearity within an excised breast (left panel) compared to the backscatter tomogram (right panel). The two types of images result from two entirely different processes of wave propagation and should relate to different characteristics of the tissue. (Reproduced with permission from Greenleaf, J. F., and Ylitalo, J., Doppler tomography, *1986 Ultrasonics Symposium Proceedings*, November 17-19, 1986, Williamsburg, VA (In Press))

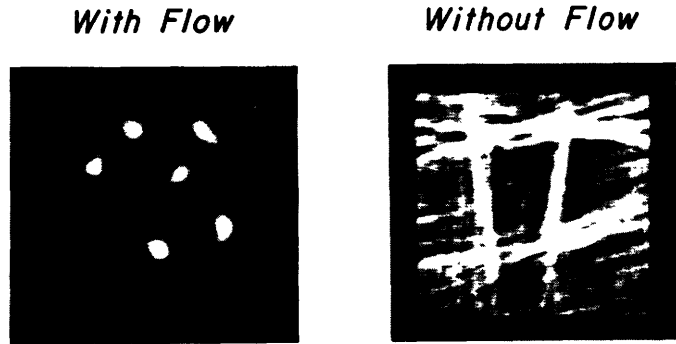


08/86/JFG

Fig. 8 Schematic diagram of the experimental set up used to obtain Doppler tomograms. An annular array is used to insonify the tissue with CW and receive the backscattered Doppler signal. The transducer is scanned in a linear translate fashion while the object is rotated. The Doppler shifted frequencies are digitized for analysis by computer.

## REFERENCES

- Burns, P. N., Virjee, J. M., Gowland, M., Rimmer, S., and Wells, P. N. T., The origin of Doppler shift signals from breast tumours, in *Ultrasonic Examination of the Breast*, J. Jellins, and T. Kobayashi, eds., pp. 379-384 (John Wiley & Sons, Ltd., 1983).
- Carson, P. L., Oughton, T. V., Hende, W. R., and Ahuga, S. A., Imaging soft tissue through bone with ultrasound transmission tomography reconstruction, *Medical Physics* 4, 302-309 (1977).
- Chandrasekaran, K., Greenleaf, J. F., Robinson, B. S., Edwards, W. D., Seward, J. B., and Tajik, A. J., Echocardiographic visualization of acute myocardial ischemia--in vitro study. *Ultrasound in Medicine and Biology* 12, 785-793 (1986).
- Devaney, A. J., A filtered backpropagation algorithm for diffraction tomography, *Ultrasonic Imaging* 4, 336-350 (1982).
- Glover, G. H., and Sharp, J. L., Reconstruction of ultrasound propagation speed distribution in soft tissue: Time-of-flight tomography, *IEEE Transactions on Sonics and Ultrasonics SU-45*, 229-234 (1977).
- Goss, S. A., Johnston, R. L., and Dunn, F., Comprehensive compilation of empirical ultrasonic properties of mammalian tissues, *Journal of the Acoustical Society of America* 64, 324-457 (1978).
- Greenleaf, J. F., Computerized transmission tomography, in *Methods of Experiment Physics Ultrasound*, P. D. Edmonds, ed., 19, pp. 563-589 (Academic Press, New York, 1981).
- Greenleaf, J. F., A graphical description of scattering. *Ultrasound in Medicine and Biology* 12, 603-609 (1986).
- Greenleaf, J. F., Bahn, R. C., and Gisvold, J. J., Dynamic ultrasonic breast mammography, in *Fourth International Congress on the Ultrasonic Examination of the Breast*, J. Jellins, G. Kossoff, and J. Cross, eds., pp. 221-225 (International Congress on the Ultrasonic Examination of the Breast, St. Leonards, Australia, 1985).
- Greenleaf, J. F., Three-dimensional imaging in ultrasound, *Journal of Medical Systems* 6, 579-589 (1982).
- Greenleaf, J. F., Ylitalo, Y., Doppler tomography, *1986 Ultrasonics Symposium Proceedings*, November 17-19, 1986, Williamsburg, VA (In Press).
- Greenleaf, J. F., and Chu, A., Multifrequency diffraction tomography, in *Acoustical Imaging*, M. Kaveh, R. K. Mueller, and J. F. Greenleaf, eds., 13, pp. 43-45 (Plenum Publishing Corporation, New York, 1984).
- Kaveh, M., Soumekh, M., and Mueller, R. K., A comparison of Born and Rytov approximations in acoustic tomography, in *Acoustical Imaging*, J. P. Powers, ed., 11, pp. 325-335 (Plenum Press, New York, 1982).
- Kaveh, M., Soumekh, M., and Greenleaf, J. F., Signal processing for diffraction tomography, *IEEE Transactions on Sonics and Ultrasonics SU-32*, 230-239 (1984).
- Kaveh, M., Soumekh, M., Lu, Z. Q., Mueller, R. K., and Greenleaf, J. F., Further results on diffraction tomography using Rytov's approximation, in *Acoustical Imaging*, E. A. Ash and C. R. Hill, eds., 12, pp. 599-608 (Plenum Press, New York, 1981).
- Mueller, R. K., Diffraction tomography. I. The wave equation, *Ultrasonic Imaging* 2, 213-222 (1980).
- Mueller, R. K., Kaveh, M., and Wade, G., Reconstructive tomography and applications to ultrasonics, *Proceedings of the IEEE* 67, 567-587 (1979).
- Robinson, B. S., and Greenleaf, J. F., Computerized ultrasound tomography, in *Three-Dimensional Biomedical Imaging*, R. A. Robb, ed., II, pp. 57-78 (CRC Press, Boca Raton, FL, 1985).
- Robinson, B. S., and Greenleaf, J. F., The scattering of ultrasound by cylinders: Implications for diffraction tomography. *Journal of the Acoustical Society of America* 80, 40-49 (1986)



*100 Views, 128 Pulses, 1.25-2.5 kHz,  $f_0 = 2.0$  MHz*

Fig. 9 Doppler tomograms through a flow phantom. A phantom consisting of looped tubes through which was flowing water containing talcolm powder was used to demonstrate this tomogram of flow. The images with flow and without flow are both scaled to peak so the clutter without flow can be visualized.

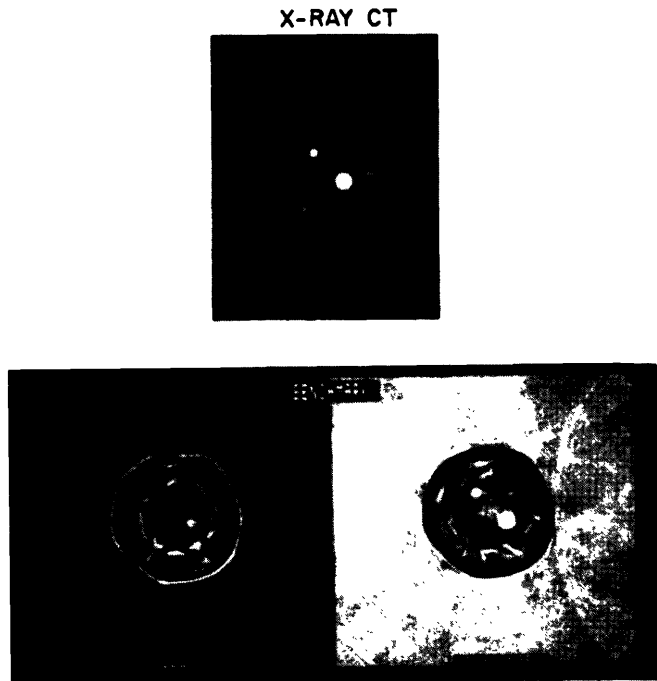


Fig. 10 Real and imaginary parts of the diffraction tomograms computed using the Born approximation (lower panel). Data were obtained from plane waves scattered from a breast phantom an x-ray CT through which is shown (upper panel). Although the brightness of these images is not quantitative, the position of the scatterers and their sizes are accurate, unlike tomograms obtained from straight line approximations.

- Sandritter, W., and Thomas, C., *Color Atlas and Textbook of Histopathology* (Yearbook Medical Publishers, Chicago, IL, 1979).
- Schreiman, J. S., Gisvold, J. J., Greenleaf, J. F., Bahn, R. C., Ultrasound transmission computed tomography of the breast, *Radiology* 150, 523-530 (1984).
- Sehgal, C. M., and Greenleaf, J. F., Derivation of scatter and absorption images from speed and attenuation reconstructions, *Ultrasonic Imaging* 7, 98-99 (1985) (Abstract).
- Sehgal, C. M., B. Porter, and Greenleaf, J. F., Relationship between acoustic nonlinearity and the bound and the unbound states of water, *IEEE 1985 Ultrasonics Symposium Proceedings* 85CH2209-5, II-883-886 (1985).
- Wells, P. N. T., Halliwell, M., Skidmore, R., Webb, A. J., and Woodcock, J. P., Tumour detection by ultrasonic Doppler blood-flow signals, *Ultrasonics* 15, 231-232 (1977).



## HIGH-DEFINITION REFLECTION MODE TOMOGRAPHY

A. Herment, S. Cherif, G. Demoment<sup>+</sup>, J.P. Guglielmi.

INSERM U. 256, Hôpital Broussais, Paris, France.

<sup>+</sup> Laboratoire des Signaux et Systèmes (CNRS/ESE), Gif-sur-Yvette, France.

Keywords : backscattering imaging - deconvolution - image reconstruction - echography.

### ABSTRACT

A method allowing for a high-resolution imaging, with a good S/N ratio, together with a reduced computational burden, is described in the present paper. It consists in the association of an axial deconvolution of B-scan images with a filtered backpropagation reconstruction over a limited angle.

- . A total time of image processing roughly equal to twice the square root of the time required for 2D deconvolution,
- . An improvement of the S/N ratio, close to the square root of the number of acquired images, as indicated by the theory,
- . An ideal choice for the scanning angle, of about 120 degrees for sector images of 90 degrees,
- . A very strong influence of the reconstruction filter amplified by the former deconvolution procedure.

### I. INTRODUCTION

The definition of acoustic images is strongly limited by the relative spreading of the point spread function of the echograph. This phenomenon is associated with the wavelengths employed, because of the important attenuation of the ultrasonic wave in tissues. However, it is possible, by means of a numerical restoration of the sampled signals, to compensate for the filtering effect of the echograph and to obtain ultrasound images with a higher resolution. In the particular case of imaging, a simplified procedure of restoration by deconvolution can be applied (1, 2, 3). It will constitute an arrangement between the improvement in definition and the complexity of calculations.

### II. DIFFERENT APPROACHES OF THE PROBLEM

The simplest and quickest approach consists in solving the problem in an unidimensional way, and by only correcting the smearing effect of the echograph in the axial direction (4). This method is of little interest since axial definition is still higher than the lateral one on the original image.

A closer approach consists in achieving a bidimensional deconvolution of the image (5, 6). The results obtained are generally rather good, with an improvement in the direction of propagation higher than in the transversal one. This is caused by the characteristics of the point spread function of the echographs (band-pass filter in the axial direction, low-pass filter with a quasi-gaussian spectrum in the lateral one). However, this approach requires generally important amounts of calculations, since their number is squared with respect to the previous case.

Fig. 1. Point spread function of the imaging system (video presentation)). A. Echography. B. Echography and axial deconvolution. C. Echography and 2D deconvolution. D. Reflection tomography and 1D deconvolution.



Fig. 2. Principle of acquisition with a sector scanner. Angle of the image :  $88^\circ$ . Number of lines : 44 for the presented applications.

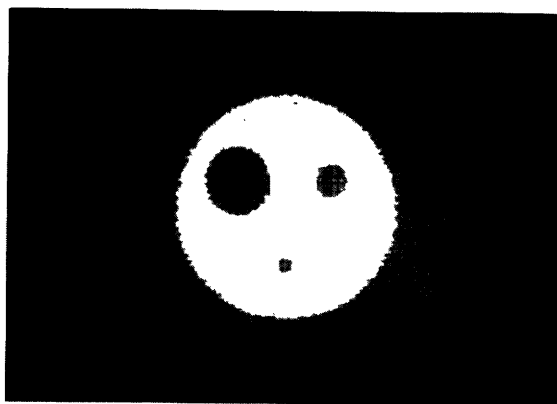
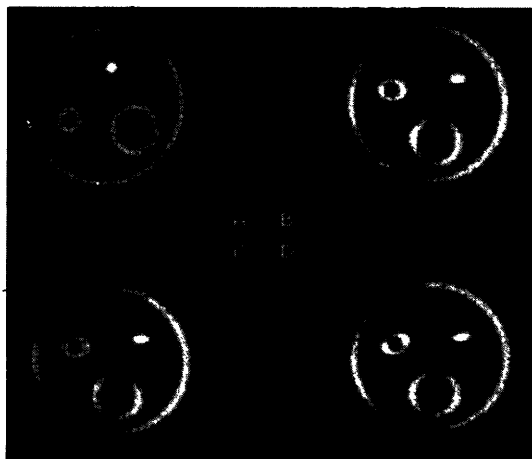


Fig. 3. Image reconstruction of raw images. Influence of the interpolation filter. A. 44 images distributed on  $180^\circ$ . B. 19 images distributed on  $90^\circ$ . C. 9 images distributed on  $90^\circ$ . D. 4 images distributed on  $90^\circ$ .





It is however possible to offer a third solution, allowing to conciliate a real bidimensional image improvement with reasonable computation times. It consists in using a filtered backprojection approach, in which projections are deconvolved, by the axial impulse response of the echograph, before reconstruction (7). Moreover, this approach is more suitable in leading to images that have a better signal-to-noise ratio than the previous ones due to the procedure of image reconstruction.

Figure 1 allows to compare the results obtained with these different approaches in the same conditions of acquisition . The deconvolution processes are always applied on the R.F. signals, in order to comply with the linear hypotheses imposed by deconvolution ; however, the results are presented in video format, after detection, like in conventional echography.

In A, the point spread function of the echograph clearly shows an axial definition higher than the lateral one. The image B corresponds to the result of the axial deconvolution alone ; of course, there is no improvement, in that case, of the lateral image definition. In C, the deconvolved point spread function presents a higher gain in axial definition than that obtained laterally, as it has already been noted. Lastly, in D, the point spread function restored by tomographic approach has the best definition.

### III. METHODOLOGY

#### III.1. Signal processing

The different steps used for image construction are as follows :

- . Data acquisition
- . Line-by-line deconvolution
- . Detection of each line (rectification + low-pass filtering)
- . Convolution of each line by a weighted  $\rho$  filter
- . Back-projection procedure

This approach, which was only used for high-resolution image reconstruction,, can be easily modified in order to be applied in tissue characterization. For instance, if the detection step is replaced by a double integration, the impedance image can be reconstructed (8). We must also emphasize that back-propagation reconstruction techniques can also be associated to deconvolution.

#### III.2. Data acquisition

A modification of tomographic approach was studied in order to break away from acquisition drawbacks inherent in this technique.

Though the choice of reflection tomography widens the number of structures that can be examined, and since the organ to be investigated is no more placed between two probes (transmission tomography), the use of a total angle of acquisition lower than  $180^\circ$  seemed to further improve this mode of investigation.

However, in order to maintain a correct filling of the Fourier domain, thus keeping a good quality of the reconstructed image, we have employed a sectorial image provided by an echograph instead of an usual projection, as

Fig. 4. Original data for reconstruction. A. S/N = 20 dB. B. S/N = 15 dB. C. S/N = 10 dB. D. S/N = 5 dB.

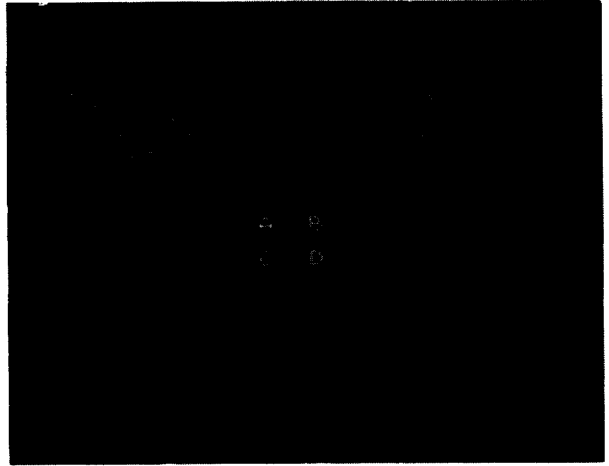
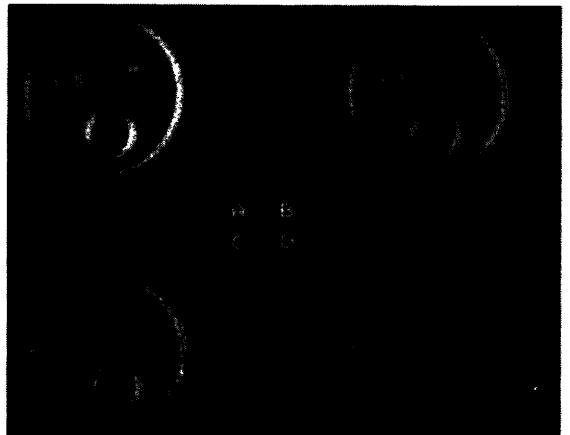


Fig. 5. Raw reconstruction with a soft ( $\alpha = 10\%$ ) tomographic filter. A. S/N = 20 dB. B. S/N = 15 dB. C. S/N = 10 dB. D. S/N = 5 dB.



Fig. 6. Raw reconstruction with an abrupt ( $\alpha = 90\%$ ) tomographic filter. A. S/N = 20 dB. B. S/N = 15 dB. C. S/N = 10 dB. D. S/N = 5 dB.



the original information. The redundancy of this information is an asset to the quality of reconstruction.

Figure 2 illustrates the choice of the method of acquisition considered for this simulation study. The acquisition of the image is achieved via a mechanical, sectorial system presenting a 88° sector. Only 44 lines of this image will be used for reconstruction. Each line includes 500 points sampled at 25 MHz. The probe frequency is 2.5 MHz. Nineteen incidences are collected with a 4.5° step over a total angle of 85.5°.

The studied object is made of a cylindrical, 8 mm-diameter phantom, hollowed out by three holes of .6 mm, 1.2 mm and 2.4 mm, respectively, which are distributed every 120°.

### III.3. Image deconvolution

The different R.F. images are deconvolved line by line by the axial impulse response of the echograph. In the present case, this response was sampled on 64 samples.

The performances of deconvolution, with respect to the noise, to the frequency-dependent attenuation, to the modification of echoes by the geometry of the medium, have been discussed elsewhere (2, 3, 5, 9) and will not be described here.

The deconvolution used, which was developed by Demoment et al (9), lies on a stochastic approach of the restoration problem. The fast algorithm which is developed is operated on by using a sub-optimal Kalman filter in which data are processed on line. The results obtained lead to achieve deconvolution, under the above mentioned conditions of acquisition, in a duration roughly equal to that of reconstruction. From this standpoint, the method proposed seems to allow for an interesting optimization of the ratio : definition improvement versus computation time.

### III.4. Detection

The detection used for imaging is simply obtained by rectification and low-pass filtering of echos.

### III.5. Tomographic filter

Then, each projection is convolved by the function :

$$f = \frac{\alpha^2}{4d} [2 \operatorname{sinc}(\alpha m) - \operatorname{sinc}^2(\alpha m/2)]$$

where  $\alpha$  is the fraction of the total spectrum up to the cutoff frequency ( $1/2 d$ ) that is passed by the filter,  $d$  is the sampling period of the signal,  $\operatorname{sinc}(\alpha m) = \sin 2\pi\alpha m / 2\pi\alpha m$ , proposed by Bracewell and Riddle. Here, the  $\alpha$  parameter must be optimized with respect to the parameters used in the deconvolution filter, in order to obtain on the reconstructed image the best agreement between the improvement in definition and the noise increase.

Fig. 7. Reconstruction associated with the 1D deconvolution using a soft filter. A. S/N = 20 dB. B. S/N = 15 dB. C. S/N = 10 dB. D. S/N = 5 dB.

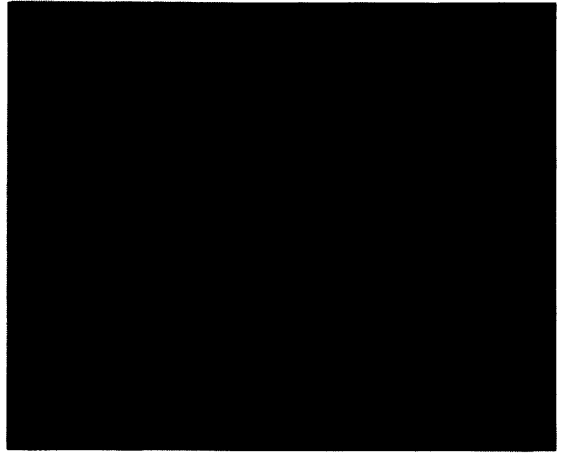
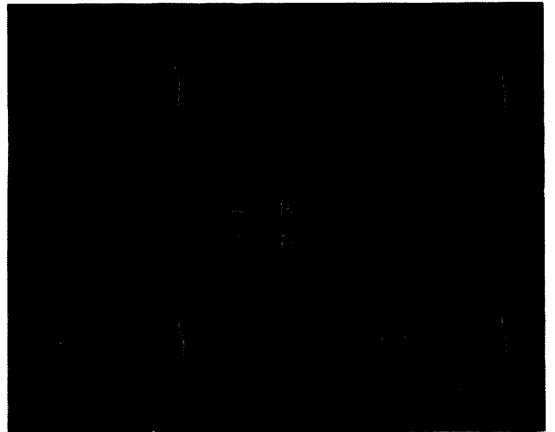


Fig. 8. Reconstruction associated with the 1D deconvolution using an abrupt filter. A. S/N = 20 dB. B. S/N = 15 dB. C. S/N = 10 dB. D. S/N = 5 dB.



### III.6. Reconstruction

We use a modified back projection method, in which data are projected on circles, to compensate for the geometry of acquisition, and estimated by linear interpolation from the four nearest neighbours.

Figure 3 shows the reconstruction, without deconvolution, of the simulated object, as a function of the number of images employed for this reconstruction. In A, the image was reconstructed from 44 sectorial images distributed along  $180^\circ$ ; thus, there is no restraint on the acquisition angular window. The image B corresponds to the choices above decided, in this simulation. It has been reconstructed from 19 images distributed along  $85.5^\circ$ . The modification of interfaces thickness shows the loss of information caused by the limited scanning. Figures C and D, reconstructed from only 9 and 4 sectorial images distributed on  $81^\circ$  and  $72^\circ$ , respectively, show the interest of the interpolation method employed.

### IV. RESULTS

The images of the object were reconstructed without and with deconvolution, from data collected under the above mentioned conditions (§. III.2.), for noise levels varying between 20 and 5 dB, and for two different settings of the reconstruction filter.

Figure 4 presents the original sectorial images for noise levels of : S/N = 20 dB in A, S/N = 15 dB in B, S/N = 10 dB in C, and S/N = 5 dB in D. As images A and B are presented on 4 positive levels and on 4 negative ones, they do not allow to display correctly a noise whose amplitude is quite always lower than the fourth of that of signals.

Figures 5 and 6 represent the reconstructed object in the same noise conditions. On Figure 5, a "soft" tomographic filter ( $\alpha = 0.1$ ) was used. This filter does not restore all the high spatial frequencies that are lost by reconstruction, but it limits the noise on the reconstructed image. On Figure 6 an "abrupt" tomographic filter was employed ( $\alpha = 1$ ), leading to an optimal definition but to a noise increase on the reconstructed image. The influence of this filter is specially obvious in 5D, where the preponderance of spatial low frequencies over the final image causes, after detection, a quasi continuous component, and, in 6C and D, where reconstruction artefacts become visible on the reconstructed image, which is very rich in high frequencies.

Figures 7 and 8 show the result of reconstruction, after deconvolution, for the same signal-to-noise ratios and for the two same tomographic filter settings ( $\alpha = .1$  in 7) and ( $\alpha = 1$  in 8). It is interesting to note that the improvement in definition caused by deconvolution partially lessens the modification of interface thickness due to a limited angular window. It is also clearly obvious that the definition gain and the noise on the reconstructed image depend directly on both the deconvolution filter parameters and on those of the reconstruction filter.

## V. CONCLUSION

The results of this preliminary study seem to indicate that the number of lines, on each sectorial image, as well as the number of chosen images, are sufficient to application to high definition imaging with S/N ratios of about 10 dB. On the other hand, the acquisition angular window should be enlarged ( $120^\circ$ ) in order to improve the quality of interface reconstruction.

Lastly, it clearly appeared that an optimization of the reconstruction filter, with respect to the parameters of the deconvolution filter, should be contemplated in order to have a balance between the improvement in definition and the increase in noise on the image.

## REFERENCES

- [1] Papoulis, A., and Chamzas, C., Improvement of range resolution by spectral extrapolation, *Ultrasonic Imaging*, 1, pp. 121-135 (1979).
- [2] Robinson, D.E., and Wing, M., Lateral deconvolution of ultrasonic beams, *Ultrasonic Imaging*, 6, n° 1, pp. 1-12 (1984).
- [3] Liu, N.C., Fatemi, M., and Waag, R.C., Digital processing for improvement of ultrasonic abdominal images, *IEEE Transactions on Medical Imaging*, MI-2, n° 2, pp. 66-75 (1983).
- [4] Herment, A., and Demoment, G., Improvements in resolution of echographs through 1D on-line deconvolution, pp. 67-86, in *Ultrasonic Tissue Characterization 4*, J.M. Thijssen and M. Smith Eds, (1984).
- [5] Fatemi, M., and Kak, A.C., Ultrasonic B-scan imaging : theory of image formation and a technique for restoration, *Ultrasonic Imaging*, 2, n° 1, pp. 1-47 (1980).
- [6] Saint-Felix, D., Herment, A., and Du, X.C., Fast deconvolution, application to acoustical imaging, in : *Ultrasonic tissue characterization and echographic Imaging 5*, J.M. Thijssen and V. Mazzeo Eds, (1986).
- [7] Roberts, B.A., and Kak, A.C., Reflection mode diffraction tomography, *Ultrasonic Imaging*, 7, pp. 300-320 (1985).
- [8] Lefebvre, J.P., Acoustic impedance tomography, *Traitement du signal*, 2, n° 2, pp. 103-110 (1985).
- [9] Demoment, G., Reynaud R., and Herment, A., Range resolution improvement by a fast deconvolution method, *Ultrasonic Imaging*, 4, n° 4, pp. 435-451 (1984).
- [10] Image reconstruction from projections. *Topics in applied physics*, vol. 32. G.T. Herman Ed., Springer Verlag, Berlin - New-York (1979), p. 32.

# THE DELFT ACOUSTIC MICROSCOPE AND SYNTHETIC FOCUSING

Wim van Hoorn and A.J. Berkhout  
Lab. of Seismics and Acoustics  
University of Technology  
P.O. Box 5046, 2600 GA Delft

Our recently started project concerning acoustic microscopy will be introduced. The microscope image is obtained by means of synthetic aperture techniques. A general overview of these techniques will be given, followed by an example: zero-offset focussing. It will be shown that the lateral resolution of this imaging technique is superior to that of the conventional acoustical imaging techniques.

**Keywords:** aperture synthesis, focussing, scanning acoustic microscopy

## 1 INTRODUCTION

Since 1975 our group has carried out research in the field of ultrasonic medical imaging and information extraction techniques. Now we want to extend our activities to tissue characterization. At the beginning of this year we started the construction of a Scanning Acoustic Microscope (SAM). The aim of our new project is to study the interaction between tissue and acoustic wavefields in more detail than can be done with conventional scanners. The extrapolation of results of the high resolution (high frequency) studies to the lower resolution (lower frequency) situation should lead to a better understanding of the important low frequency interaction mechanisms, and thus facilitate clinical tissue recognition.

Since the ins and outs of conventional scanning acoustic microscopy are discussed extensively elsewhere (Quate<sup>(1)</sup>, Kessler<sup>(2)</sup>, Briggs<sup>(3)</sup>), we shall restrict ourselves to a brief description of the microscope working in the reflection mode. The object, e.g. a tissue sample, is scanned with a focussed electro-acoustic transducer. At every point of a rectangular

grid a point measurement is carried out. The peak value of the detected signal within a time interval corresponding with reflection within the focal zone of the transducer is stored into a computer memory. The contents of the memory are then displayed on a video screen.

Our acoustic microscope differs from the above described microscope in two important aspects. First: instead of detecting a peak value of the signal, we will digitize the complete RF-signal, preserving the original amplitude and phase spectrum. Second: instead of imaging the object by means of a focussed acoustic beam, we will use omni-directional sources and detectors and calculate the image by means of synthetic aperture techniques. In the next chapter an outline will be given of echo-acoustic synthetic aperture techniques in general. In chapter 3 the use of those techniques will be demonstrated by an example and it will be shown that they produce a high resolution image for all depth levels.

## 2 APERTURE SYNTHESIS

In ultrasonic imaging almost always use is made of focussed acoustic wavefields. The imaging of the object is realized by the relatively small lateral extension of the acoustic beam in the focal zone. The reflected acoustic energy mainly comes from diffractors in the focal zone and every point in the object is illuminated only once. Every measurement images another part of the object.

Imaging by means of synthetic aperture techniques differs fundamentally from the above mentioned technique. Sources and detectors do not have a fixed focus, but are essentially omni-directional, and every point of the object is illuminated many times and from many directions. Doing so, the information of every object point is spread out over the recorded image. This smearing of the information is dealt with by combining all measurements and, using knowledge about wave propagation, calculating the sharp image from the measurements. This image can have an optimal lateral resolution for every depth level.

In this chapter we discuss echo-acoustic aperture synthesis in general. First the model that describes the experiment will be introduced: " the forward problem ". Then, armed with the forward model, we will show how the measured data can be mapped into an image of the object: " the inverse problem ". A more extensive treatise on this subject can be found in Berkhout (4).



## 2.1 The model, the forward problem: the measured data

The forward problem can be formulated as follows:

" Given the incident acoustic source field at the surface of the object and given the acoustic parameters of the object, what will be the reflected acoustic wave field at the surface of the object ? "

In the following section we refer to figure 2.1. An arbitrary acoustic source is situated at the surface of the object, at depth level  $z = z_0$ . Due to the limited spectral bandwidth we don't need to characterize the wavefields and object continuously in space and time, but are permitted to

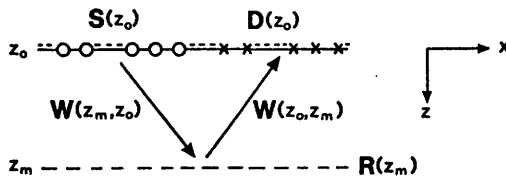


Fig. 2.1 The forward model

use a spatially and temporally sampled description of wavefields and object. For simplicity we restrict ourselves to one lateral dimension,  $x$ , without loss of validity of the hereafter presented model. The source wavefield at the surface is then denoted by the vector  $S(x, z=z_0, f)$ , i.e. the spectral wavefield component with temporal frequency  $f$  (parameter) at lateral position  $x$  (variable) and at depth level  $z = z_0$  (parameter). If, for example, a single omni-directional transducer is used, all elements of vector  $S$  are zero, except for the one corresponding with the  $x$ -position of the transducer. The emitted wavefield propagates to depth level  $z = z_m$ , described by the propagation (matrix) operator  $W(x, z_m, z_0, f)$ . Omitting the  $x$  and  $f$  argument, we can write for the source wavefield at depth level  $z = z_m$ :

$$S(z_m) = W(z_m, z_0)S(z_0) . \quad (2.1)$$

At depth level  $z = z_m$  the source wavefield is reflected, described by matrix operator  $R(x, z_m, f)$ . The reflected wavefield at  $z = z_m$  is given

by:

$$P_r(z_m) = R(z_m) W(z_m, z_0) S(z_0) . \quad (2.2)$$

Next we can describe the propagation of the reflected wavefield to the surface of the object ( $z = z_0$ ) by a third operator:

$$P_r(z_0) = W(z_0, z_m) R(z_m) W(z_m, z_0) S(z_0) . \quad (2.3)$$

Since the back propagated reflected wavefield is not in every experiment detected at every  $x$ -position, but only at certain (one or more) detector positions, we have to insert a detector operator  $D(x, z, f)$ , which accounts for all spatial, angular and frequency dependence of the detectors:

$$P(z_0) = D(z_0) W(z_0, z_m) R(z_m) W(z_m, z_0) S(z_0) . \quad (2.4)$$

This is the measured response coming from depth level  $z = z_m$  of the object. By repeating this process for all depth levels and frequencies of interest and combining the results, the response of the complete object can be modelled.

When repeating this experiment with different source and detector positions, we can join the various source vectors in a source matrix  $S(x, z, f)$  and do the same with the various response vectors to form a response matrix  $P(x, z, f)$ . Now the complete assembly of experiments can be denoted by:

$$P(z_0) = D(z_0) W(z_0, z_m) R(z_m) W(z_m, z_0) S(z_0) . \quad (2.5)$$

With this equation we mean to say: during the  $i^{\text{th}}$  echo experiment we measured a response written down in the  $i^{\text{th}}$  column of matrix  $P$  and it can be modelled by application of the operator  $DWRW$  on the  $i^{\text{th}}$  column of the source matrix  $S$ , containing the then used source wavefield.

## 2.2 The inverse problem: the image

The inverse problem can be formulated as follows:

" Given the reflected wavefield and given the incident source wavefield at the surface of the object, what are the acoustic parameters of the object ? "

For the solution of this problem we take equation 2.5 as a starting point and aim now at the estimation of matrix operator  $R$ . From eq. 2.5 it will be clear that the measured data matrix  $P$  contains all the information of matrix  $R$ , but it is distorted by the source matrix  $S$ , detector matrix  $D$  and the propagation matrices  $W$ . In other words: in order to reconstruct the reflection properties of the object( i.e. to image), we have to compensate for the propagation of the wavefields in the object and for the source and detector configuration.

First we compensate for the propagation of the source wavefield in the object, by using an inverse operator defined by:

$$F(z_0, z_m) = ( W(z_m, z_0) S(z_0) )^{-1} . \quad (2.6)$$

The  $-1$  denotes inversion in some optimum sense. Application of this operator to  $P$  gives:

$$\begin{aligned} P(z_0) F(z_0, z_m) &= \\ &= D(z_0) W(z_0, z_m) R(z_m) W(z_m, z_0) S(z_0) F(z_0, z_m) \\ &\approx D(z_0) W(z_0, z_m) R(z_m) \end{aligned} \quad (2.7)$$

where the  $\approx$  sign accounts for the approximation of the inverse operator. If we compensate analogously for the propagation of the upward travelling reflected wavefield with operator  $F(z_m, z_0)$ :

$$F(z_m, z_0) = ( D(z_0) W(z_0, z_m) )^{-1} \quad (2.8)$$

then we get:

$$\begin{aligned}
 F(z_m, z_0) P(z_0) F(z_0, z_m) &\approx \\
 &\approx (D(z_0) W(z_0, z_m)^{-1}) D(z_0) W(z_0, z_m) R(z_m) \\
 &\approx R(z_m) .
 \end{aligned}
 \tag{2.9}$$

Repeating this process for all depth levels and all frequencies of interest will give the image of the complete object. This will be demonstrated from an example in the next chapter.

### 3 SYNTHETIC ZERO-OFFSET FOCUSING

The general inverse procedure as treated in chapter 2 is in many practical situations unnecessarily complicated and (computer)time consuming. In most medical situations the object is more or less homogeneous for wave propagation velocity and data acquisition is carried out with coinciding source and detector (zero offset between source and detector). These two facts facilitate the imaging a great deal. We will first show that under these assumptions the operator  $W$  is a very simple one and that the inverse operator  $F$  is easy to derive. Then a mathematical trick and a reformulation of our model will be introduced which enable the imaging of all depth levels in one operation.

Due to the fact that the object is homogeneous for wave propagation, we can take advantage of working in the wavenumber-frequency domain. By two dimensional Fourier transformation of a wavefield we decompose the complicated wavefield into a set of simple plane waves. The propagation of a plane wave over a distance  $z$  in the  $z$ -direction in a medium with wave propagation velocity  $c$  can be described by a simple phase shift:

$$P(k_x, z, \omega) = \exp(-jk_z z) P(k_x, 0, \omega) , \tag{3.1}$$

where  $k_z = ((\omega/c)^2 - k_x^2)^{1/2}$ ,  $k_x$  the wavenumber in the  $x$ -direction, and  $j^2 = -1$ . This means, that we can take the exponent in eq. 3.1 to be the continuous Fourier representation of the propagation

operator  $W$ . Now it is easy to see that the inverse propagation of a plane wave is described by a phase shift in the opposite direction:

$$P(k_x, 0, \omega) = \exp(+jk_z z) P(k_x, z, \omega), \quad (3.2)$$

which gives us the operator  $F$ . In principle the inverse problem has now been solved, but we still have to do the job for all depth levels separately. The fundamental reason for this is that although every separate echo experiment can be described by the wave equation, this does not hold for the ensemble of the measurements. However, for this special case of coinciding source and detector in every measurement, we can reformulate the problem in such a way, that the wave equation holds for the ensemble of measurements. This new model is called the exploding reflector model with the half velocity substitution. Instead of a model with sources and detectors at the surface of the object, we use a model with only detectors at the surface of the object and where all diffractors and reflectors in the object are substituted by acoustic (point) sources. At time  $t = 0$  all these sources start to emit acoustic energy. These waves propagate to the surface of the object with half the original propagation velocity:  $\hat{c} = c/2$ , see fig. 3.1. In this model the recorded traveltimes are correct, but the amplitude is slightly distorted, compared to the correct model.

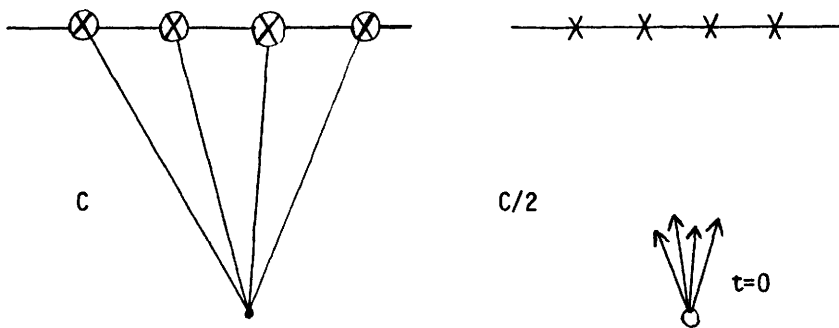


Fig. 3.1 The reformulation of the model: the exploding reflector model

Now we can estimate the reflectivity distribution in the object by calculating the pressure distribution at time  $t = 0$ , when all sources

started to send out their waves. So the question is:

Given the measured response  $p(x,z=0,t)$ , what was  $p(x,z,t=0)$  in our exploding reflector model ?

We start the derivation with a two-dimensional Fourier transform of the wanted result and then work backward to the measured wavefield:

$$p(x,z,t=0) = (1/2\pi)^2 \iint P(k_x, z, \omega) \exp(-jk_x x) d\omega dk_x \quad (3.3)$$

Next we apply an inverse wavefield extrapolation to depth level  $z = 0$ :

$$P(k_x, z, \omega) = P(k_x, 0, \omega) \exp(+jk_z z) \quad (3.4)$$

where  $k_z = (k^2 - k_x^2)^{1/2}$ ,  $k = \omega/\hat{c}$  and  $\hat{c} = c/2$ . Following Stolt (5) we map the  $\omega$ -axis into the  $k_z$ -axis ( see fig. 3.2):

$$P(k_x, 0, \omega) = P(k_x, 0, \hat{c}(k_x^2 + k_z^2)^{1/2}) \longrightarrow P'(k_x, k_z, t=0) \quad (3.5)$$

and replace the integration variable  $\omega$  by  $k_z$ :

$$d\omega = \hat{c} \left[ \frac{k_z}{\sqrt{k_x^2 + k_z^2}} \right] dk_z = J dk_z \quad (3.6)$$

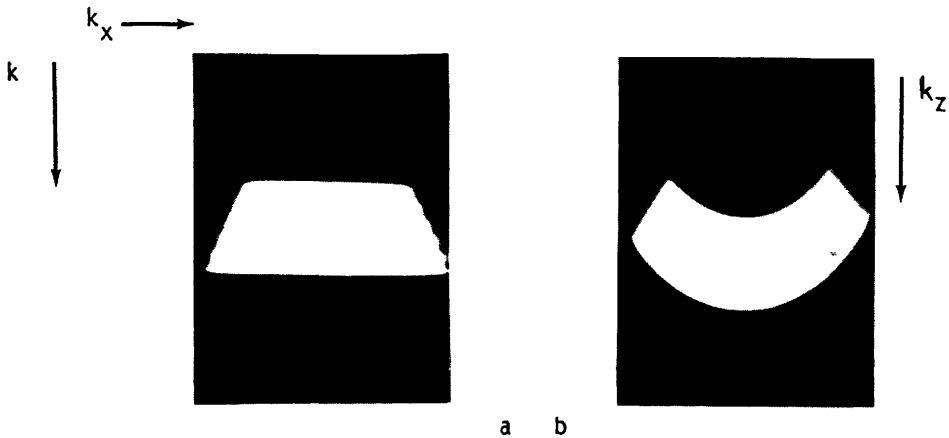


Fig. 3.2a Data in  $k_x - \omega$  domain, before mapping of  $\omega$ -axis to  $k_z$ -axis  
 b Data in  $k_x - k_z$  domain, after mapping

Combining eqs. 3.3 to 3.6 we get:

$$p(x,z,t=0) = (1/2\pi)^2 \iint P'(k_x, k_z, t=0) \exp(jk_z z) \exp(-jk_x x) J dk_x dk_z \quad (3.7)$$

where

$$P'(k_x, k_z, t=0) = P(k_x, z=0, \hat{c}(k_x^2 + k_z^2)^{1/2}) \quad (3.8)$$

The result of this focussing procedure applied to the dataset of fig. 3.2d is given in fig. 3.2e . It is clear that the object is imaged sharply at every depth level and the lateral resolution is even better than the axial resolution. The same object has been scanned with a real-time scanner having one focus distance in transmission ( at  $z = 90$  mm) and time varying focus distance in reception and the produced image can be seen in fig. 3.2f. Apart from the depth varying focus quality, the lateral resolution is worse due to the limited aperture angle of such a scanner.

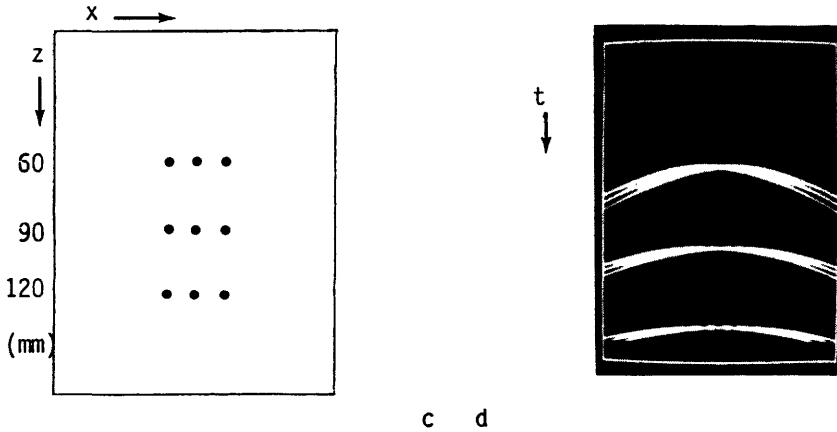


Fig. 3.2c The object

d The measured Zero-Offset dataset

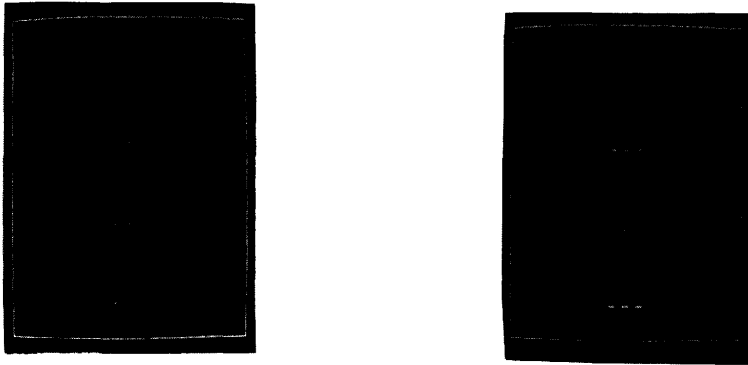


Fig. 3.2e The image after synthetic focussing of the dataset of fig. 3.2d  
3.2f The image as produced by real-time scanner having a fixed focus  
in transmission ( at  $z = 90$  mm) and a time varying focus in  
reception.  
Dynamic range 20 dB in both images

### LITERATURE

- (1) Quate, C.F., Acoustic microscopy, Physics Today, august 1985.
- (2) Kessler, L.W. and D.K. Yuhas, Acoustic microscopy: a tutorial review,  
in 1979 Acoustical Imaging proceedings, vol 9, pp 275 - 300.
- (3) Briggs, A., An introduction to scanning acoustic microscopy  
( Oxford University press, 1986)
- (4) Berkhout, A.J., Seismic migration part A, theoretical aspects  
( Elsevier scientific publishing company Amsterdam, 1982)
- (5) Stolt, R.H., Migration by Fourier transform, Geophysics vol. 23, no. 1  
1978



Session 2 - TEXTURE

Chairmen : D. Nassiri, D. Nicholas



## TC – SYSTEM INFLUENCE ON THE B – MODE IMAGE FEATURES

Ivan Zuna, Jochen Volk, Ulrich Raeth\*, Dieter Schlaps, Wilfried Naves, Adolf Lorenz, Dorothea Lorenz, Gerhard van Kaick, Walter J. Lorenz

Institute of Nuclear Medicine, German Cancer Research Center, Heidelberg, West Germany, and the \*Department of Gastroenterology, University of Heidelberg Hospital and Medical School, Heidelberg, West Germany

To test the degree of transferability of ultrasound image texture parameters, an electronic phased array sector – and static grey scale compound system have been compared using the results of our liver and thyroid clinical studies. It is shown that, for the thyroid studies, the normalized values of the relative frequency of edge elements, entropy from the cooccurrence matrix and mean greylevel are transferable from one system to the other without loss of diagnostic accuracy. For the liver studies however, only the relative frequency of edge elements, entropy and correlation from the cooccurrence matrix are equally well transferable. The diagnostic information however obtained by the mean greylevel differs in both systems. It is demonstrated, that the diffraction – correction of images from the phased array sector system significantly improves the transferability of the parameters.

**Key Words:** B – scan image analysis; liver disease; pattern recognition; rf – signal analysis; thyroid disease; ultrasonic tissue characterization

### INTRODUCTION

Over the past five years two different ultrasonic tissue characterization systems have been used at the Institute of Nuclear Medicine of the German Cancer Research Center [1]. In several clinical studies a texture parameter set of about 20 individual features based on the cooccurrence and runlengths matrices, on the first order greylevel and gradient statistics and on the two dimensional power spectrum have been selected to describe tissue specific signatures.

Obviously, the actual values of image texture parameters depend on physical properties and the hardware/software configuration of the ultrasonic tissue characterization system. To test the degree of transferability of these parameters, we compared our electronic phased array sector – and static grey scale compound systems using the results of clinical liver and thyroid studies.

After discussing the transferability of texture features, we describe our method to obtain the power spectrum and the envelope of the rf echo signal from an downmixed intermediate signal.

**Fig. 1. Brightness diffraction correction function used.**

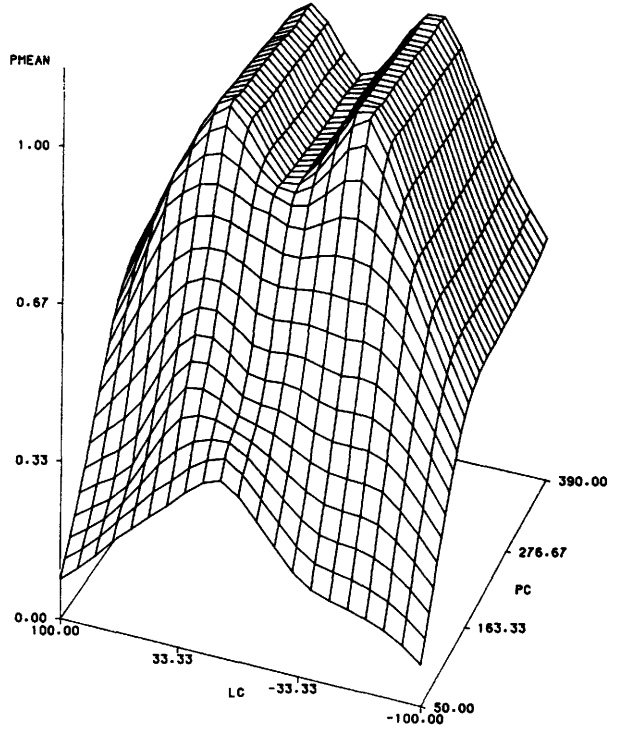
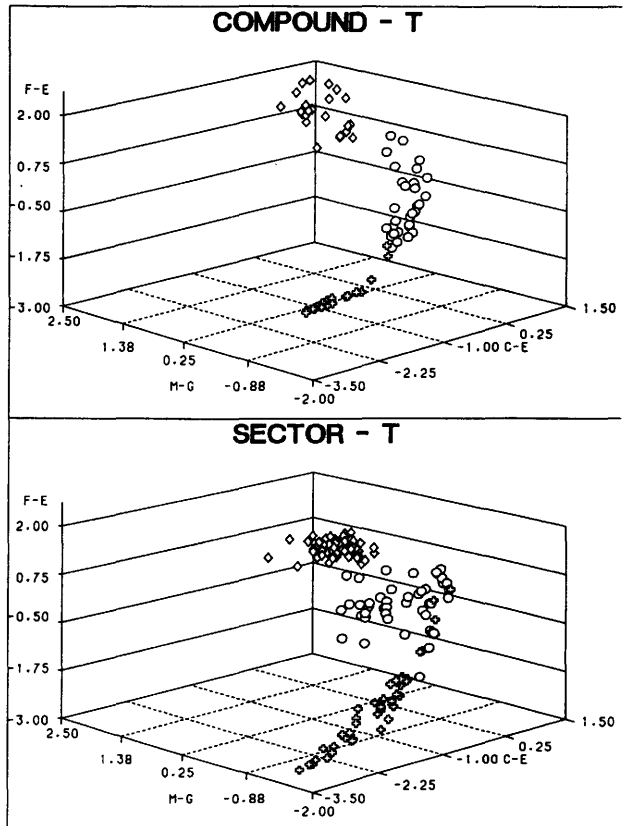


**Fig. 2. Thyroid comparison study: discrimination results using both systems. Tissue states examined are 'normal', 'malignant' and 'cystic'.**



## DATA ACQUISITION SYSTEMS

In this study, two different data acquisition and evaluation systems have been used.

The Picker Echoview 80 L static grey scanner with a 3.5 MHz (liver study) and a 5 MHz (thyroid study) single crystal transducer is used as a front end in the first system. Each liver or thyroid scan consists of 1024 video A-lines which are sampled and digitized with an amplitude resolution of 8 bit. Data acquisition is carried out using a standard PDP-11/34 computer. The acquired amplitude and location data are stored on a magnetic tape. Further processing is performed off line by means of a VAX-11/780 computer.

From the set of A-lines and the location information, the two-dimensional digital image is generated using the interpolation scan conversion method and displayed on a Ramtek image display system. The image matrix with a pixel resolution of 1.2 mm for the liver image and 0.3 mm for the thyroid image respectively is created by choosing a ROI from a RAMTEK display and stored for further mathematical processing.

A Hewlett Packard HP77020A phased array electronic sector scanner (Radiology version) is used to acquire the video A-lines. The 90 degrees sector image is acquired in 120 consecutive lines of 396 points each, with a amplitude resolution of 6 bits. Using the interpolation scan conversion method, the image matrix with a pixel resolution of 0.47 mm for the liver image and 0.33 mm for the thyroid image respectively is build up and stored for further processing. No attenuation correction before texture analysis is done.

In addition, the intermediate signals with a carrier frequency of 2.1 MHz for the 3.5 MHz transducer and of 2.5 Mhz for the 5Mhz transducer respectively, are acquired within the selected region-of-interest and sampled at a frequency of 16 MHz and an amplitude resolution of 8 bits and stored with the location information on the disk.

The highspeed data interface is driven by a Hewlett Packard HP1000-A600 microcomputer (main storage capacity being 2 Megabytes, disk storage capacity 64 Megabytes) providing sufficient memory and processing speed to acquire, process and store the ultrasonic information.

## TEXTURE ANALYSIS

The software components of both systems enable to calculate a basic texture parameter set of more than 100 individual features. The parameters originate from the first-order greylevel statistics, i.e. greylevel histogram, the first order gradient statistics, the power spectrum, the second-order greylevel or gradient statistics, i.e. the greylevel or gradient cooccurrence matrix and from the greylevel runlength histograms.

From this set of parameters which is described in detail elsewhere [2], nineteen optimum parameters have been selected using the factor and discriminant analysis approaches (mean greylevel, variance of greylevels, ten percent quantile, skewness and curtosis of the greylvel distribution, mean gradient, variance of gradients and relative frequency of edge elements, central ring sum and sector sums in the axial

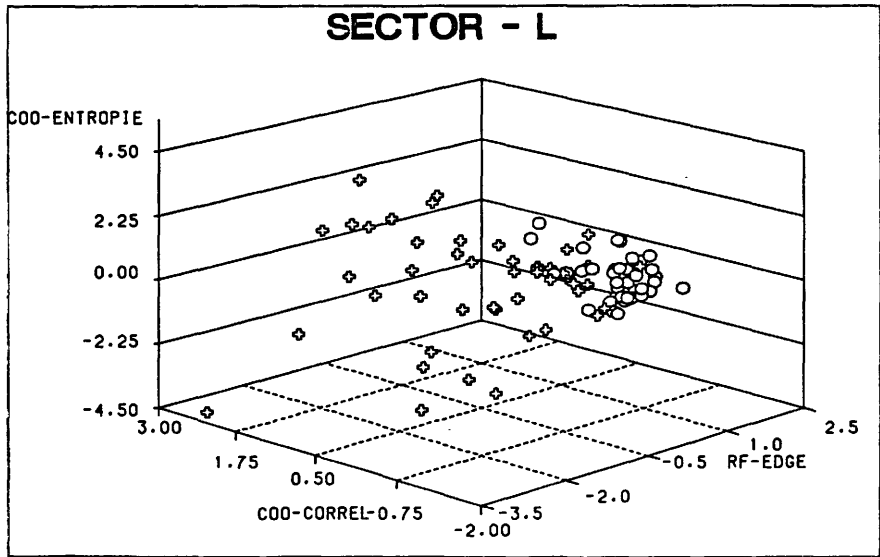
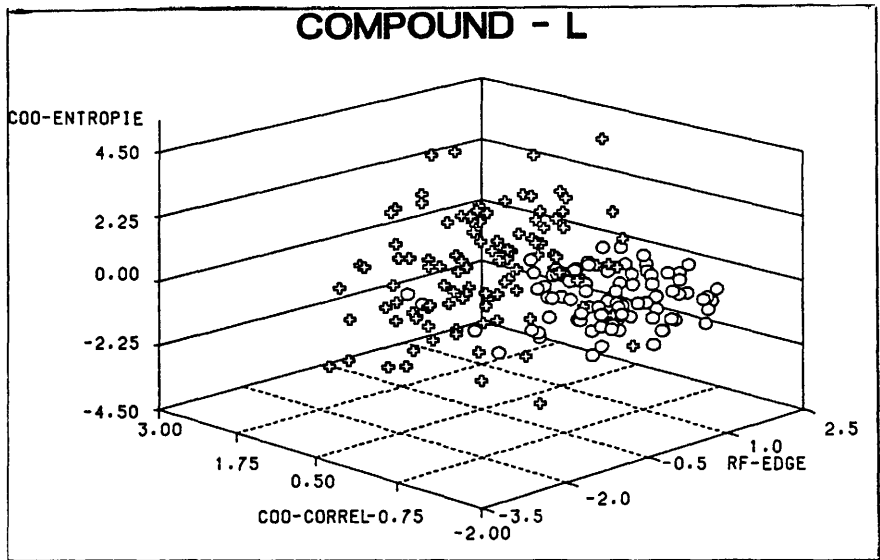


Fig. 3. Liver comparison study: discrimination results using both systems. Tissue states examined are 'normal' and 'malignant'.

and lateral direction respectively from the power spectrum, contrast, second angular moment, entropy and correlation from the greylevel cooccurrence matrix with the displacement of four pixels in the axial direction, and run percentages, long-run emphasis, greylevel distribution and runlength distribution from the greylevel runlength matrix with the axial runs and 4 byte greylevel resolution).

The above features have been tested for transferability.

## PROOF OF TRANSFERABILITY

The following statements describe our method to obtain transferable features:

A. For a given tissue characterization system, there is a set  $A$  of orthogonal B-mode image features, describing the system image properties. This set can be found using the factor analysis approach.

B. For a given clinical problem, there is a set  $B$  of B-mode image features, which carry diagnostic information about the tissue of interest. This set can be found using the discriminant analysis approach.

C. For a given tissue characterization system  $S_1$  and a given clinical problem, the intersection  $(A \cap B)/S_1$  is obviously a set of diagnostically relevant B-mode image features, which are mutually orthogonal.

D. For two different systems  $S_1$ ,  $S_2$  and a given clinical problem, all features, which are contained in the intersection  $(A \cap B)/S_1$   $(A \cap B)/S_2$  are suitable for proof of transferability.

E. After normalization, the features yielding a similar discrimination between defined diagnostical classes in both systems are transferable.

## DIFFRACTION CORRECTION

In radiofrequency signal analysis, it is generally accepted that diffraction correction must be applied to eliminate transducer-specific properties from the signal spectra. Using a tissue mimicking phantom, Volk [3] has shown, that the spatial distribution of greylevels in the phased array sector B-mode image is strongly position-dependent without brightness diffraction correction.

To tackle this problem, we measured the image brightness as a function of depth and angle using a movable tissue phantom in a water tank. The phantom was positioned at varying depths and angles, and the brightness was measured just below the top of the phantom to find the correction function value for different depth and angle settings. From these measurements a brightness diffraction correction function was calculated (see figure 1.) and used to correct all liver images from the phased array sector system.

## CLINICAL RESULTS

To evaluate our approach, 23 images of normal thyroids, 32 images of thyroidal carcinomas and 21 images with cystic lesions was selected from the Picker system. 60 images of normals, 48 images of thyroidal carcinoma and 54 images of thyroidal

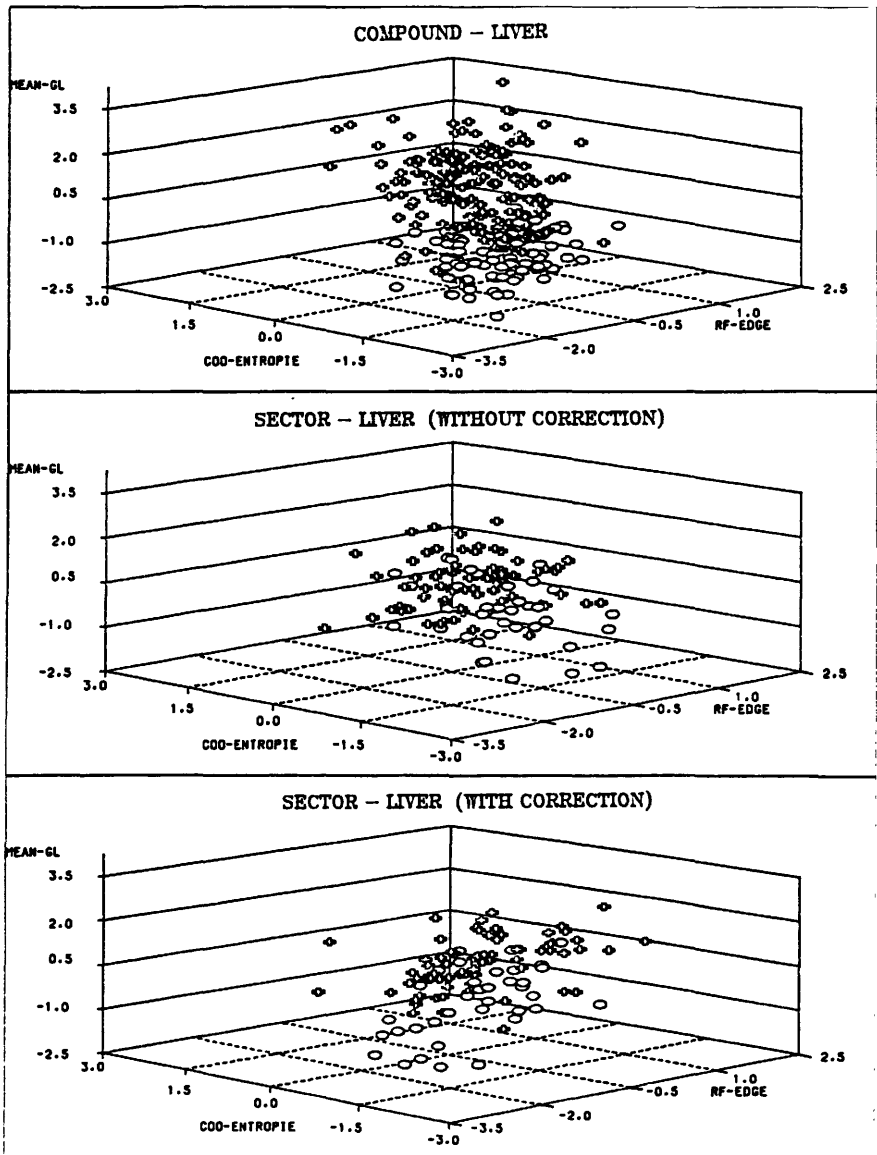


Fig. 4. Liver comparison study: discrimination results using both systems. Tissue states examined are 'normal' and 'diffuse disordered'.



cysts have been obtained from the HP sector scanner.

After gaussian normalization, the mean greylevel, relative frequency of edge elements and entropy yielded the best discrimination between the defined tissue classes ( Fig. 2). The diamonds represent normal images, the circles the tumors and crosses the cysts. The full transferability of features is demonstrated by the almost identical location of clusters.

In the liver studies, 181 images showing diffuse liver diseases, 109 images showing malignant liver diseases and 91 normals acquired with the Picker system were selected. Further, 78 images of diffuse liver diseases , 48 of malignant liver diseases and 38 normals acquired with the HP system have been analyzed.

For the discrimination of malignant liver tissue (crosses on the fig.3) from normal liver (circles on the figure 3.), the relative frequency of edge elements, entropy and correlation proved to be transferable from one system to the other (see figure 3.).

For the discrimination between diffuse liver diseases and normals, the mean greylevel, entropy and relative frequency of edge elements yielded a good results using the Picker system (upper section of fig.4). The crosses represent diffuse, circles normal liver images.

Using the HP system without a diffraction correction however, discrimination of the two classe was not possible (intermediate section of fig.4).

After diffraction correction (lower section of fig.4) , the discriminative power and the degree of transferability of both the relative frequency of edge elements and entropy was significantly higher. The correction however failed to improve the discriminative power of the mean greylevel in the HP system.

## OUTLOOK

Recently, three interesting ultrasonic tissue scattering parameters have been defined and accurately measured from the first- and second-order statistical properties of the intensity image texture [4]. To calculate these features as well as the attenuation coefficient, the envelope and the power spectrum of the unprocessed rf-signals must be available.

A method to reconstruct the original rf-signal from the downmixed intermediate frequency signal is shown for the 3.5 MHz transducer in the figure 5.

This reconstruction will us enable to calculate the above scattering and attenuation parameters to test the diagnostic performance of these parameters using our extensive databank of liver images in comparison to the diagnostical power of our B-mode images parameters.

## REFERENCES

- [1] Zuna, I., Schlaps, D., Raeth, U., et al., et al., System Dependency of B-Mode Image Parameters, , in Ultrasonic Tissue Characterization and Echographic Imaging 5, J.M. Thijssen and V. Mazzeo, ed., Proceedings of the fifth European Communities Workshop, pp. 147 - 152 (1985)
- [2] Raeth, U., Schlaps, D., Limberg, B., Diagnostic Accuracy of Computerized B-Scan Texture Analysis and Conventional Ultrasonography in Diffuse Parenchymal

and Malignant Liver Disease, J Clin Ultrasound 13, 87 - 99, 1985

[3] Volk, J., Zuna, I., Schlaps, D., et al., Scanner Dependence and System Correction of the Mean Grey Level B-mode Image Parameter, Ultrasonic Imaging 8, 62 (1986)

[4] Insana, M. F., Wagner, R. F., Garra, B. S., et al., Analysis of ultrasound image texture via generalized Rician statistics, Optical Engineering, Vol.25 No.6, 1986

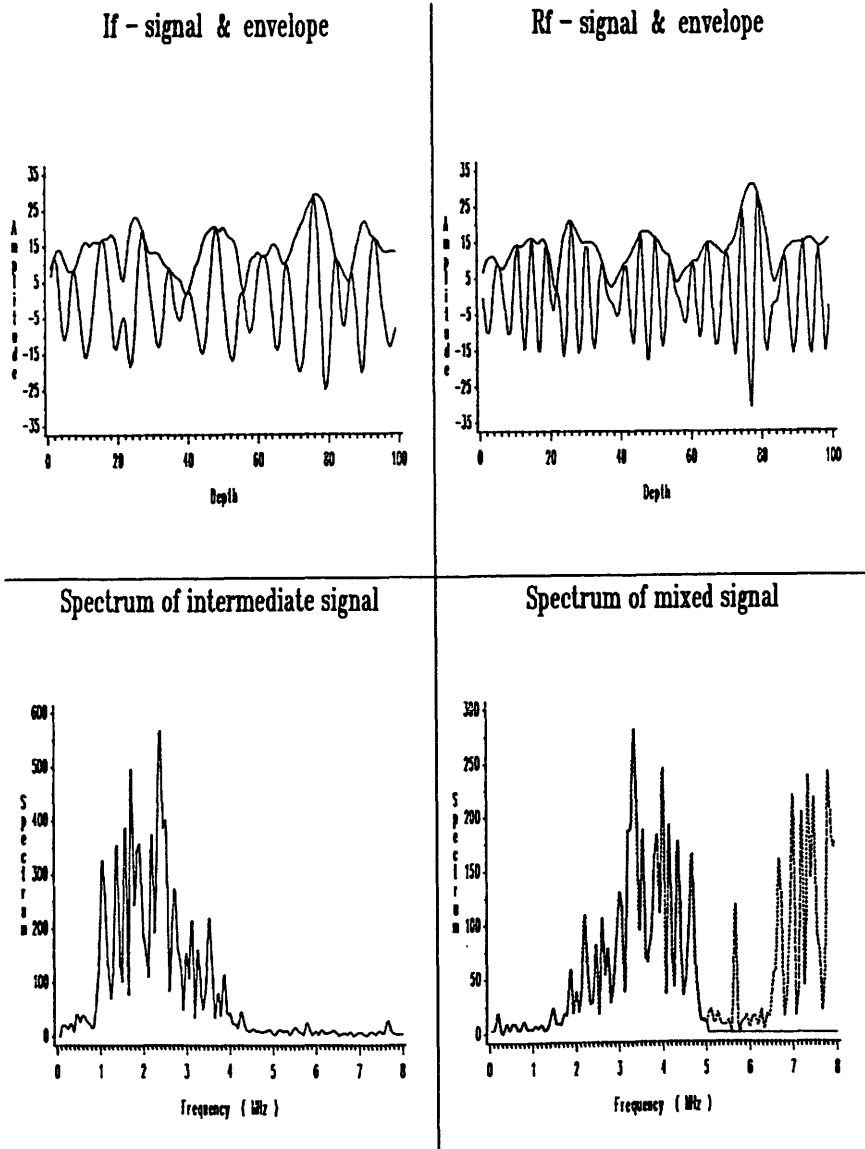


Fig. 5. Reconstruction of the original rf-signal from the intermediate frequency signal.

# PREPROCESSING AND TEXTURE ANALYSIS OF IN VIVO B-MODE ECHOGRAMS

B.J.Oosterveld, J.M.Thijssen, P.Hartman, G.Rosenbusch

Biophysics Lab. of the Institute of Ophthalmology  
and the Dept. of Radiology,  
St. Radboud Hospital, University of Nijmegen,  
P.O.box 9101, 6500 HB Nijmegen, The Netherlands

## ABSTRACT

A preparatory study of the feasibility of tissue characterization with ultrasound has resulted in the development of a mobile measurement set-up, which can be employed in clinical use. Several corrections have to be carried out on the RF-signals before analysis can take place. Equipment dependencies that have to be corrected for are the time gain compensation, the gain compression and the diffraction and focussing effects. These corrections and additionally a correction for the attenuation, also have to be applied to the RF data prior to B-mode image construction and subsequent statistical texture analysis. The preliminary results of a clinical in vivo pilot study are discussed.

Key words: attenuation, cirrhosis, correction, diffraction effect, focussing effect, liver, speckle, texture, ultrasound

## 1 INTRODUCTION

Several years ago in-vitro experiments were performed in our laboratory to investigate the possibilities of differentiation of pathological from normal tissue, using acoustic parameters, like attenuation and sound velocity, and echographic texture parameters like reflectivity and correlation distance [1]. The goal was to find a method that would be clinically applicable. The experiments were performed on liver biopsies, first of the goat and later of the human. After each experiment the histology was judged by a pathologist, which procedure enabled the search for correlations between histologic and acoustic parameters. In order to be able to avoid inconsistent results a good understanding is needed of the physical mechanisms that influence the estimation of the echographic and acoustic parameters. Therefore an extensive computer simulation study was carried out, concerning the production, the propagation through tissue, the scattering and the reception of ultrasound pulses [2,3]. From these studies the conclusion was drawn that a depth independent estimation of the parameters can only be obtained if corrections are carried out for the diffraction and focussing effects, which are caused by the transducer geometry. In case of B-mode analysis also a correction for the attenuation, caused by the tissue should be applied.

## 2 MEASUREMENT SET-UP

The measurement set-up [4] is controlled by a Professional 380 microcomputer (Digital), which is also used for the storage of the data. As ultrasonic frontend a Sonoline 3000 (Siemens) is used. This

is a conventional B-mode sector scanner with a fixed focus transducer ( $f = 3.0$  MHz, bandwidth = 1.1 MHz, focus = 7.5 cm). The RF signals are tapped off after the time gain compensation (TGC) amplifier, and prior to the logarithmic compression and the demodulation. The signals are digitized by a BE256 transient recorder (Bakker Electronics) which has a resolution of 8 bits, and which can operate at sampling frequencies up to 50 MHz. Along with the RF signals the steering voltage of the TGC amplifier is recorded and stored. The recorded RF signals correspond to a region of interest (ROI) that can be selected on the screen of the Sonoline scanner.

### 3 PARAMETERS FOR TISSUE CHARACTERIZATION

The parameters we want to estimate from the echosignals are the ones that proved useful in the in-vitro and computer simulation studies. These are supplemented with some parameters taken from literature.

The acoustic parameters are the slope of the frequency dependent attenuation coefficient, the attenuation at the working frequency of the transducer and the backscatter coefficient. Apart from being a tissue characterizing parameter, knowledge of the attenuation coefficient is necessary for the correction of the B-mode images.

The texture parameters (parameters estimated from the B-mode images) fall into two categories: the first and second order statistical parameters. The first order parameters are determined from the amplitude histogram. They are the average echoamplitude ( $\mu$ ) and the average divided by the standard deviation, also termed the Signal to Noise Ratio (SNR). In our simulation studies [3] we found, as can be expected on theoretical grounds, that

$$\mu (:) \sqrt{n} \tag{1}$$

in which  $n$  is the number of scatterers contributing to the detected echo signal. The SNR was found to increase with the number of contributing scatterers, until a limit of 1.91 was reached at high densities. This limit is also known as the Rayleigh limit.

The second order parameters are measures of the spatial properties of the texture. From the autocovariance function (ACVF) of a B-scan the average size of the speckle can be estimated. The parameters related to this size are the Full Width at Half Maximum (FWHM) in axial and lateral directions. Our simulation study [3] showed that these parameters decrease with increasing number of contributing scatterers, until a limit is reached at high densities. In this limit these parameters can be shown to depend on transducer characteristics only [5]. Since there are indications that scattering structures are present in tissues (liver) with densities well below the Rayleigh limit, we think it is worthwhile to estimate these parameters.

In addition to the parameters related to the size of the speckle the ACVF, or its Fourier transform, which is the power spectrum (PS), allows the estimation of a parameter related to the regularity of the texture pattern. This parameter has been called mean scatterer spacing in literature [6,7], because it is thought to correspond to structured, or coherent scattering in the tissue. The parameters listed so far all have some physical basis. In literature also a wide

variety of texture parameters is used without a direct physical meaning, such as those determined from the cooccurrence matrix and the greylevel runlength matrix [8].

## 4 CORRECTIONS

### 4.1 Theoretical Background

The echoes received by the transducer are the result of the coherent accumulation of backscatterings from inhomogeneities in the tissue. The signal as it is observed depends on the transducer geometry and the properties of the interrogated medium. This can be described by various transfer functions, of which the following can be distinguished:

\*  $P(f)$  the electroacoustic roundtrip transfer function of the piezoelectric material of the transducer, which is involved in the conversion of electric energy to acoustic energy and vice versa,

\*  $S(f)$  the average backscatter coefficient of the tissue inhomogeneities, which is assumed to be space invariant in the region of interest (homogeneous and isotropic),

\*  $D'_t(f, \vec{r})$ ,  $D'_r(f, \vec{r})$  the transfer functions associated with the impulse response function of the transducer at position  $\vec{r}$ , in transmission and reception, respectively. These transfer functions depend on the transducer geometry and the propagation characteristics of the medium. If the point  $\vec{r}$  is approximately equidistant to all points of the transducer aperture, these transfer functions may be separated in a tissue transfer function and a diffraction transfer function:

$$\begin{aligned} D'_t(f, \vec{r}) &= D_t(f, \vec{r}) A(f, r) \\ D'_r(f, \vec{r}) &= D_r(f, \vec{r}) A(f, r) \end{aligned} \quad (2)$$

The functions  $D_t(f, \vec{r})$  and  $D_r(f, \vec{r})$  relate to the impulse response functions in a lossless medium and are identical due to the validity of reciprocity in pulse-echo mode.

A general description of the tissue transfer function is given by

$$A(f, r) = \exp[-\alpha(f)r] \quad (3)$$

Usually the attenuation coefficient  $\alpha(f)$  is approximated to be linear with frequency

$$\alpha(f) = \alpha_1 \cdot f \quad (4)$$

Using the described transfer functions the echosignal due to one scatterer at position  $r$  can be described by

$$\begin{aligned} E(f) &= P(f) D'_t(f, \vec{r}) S(f) D'_r(f, \vec{r}) \\ &= P(f) D^2(f, \vec{r}) A^2(f, r) S(f) \end{aligned} \quad (5)$$

Written as a function of time we have

$$e(t) = p(t) * d(t, \vec{r}) * a(t, r) * s(t) * a(t, r) * d(t, \vec{r}) \quad (6)$$

where \* denotes a convolution. If there is more than one inhomogeneity present in the tissue the resulting echosignal is the coherent summation of the individual echoes

$$e(t) = \sum_j e_j(t) \quad (7)$$

in which j is the index of the scatterer at position  $\vec{r}_j$ . In the frequency domain this is equal to

$$\begin{aligned} E(f) &= \sum_j E_j(f) \\ &= P(f) S(f) \sum_j D^2(f, \vec{r}_j) A^2(f, r_j) \\ &= P(f) S(f) \sum_j D^2(f, \vec{r}_j) \exp[-2\alpha(f)r_j] \quad (8) \end{aligned}$$

provided the backscatter function S(f) is the same for all inhomogeneities. If only a small time portion of the echosignal is considered the individual echoes  $e_j(t)$  will come from inhomogeneities in a small volume at axial distance z from the transducer. The distances  $r_j$  are approximately equal to this depth z and therefore the attenuation factor can be approximated by  $\exp[-2\alpha(f)z]$  Also the diffraction transfer function can be approximated by an average transfer function dependent on depth D(f,z). The echosignal from a volume at depth z can now be written as

$$E_z(f) = P(f) S(f) D^2(f, z) \exp[-2\alpha(f)z] \quad (9)$$

From this equation it is clear that a depth independent estimation of the attenuation is only possible if the average transfer function due to diffraction and focussing  $D^2(f, z)$  is known.

#### 4.2 Correction Methods

Before any analysis can be performed the TGC must be removed from the signals. The steering voltage of the TGC amplifier, which was recorded along with the RF signals, corresponds to a certain amplification factor. This relationship was determined by measuring the echo of a single scatterer at a number of TGC amplification levels. The frequency dependence of the amplification was determined from the power spectra of the echosignals. Figure 1 shows that we can do with one TGC correction curve for all frequencies.

The average transfer function due to diffraction and focussing  $D^2(f, z)$  was measured by estimating the power spectra of the echo signals from a tissue mimicking phantom for a range of depths. The phantom was placed in a waterbath, and for every depth the transducer was repositioned in such a way that the recorded echosignals came from the same volume. For each depth 100 independent RF-scans were recorded. Then the power spectra of a windowed section of these signals, corresponding to the chosen volume, were averaged. This was repeated for 38 distances between the transducer and the surface of the tissue phantom. The resulting spectrogram (fig. 2) is the average

diffraction filter multiplied with the transfer function  $S_{ph}$  of the scatterers in the phantom  $|D^2(f, z)|^2 \cdot S_{ph}(f)$ . The latter term is divided out in the procedure to estimate the attenuation coefficient. Together with the TGC correction this procedure yields an unbiased estimate of the attenuation from the power spectra of the echosignals in a certain usable bandwidth.

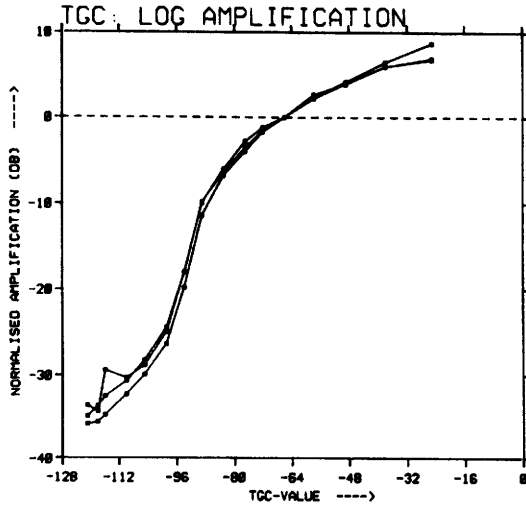


Figure 1. Amplification as a function of the steering voltage of the TGC amplifier for the central frequency and two frequencies at either boundary of the used frequencyband.

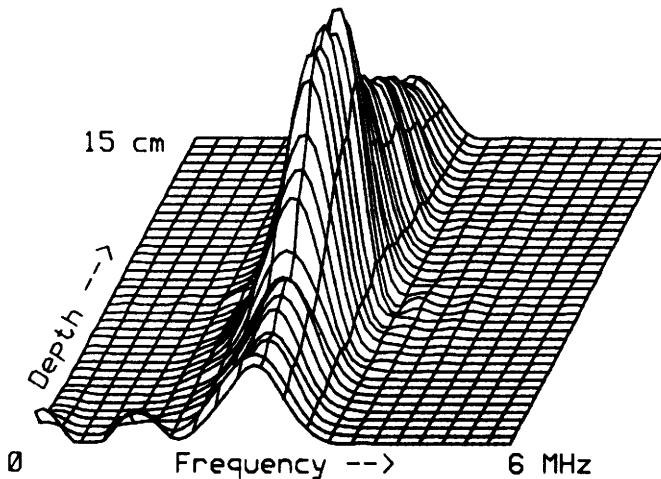


Figure 2. The diffraction spectrogram.

If we want to correct B-mode scans, the RF-signals themselves have to be corrected. After the TGC is removed from the RF-signals we should compensate for as well diffraction and focussing effects as the attenuation, since both phenomena cause a depth dependent texture. The best way one could correct for diffraction and focussing effects is by inverse filtering for the depth dependent point spread function of the transducer. This involves two dimensional convolutions in a number of sections of the image. Because this method would be very time consuming we have tried a one dimensional deconvolution for removing attenuation and diffraction effects instead. Figure 3 shows that this method accomplishes a correction with respect to the first order characteristics of the texture. If however the size of the speckle is considered it will be clear that this method does not achieve a satisfactory depth independence with respect to the second order characteristics. Obviously a deconvolution also in the lateral dimension is necessary, when the texture is to be analysed.

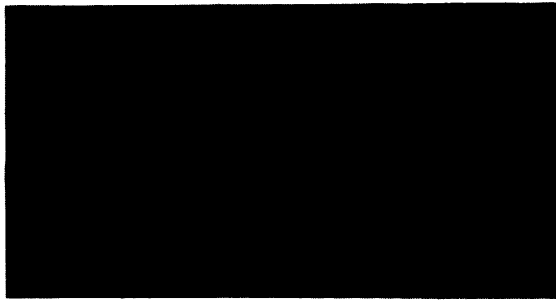


Figure 3. Original sectorscan with TGC and image with attenuation correction.

## 5 PILOT STUDY (LIVER) AND ATTENUATION RESULTS

In cooperation with the departement of Radiology in our hospital we have started a pilot project in which an attempt will be made to differentiate patients having a biopsy proved liver cirrhosis from patients with a normal liver. We have acquired data from a group of healthy volunteers, which will serve as control group. For this group we have determined the attenuation coefficient  $\alpha_1$  [9]. This was done by calculating the power spectra in 50% overlapping windows averaged over the recorded RF-signals. After dividing these power spectra by the corresponding diffraction spectra, a straight line was fit in the depth direction, through the resulting spectra, for every frequency in the chosen frequency band, resulting in slope values  $\alpha_1 f_i$  for every frequency sample  $f_i$ . Through these figures a straight line was fit in the frequency direction, resulting in estimations for  $\alpha_1$ . The unit of  $\alpha_1$  is Np/cm.MHz. In units of dB/cm.MHz a factor of  $20/\ln 10$  must be taken into account.

The results for the group of volunteers are shown in the histogram of figure 4. The average value for the attenuation coefficient in this group was found to be 0.70 (0.05) dB/cm.MHz.



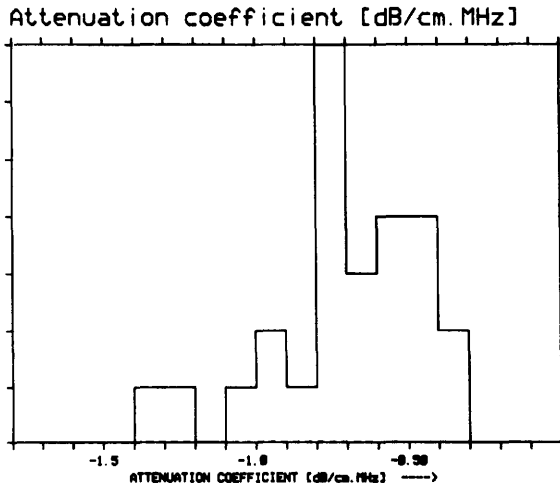


Figure 4. Histogram of the attenuation coefficient for the control group

## 6 SUMMARY

A measurement set-up was developed which can be used in the clinic. Using this set-up we are performing a pilot experiment for the differentiation of liver cirrhosis. Data were acquired from a group of healthy volunteers, which will serve as control group. The average value of the attenuation found in this group was 0.70 dB/cm.MHz.

In the meantime we will continue working on a satisfactory strategy to correct B-mode image texture for the depth dependence caused by diffraction and focussing effects and by attenuation

## ACKNOWLEDGEMENTS

This work is supported by the Netherlands' Technology Foundation (STW), future Technical Science Branch of the Netherlands' Organization for the Advancement of Pure Research (ZWO), and performed within the framework of the concerted action programme on Ultrasonic Tissue Characterization and Echographic Imaging of the European Community.

## REFERENCES

- [1] M.J.T.M.Cloostermans, H.Mol, W.A.Verhoef and J.M.Thijssen, In vitro estimation of acoustic parameters of the liver and correlations with histology, Ultrasound in Med. and Biol., Vol 12, p 39-51, 1986.
- [2] W.A.Verhoef, M.J.T.M.Cloostermans and J.M.Thijssen, Diffraction and dispersion effects on the estimation of ultrasound attenuation and velocity in biological tissues,

IEEE Trans. on Biom. Eng., Vol 32, p 521-529, 1985.

- [3] B.J.Oosterveld, J.M.Thijssen and W.A.Verhoef, Texture of B-mode echograms: 3-D simulations and experiments of the effects of diffraction and scatterer density, Ultrasonic Imaging, Vol 7, p 142-160, 1985.
- [4] W.H.Kruimer, J.H.E.Lammers and J.M.Thijssen, Ultrasonic Biopsy Apparatus, Acoustical Imaging, Vol 14, A.J.Berkhout, J.Ridder and L.F.van der Wal eds., Plenum Press, New York, 1985.
- [5] R.F.Wagner, S.W.Smith, J.M.Sandrik, H.Lopez, Statistics of speckle in ultrasound B-mode scans, IEEE Trans. on Son. and Ultras., Vol 30, p 156-163, 1983.
- [6] R.F.Wagner, M.F.Insana and D.G.Brown, Unified approach to the detection and classification of speckle texture in diagnostic ultrasound, Opt. Eng., Vol 25, p 738-742, 1986.
- [7] M.F.Insana, R.F.Wagner, B.S.Garra, D.G.Brown, T.H.Shawker, Analysis of ultrasound image texture via generalized Rician statistics, Opt. Eng., Vol 25, p 743-748, 1986.
- [8] U.Raeth, D.Schlaps, B.Limberg, I.Zuna, A.Lorenz, G.van Kaick, W.J.Lorenz, B.K.Kommerell, Diagnostic accuracy of computerized B-scan texture analysis and convention ultrasonography in diffuse parenchymal and malignant liver disease, J.Clin.Ultrasound, Vol 13, p 87-99, 1985.
- [9] M.J.T.M.Cloostermans and J.M.Thijssen, A beam corrected estimation of the frequency dependent attenuation of biological tissues from backscattered ultrasound, Ultrasonic Imaging, Vol 5, p 136-147, 1983.

FIRST AND SECOND ORDER STATISTICS FOR  
ATHEROSCLEROSIS DETECTION

Casini A., Lotti F. - Ist. Ricerca Onde Elettrom. (CNR), Firenze, I  
Bernardi P. - Dip. Ing. Elettronica, Università di Firenze, I  
Lattanzi F., Picano E. - Ist. Fisiologia Clinica (CNR), Pisa, I

This study was designed to determine whether a quantitative analysis of integrated backscatter amplitude is potentially useful in characterizing the atherosclerotic lesion. 1024 (32 X 32) measurements were made on fixed aortic regions ( $\sim 2$  cm X 2 cm) of 3 normal and 8 atherosclerotic walls. A 5 MHz transducer was used. First and second order statistics of the integrated volume backscatter amplitude were calculated.

First order Standard Deviation, Energy and Entropy and second order Contrast and Entropy appeared to be good candidate features for classification ('normal' versus 'atherosclerotic').

Key words:

ultrasonic tissue characterization, integrated backscatter, atherosclerosis, image analysis, statistical classification, echocardiography.

INTRODUCTION

In previous studies we evaluated the acoustic properties of arterial tissue by estimating different parameters such as ultrasonic attenuation [5], angular behaviour of the internal backscatter [6], backscatter value as a function of frequency [7]. In particular, we have also shown the usefulness of assessing histograms of echo amplitude in normal and diseased arterial regions [8].

The two-dimensional spatial pattern of grey levels, however, may contain more information than what is apparent in the first order overall distribution of echo amplitudes [2, 3, 13].

We postulated that the analysis of second order histograms could supply accurate methods to differentiate normal from abnormal arterial structures. Therefore we planned to perform some 'in vitro' experimental tests on images generated by volume backscattered signal.

## EXPERIMENTAL PROCEDURE

Specimens of arterial wall were taken from human aortas at autopsy, cut down the anterior midline and placed in 5% formalin. They were selected to consist of diseased - non grossly calcific - atherosclerotic regions along with regions, whenever possible, of relatively normal tissue. The presence of macroscopic calcification was a criterion of exclusion from the study.

For the ultrasonic measurements, the excised samples of aortas were opened flat, mounted on a metallic hollow-rimmed sample-holder, placed in a water tank (20° C) with the endothelium facing the transducer. The distance of the transducer from the sample-holder base was kept constant for all the experiments (60  $\mu$ sec), corresponding to a distance of 33 mm from the outer coat of the aortas.

The transducer was a broadband unfocussed transducer OTE 127200H, 6 mm diameter, 5 MHz of nominal frequency, which was actuated as both transmitter and receiver by means of a broadband pulser/amplifier [14]. The operating frequency of the transducer was nearly the maximum allowed by the digitizer used at IROE/DIE when the measurements were started. A faster one is now available [15] and will be eventually used to get new sets of measurements.

A 19.37 mm X 19.37 mm region of each tissue sample was scanned by the perpendicular ultrasonic beam at the 1024 sites of a 32 X 32 square array. The precision of the computer controlled mechanical movements was 0.01 mm.

The received R.F. signals were digitally captured at a sampling rate of 16.6 MHz (61 nsec sampling time), 8 bits of quantization.

## ULTRASONIC DATA ANALYSIS

During the acquisition, the gate length was fixed at 15.6 microsec (256 time samples) to allow digitization of the signal from the full thickness of the specimen.

After the acquisition, in order to separate volume backscattering from water-tissue interface echoes, the operator isolated the interfaces on each stored RF trace by means of interactive software which allowed him to exploit some contextual information.

In fact, the traces were presented on a graphic screen in frames of 32, corresponding with the 32 sites of a row (column) of the 32 X 32 array.

The operator could move a cursor along each trace and command to store its position when he estimated to have identified the end of the echo from the first water-tissue interface. The initial position at which the cursor was displayed on each trace was that which had been stored for the homologous trace of the previous frame.

The spatial oversampling (0.625 mm sampling step) was chosen not only because we wanted to be free of discarding redundant information in a second time, but also because the detection of the water-tissue interfaces was eased by a moderately high density of traces. In fact, the observation of the neighbour traces could supply more hints to solve possible local uncertainty in some trace.

Fifteen time samples of volume-backscattered signal corresponding to a time interval of 0.85 microsec (0.64 mm), were so extracted from each record. The obtained data were then normalized for the different amplification gains used for the different specimens.

The integrated backscatter

$$IB = \left[ \sqrt{\sum_{i=1}^N a_i^2} \right] / N \quad N = 15, a_i = \text{amplitude level of the } i\text{-th sample.}$$

was then calculated record by record and used as the grey-level of the pixels in a 32 x 32 "image" of each specimen.

#### IMAGE ANALYSIS ALGORITHMS

For the analysis of the images we used both first-order and second-order statistical algorithms.

First-order statistical analysis gives overall information on how the random variable 'grey-level' is distributed on an image, while second-order analysis takes into account even the spatial dependences between couples of grey-levels and can supply textural characterization.

As shown in figure 1 and in figure 2, the integrated-backscatter images appear to be without any textural organization because of the inhomogeneity of the tissue. That does not mean that second order analysis cannot yield useful features for classification.

From the first-order grey-level histogram of each image we calculated the Mean, the Variance, the Skewness, the Kurtosis, the Energy and the Entropy (see Appendix for the definitions).

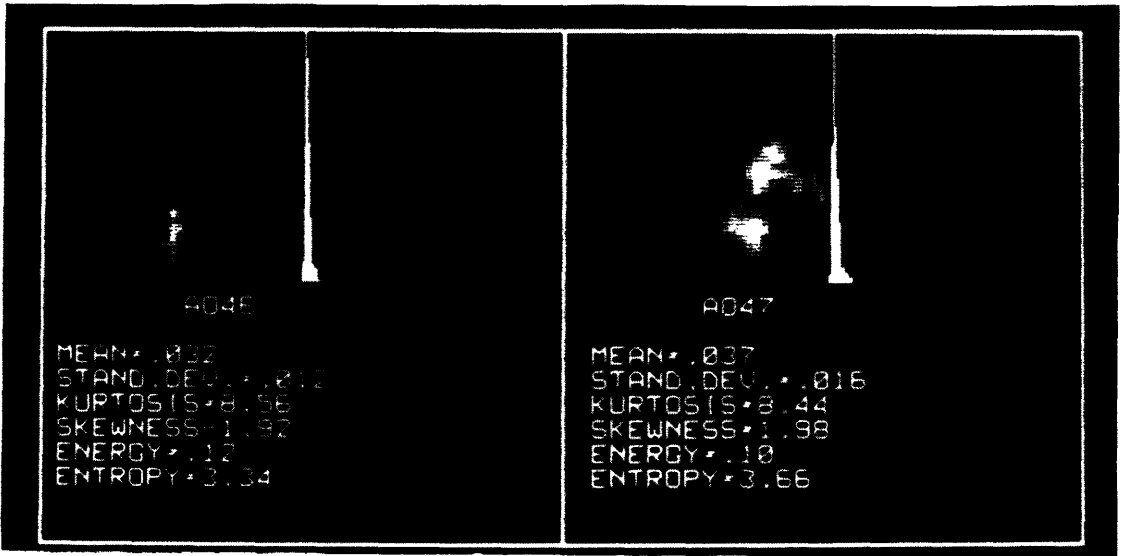


Fig. 1 Integrated backscatter ultrasound images of two normal aortas (top left); first order histogram (top right); first order statistics (bottom).



Fig. 2 Integrated backscatter ultrasound images of two atherosclerotic aortas (top left); first order histogram (top right); first order statistics (bottom).

Table I - First order histogram features for normal and atherosclerotic human aortic walls.

Test Sample	NORMAL			ATHEROSCLEROTIC							
	A041	A046	A047	A035	A042	A048	A049	A051	A053	A045	A055
MEAN	.066	.032	.037	.056	.080	.056	.080	.270	.180	.120	.100
ST. DEV.	.007	.012	.016	.040	.083	.047	.075	.250	.160	.036	.077
KURTOSIS	10.1	8.6	8.4	15.8	23.0	7.3	7.0	2.9	5.4	11.2	4.0
SKEWNESS	1.9	1.9	2.0	3.2	4.1	2.1	2.1	1.1	1.7	2.1	1.3
ENERGY	.190	.120	.100	.072	.092	.065	.045	.012	.019	.042	.027
ENTROPY	2.7	3.3	3.7	4.3	4.3	4.6	5.2	6.9	6.4	4.8	5.7

Table II - Second order cooccurrence matrix features for normal and atherosclerotic human aortic walls.

Test Sample	NORMAL			ATHEROSCLEROTIC							
	A041	A046	A047	A035	A042	A048	A049	A051	A053	A045	A055
A.S.M.	.130	.056	.034	.024	.050	.017	0.10	.003	.007	.007	.012
CONTRAST	2	5.6	8	42	160	64	120	260	130	48	37
CORREL.	.06	.12	.22	.11	.27	.23	.28	.52	.33	.20	.26
ENTROPY	3.5	4.9	5.6	6.4	6.3	7.2	7.7	9.2	8.3	7.7	7.4

From each image we also calculated a cooccurrence matrix, which is a second-order grey-level histogram of the pixel pairs situated at a fixed oriented distance. In our case the distance was  $d=6$  pixels ( $\sim$  half beamwidth) along four directions ( $0^\circ, 45^\circ, 90^\circ, 135^\circ$ ). The angular second moment (ASM), the contrast, the correlation and the entropy were then computed and averaged on the four directions (see Appendix).

## PATHOLOGICAL EXAMINATION

After ultrasonic measurements each aortic region was studied histologically with Weigert-Van Gieson stain.

According to generally accepted criteria, a normal and four pathologic subsets were identified: normal aortic walls, fatty plaques (characterized by the accumulation of lipids), fibrofatty plaques (characterized by a fibrous cap and a lipid core), fibrous plaques (i.e. walls thickened by connective tissue) and calcified plaques (walls in which the atheromata were calcified).

In the present study we aimed only at the classification in the main two classes: "normal" and "atherosclerotic".

## RESULTS

Table I reports the values of the first order histogram features evaluated from 11 specimens, 8 of which were classified as "atherosclerotic" and the other 3 as "normal". In figs. 1 and 2 four examples are shown of the grey-level distribution of the sample A046, A047, A051, A053.

From the obtained results we can observe that the two features Kurtosis and Skewness show, for this data set, a large overlap and seem of no help as discriminating parameters. The values of the three features Standard Deviation, Energy and Entropy group the specimens in two well separated ranges and therefore can be suitable for classification purpose. The feature Mean shows a weak separation: one of the normal samples (A041) overlaps with some abnormal ones (A035, A048).

Table II shows the results of the second order analysis for the same experiments. Even in this case we can extract two features, Contrast and Entropy, showing a very neat separation between the two classes, while a weaker discrimination is given by ASM and Correlation.



## DISCUSSION

In the present study we found that the atherosclerotic regions exhibit altered local grey-level patterns, measurable by statistical analysis applied to an image generated from integrated RF backscatter. A distinction between normal and pathologic regions can be accomplished by selecting suitable features extracted from the first and second order histograms.

These findings suggest that quantitative statistical calculation may be a useful approach to atherosclerosis tissue characterization. A numerical approach of the first as well as the second order statistics (the latter typical of texture analysis) is not original, since both qualitative and quantitative statistical image analysis has been usefully applied to many pathological situations [2, 3, 13]. The application of this approach to atherosclerosis had not yet been performed, however it seemed reasonable because the biological basis for an increased heterogeneity is present in the atherosclerotic process, where "the only constant feature, from the pathologist point of view, is variability". Moreover, from the clinical viewpoint, the difference in local two-dimensional echo density of the wall is an accepted criterion for the detection of left main coronary disease [10].

Our approach minimizes the possible artifactual sources of variations occurring in vitro. Obviously, this encourages to evaluate these same parameters in vivo, ideally on a digital image generated from the radiofrequency signal with a quantitative grey-level representation.

In conclusion, second order statistic features provide further useful information suitable to be integrated with first order algorithms to the goal of differentiating normal versus atherosclerotic specimens in vitro.

## REFERENCES

- [1] Bahandari A.K., Nanda N.C., Myocardial texture characterization by two-dimensional echocardiography, *American Journal-Cardiology*, 817, pp. 51 (1983).
- [2] Skorton D.J., Melton H.E., Pandian N.G., Nichols J., Koyanagi S., Marcus M.L., Collins S.M., Kerber R.E., Detection of acute myocardial infarction in closed-chest dogs by the analysis of regional two-dimensional echocardiographic grey-level distributions, *Circulation Research*, 52, pp. 36-44 (1983).
- [3] Skorton D.J., Collins S.M., Nichols J., Pandian N.G., Bean

- J.A., Kerber R.E., Quantitative texture analysis in two-dimensional echocardiography: application to the diagnosis of experimental myocardial contusion, *Circulation*, 68, pp. 217, (1983)
- [4] Picano E., Landini L., Distante A., Benassi A., Sarnelli R., L'Abbate A., Fibrosis, lipids and calcium in human atherosclerotic plaque, *Circulation Research*, 56, pp. 556 (1985).
- [5] Picano E., Landini L., Distante A., Sarnelli R., Benassi A., L'Abbate A., Different degrees of atherosclerosis detected by backscattered ultrasound: an in vitro study on fixed human aortic walls, *Journal Clin. Ultrasound*, 11, pp. 375, (1983).
- [6] Picano E., Landini L., Distante A., Salvadori M., Lattanzi F., Masini M., L'Abbate A., Angle dependence of backscatter in arterial tissues: a study in vitro, *Circulation* 72, pp. 572 (1985).
- [7] Landini L., Sarnelli R., Picano E., Salvadori M., Evaluation of frequency dependence of backscatter coefficient in normal and atherosclerotic aortic walls, *Ultrasound in Medicine and Biology* (in press).
- [8] Picano E., Landini L., Lattanzi F., Mazzarisi, Sarnelli R., Distante A., Benassi A., L'Abbate A., Frequency histogram of ultrasonic backscatter amplitudes for in vitro atherosclerosis detection, *Circulation*, (in press).
- [9] Landini L., Picano E., Sarnelli R., Attenuation measurements in atherosclerotic tissues: problems with phase cancellation artifacts, *Med. Biol. Comput.*, 23, pp. 220 (1985).
- [10] Chen C.C., Morganroth J., Ogawa S., Mardelli T.J., Detecting left main coronary artery disease by apical cross-sectional echocardiography, *Circulation*, 62, pp. 288 (1980).
- [11] Skorton D.J., Collins S.M., Digital computer image analysis in echocardiography, *Echocardiogr. Review Cardiovasc. Ultrasound*, 1, (1984).
- [13] Collins S.M., Skorton D.J., Prasad N.V., Olshansky B., Bean J.A., Quantitative echocardiographic image texture: Normal contraction-related variability, *IEEE Trans. on Medical Imaging*, 4, pp. 185-192 (1985).
- [14] Bertini A., Casini A., Castellini G., Cavallini M., Ciocia G., Lombardi C., Lotti F., Masotti L., Rocchi S., Review and perspective of biological tissue characterization, in *Ultrasonic Tissue Characterization*, J.M. Thijssen, D. Nicholas ed., pp. 26-32 (Martinus Nijhoff, The Hague, 1982).
- [15] Calzolari, Rocchi S., Grimaldi A., Masotti L., Castellini G., Tesi M., Data acquisition systems and their applications to tissue characterization, *Proc. VI Eurech Workshop* (this vol.)

APPENDIX

Definition of the first order features:

$$\begin{aligned}
 \text{- Mean} \quad \bar{g} &= \sum_{g=0}^{N_g-1} g \cdot P(g) \\
 \text{- Stand. dev. } \sigma &= \sqrt{\sum_{g=0}^{N_g-1} (g - \bar{g})^2 \cdot P(g)} \\
 \text{- Skewness} &= \sigma^{-3} \cdot \sum_{g=0}^{N_g-1} (g - \bar{g})^3 \cdot P(g) \\
 \text{- Kurtosis} &= \sigma^{-4} \cdot \sum_{g=0}^{N_g-1} (g - \bar{g})^4 \cdot P(g) \\
 \text{- Energy} &= \sum_{g=0}^{N_g-1} P(g)^2 \\
 \text{- Entropy} &= - \sum_{g=0}^{N_g-1} \log_2 [P(g)] \cdot P(g)
 \end{aligned}$$

where  $P(g) = N(g)/N_t$  is the ratio between the number  $N(g)$  of pixels with grey-level  $g$  and the total number  $N_t$  of pixels.

$N_g$  is the number of grey-levels.

Definition of the second order features:

Any element in the cooccurrence matrix is defined as

$$P(d, \alpha, i, j) = N(d, \alpha, i, j) / N_t(d, \alpha)$$

where  $N(d, \alpha, i, j)$  is the number of pixel pairs at distance  $d$  along the direction  $\alpha$ , one with grey-level  $i$  and the other with grey level  $j$ .  $N_t(d, \alpha)$  is the total number of pixel pairs at distance  $d$  along  $\alpha$ .

$$\text{- A.S.M.} = \sum_{\alpha} \sum_{i, j=0}^{N_q-1} P(d, \alpha, i, j)^2$$

$$\text{- Contrast} = \sum_{\alpha} \sum_k \sum_{i, j=0}^{N_q-1} k^2 \cdot P(d, \alpha, i, j) \quad |i-j|=k$$

$$\text{- Correlation} = \left[ \sum_{\alpha} \sum_{i, j=0}^{N_q-1} i \cdot j \cdot P(d, \alpha, i, j) - \bar{g}_x \cdot \bar{g}_y \right] \cdot \sigma_x^{-1} \cdot \sigma_y^{-1}$$

$$\text{- Entropy} = - \sum_{\alpha} \sum_{i, j=0}^{N_q-1} \log_2 [P(d, \alpha, i, j)] \cdot P(d, \alpha, i, j)$$

$N_q$  is the number of quantization levels used to calculate the cooccurrence matrix ( $\leq$  the number of grey-levels  $N_g$  in the image).

For the reported results  $N_q = 32$ ,  $N_g = 256$ ;  $\alpha = 0^\circ, 45^\circ, 90^\circ, 135^\circ$ .

## B-SCAN TEXTURE AS AN INDICATOR OF DIFFUSE LIVER DISEASE

D. Nicholas  
M. Bamber  
D. Nassiri

Norfolk and Norwich Hospital, U.K.  
Royal Free Hospital, London, U.K.  
St. Georges Hospital, London, U.K.

### Abstract

Present day usage of ultrasound sector B-scanning as an aid to the diagnosis of diffuse hepatic disorders is generally limited to predicting the existence of abnormality and subjectively commenting upon the texture and attenuating properties of the tissue. To date a definitive classification of disease is unavailable.

In an attempt to quantitatively evaluate the textural information contained in such images we have devised a method whereby a number of statistical parameters have been computed from a data set of 40 patients with biopsy proven liver disorders. The subsequent use of multi-variate and discriminant analysis indicates an 89 per cent success when classifying four diffuse hepatic conditions with a combination of eight texture parameters.

Key words: TEXTURE; B-scan; liver; diffuse disease;  
Discriminant Analysis.

### Introduction

To date, the major diagnostic use of the parenchymal echoes present in sector B-scan images of the soft tissues is for the characterization of space occupying lesions on the basis of a contrast difference between adjacent normal and abnormal regions. However, an increasing interest is being shown in the spatial distribution of such echoes. Although useful information is being obtained, it is derived primarily from a subjective and non-quantitative evaluation of the images.

In a preliminary report (1) we outlined an approach to retrospective quantitative analysis of the texture displayed in conventional sector B-scan images. Whilst other workers have reported work on similar lines (2), to our knowledge, no one has attempted texture analysis on the image presented to the clinician for visual appraisal. In this paper we will report on our success in developing a classification for the in-vivo appraisal of diffuse hepatic disorders.

The abundance and complexity of data present in a conventional ultrasound tomogram convinced us of the need to use machine/operator interplay to both limit the data collected and pre-select regions of clinical interest. Where homogeneous disease conditions are encountered (such as diffuse liver disease) one then assumes that selected portions of the image are representative of the general condition. Details of our equipment and techniques have been reported elsewhere (3), and it will suffice to stress that we limit data collection to a 3 x 3 cm region

of tissue digitised to 64 x 64 pixel resolution with 6 bits of accuracy. A "joy stick" control enables the operator to position the region to be digitised on the ultrasound image (see Figure 1). During the period of these investigations the same apparatus was used and every effort made to ensure that the quality of image was maintained for all data.



Figure 1. Conventional longitudinal sector B-scan through the right lobe of liver; the vertical lines indicate the region selected for digitisation.

#### Methods

Liver scans were obtained with the subjects (40) lying supine and holding a diaphragmatic breath. The majority of scans were longitudinal subcostal scans with the transducer being tucked under the costal margin and swept inferiorly. Transverse scans in the sub-xiphisternal space were also performed for lateral right lobe examination. Although many tomographic slices were produced, images which included obvious artefacts were excluded from computer analysis. Random regions within the liver parenchyma were digitised and transferred to the computer. A restriction was that the regions selected should be within 45 to 120 mm distance of the transducer/skin interface. This effectively eliminated the unwanted transducer effects associated with either the near field or the beam spreading at distance. A final set of 208 images, from four categories of biopsy proven diffuse hepatic disorder (cirrhosis, hepatitis, pure fatty and a combination of hepatitis and cirrhosis), were input into our study.

#### Results

When attempting to analyse the texture or pattern of the echoes it is necessary to first quantify the region using a variety of features. We used a total of 24 features which have been discussed in detail elsewhere (3) and will not be repeated herein. These features were calculated for each digitised region, averaged to yield a single value for each patient (on average ten regions were digitised for each patient examination) and analysed under the discriminant analysis package

(SPSS - Statistical Package for the Social Sciences) available on CDC 7600 machines at the University of London Computer Centre. This package (4) attempts discrimination by forming one or more linear combinations of the discriminating variables through a multi-variate analysis of variance. The analysis chosen for the data reported here proceeded through a stepwise selection of the 'best' set of discriminating variables using a minimum Wilks' lambda criterion. Following selection of the 'optimal' discriminant functions or scores (see Figure 2), the data were then classified into one of the four categories: cirrhotic, hepatitic, fatty or a combined hepatitic and cirrhotic, taking account of the number of data in each group when computing prior probabilities. The analysis was performed several times, each time restricting the number of features available for discrimination. This restriction is extremely important as one must be careful not to have a large number of variables (L) contributing to the discrimination compared with the number of data within a group (N). Although it is recognised that the greater the ratio of N/L the more stable the results, a reasonable guide for this probability exercise is to ensure that the ratio of sample to feature size is greater than three.

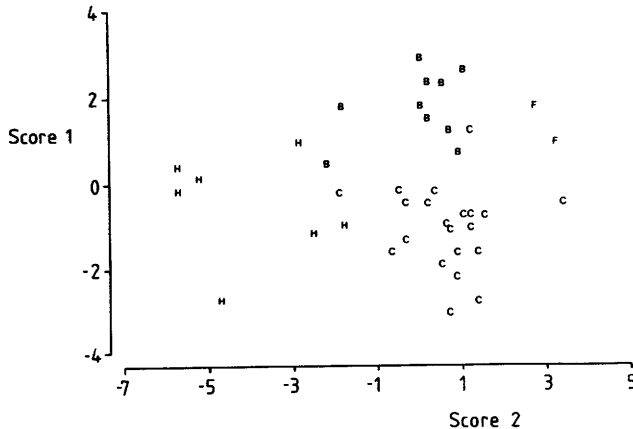


Figure 2. Two-dimensional scatter map of the discriminant scores for 40 diffuse hepatic disorders.  
C = cirrhosis; H = hepatitis; F = fatty; B = combination of hepatitis and cirrhosis.

In Figure 3 (a) the average classification success rate is shown as a function of the number of discriminating variables used. Under the assumption of a multi-variate normal distribution, the classification scores can be converted into probabilities of group membership. This latter function also depicted in Figure 3 (a) yields a better interpretation of the ability to discriminate accurately between the groups as it accepts that the groups may not be completely separated.

Based upon these results it is shown that for three features an overall classification success of 77 per cent is achieved. However, as stressed above this only relates to a 52 per cent probability of success.

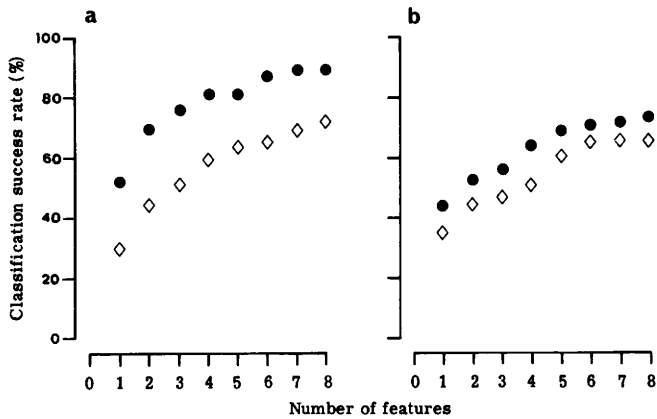


Figure 3. Computer classification success rates as a function of the number of features used.  
 (a) Average data set, actual classification success, probability of success.  
 (b) Individual images, actual classification success, probability of success.

In order to overcome the problems associated with the small sizes of data sets we have analysed the full set of images independently, i.e. 208 images in total (an average sample size (N) of 50). Figure 3 (b) depicts the results obtained when performing an analysis procedure similar to that above. As expected the overall probability of success is reduced as there is a greater variance in the data associated with individual scans. However, we can now justify using a larger number of features for discrimination as our data set is larger. Furthermore, if we now classify an individual patient based upon the classification of his/her separate images we derive a classification success rate similar to the analysis performed upon the averaged data set (Table I).

#### Discussion

The results presented in this paper require careful consideration and interpretation. The use of a multi-variate discriminant analysis can lead to erroneous results if care is not taken in its application. One important assumption underlying the method is that the data can be classified into the groups specified and do not belong to some other grouping. This may not be totally true for our data as the spread of values for a feature do not follow a Gaussian distribution for each data set. An alternative grouping of data may need to be made and it is suggested that the fat and fibrosis content of the tissue may determine the true classification as depicted by ultrasound.



Table I. Classification of single images as a function of the number of discriminating features used.

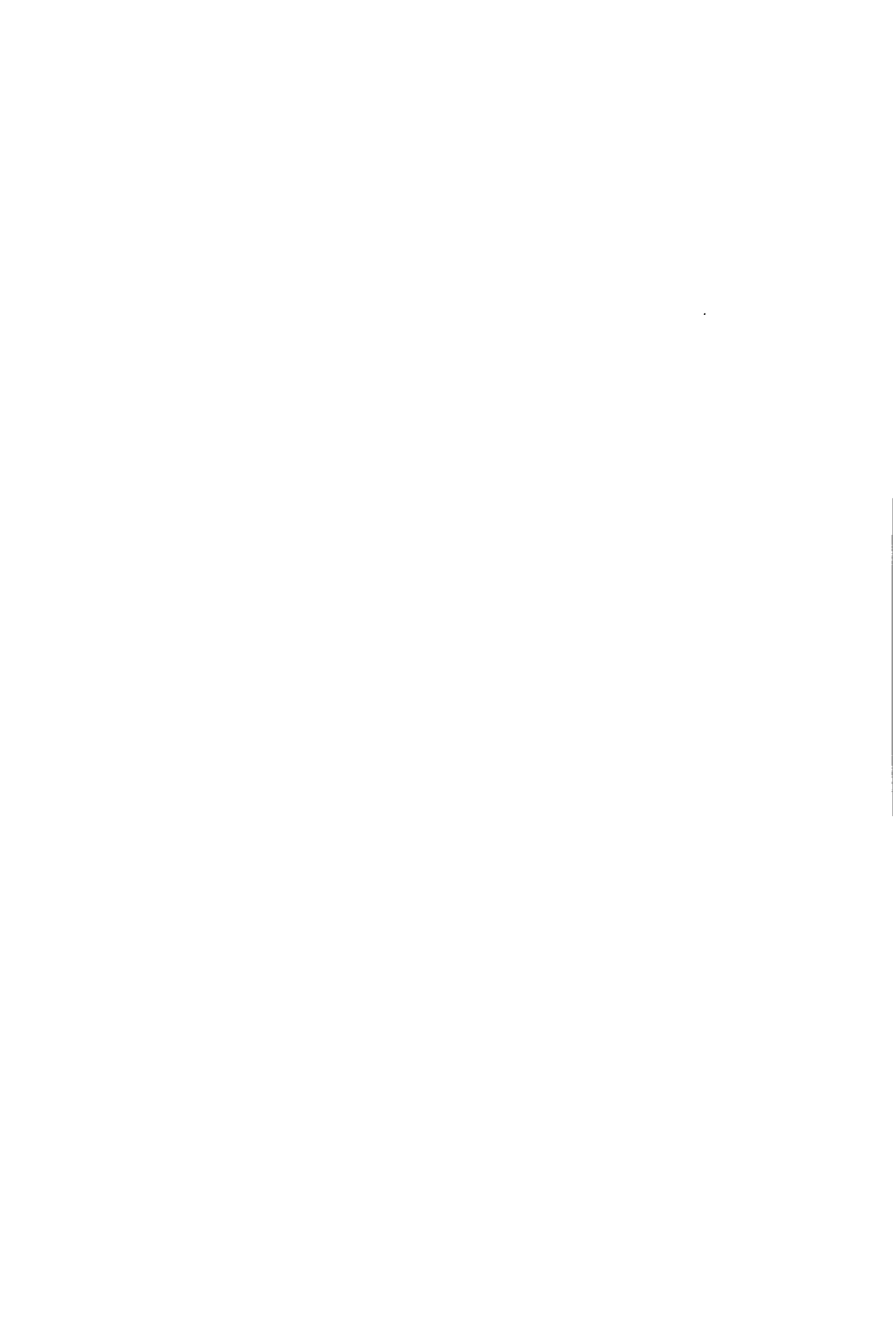
---

Number of features	Overall success 208 scans	Probability of success 208 scans	Grouped success 40 patients
1	44	35	52
2	53	44	70
3	55	46	75
4	64	50	80
5	70	60	80
6	72	65	87
7	73	66	89
8	75	66	89

---

References:

- (1) Nicholas, D., Barrett, A., Chu, J.M.G., Cosgrove, D.O., Garbutt, P., Green, S., Pussell, S. and Hill, C.R., Computer Analysis in Grey Scale Tomograms, in *Acoustical Imaging 8*, A. Metherell, ed., 731-844 (Plenum Press/ New York 1980).
- (2) Raeth, U., Schlaps, D., Limberg, B., Zuna, I., Lorenze, A., van Kaick, G., Lorenz, W.J. and Kommerell, B., Diagnostic Accuracy of Computerised B-Scan Texture Analysis and Conventional Ultrasonography in Diffuse Parenchymal and Malignant Liver Disease, *Ultrasonic Imaging 8*, (1986).
- (3) Nicholas, D., Nassiri, D.K., Garbutt, P. and Hill, C.R., Tissue Characterization from Ultrasound B-Scan Data, *Ultrasound in Med. and Biol.* 12, 135-143 (1986).
- (4) Klecka, W.R., *Discriminant Analysis*, in *Statistical Package for the Social Sciences*, Chap. 23, (McGraw Hill/New York, 1975).



# APPLICATION OF SIGNAL RESTORATION TECHNIQUES TO B-SCAN IMAGES

D. Iracà, L. Landini

Centro "E Piaggio" Faculty of Engineering and C.N.R. Institute of Clinical Physiology, University of Pisa, Pisa, Italy.

**Key words:** Image restoration, ultrasonic tissue characterization, resolution enhancement.

## **ABSTRACT**

Two techniques have been proposed for the evaluation of the response of an ultrasonic imaging system. One technique measures the system's line spread function (l.s.f.) as response of the system to a thin target wire placed in the focus of the transducer; a second homomorphic technique is based on the impulse response estimation, starting from the same image to be restored. The two system's responses have been used to implement two filters for image restoration. The filtering results suggest: images of simple targets can be well restored by using the measured l.s.f.; image restoration of tissues based on homomorphic technique appears promising and it has potential for in vivo applications.

## **INTRODUCTION**

Ultrasonic B-scan imaging systems are widely used in medicine to detect tissue's features. However, a limitation of such systems is the poor resolution [1-2]. Among the causes of such drawbacks are the transducer's geometry that influences the lateral resolution and the finite bandwidth of the system that reduces the axial resolution. In principle, by knowing the response of the imaging system, an inverse filter can be implemented for resolution improvement. However, in real applications a number of problems arise. In fact, the actual electromechanical properties of the transducer are difficult to know accurately; furthermore, the imaging system's response is randomly distorted due to the propagation medium.

In this report, the system's response is evaluated through two techniques. One technique is based on the measurement of a thin target wire response [1], so the electromechanical properties of the transducer are experimentally evaluated. Such technique is not suitable for in vivo applications. An homomorphic technique [3] is also proposed for the impulse response estimation that starts from the same image to be restored. Such technique allows to determine the effects on the image of the random distortions due to the interposed tissue. Therefore, it has potential for in vivo applications.

The results of the two techniques have been used to implement two filters for image restoration of test objects and tissue specimens.

## **MATHEMATICAL BACKGROUND**

In order to establish the potentialities of the restoration technique for improving the resolution in ultrasonic systems, two different filters have been tested.

One filter was implemented with the measured l.s.f., according to the following relationship [3]:

$$F_p(u,v) = \frac{H^*(u,v)}{|H(u,v)|^2 + \gamma} \quad (1)$$

where  $F_p(u,v)$  is the expression of the pseudo inverse filter;  $H(u,v)$  is the 2D-FFT of the l.s.f.;  $\gamma$  is a constant experimentally determined.

Furthermore, an homomorphic filter  $F_H(u,v)$  was implemented, as follows [3]:

$$F_H(u,v) = \left[ \frac{P_f(u,v)}{P_g(u,v)} \right]^{1/2} \quad (2)$$

where  $P_f$  and  $P_g$  are respectively the power spectra of the actual image and the image degraded by the measurement system. A source of difficulty in solving eq.(2) is the presence of noise (such as quantization noise). Because of this, the evaluation of  $F_H(u,v)$  was accomplished by defining a truncated form of  $P_g(u,v)$  in order to exclude low amplitudes.

Assuming the tissue modelled as a generalized Poisson process [1],  $P_f$  can be assumed constant. As far as  $P_g$ , it was estimated from the degraded image as average of  $n$  2D-FFT,  $n$  being the number of overlapped blocks in which the image has been divided. Such technique assumes the power spectra equality of the actual and the estimated images.

The filter in (2) is obviously a zero-phase filter. A compensation procedure would be required to account for the phase term due to different ultrasonic paths from the transducer to the observation point. However, in this implementation the phase compensation was not carried out.

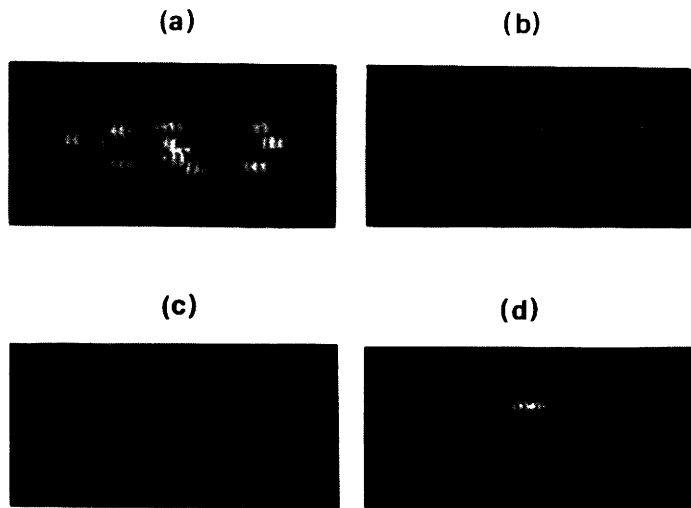


Fig. 1. Images of human hairs before (a) and after filtering ( in b is lower than in c), by pseudo inverse technique; in d the l.s.f. used for filter implementation is shown.

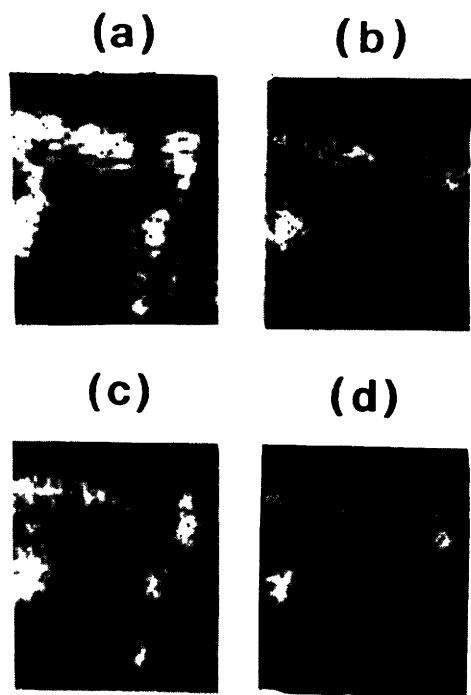


Fig. 2. Pig myocardial wall before (a) and after filtering (b: pseudo inverse filtering, c, d: homomorphic filtering,  $P_g$  bandwidth in c is lower than in a).

## APPLICATION OF THE RESTORATION TECHNIQUES

A circular focused transducer (Aerotech, model gamma, 2.25 MHz, 8 cm of focal distance) was mechanically moved over the target object at steps of 0.5 mm. The movement accuracy was better than  $1\ \mu\text{m}$ . Broadband signals were generated by a pulser-receiver apparatus (KB-Aerotech, model UTA-4). Data acquisition was performed by a transient recorder (Le Croy, model 8013, sampling frequency 100 MHz, 8 bits of amplitude resolution, buffer length 32 kbytes). Sampling was performed at 12.5 MHz. Data from the transient recorder are transferred to a minicomputer (HP-1000) under control of a personal computer (IBM PC-AT). A set of measurements was performed to digitize: the system's l.s.f.; a model of thirteen random human hairs,  $40\ \mu\text{m}$  in diameter and a pig myocardial wall.

Data analysis was performed by using eqs.(1), (2). Our previous studies [4] have shown that in a region  $z$  around the focal point  $z_f$ , such as  $z/z_f \approx 25\%$ , the impulse response can be assumed position invariant. This allows to perform the image restoration by dividing the image in bands over which D.F.T. methods can be employed. In this work, each restoration filter was implemented over a 2 cm region.

After processing, echoes underwent Hilbert filtering transformation to obtain the corresponding analytical signal and, after, the module of the processed signal.

The human hairs images are reported before filtering (Fig. 1a) and after filtering (Fig. 1b,c) by pseudo inverse technique; in figure 1 d the experimental l.s.f. employed for filter implementation is also shown. The resolution improvement is quite evident.

Also, an application of the homomorphic technique was considered. Figure 2 shows the image restoration of a pig myocardial wall: in a, b, c and d are respectively reported the original image, the pseudo inverse filtered image and the homomorphic filtered images with two different

bandwidths of Pg. The results of the homomorphic filtering are quite preliminary. However, from the comparison of the images filtered with the two techniques, the homomorphic filter introduces a lower noise and a better image definition. Further studies on tissue models are necessary to evaluate the real resolution improvement of the filter.

## CONCLUSIONS

We have shown a resolution improvement when the pseudo inverse filter is used in image restoration of simple objects as the human hairs model. That means the measured l.s.f. well reproduces the degradation process. However, with such technique, the in vivo system's response evaluation is impossible.

The homomorphic technique, albeit based on preliminary results, appears a promising technique for in vivo applications. However, a deeper investigation occurs.

## REFERENCES

- [1] Fatemi, M., and Kak, A.C., Ultrasonic B-scan imaging: theory of image formation and a technique for restoration, Ultrasonic Imaging 2,1-47 (1980).
- [2] Kuc, R.B., Application of Kalman filtering techniques to diagnostic ultrasound, Ultrasonic Imaging 1, 105-120 (1979).
- [3] Andrews, H.C., and Hunt, B.R., Digital image restoration, Prentice-Hall, inc., Englewood Cliffs, New Jersey, 1977.
- [4] Iracà, D., Landini, L., and Verrazzani, L., A model of ultrasonic image formation implementable with invariant filters, IEEE Trans on Ultrasonics, Ferroelectrics and Frequency Control (in press).



DATA ACQUISITION SYSTEMS AND THEIR APPLICATIONS  
TO TISSUE CHARACTERIZATION

Biagi E.\*, Calzolari M.\*, Castellini G.+, Grimaldi A.\*, Masotti L.\*\$, Rocchi S.\*

- \* Dipartimento di Ingegneria Elettronica, Università degli Studi di Firenze, Via S. Marta, 3 - 50139 Firenze
- + Istituto di Ricerca sulle Onde Elettromagnetiche del C.N.R., Via Panciatichi, 64 - 50127 Firenze
- \$ Responsible for correspondance

A digital system for acquisition and processing of ultrasound signals in echographic apparatus is presented. The system is based on a high capacity and velocity buffer memory, a signal processing card and an intelligent controller. The aim of the work is to process directly R.F. data to enhance the ultrasound system and to better characterize the human tissues. One application in medical researches is presented.

Key words:

front-end equipment, acquisition system, signal processing, ultrasonic tissue, ophthalmology.

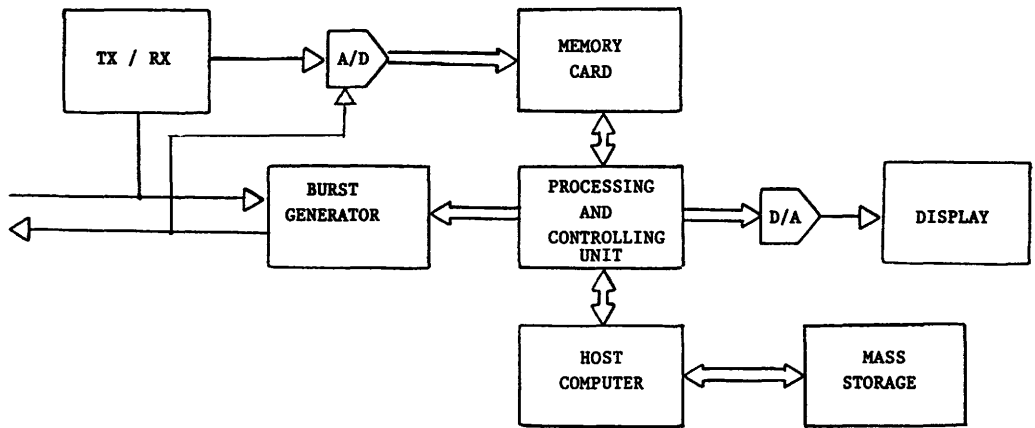
INTRODUCTION

In these last years ultrasonic apparatus improvement for diagnostic purposes is essentially due to the better quality of the images.

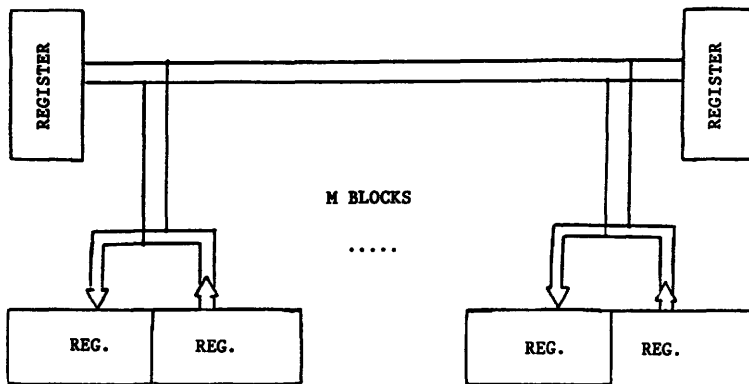
New digital imaging systems give the possibility to implement algorithms to reconstruct, enhance and analyse ultrasonic images. However original data quality limits sophisticated numerical applications.

Transducer, with the related electronics and digital interfacing system are critical items for any digital ultrasonic equipment: signal to noise ratio, bandwidth, dynamic range, sampling jitter compromise the use of some image processing approaches (3).

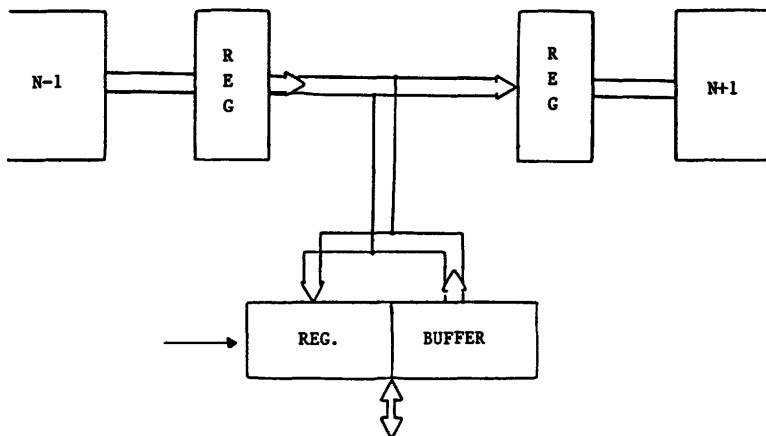
Our Laboratory has realized an experimental digital system which is now used in echographic signal processing to solve some of these deficiencies, yet its single blocks present interesting characteristics useful in many other applications.



1) Block scheme of the system



2) Logically very simple structure of the memory card



3) Memory card structure with digital delay line

The system will be used in different medical applications: one of these concerns the characterization of the orbital tissue.

## DIGITAL SYSTEM

The equipment may act as an high frequency (up to 50 MHz) acquisition system or as a signal synthesis system under the control of a processing card.

The system meets two important requests:

- 1) it has to be portable and usable both as a stand alone ultrasonic equipment and as a slave instrumentation of traditional echographic equipments;
- 2) it has to be dynamically reconfigurable under the control of a Personal Computer through standard interfaces.

The apparatus can be used to acquire video images, R.F. signals from traditional echographic instrumentation or to excite transducers with a preshaped signal (synthesizer configuration). These two features have proved it to yield an important instrument in an ultrasonics laboratory, because front-end ultrasonic equipment is completely controlled (fig 1).

The system may be divided in three functional blocks:

- 1) The storage block includes a memory card, with a maximum frequency clock of 50 MHz and a storage capacity of 512 Kbytes.
- 2) The input-output block is formed by an high speed A/D and a D/A converter (50 MHz, 8 bits), a programmable burst generator and a wide band analog block, comprehensive of the ultrasonic transducer transmitting and receiving functions. A lower speed section controls information exchanging with a Personal Computer through standard input-output (RS232, IEEE488).
- 3) The high speed processing card is based on a signal processing chip (TMS320/10). The DSP chip presents many characteristics typical to general purpose processors. The previous characteristics are necessary in this application since the card is used as a processing unit and at the same time as a system controller (1), (2).

## MEMORY CARD

The most important characteristics of this card are flexibility, simplicity and velocity. These are due to its data

flow structure and to the fact that the memory card is completely slave to data incoming or data request.

The card is built up by standard TTL FAST components and presents a pipelined structure without internal clock and feedback for optimizing the timings. In fact there is an almost total absence of combinatory logics to avoid delay uncertainties with consequent different effects in the wide working frequency range (DC to 50 MHz).

A compromise between velocity and cost has led to the choice of CMOS memory chips commercially available with 32 Kbytes capacity and 120 ns. minimum access time. The card is composed of eight memory banks. This number could become higher, in fact it has a modular structure, pipeline organized, driven by only one clock.

For analysing the storage card it is important to resume the steps leading to the final realization.

The logical simpler structure (fig 2) is the parallel connection of memory banks (one memory chip, one register for input data, one register for output data); this is apparently a simple organization, however the clock of each bank may be one clock period shifted with the other: a complicated and sensible logic control would be necessary.

A great simplification is obtained by introducing a digital delay line, being determined by the ratio between memory access time and conversion time. So all bank timings are synchronous and the time shifting of the previous version is substituted by data shifting through pipeline levels. In this structure maximum shifting speed is given by the single component minimum delay (fig 3).

Finally an improvement is obtained by the scheme of figure 4 where all data I/O registers have the fundamental clock and all the memory banks and I/O bus buffers are synchronous.

So the memory structure becomes easily testable and no delay problem arises when changing the clock frequency.

#### INPUT-OUTPUT BLOCK

This is a very heterogeneous block characterized by different speeds and different technologies.

Logically it can be divided into four parts:

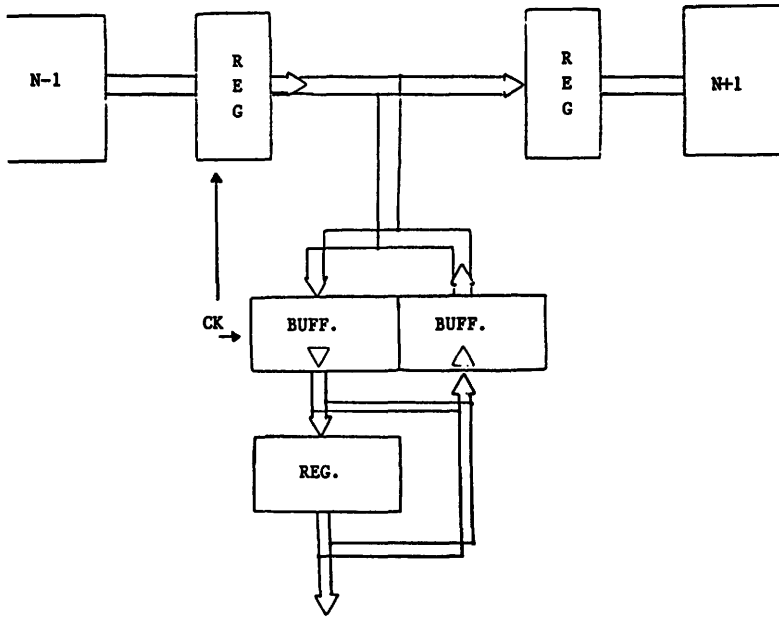
- 1) Sampling and conversion card based on an A/D high speed ECL converter (TRW-TDC1025E1C) with 50 MHz sampling rate and about 48 dB dynamic range and, a D/A conversion section with the

same sampling rate and dynamic range, useful for displaying different output signals also when the system is used as a signal synthesizer.

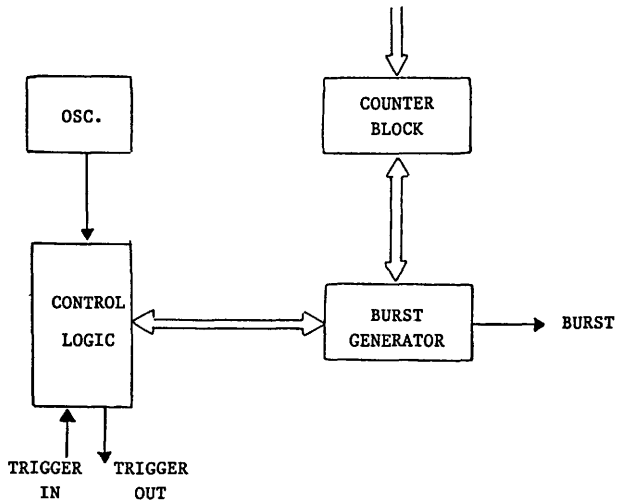
- 2) Analog section for eventually exciting the ultrasonic transducer and amplifying echosignals. Both for transmitting and for receiving blocks two demands have been met: they have to be wide-band systems (about up to 20 MHz) and adaptable to different transducers.
- 3) Programmable burst generator to choose the acquisition range gate. After the start strobe acknowledgment and a programmable delay, a programmable number of pulses (counter block in figure 5) goes to the A/D converter, a pulse train whose length has to be exactly the programmed one in order to find the exact acquired signal portion in the storage card. Pulses have to possess a duty cycle suitable to the A/D converter, for all possible clock frequencies and exactly the same both in the beginning and in the end of the burst. Start strobe can be an internal or external trigger. In the latter case it has to be acknowledged with maximum precision to minimize sampling jitter (100 MHz clock period given by a high stability oscillator) between different echoes or, it has to be resynchronized with the same precision by the system clock: conditions necessary for implementing synthetic aperture and focusing techniques. The answer to these requests is given by a particular logic structure realized with traditional FAST technology components (fig 5).
- 4) Lower speed section based on parallel and serial standard connections for Personal Computer communications. Information can be programs for system reconfiguration or data for mass storage acquisition.

#### PROCESSING AND CONTROLLING CARD

The processing card has been implemented using the Texas Instruments TMS 320/10 signal processor chip, which appeared particularly interesting for its peculiar memory structure, in addition to its computation capabilities. Unlike other signal processors, the TMS 320/10 allows the mixing of data and instructions in the same memory bank and the addressing of memory external to the chip. As a matter of fact either an internal ROM, or a combination of internal ROM and external RAM, or a completely external RAM can be used. The last choice is obviously the most convenient in experimental systems or when a low production of



4) Final memory card structure



5) Block scheme of the burst generator

equal cards is required.

Another advantage can be mentioned. Dynamically reconfigurable systems are implementable using an external RAM for data and program storage. Moreover due to the possibility of mixing data and instructions in the addressable RAM, the chip is usable also as a general microprocessor, which can run software to control the processing card and to debug the programs themselves.

The block diagram of the implemented card is shown in fig 6, where two main characteristics of the chosen architecture can be easily singled out. The first is the existence of a second microprogram memory (M2) in parallel to the TMS 320/10 program memory (M1), whilst the second is the splitting of the memory in two banks of 4 kwords, one implemented with static RAM chips (M1, M2), the other with EPROM chips (M1', M2'). The M2 memory contains all the information which is necessary to control the circuitry on the card without a direct intervention of the TMS 320/10 chip.

Using the microprogram bits in M2, for instance, it is possible to control all the input-output system (polling of the I/O channels) and to synchronize the acquisition of data, without any load on the signal processing chip.

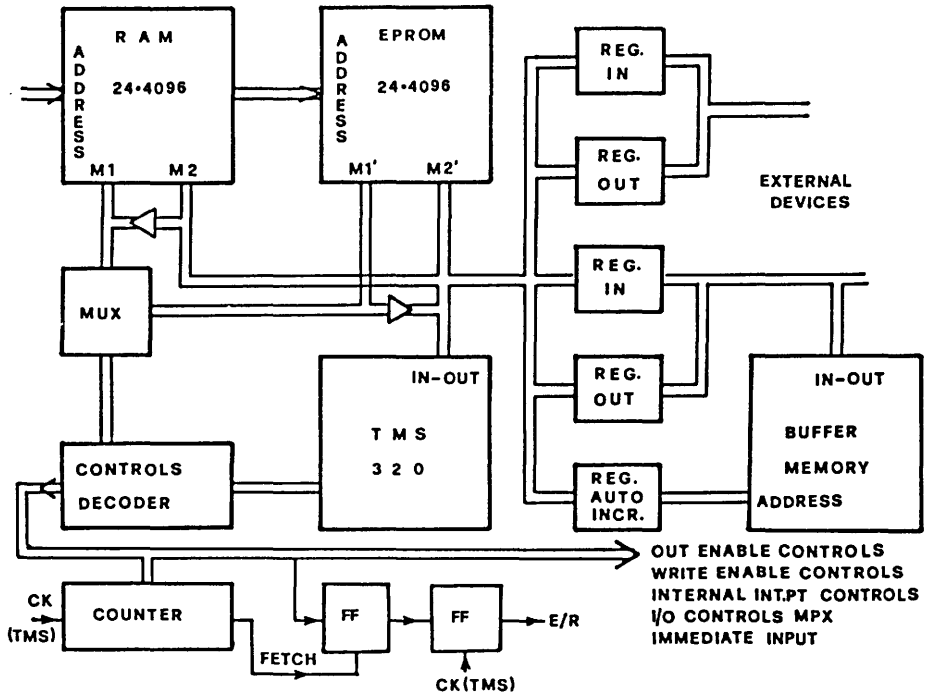
It can be observed that the maximum speed in signal processing applications can be obtained with completely sequential programs, where control and branch instructions are reduced to a minimum. That means that long programs result also with relatively simple algorithms. Therefore a separate microprogrammed control of the card and the use of the chip only for number crunching operations during the execution of computation intensive algorithms is very convenient.

The complete control of the TMS 320/10 chip and the monitoring of its operation cycles (e.g. the fetch cycle) allows also the use of different 4-Kwords memory banks. The switching from one memory bank to the other is obtained by means of a branch instruction with appropriate microprogram bits.

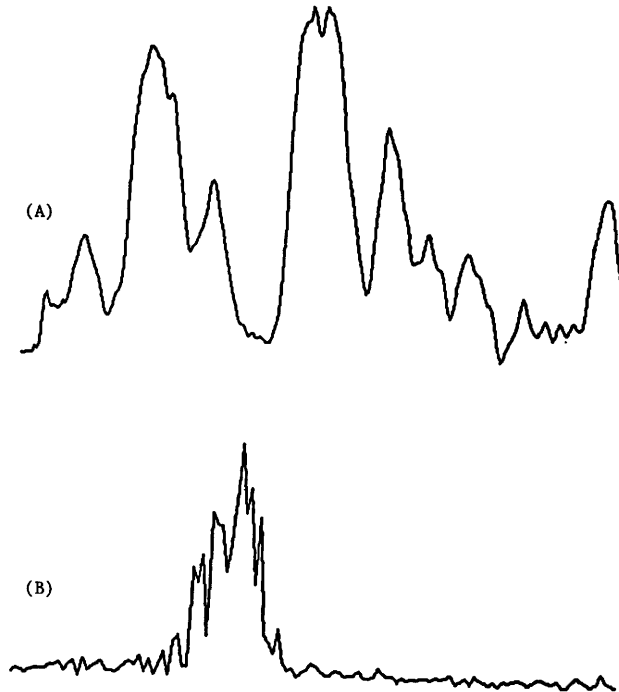
When the card is used inside the general processing system, the bootstrap and a debugger program are present in the EPROM memory. At power-on, the system starts running the bootstrap in EPROM and the application program is loaded into the RAM through the microprogram bus.

When the card is used as stand-alone processing system, the entire program is stored in EPROM and, if necessary can be transferred into RAM before its execution.

Two main applications have been developed up to now: an en-



6) Block scheme of the processing and controlling card



7) (A) A-Mode and (B) power spectrum of a typical pathology



velope detector using the Hilbert bandpass filtering approach and a spectrum analyser for echosignal in ultrasound applications which is employed in a commercial machine.

The envelope detector consists of two transversal digital filters with 21 coefficients, one of which is a bandpass filter and the other is a band-pass Hilbert transformer with the same bandwidth.

The outputs of the two filters are then squared and summed to extract the envelope with a final square-root evaluation. The computing time for each output point is 23.4 microseconds and 117 instructions are necessary.

## APPLICATIONS

In the orbital tissue characterization, radiofrequency analysis adds important informations, in fact the eye diagnosis is supported not only by common A-mode analysis, but also by the spectral one. Spectral analysis is used for attenuation and velocity dispersion measurement and power spectrum morphology (typical scalloping) gives informations about scatterer distribution and dimensions.

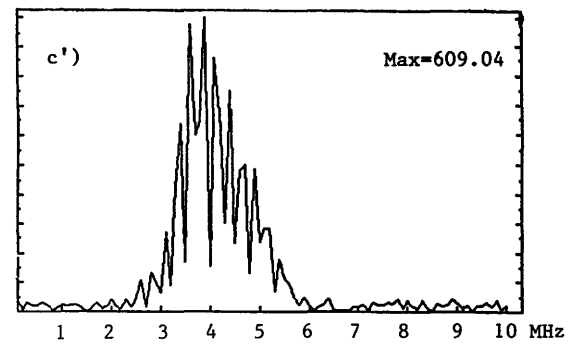
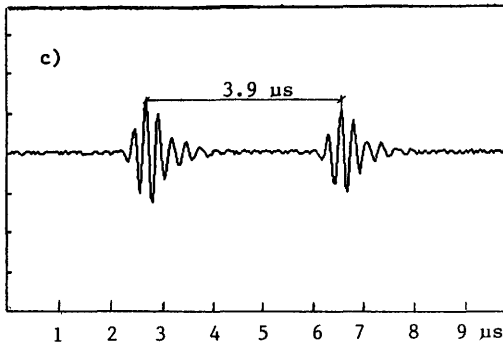
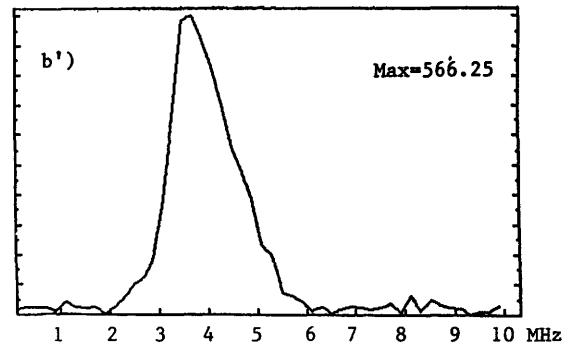
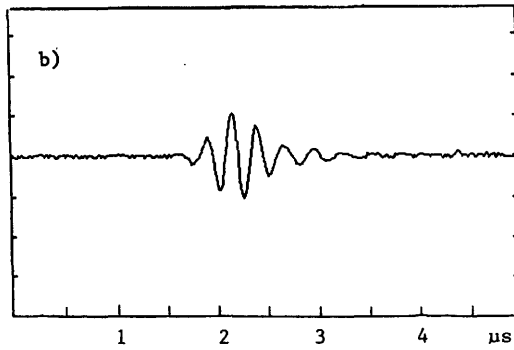
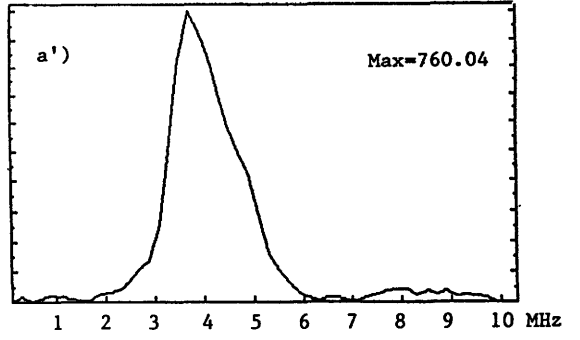
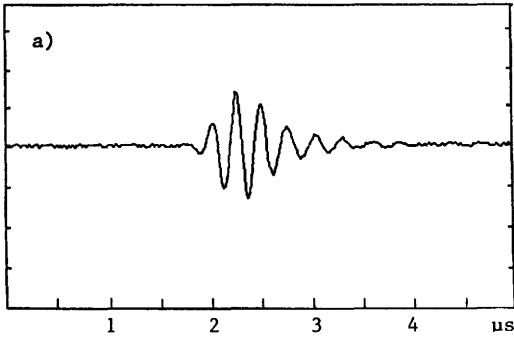
Our studies are devoted to the orbital zone and are developed in co-operation with the "Istituto di Scienze Oftalmologiche dell'Università di Siena". In the preliminary phase of this work some different pathologies of R.F. echosignals are acquired. A 8 MHz nominal frequency and 2.4 MHz at 6 dB bandwidth transducer was used. An A-mode 7200 MA Kretztechnik as echograph and a digital oscilloscope PM 3310 Philips as acquisition system was the available instrumentation in this first approach. Spectrum analysis parameters proposed by Lizzi et alii (4), (5), (6) are evaluated: power spectrum, estimation based on the 27 echosignal power spectrum average (smoothed power spectrum) and its linear regression were implemented.

The research is now developed following two different methodologies.

The first one is devoted to verify the significance of the parameters proposed by Lizzi et alii .

The second one, instead of processing the smoothed power spectrum is devoted to the research of the relation between the distribution of the scalloping in the frequency domain and the distribution of the scatterers in the space domain (fig 7).

This relation is evident in the following simple example: two nylon ( $\rho=0.1$  mm) wires are insonified by a 3.5 MHz ultrasonic



8) R.F. echosignals from the wires (a, b, c) and correspondent power spectrum (a',b',c')

transducer and the figure 7 shows the connection between spectrum periodic scalloping and mutual wires' distance (fig 8).

Study development will be now supported by an instrumentation improvement:

- 1) Wide band transducer
- 2) Powerful system above described

Therefore it is possible: to avoid non-linear processing showing in traditional instrumentation, to improve resolution by using synthetic aperture and focusing techniques or by exciting transducer with particular signals and to obtain available quasi-real time results of many preprocessing algorithms.

## REFERENCES

- (1) Castellini G., Emiliani P.L., Rocchi S., A new bit-slice structure and its application to ultrasound data processing  
EUSIPCO-83 Signal Processing: Theories and Applications, pp. 813-816
- (2) Casini A., Castellini G., Emiliani P.L., Rocchi S., An auxiliary processor of biomedical signals based on a signal processing chip  
Digital Signal Processing-84, pp.228-232
- (3) Schafer M.E., Lewin P.A., The Influence of Front-End Hardware on Digital Ultrasonic Imaging  
IEEE Transactions on Sonics and Ultrasonics, SU-31 n.4, pp. 295-306, July 1984
- (4) Coleman D.J., Lizzi F.L., Computerized ultrasonic tissue characterization of ocular tumors  
American Journal of Ophthalmology, 96, pp. 165-175, 1983
- (5) Masotti L., Frezzotti R., Brocchi R., Esposti P., Biagi E., Motolese E., Calzolari M., Malpassi C., Grimaldi A., Patachini E., Rocchi S., Casini A., Castellini G., Prospettive di sviluppo della ecografia orbitaria: caratterizzazione dei tessuti mediante l'analisi spettrale computerizzata del segnale a radiofrequenza  
Relazione al 65 Congresso di Patologia, e Terapia delle Malattie dell'Orbita, pp. 79-100, Siena 5-8 dicembre 1985
- (6) Feleppa E.J., Lizzi F.L., Coleman D.J., Yaremko M.M., Diagnostic Spectrum Analysis in Ophthalmology: a Physical Perspective  
Ultrasound in Med. & Biol, 12 n.8, pp. 623-631, 1986

**Session 3 - ATTENUATION I**

**Chairman : U. Raeth**



## IN VIVO ATTENUATION MEASUREMENT METHODS AND CLINICAL RELEVANCE

Brian S. Garra, Thomas H. Shawker,  
Michael F. Insana, Robert F. Wagner

### Introduction:

Since the earliest clinical uses of ultrasonic imaging, attenuation estimates have been an important part of the interpretation of ultrasound (US) images. For focal lesions, attenuation within the lesion is based on the presence of "acoustic enhancement" or "acoustic shadowing" in which increased or decreased echoes are seen posterior to a lesion relative to the adjacent background. This is due to the attenuation in the lesion being different from that of adjacent tissues. In clinical practice one tends to think of a lesion which shows enhancement as being fluid filled and one showing shadowing as being gaseous, bony, or a calculus. Our inability to accurately quantify the degree of shadowing or enhancement (i.e. the attenuation) makes it nearly impossible to accurately diagnose many lesions where only slight enhancement or shadowing is present.

For example, solid lymphomatous lesions may often show acoustic enhancement (Fig. 1) due to low attenuation or refraction<sup>1,2</sup> while myomas may give either enhancement or shadowing depending on the degree of calcification present.

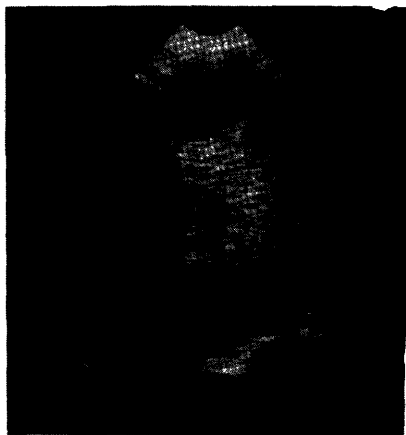


Fig. 1 Strong acoustic enhancement posterior to a lymphomatous mass in the liver.

For entire organs estimation of attenuation is even more difficult depending on the subjective impression that higher than usual gain and TGC settings must be used to penetrate the organ. An example of this is shown in a patient with fatty infiltration of the liver (Fig. 2) where difficulty penetrating the liver to see the diaphragm was noted. Gosink et.al.<sup>3</sup>

noted that the degree of beam penetration was the most difficult criterion to apply for diagnosis in 61 patients with various types of diffuse liver disease. Dewberry<sup>4</sup> studied 67 patients with cirrhosis and found attenuation effects on the B-scan images, but concluded that the observation was too subjective to be of value. In addition to the subjective nature of visual interpretation, other factors which hamper our ability to detect attenuation changes and diffuse disease in general include TGC variation, transducer focusing effects, and variable pre/post processing. Out of the above studies and others grew an interest in doing quantitative ultrasonic tissue characterization. Quantitative analysis has the advantages of less operator dependence, potential to detect smaller changes in acoustical parameters than the eye, making available to the observer information only indirectly observable on the image (attenuation, speed of sound), and of bringing out features that are not perceived by the eye such as the mean spacing between scatterers.

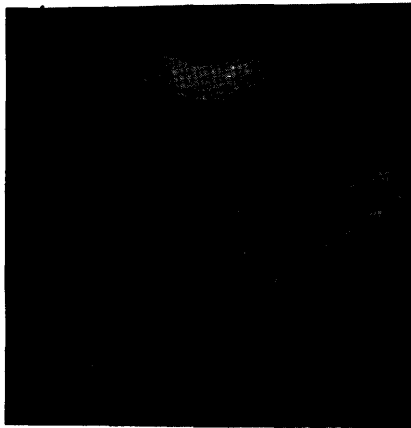


Fig. 2 Weak diaphragmatic echos suggesting a highly attenuating liver in a patient with Type I Glycogen Storage Disease

The purpose of this paper is first to briefly review the methods of attenuation measurement in vivo with their advantages and disadvantages. Next, the results in humans obtained by these methods will be reviewed. Finally, conclusions regarding the role of attenuation measurement and how it may be used as part of a multiparameter tissue characterization approach will be discussed.

#### Methods overview:

Several methods of attenuation measurement have been developed which involve both frequency and time domain signal processing. One popular method is the Spectral Difference Method<sup>5</sup> in which the radio frequency (RF) signals from various depths are converted to power spectra. The log spectra from two depths are subtracted from each other and a line (either straight or power law) is fitted to the result. Attenuation in soft tissue is commonly modeled using a power law function ( $\alpha = \beta \times f^N$ ) where  $\alpha$  is attenuation in dB/cm,  $\beta$  is the frequency dependent coefficient in dB/cm/MHz, and  $N$  is the power law dependency (usually between 0.9 and 1.4).



The spectral difference method has the advantage of giving both  $\beta$  and  $N$ . In addition, it does not assume a specific shape to the spectrum of the US pulse as do many other methods. Some disadvantages of the method include sensitivity to the beam pattern of the transducer and rather variable results obtained in vivo by different workers due in part to noise present in the calculated power spectra. A variation of the spectral difference method is the method of Lizzi<sup>6</sup> where spectra from different depths are subtracted from the spectrum reflected from a metal plate and a straight line fitted to each result. The slopes of the linear fits are plotted vs. depth and the slope of this plot is the attenuation value  $\beta$ . A similar method was used by Wilson et.al.<sup>7</sup> except that a different method for correcting for transducer focusing/diffraction effects was used.

Another common method for in vivo attenuation measurement is the Spectral Shift Method where the US pulse is assumed to have a Gaussian spectrum and the tissue is assumed to have a linear frequency dependence of attenuation ( $N=1$ ). Under these conditions the bandwidth of the pulse remains constant but the mean or center frequency shifts downward as the beam traverses tissue. If the center frequency is plotted vs. depth, the slope of that linear plot may be used to calculate the attenuation:

$$\text{slope}/4BW=\beta \quad (1)$$

BW is the variance of the US beam in MHz squared. The center frequency may be estimated two different ways. One may measure the mean frequency (centroid) of power spectra at different depths or one may count the number of zero crossings of the RF at different depths. This method has been studied by several workers<sup>8,9</sup> and was incorporated into several prototype commercial sector scanners for in vivo measurements. Unfortunately, initial results in clinical trials showed large variations (on the order of 100%) in the measurements.<sup>10</sup> Ophir et.al.<sup>11</sup> then showed that to reduce variation to acceptable levels using zero crossings, more data would have to be collected and averaged than would be feasible in an ordinary clinical setting. This problem plus problems making the needed transducer focusing/diffraction corrections have damped initial optimism regarding this method.

Rather than measuring spectral shifts or analyzing power spectra, a simpler approach is to measure the loss in amplitude over depth at a single frequency. The earliest attempts to measure US attenuation<sup>12</sup> were amplitude based methods. Since standard US scanners measure amplitudes to generate images, amplitude based methods are easier to implement than methods based on spectral parameters. In the method described by Ophir<sup>13</sup>, a narrow band pulse is used which allows a simple amplitude relationship to be used:

$$A_d = A_o e^{-\beta 2df} \quad \text{and} \quad \frac{\log A_o - \log A_d}{2df} = \beta \quad (2)$$

$A_d$  is the amplitude at depth  $d$ , and  $A_o$  is the amplitude at the initial depth. Thus taking the difference of the log amplitudes gives the

attenuation at frequency  $f$ . One does not have to contend with center frequency shifts as a function of depth. By averaging many amplitude differences within a region of interest (ROI), the random variability can be made very low. Transducer focusing effects are eliminated by moving the transducer closer to the patient when data from deeper tissues are to be collected, allowing data collection at the same distance from the transducer surface. The disadvantage of this is that it is too cumbersome a scanning method for routine use. Since attenuation is obtained only at a single frequency, one cannot obtain the power dependence of attenuation vs. frequency and one must assume a value (usually  $N=1$ ) to obtain  $\beta$ .

Recently a new amplitude based method has been described<sup>14</sup> which uses a broadband beam. The transducer is weakly focussed to minimize error due to focusing effects. The attenuation is calculated based on the slope of the TGC amplifier curve after that curve has been set to give constant echo amplitude vs. depth in the ROI. The attenuation in dB/cm is then divided by the average frequency in the ROI (measured from zero crossings) to give an attenuation slope in dB/cm/MHz. The method assumes an approximately gaussian shaped spectrum for the US pulse and a linear frequency dependence of attenuation. In both patients and phantoms it gave lower variability than the spectral shift method.

Finally, our own amplitude based method developed in 1984-85<sup>15,16</sup> is also a broadband method based on the same assumptions. In our method root mean square (RMS) amplitudes are calculated at multiple depths within the ROI. TGC and transducer focusing effects are corrected for using calibration phantom amplitudes obtained at the time each patient is scanned. Backscatter amplitudes (relative to the phantom) corrected for attenuation are then calculated using different attenuation ( $\beta$ ) values until the backscatter amplitudes vs. depth remain constant. Attenuation values obtained by this method show lower variability than do those obtained using the Spectral Difference method in phantoms, in patient groups, and over time.

#### IN VIVO RESULTS:

Using the methods outlined above in vivo attenuation measurements have been obtained in several organs. The vast majority of the measurements have been obtained from liver<sup>5,6,7,10,12,14,15,17-26</sup> because of its accessibility to the US transducer, large size, homogeneous texture, and number of diffuse diseases which may affect it. Attenuation estimates have also been made in focal lesions of the liver<sup>6,7</sup> normal spleen<sup>18</sup> muscle<sup>13,27</sup>, pancreas<sup>18</sup>, and heart.<sup>28</sup> The results for tissues other than liver are summarized in Table 1. The results are too limited to draw any conclusions other than that attenuation measurement is possible and that one may be able to separate normal muscle from abnormal using attenuation. Further studies in other organs are needed but are hampered by the small regions of interest that must be used in organs other than liver.

Table 1. IN VIVO RESULTS -- NON LIVER

ORGAN	PATIENTS	ATTEN. (dB/cm/MHz)	METHOD
Nl. Spleen	30	0.21±.07 (N=1.1 to 1.6)	Spect. Diff.
Nl. Muscle	10	4.71± .44 dB/cm	Narrow band Amp. (4.3MHz)
" "	13	0.51± .15	Spect. Shift
Musc. Dyst. Carriers	24	0.65± .08	Spect. Shift
Pancreas	30	0.38± .09 (N=1.1 to 1.3)	Spect. Diff.

For the human liver, enough results have accumulated to allow some conclusions to be drawn both about methods and about the clinical results. Values reported in the literature for attenuation in normal liver are summarized in Table 2. The attenuation of normal liver has generally been reported to be between 0.5 and 0.6dB/cm/MHz. Some of the very early reports gave lower values with higher values being reported in 1984. The most recent reports have given values of about 0.5dB/cm/MHz and more importantly have shown less variability than some of the earlier work.<sup>21</sup> In particular, the amplitude based methods have shown less random variation than either the spectral shift or spectral difference methods.<sup>14,15</sup>

Most of the attenuation measurements in diseased liver have been in diffuse diseases including cirrhosis (alcoholic, primary biliary, cardiac, and that due to hepatitis and hemochromatosis), chronic hepatitis, fatty liver, diffuse tumor infiltration, and Gaucher's disease. In most cases the diagnoses was confirmed either by liver function tests or by biopsy. An ultrasonic method of detecting and grading many of these diseases would be extremely helpful as both the initial biopsy for diagnosis, and later biopsies to evaluate disease progression could then be avoided. The attenuation results for cirrhotics are listed in Table 3. Early results suggested that cirrhotics had elevated attenuation values. However, later studies of both alcoholic and non alcoholic cirrhosis<sup>14,15</sup> did not confirm this. These studies suggest that elevated attenuation in cirrhotics is not due to fibrosis but is instead due to concomitant fatty infiltration. This is unfortunate since fatty infiltration is reversible and of no real prognostic significance. Clinicians are primarily interested in the amount of fibrosis and inflammation.

Table 2.

## IN VIVO RESULTS -- NORMAL LIVER

AUTHOR	PATIENTS	ATTEN. (dB/cm/MHz)		N	METHOD
		mean	S.D		
Kuc (1980)	42	0.43 ± .07		--	Spect. Diff.
Jones (1981)	30	0.47 ± .07		0.9-1.1	Spect. Diff.
Cooperberg (1984)	10?	0.68 ± .14		--	Zero Cross
Garra (1984)	31	0.63 ± .13		--	Zero Cross
Kuc (1984)	50	0.55		--	Spect. Diff.
Maklad (1984)	39	0.52 ± .03		--	Amplitude
Parker (1984)	11	0.59 ± .21		.81-1.5	Spect. Diff. (variant)
Sommer (1984)	3	0.71 ± .07		--	Spect. Shift
Wilson (1984)	12	0.53 ± .10		--	Spect. Diff. (variant)
Fredfeldt (1985)	13	0.72 ± .14		--	Amplitude
King (1985)	10	0.79 ± .09		--	Spect. Diff. (variant)
Taylor (1986)	26	0.52 ± .12		--	Amplitude
	26	0.50 ± .20		--	Spect. Shift
Garra (1986)	18	0.49 ± .12		--	Amplitude
	18	0.62 ± .18		--	Spect. Diff.
Parker (1986)	21	0.47 ± .08		--	Spect. Diff. (variant)

Table 3.

## IN VIVO RESULTS -- CIRRHOSIS

AUTHOR	TYPE	NO. PTS	ATTEN. (dB/cm/MHz) mean $\pm$ S.D. [range]		Nl. RANGE
<b>CLINICAL</b>					
Sommer ('84)	Hep.	7	0.93	[.85-.98]	.65-.77
Wilson ('84)	?	9	0.64	[.39-.87]	.38-.63
Maklad ('84)	Cardiac	4	0.66		.48-.55
King ('85)	ETOH	8	1.07 $\pm$ .20		.79 $\pm$ .09
<b>HISTOLOGIC</b>					
Maklad ('84)	ETOH	5	0.83	[.72-.92]	.48-.55
Fredfeldt ('85)	MTX	5	0.72 $\pm$ .12		.72 $\pm$ .14
Taylor ('86)	ETOH	23	0.57 $\pm$ .14		.52 $\pm$ .12
	(without fat)	16	0.53 $\pm$ .11		.52 $\pm$ .12
	Hemo.	2	0.43 $\pm$ .11		.52 $\pm$ .12
Garra ('86)	Hep.	11	0.45	[.22-.57]	.29-.60
	Hemo.	2	0.47	[.27-.68]	.29-.60

Note: The range of values for attenuation is given whenever available, otherwise the Std. Deviation is given.  
 Hep.= Chronic Hepatitis, Cardiac = cardiac cirrhosis  
 ETOH = cirrhosis due to ethanol abuse  
 MTX = methotrexate therapy  
 Hemo. = Hemochromatosis

The results of two studies on chronic hepatitis are shown in Table 4. These studies have suggested that lower attenuation is present in inflamed livers, but further studies closely correlated with histology will be necessary to determine if this change is enough to be clinically useful.

Table 4.

## IN VIVO RESULTS -- CHRONIC HEPATITIS

AUTHOR	NO. PTS	ATTEN. (dB/cm/MHz) mean $\pm$ S.D. [range]		Nl. RANGE
Maklad ('84)	13	.52 $\pm$ .04		.48-.55
Garra ('86)	29	.50 $\pm$ .18	[.21-.90]	.29-.60
low subgroup	24	.42 $\pm$ .09	[.21-.55]	.29-.60

Note: The low subgroup represents the lower group of the bi-modal chronic hepatitis group (see reference 16).

Table 5 shows the results for fatty livers. Earlier studies gave somewhat variable attenuation values for fatty infiltrated livers but two of the most recent studies show that fatty livers have increased attenuation and that this increase correlates with the amount of triglyceride present. In fatty livers, both  $\beta'$  and N may be increased. There is evidence that intrahepatic accumulations of other lipids (sphingomyelin in Niemann-Pick) may increase attenuation as well.<sup>16</sup>

Table 5. IN VIVO RESULTS -- FATTY LIVER

AUTHOR	CAUSE	NO. PTS	ATTEN (dB/cm/MHz) mean $\pm$ S.D. [range]	Nl. RANGE
Kuc ('80)	?	4	0.49 $\pm$ .09 [.41-.62]	.44 (one)
Maklad ('84)	?	5	0.49 $\pm$ .11 [.37-.66]	.48-.55
Wilson ('84)	?	3	0.87 [ .47-1.34]	.38-.63
Fredfeldt ('85)	MTX	9	0.91 $\pm$ .16	.72 $\pm$ .14
Taylor ('86)	MTX	7	0.77 $\pm$ .11	.52 $\pm$ .12
Garra ('86)	GLY	6	0.85 $\pm$ .12 [.68-1.06]	.29-.60

MTX = methotrexate therapy      GLY = Glycogen storage disease

Table 6 lists results for various other diseases including values obtained from focal lesions such as metastases. Gaucher's disease (glycolipid accumulation in the liver) does not increase attenuation but does increase echogenicity somewhat. The primary biliary cirrhosis patients had normal attenuating livers, but this disease is heterogeneous with inflammation predominating early and cirrhosis late. More cases with histologic correlation will be needed to determine if significant attenuation changes are truly present at some stages. The study of focal disease is tantalizing but the number of patients studied so far is too small to draw meaningful conclusions. The small size of focal lesions is a major obstacle to obtaining accurate attenuation estimates.

In summary, the newer methods of attenuation estimation, particularly the amplitude based methods, have given less random variation making it easier to separate normals from certain diseases. Unfortunately, in liver elevated attenuation appears to be primarily related to fatty infiltration instead of to the more important changes of inflammation and fibrosis. This fact means that attenuation alone has very limited usefulness in the characterization of diffuse liver disease. For other organs and for focal disease, the answers are not yet in.

Table 6. IN VIVO RESULTS -- OTHER LIVER DISEASE

AUTHOR	NO. PTS	ATTEN. (dB/cm/MHz) mean ± S.D. [range]	Nl. RANGE
-----			
PRIMARY BILIARY CIRRH.			
Maklad ('84)	2	0.56 and 0.57	.48-.55
Garra ('86)	4	0.50 ± .21 [.29-.86]	.29-.60
GAUCHER'S DISEASE			
Garra ('86)	30	0.49 ± .10 [.31-.69]	.29-.60
LYMPHOMA			
Maklad ('84)	1	0.39	.48-.55
Garra ('86)	1	0.54	.29-.60
NIEMANN-PICK			
Garra ('86)	4	0.76 ± .30 [.43-1.15]	.29-.60
COLON METASTASIS			
King ('85)	1	0.56	.79 ± .09
Wilson ('84)	4*	0.35 [.30-.40]	.38-.63
Wilson ('84)	2**	0.62, 0.82	.38-.63
HEMANGIOMA			
King ('85)	1	1.25	.79 ± .09
HEPATOMA			
King ('85)	1	0.65	.79 ± .09
-----			

\* mucin producing

\*\* non mucin producing

Other diffuse and focal diseases where only one case has been reported are not listed. These include: Wilson's disease, leukemia, cholangiocarcinoma, liver transplant, sclerosing cholangitis, breast carcinoma (met), ovarian carcinoma (met).

ATTENUATION IN MULTIPARAMETER ANALYSIS:

Although attenuation by itself is of limited usefulness, we believe that it has an important role in multiparameter analysis. Several groups have recently tried various multiparameter approaches to increase the sensitivity and specificity of ultrasound for disease detection.<sup>6,22,23,29,30</sup> Our approach<sup>31</sup> currently uses five different parameters:  $\beta$ , Arms-the average backscatter amplitude from the ROI,  $r$ -the ratio of diffuse to specular backscatter intensity, the mean scatterer spacing ( $\bar{d}$ ), and the variance of the specular backscatter intensity. The attenuation and backscatter amplitude are calculated as

described earlier. The other parameters are obtained from the average autocorrelation function and its Fourier transform (the speckle power spectrum) using methods previously reported.<sup>32</sup> After the five parameters have been calculated and averaged for six regions of interest per patient, a discriminant function is used to classify the patients based on the five parameters. The function used is a linear Bayes classifier which is a rule intended to minimize the cost of a misclassification.

$$\bar{\mathbf{m}}^T \mathbf{x} - \frac{1}{2} \bar{\mathbf{m}}^T (\bar{\mathbf{x}}_1 + \bar{\mathbf{x}}_2) \leq \ell'$$

$$\ell' = \ln \left[ \frac{P(\omega_1) c_{12}}{P(\omega_2) c_{21}} \right] \quad (3)$$

A prewhitening matched filter ( $\bar{\mathbf{m}}^T$ ) is multiplied by the 5-D measurement ( $\bar{\mathbf{x}}$ ) and is compared to a point midway between the two groups to be classified. A patient is classified into one group or another depending on whether the difference is less than or greater than a threshold value ( $\ell'$ ). The threshold value is the ratio of diagnosis prevalence within the population multiplied by the ratio of the costs of misclassifying a patient from one group into the other.

Often one does not have good data on either the disease prevalence or on the cost of a misdiagnosis. Fortunately one can compare two tests over the entire range of threshold values using receiver operating characteristic analysis (ROC). To generate an ROC curve from the discriminant function,  $\ell'$  is varied and the number of cases classified correctly and incorrectly at each  $\ell'$  value are counted. Then the true positive fraction is plotted against the false positive fraction for each  $\ell'$  value used. The area under the ROC curve is often used as an index of the overall performance of a diagnostic test. Pure guessing gives an area of 0.5 while a perfect test gives an area of 1.0.

In Figure 4, ROC curves obtained using our five parameter technique for normals vs. chronic hepatitis, normals vs. Gaucher's disease and Gaucher's disease vs. hepatitis are shown and are compared to the ROC for the PAP smear (an accepted, reliable diagnostic test for cervical carcinoma). The five parameter method works quite well as can be seen by comparing the areas under the ROC curves. Human observer ROC studies recently conducted using five experienced sonographers and physicians<sup>31</sup> yield an area under the average ROC curve of only 0.63 for normal vs. chronic hepatitis. Thus as expected, humans looking at B-scans do poorly relative to the machine and do little better than guessing. The addition of attenuation to the parameters used in classification helps most for diseases where fatty infiltration is present. In Figure 5 the ROC curves using three and five parameters for detection of glycogen storage disease are shown. A dramatic improvement in performance (from an area of 0.83 to an area of 1.00) is seen when five parameters are used.



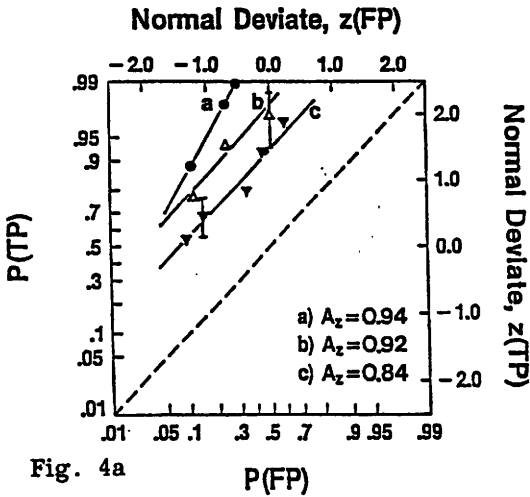


Fig. 4a

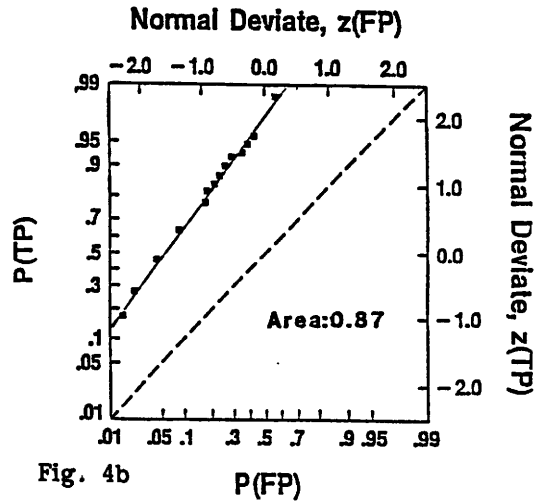


Fig. 4b

Fig. 4 a) ROC curves for machine detection and classification using 5 parameters. Curve (a) shows performance for separating normals (18 cases) from Gaucher's patients (42 cases). Curve (b) is for normals vs chronic hepatitis (46 cases) and curve (c) shows performance for separating Gaucher's disease from chronic hepatitis.

b) The ROC curve for detection of cervical carcinoma using the PAP smear (after J.W. Bacus et al in "Malignant Cell Detection and Cervical Cancer Screening" Analytical and Quantitative Cytology (6) p.125, International Academy of Cytology, 1984).

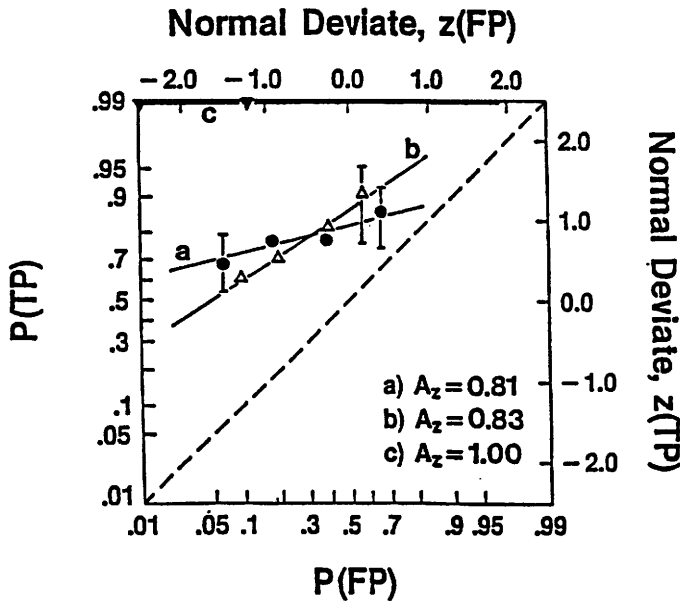


Fig. 5 ROC curves for separation of (a) normals (30) vs. primary biliary cirrhosis patients (13) using 3 parameters (d,r, variance of specular intensity), (b) normals (31) vs. Glycogen Storage disease using same 3 parameters, (c) normals (18) vs. 7 Glycogen Storage Disease patients using all 5 parameters (10).

In conclusion, we feel that a multiparameter approach will eventually be the most powerful tool for ultrasonic detection, classification, and grading of diseases both in the liver and in other organs. Attenuation measurement will continue to be an important part of future multiparameter methods.

#### References

1. Callen PW, Marks WM. Lymphomatous masses simulating cysts by ultrasonography. *J Can Assoc Radiol* 30:244-246 (1979).
2. Sheu JC, Sung JL, Chen DS, Yu JY, Wang TH, Su CT and Tsany YM: Ultrasonography of small hepatic tumors using high resolution linear-array real time instruments. *Radiology* 150:797-802 (1984).
3. Gosink BB, Lemon SK, Scheible W, and Leopold GR. Accuracy of ultrasonography in diagnosis of hepatocellular disease. *AJR* 133:19-23 (1979).
4. Dewberry KC, Clark B. The accuracy of US in the detection of cirrhosis of the liver. *Brit J Rad* 52:945-948 (1979).
5. Kuc R. Clinical application of an ultrasound attenuation coefficient estimation technique for liver pathology characterization. *IEEE Trans Biomed Engineering* BME-27:312-319 (1980).
6. King DL, Lizzi FL, Felippa EJ, Wai PM, Yaremko MM, Rorke MC, Herbst J. Focal and diffuse liver disease studied by quantitative microstructural sonography. *Radiology* 155:457-462 (1985).
7. Wilson LS, Robinson DE, Doust BD. Frequency domain processing for ultrasonic attenuation measurement in liver. *Ultrasonic Imaging* 6:278-292 (1984).
8. Dines KA, Kak AC. Ultrasonic attenuation tomography of soft tissues. *Ultrasonic Imaging* 1:16-33 (1979).
9. Kuc R, Schwartz M, Von Micsky L. Parametric estimation of the acoustic attenuation coefficient slope for soft tissue. *IEEE Ultrasonics Symposium Proceeding*. pp 44-47 (IEEE Cat. No. 76CH 1120-5SU) (1976).
10. Garra BS, Shawker TH, Nassi M, Russell MA. Ultrasound attenuation measurements of the liver in vivo using a commercial sector scanner. *Ultrasonic Imaging* 6:396-407 (1984).
11. Ophir J, Ghouse MA, Ferrari LA. Attenuation estimation with the zero crossing technique: phantom studies. *Ultrasonic Imaging* 7:122-132 (1985).

12. Mountford RA, Wells PNT. Ultrasonic Liver Scanning: The A-scan in the normal and cirrhosis. *Phys Med Biol* 17(2):261-269 (1972).
13. Ophir J, Maklad NF, Bigelow RH. Ultrasonic attenuation measurements of in vivo human muscle. *Ultrasonic Imaging* 4:290-295 (1982).
14. Taylor KJW, Riely CA, Hammers L, Flax S, Weltin G, Garcia-Tsao G, Conn HO, Kuc R, Barwick KW. Quantitative US attenuation in normal liver and in patients with diffuse liver disease: importance of fat. *Radiology* 160:65-71 (1986).
15. Garra BS, Insana MF, Shawker TH, Russell MA. Quantitative attenuation and echogenicity estimation in diffuse liver disease. *Ultrasonic Imaging* 8(1):54 1986 (Abstract only).
16. Garra BS, Insana MF, Shawker TH, Russell MA. Quantitative estimation of attenuation and echogenicity in normals and in diffuse liver disease. *Radiology* (in press).
17. Kuc R, Taylor KJW. Variation of acoustic attenuation coefficient slope estimates for in vivo liver. *Ultrasound in Med and Biol* 8(4):403-412 (1982).
18. Jones JP, Behrens M. In vivo measurement of frequency dependent attenuation in normal liver, pancreas and spleen. *Ultrasonic Imaging* 3:205 (1981) (Abstract only).
19. Cooperberg PL. Clinical value of attenuation measurements in diffuse disease of the liver and spleen. *J Ultrasound in Medicine* 3(9):52 (1984) (Abstract only).
20. Kuc R, Regula DP. Diffraction effects in reflected ultrasound spectral estimates. *IEEE Transactions on Biomedical Engineering* BME 31(8):537-545 (1984).
21. Maklad NF, Ophir J, Balsara V. Attenuation of ultrasound in normal liver and diffuse liver disease in vivo. *Ultrasonic Imaging* 6:117-125 (1984).
22. Parker KJ, Lerner RM, Waag RC. Attenuation of ultrasound: magnitude and frequency dependence for tissue characterization. *Radiology* 153:785-788 (1984).
23. Sommer FG, Gregory PB, Fellingham LL, Stern RA, Nassi M, Weissberg J, Solomon H. Measurement of attenuation and scatterer spacing in human liver tissue: preliminary results. *J Ultrasound Med* 3:557-561 (1984).

24. Fredfeldt K-E, Foged E, Sogaard H. Attenuation of ultrasound in the liver from patients treated with methotrexate. Proc 5th European Comm. Workshop on Ultrasonic Tissue Characterization and Echographic Imaging pp 71-75 (1985).
25. Parker K, Asztely M, Lerner R, Schenk E, Waag R. An in vivo study of ultrasonic attenuation in normal and abnormal liver. J Ultrasound in Medicine 5(9):118 (1986) (Abstract only).
26. Duerinckx A, Aufrichtig D, Rosenberg K, Hoefs J, Ferrari L, Cole-Beuglet C. Estimation of acoustic attenuation in liver: difficulties with a narrow band estimator and the importance of fat. J Ultrasound in Medicine 5(9):119 (1986) (Abstract only).
27. Berger G, Laugier P, Perrin J. A field of application for ultrasound attenuation: Duchenne muscular dystrophy. Proc 5th European Comm. Workshop on Ultrasonic Tissue Characterization and Echographic Imaging pp 77-83 (1985).
28. Mottley JG, Glueck RM, Perez JE, Sobel BE, Miller JG. Regional differences in the cyclic variation of myocardial backscatter and modification by ischemia. Ultrasonic Imaging 5:183 (1983) (Abstract only).
29. Insana MF, Wagner RF, Garra BS, Shawker TH. A statistical approach to an expert diagnostic ultrasonic system. Proc SPIE Vol 626 Medicine XIV/PACS IV pp 24-29 (1986).
30. Rath U, Zuna I, Lorenz A, Layer G, Schlaps D, Zerban H, Volk J, van Kaick G, Lorenz WJ, Bannasch JP. The ultrasound image texture of liver tumors. Ultrasonic Imaging 8(1):63 (1986) (abstract only).
31. Garra B, Insana M, Shawker T, Wagner R, Russell M. Detection and characterization of diffuse liver disease by ultrasound - a multiparameter approach. J Ultrasound in Medicine 5(9):117 (1986) (abstract only).
32. Insana MF, Wagner RF, Garra BS, Brown DG, Shawker TH. Analysis of ultrasound image texture via generalized Rician statistics. Opt Engineering 25(6):743-748 (1986).

## ATTENUATION AS AN ADDITIVE CLINICAL INDICATOR

G. Berger<sup>1</sup>, P. Laugier<sup>1</sup>, M. Fink<sup>1,2</sup>, and J. Perrin<sup>1</sup>

<sup>1</sup>Lab. of Biophysics - UA CNRS 593 - CHU Cochin  
24, rue du Fbg St. Jacques, 75674 Paris France

<sup>2</sup>GPS, Universite Paris VII, 2 Pl. Jussieu  
75005 Paris, France

This paper deals with the clinical interest of the measurement of attenuation in muscle. The precision of this estimation in vivo becomes an important parameter and will be compared to the theoretically expected variance. The results allow a comparison of the attenuation of a population of normal volunteers with a population of carriers of Duchenne Muscular Dystrophy. From the clinical standpoint, attenuation when estimated simultaneously with serum creatine-kinase level improves largely the detection of obligate carriers. Some particular cases in the women investigated allow to correlate the attenuation with some muscular modifications.

**Key words:** Attenuation; carriers of Duchenne Muscular Dystrophy; muscle; ultrasound

### I. INTRODUCTION

Different methods have been developed up to now in order to estimate the frequency dependence of attenuation, expressed in dB/cm.MHz. The different publications relative to in vivo measurements that can be found in the literature since 1980 [1] do not allow to draw definitive conclusions. Most of the measurements have actually been performed on liver. The choice of this organ is mainly due to the fact that accurate attenuation measurements can only be done on quite large tissue samples. This constraint is solved in liver which offer a large size and an homogeneous texture affected by diffuse diseases. There appears to be an overlap between the attenuation distribution of the normal livers and livers affected by most of the diffuse pathologies. On the other hand there appears to be a correlation between an increased attenuation and a fatty infiltration in the liver [ 2 ].

Our attention in the clinical domain is devoted to the measurement of attenuation in muscle. We aim at the detection of the carriers of DMD. In this the way, we would like to point out how the muscular attenuation estimation can be included in the actual detection procedure of those women and what is the clinical interest. We will then attempt to relate the attenuation to the muscular modifications.

Before the presentation of the clinical results, we would like to give some considerations on the precision of the estimator which is an important factor in the comparison of two populations.

## II. IN VIVO VARIANCE OF THE ATTENUATION IN MUSCLE

### 1. Theoretical expression of the variance.

The Echographic signal  $s(t)$  is the coherent sum on the front face of the probe of all the elementary waves scattered by the inhomogeneities located at a distance  $r$  from the probe such that  $2r = ct$ , where  $c$  is the mean speed of sound in the medium. These random interferences are responsible for the stochastic nature of the echographic signal. Their effect is quite visible on the scalloping of the running spectra calculated with a short time Fourier analysis on a single A-line. An averaging of the time-frequency representation is then necessary.

Kuc first derived the statistical properties of randomly distributed scatterers and showed that the standard deviation of the additive noise on the log-spectra denoted by  $\sigma_r$  is 5.6 dB whatever the frequency is [3,4]. This value, predicted by theory is confirmed by processing in vivo data on muscles [ 5,6 ] and allows to derive the bounds on attenuation measurements. The theoretical expression of the variance can be given for both of the algorithms we apply on the Time-Frequency representation : the spectral centroid shift [7] and the narrow-band Log-intensity decay [8, 17]

When the tissue is modeled as a homogeneous medium with randomly distributed scatterers, both algorithms lead to the same standard deviation on the estimation of the attenuation coefficients for a

single A-line [6] :

$$\text{var}(\beta) = \frac{18 c \sigma_r^2}{(\text{WD})^3 (1-1/L^2)} \quad (1)$$

where  $c$  is the mean speed of sound in tissue,  $\beta$  is the slope of attenuation coefficient in dB/cm. MHz, and  $\text{var}(\beta)$  is the variance of this estimate on a tissue depth  $D$  (where  $L$  possible non overlapping windows can be located), with a usable frequency bandwidth of  $W$ . In the centroid algorithm, the usable bandwidth  $W$  is the difference between the two frequency limits used for the centroid calculation (Fig. 1a). In the narrow band algorithm, the usable bandwidth  $W$  is the difference between the two frequency limits of the regression fit of the attenuation coefficient (Fig. 1b). This value is directly related to the bandwidth (defined at the - 6 dB level) of the probe.

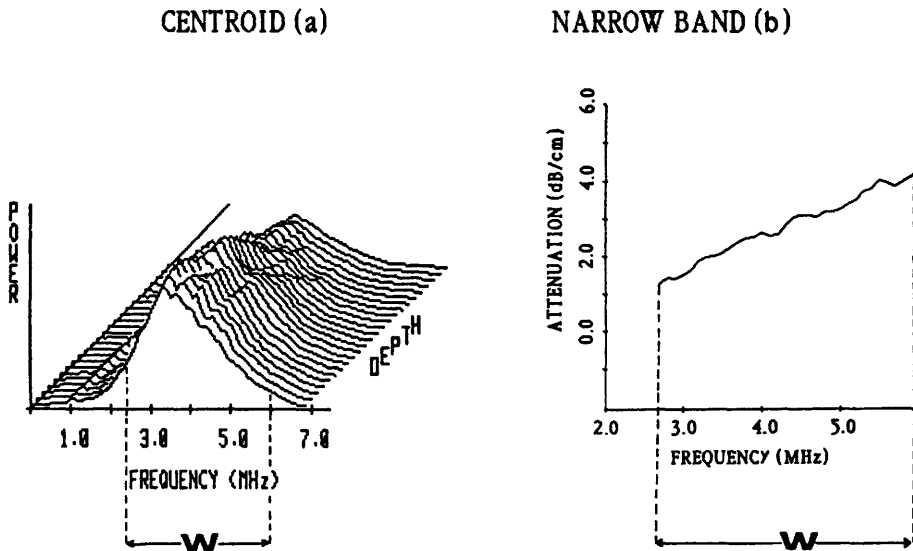


Fig. 1 Illustration of the usable frequency bandwidth  $W$  for attenuation estimation with a centroid algorithm (a) and a narrow band algorithm (b).

The equation 1 implies the uniformity of the attenuating and scattering properties of the tissue. The bandwidth  $W$  and the tissue thickness  $D$  are very important parameters to be considered and optimized as they appear at the third power in the variance expression.

## 2. Comparison of theoretical and in vivo variances in muscles.

The vastus medialis has been chosen for our investigations because it presents very few anatomical variations. Both thighs have been systematically explored. Our experimental setting consists of a mechanical sector scan with a 5 MHz probe and a usable frequency bandwidth  $W$  of 3.5 MHz. On the transverse scan the mean available tissue depth is 3 cm. With a sampling rate of 40 ns, we obtain  $rf$  A-lines digitized in 1024 points on which 4 non-overlapping windows of 256 points could be located. The theoretically expected standard deviation in those conditions is 0.26 dB/cm. MHz on one A-line.

To improve the statistical significance of the attenuation estimation we acquire 512 A-lines for each patient resulting from the investigation of 8 muscular frames (where 32 A-lines are digitized) for each leg. The theoretically expected standard deviation under the hypothesis of the homogeneity of the tissue and no correlation between the lines becomes  $0.26/512^{1/2}$  dB/cm MHz, or 0.011 dB/cm.MHz.

Under in vivo conditions, for a given patient, the attenuation slope is estimated on each muscular frame. The averaged muscular attenuation of this patient as well as the standard deviation are calculated from the 16 attenuation values of each frame. The so-obtained standard deviation varies between the subjects from 0.03 to 0.05 dB/cm MHz. Even if this in vivo value corresponds to an acceptable accuracy of 8% on the attenuation estimation, it remains elevated with respect to theory. This difference clearly reflects the correlation between the lines for which we can give two reasons. Firstly, one has to take into account the finite cross section of the ultrasonic beam. Secondly, one has to consider the role played by the specular reflectors within the tissue [16].



### III.COMPARISON OF THE MEAN ATTENUATION OF A CONTROL GROUP AND A POPULATION OF GENETIC CARRIERS.

This study has been performed on two groups. One group comprised 27 control women without any muscular dystrophy in their family and a normal level of muscular enzymes in blood. The other group consisted of 19 obligate carriers. The latter group was selected on familial criteria : they had either one DMD son (or more) and one DMD brother, or two or more DMD sons, or one DMD son with a DMD relative in their family.

In fact, much more carriers have been investigated. We do not include here the carriers detected because of their abnormal level of muscular enzyme in blood. This would effectively bias the comparison presented in the next paragraph.

The mean attenuation coefficients as well as the standard deviations of the distributions within the two groups have been estimated for both algorithms (table 1). We can conclude that there is a significant difference of the mean attenuation values between controls and carriers. The results are not affected by the kind of algorithms we use.

	CENTROID ALGORITHM (dB/cm MHz)	NARROW BAND ALGORITHM (dB/cm MHz)
Control group (27)	0.556 ± 0.07	0.539 ± 0.06
Carriers of DMD (19)	0.673 ± 0.07	0.654 ± 0.06

Table 1 : Comparison of the mean attenuation coefficients and the standard deviations of a population of normal volunteers and a population of genetic carriers of DMD. Results are presented for two different algorithms.

Finally, there is an overlap between the two distributions. We may now discuss, even with this overlap, the interest imposed the estimation of the attenuation coefficient for carriers detection from the clinical standpoint.

#### **IV. CLINICAL INTEREST OF ATTENUATION ESTIMATION FOR CARRIER DETECTION.**

##### **1. State of the art for carrier detection.**

The problem of Duchenne muscular dystrophy (DMD) carrier and non carriers detection is only partly solved practically . In view of detecting carriers of DMD, and discriminating them from non-carriers, several biochemical and biophysical methods have been developed. The increase of serum aldolase and thereafter creatine-kinase were the first significant hematological biochemical symptoms of DMD. Applying these results to carriers allowed their recognition [9,10] .

Muscle studies by invasive techniques like biopsy, allowing culture of fibroblasts, protein biosynthesis studies ,microscopy and electron micrography gave poor results in this respect. Non-invasive techniques, mainly by imaging with echography [11,12] and computer tomography [13] are not yet entirely conclusive. Recent application of molecular genetic techniques have resulted in the localisation of the defect. Within the Human X chromosone, many new DNA segments are now used for carrier detection and prenatal diagnosis of DMD .

Given the fact that the improvement of CK estimation alone can detect almost 70 % of the obligate carriers [15]. we reasoned that association of CK and attenuation estimation could refine and improve the recognition of obligate carriers.

##### **2. Improvement of the detection with attenuation**

The results are summarized in table 2. In the control group we found a serum Creatine-Kinase of  $46.4 \pm 13.5$  U ; values of C K greater than 80 U, were considered as abnormal.

Values of the attenuation coefficient greater than 0.7 dB/cm MHz corresponding to the upper limit of the 95 per cent confidence interval, were considered as abnormal. We did not find false positive in the control group.

We observed no correlation between age and the attenuation of ultrasound. The correlation coefficients between age and attenuation were calculated for each group : controls ( $r = 0,33$ ) and carriers ( $r = 0,013$ ). Testing the null hypothesis  $r = 0$  in each case, we found that the observed values of  $r$  are not statistically significant at the 5 % significance level and the null hypothesis is not rejected.

Table 2 indicates the number of women out of 19 obligate carriers who were detected by both methods. The percentage of high level CK is 58 percent which is not significantly different from the expected percentage of 70 per cent [15]. The percentage of high attenuation values is 47 per cent which is less than the CK percentage. When taking into account CK and attenuation the percentage of detection becomes 90 per cent [14], which seems to support the view that the two abnormalities occur independently of each other.

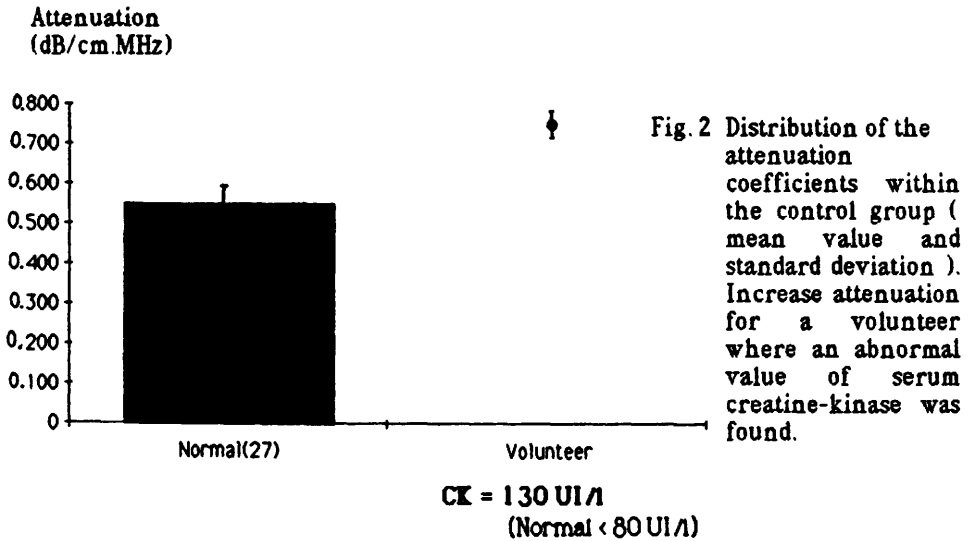
	Number of women detected	Number of women not detected	PERCENTAGE of DETECTION
CREATINE-KINASEMIA (NI < 80 U/l)	11	8	58 %
ATTENUATION (NI < 0.7 dB/cm MHz)	9	10	47 %
ATTENUATION and CK	17	2	90 %

Table 2 : Improvement of the detection of the carriers of DMD due to combination of attenuation estimation and determination of the level of muscular enzymes in blood.

## V. INTERPRETATION OF SOME PARTICULAR CASES.

### 1. About one case of volunteer.

After processing the in vivo rf data acquired on the muscle of a volunteer, we found an attenuation coefficient which was increased with respect to the normal range (Fig. 2). This woman could have been a false positive of attenuation. But, as we systematically performed a CK determination for all our normals, we had the surprise to obtain an abnormal level of creatine-kinase for this woman. The origin of this double abnormality has not been explained till now.



### 2. About two particular carriers.

Two particular symptomatic carriers have been explored. Both of them presented abnormal B - Scans, which was not the case for the other carriers investigated. Both of them also presented a very marked increase of the attenuation coefficients measured on the vastus medialis

(Fig. 3). Our hypothesis was then that the increase in attenuation could be related to muscular fatty infiltration. For this reason, we chose Nuclear Magnetic Resonance as an atraumatic way to reveal fat within muscle tissue because of the high contrast that can be obtained by this modality. The increase of attenuation of the vastus medialis could then be correlated to the presence of fat within the muscle. One of the corresponding NMR image is presented in the figure 4, where the white levels are representing the fat and the dark levels are corresponding to normal muscular fibers.

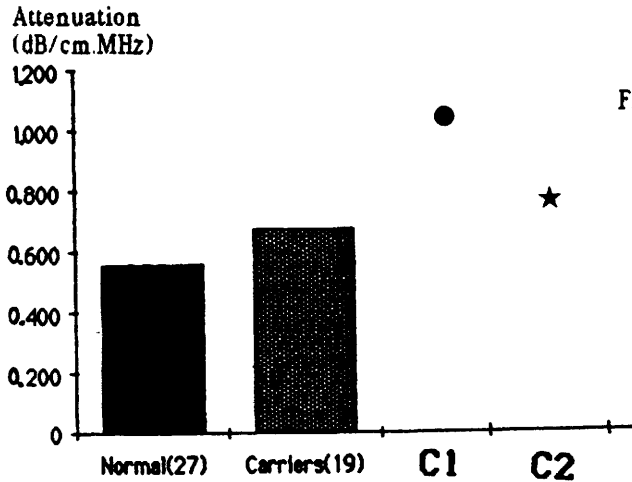


Fig. 3 Distribution of the attenuation coefficients within the control group and the carrier group. Increased attenuation for two symptomatic carriers (C1 and C2).

## VI. CONCLUSION

This paper shows that estimation of the attenuation coefficient in muscle can be very interesting from the clinical standpoint. We have especially investigated carriers of Duchenne Muscular Dystrophy because their detection is still a relevant clinical problem. The mean attenuation values of a population of normal volunteers and of a population of carriers of DMD are significantly different. Even if there is an overlap between the two attenuation distributions, ultrasound allows to increase the percentage of detection carriers when combined to creatine-kinase

assessment. We could correlate in some cases an high value of the attenuation coefficient with a fatty infiltration of the muscle, proved with NMR images of the thigh. In conclusion : attenuation, given as a global acoustic index of the muscle, can be related to pathological modifications.



Fig. 4 NMR image of the thighs of carrier C1 presenting an increased attenuation of the vastus medialis . Correlation with fatty infiltration. (light areas within muscles).

## REFERENCES

- [1] Kuc. R. , Clinical application of an ultrasound attenuation coefficient estimation technique for liver pathology characterization. IEEE Trans Biomed Engineering BME-27 : 312-319 (1980).

- [2] Taylor, K.J.W. , Riely, C.A. , Hammers, L. , Flax, S. , Weltin, G. , Garcia-Tsao, G. , Conn Ho. Kuc, R. , and Barwick, K.W. . Quantitative US attenuation in normal liver and in patients with diffuse liver disease : importance of fat, Radiology 160 : 65-71 (1986).
- [3] Kuc, R. , and Schwartz, M. , Estimating the acoustic attenuation coefficient slope for liver from reflected ultrasound signals IEEE Trans. Sonics Ultrason. SU -26 , 353-362 (1979).
- [4] Kuc, R. , Bounds on estimating the acoustic attenuation of small tissue regions from reflected ultrasound, Proc. IEEE 73,7,1159-1168 (1985).
- [5] Berger, G. , Laugier, P. , Fink, M. , and Perrin, J. , In vivo variance of the attenuation in muscle with respect to theory, simulation and pathological studies, Ultrasonic Imaging 8 , 51 (1986) (Abstract only).
- [6] Berger, G. , Laugier, P. , Fink, M. , and Perrin, J. , Optimal precision in ultrasound attenuation estimation and application to the detection of Duchenne Muscular Dystrophy Carriers, Ultrasonic Imaging (In press).
- [7] Fink, M. , Hottier, F. , and Cardoso, J. F. , Ultrasonic signal processing for in vivo attenuation measurements : short time Fourier analysis, Ultrasonic Imaging 5 , 117-135 (1983).
- [8] Hottier, F. and Bernatets, J. L. , Estimation of ultrasonic attenuation in biological tissues, Acta Electronica 26 , 33-58 (1984).
- [9] Schapira, G. , Dreyfus, J. C. , and Schapira, F. , L'élévation du taux de l'aldolase sérique, test biochimique des myopathies, Sem Hôp Paris 29 : 1917-1921 (1953).
- [10] Ebashi, S. Y. , Toyokura, H. M. , and Surgita, H. , High creatine phospho-kinase activity of sera of progressive muscular dystrophy patients, J. Biochem (Tokyo) 46 : 103-110 (1965).
- [11] Rott, H. D. , Santellani, M. , Rodl, W. , and Nebel, G. , Duchenne Muscular Dystrophy : carrier detection by ultrasound and computerised tomography. Lancet I : 1199-1200 (1983).
- [12] Rott, H. D. , and Newerla, K. , Duchenne Muscular Dystrophy : carrier detection by ultrasonic imaging techniques, Ultrasonic Imaging 6 , 236 (1984) (Abstract only).
- [13] Stern, L. M. , Cauchy, D.J. , Clar, M. S. , Penet, L. V. , and Bolok, D. W. , Carrier detection in Duchenne muscular dystrophy using computed tomography. Clin Genet 27 : 392-397 (1985).
- [14] Schapira, G. , Laugier, P. , Rochette, J. , Berger, G. , Katz, P. , and Perrin, J. , Detection of Duchenne muscular dystrophy carriers : quantitative echography and creatine kinasemia. Hum Genet. 75 , 19-23 (1987).

- [15] Dreyfus, J. C. , Schapira, F. , Demos, J. , Rosa, R. , and Schapira, G. . The value of serum enzyme determination in the identification of dystrophic carriers. Ann NY Acad Sci 138 : 304-314 (1966)
- [16] Laugier, P., Berger, G., Fink, M., and Perrin, J., Specular reflector noise : effect and correction for in vivo attenuation estimation. Ultrasonic Imaging 7, 277-292 (1985)
- [17] Cloostermans, M.J.T.M. , and Thijssen, J.M. , A beam corrected estimation of the frequency dependent attenuation of biological tissues from backscattered ultrasound, Ultrasonic Imaging 5, 136-174 (1983)



## IN-VIVO ATTENUATION FOR SMALL TISSUE VOLUMES

D. Nicholas

Norfolk and Norwich Hospital, U.K.

### Abstract

A technique has been developed which enables an assessment of the average scattered intensity from small volumes of soft human tissues (typically 30mm<sup>3</sup>). By performing such measurements at different depths within tissue it is feasible to estimate the attenuation due to the intervening tissue depth. Measurements have been derived for the attenuation at three discrete frequencies in the range 2 to 3MHz. Results will be presented from a pilot study of 54 patients exhibiting a variety of hepatic disorders.

Key words: ATTENUATION; In-vivo; Diffraction;  
Scattering; Liver; Tumours.

### Introduction

Techniques for in-vivo estimation of the attenuation of ultrasound waves in soft human tissues are currently based upon the measurement of A-scan information. The premise is that the rate of decrease of echo strength with distance into the tissue provides a measure of the bulk attenuating properties of the tissue. However, it must be stressed that the echoes returned to the scanning transducer are a consequence of scattering of the sound wave by the tissue. The complexity of such scattered waves requires that an average scattering value be assessed for the tissue being investigated at a specific depth. This cannot truly be achieved by existing A-scan methods which require at least 3 cm length of echo train for averaging.

Two specific requirements for improving the accuracy of attenuation measurements are:

an average of the scattering which accounts for its directionality (interference effects) and

an assessment of the scatter from small tissue volumes.

The latter requirement has clinical significance as it permits an assessment of attenuation over distances comparable to the volume being investigated at any one depth.

### Methods

The method adopted here for measuring the scattering from small tissue volumes utilises prototype clinical equipment described by Huggins and Phelps (1). The design of the scanning arm, depicted in figure 1, is based upon a pantograph which restricts the transducer to move in such a way that the region of interest is at an isocentre on the beam axis. Depth adjustment of the isocentre is achieved by movement of the top pivot. This has the advantage of mechanically fixing the depth of "scanning" and thereby providing an accurate measurement of depth within

the tissue at which measurements are being performed.

The relationship of diffraction phenomena to structural arrangement of tissue is normally considered to be associated with continuous waves (2).

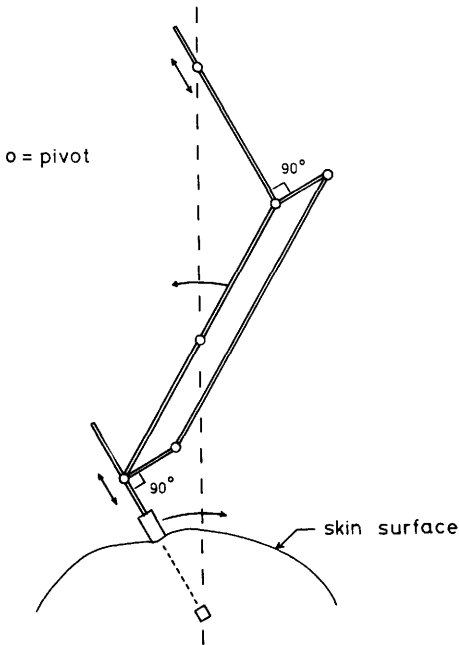


Figure 1. Schematic diagram of scanning arm, "pantograph".

This is effected by frequency filtering the time-gated portion of the back-scattered echo train. The time-gate used in the experiments reported was of 10 us duration centred on the isocentric volume. Derivation of the frequency spectrum of a gated pulse results, analytically, in a convolution of the spectrum of the pulse with that of the time gate. Hence any single component of the frequency spectrum will have an associated bandwidth of 100 kHz. The gated signals are then frequency filtered to allow investigation of the scattering at a specific frequency. The filter used has a bandwidth of approximately 20 kHz and is tunable over the range 1 to 5 MHz. A more detailed description of the equipment is provided elsewhere (3). The resulting signal is then collected as the transducer describes an arc (approximately 28 degrees) about the volume of interest. Repeat measurements at different frequencies 2, 2.5 and 3 MHz were performed. Figure 2 illustrates the resulting "diffraction patterns" associated with a hepatoma. By averaging the scattered signals over the arc of rotation a good estimate of the signal scattered from the interrogated volume is achieved. Comparison with measurements from a different depth and correcting for the characteristics of the beam allows an estimate to be made of the attenuation due to the intervening tissue at one discrete frequency.

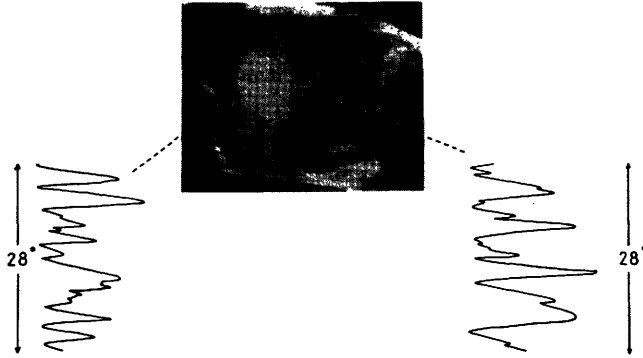


Figure 2. Diffraction patterns obtained at 2.5 MHz from within a primary liver carcinoma.

Table I. In-vivo attenuation measurements performed at three discrete frequencies 2, 2.5, 3 MHz.

Disease	Number	Attenuation dB/cm/MHz
Ca. Liver	3	0.27, 0.38, 0.41
Liver metastases:		
Ca. (solid)	7	0.41 - 0.73
Ca. (necrotic)	11	0.16 - 0.52
Lymphoma	4	0.49 - 0.39
Teratoma	3	0.21, 0.22, 0.32
Diffuse Liver Disorders:		
Cirrhosis "micro"	7	0.42 - 0.48
Cirrhosis "al"	4	0.46 - 0.57
Hepatitis "viral"	4	0.32 - 0.39
Hepatitis "al"	3	0.38, 0.40, 0.46

## Results

The results of a study conducted upon 54 patients with a variety of hepatic disorders are presented in Table I. From the measurements at three discrete frequencies a simple linear regression was performed to enable an estimate of attenuation expressed in dB/cm/MHz to be made.

## Conclusions

In summary the technique described above is primarily analogue and thereby requires minimal computation facilities. Only 256 data values are collected for each estimation of attenuation. Depending upon the inhomogeneity of the tissue to be measured and its size, any number of independent estimations can be made. The technique is capable of measuring attenuation over distances as short as 5 mm, the main error then being the accuracy of depth measurement. At present only discrete frequency information is available and the machine is cumbersome to use. However it must be stressed that some of the above results relate to tumours of less than 2 cm diameter and as such are, to the author's knowledge, the only measurements available to date.

## References:

- (1) Huggins, R.W. and Phelps, J.V., Bragg Diffraction Scanner for Ultrasonic Tissue Characterization In-Vivo, *Ultrasound Med. Biol.* 2, pp. 271-277, (1976).
- (2) Nicholas, D. and Hill, C.R., Acoustic Bragg Diffraction from Human Tissues, *Nature* 257, pp. 305-306, (1976).
- (3) Nicholas, D., Ultrasonic Diffraction Analysis in the Investigation of Liver Disease, *Br. J. Radiol.* 52, pp. 949-961, (1979).

# Attenuation and Scattering of Ultrasound in intra-ocular tumours

R.L. Romijn, B.J. Oosterveld and J.M. Thijssen

## Abstract

Diagnostic ultrasound techniques are used in order to try to characterize intra-ocular tumours. The main problem is the small size of these tumours, which makes it difficult to collect sufficient uncorrelated RF-data. A pilot study was performed on Greene's melanomas implanted in the anterior chamber of the eye of a rabbit. The ultrasound parameters used for tissue characterization are the frequency dependence of the attenuation and of the relative backscatter. In order to be able to obtain a statistically reliable value for the attenuation coefficient, a new method for estimating the frequency shift was employed. This method is based on the instantaneous frequency of the RF-signal. The frequency dependence of the relative backscatter was estimated by employing normalized backscatter spectra. Experiments were performed with a low attenuating phantom and on the intra-ocular tumours. The average scatterer diameter estimated for the phantom corresponded well with the size of the scattering spheres. All scatterers had a diameter less than 50 micro meter. The tumours could be characterized by a size of the scatterers of about 60 micro meters. These results are very promising for tissue characterization of intra-ocular tumours.

Key words : Attenuation; Scattering; Intra-ocular tumours;  
Instantaneous frequency; Scatterer size.

## Introduction

Ultrasound is of increasing importance for diagnosis in several fields of medicine. In the eye department ultrasound is already routinely employed. In order to improve diagnosis even more, especially of intra-ocular tumours, a RF-data acquisition system was build to be able to quantify tissue characteristics by acoustic parameters. The characterization of the intra-ocular tumours is extremely important for the treatment given to the patient or even a possible enucleation of the eye. Two acoustic tissue parameters were employed : the frequency dependence of the attenuation and of the relative backscatter. Since hardly any experience is being reported on very small volumes of tissue, the methods to estimate the acoustic parameters were evaluated. Results are presented on intra-ocular tumours implanted in a rabbit eye.

## Data Acquisition

The data acquisition of the RF-signals from the intra-ocular tumours in the rabbit eye was performed with a single element transducer (Panametrics V312) with centre frequency of about 8 MHz. The data were recorded with a transient recorder (Biomation 8000, sampling rate 100 MHz), just after the eye was enucleated. The eye was stored in degassed water during the measurements. The transducer could be fixed during recording and the RF-data was always recorded from the focal zone of the transducer. Of every eye, 10 different RF lines were recorded.

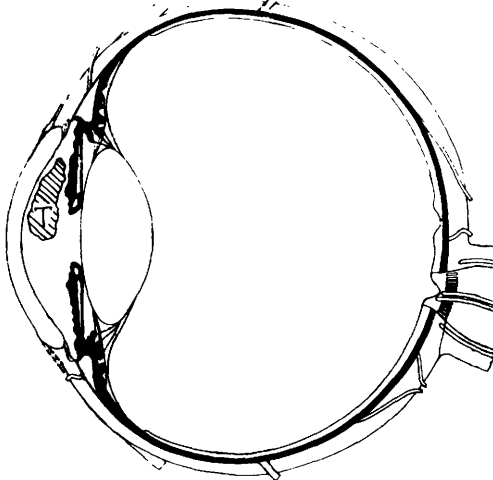


Fig.1 Cross section of the eye with Greene's melanoma.

and no comparison with other measurements can be made. The volume of the tumour is about 100 cubic millimeter, which is already very small for normal ultrasound diagnosis. An extra complication is the shape of the tumour in the anterior chamber of the rabbit eye. At this location the main direction of growth is perpendicular to the incident ultrasonic beam. In this way RF-data of only little depth can be recorded.

The Greene's melanoma in the rabbits eye is implanted in the anterior chamber (Fig.1). This is not corresponding to the location of tumours in human eyes as these are mostly situated at the posterior segment of the eye (choroid). But this difference is of minor importance if it is considered that the attenuation of the sound beam is low in vitreous. This means that for human tumour diagnosis, the lens should be avoided, as it does afflict the behaviour of the sound beam. If not, the frequency behaviour of especially the backscatter will be disturbed

## Attenuation

The frequency dependence of the attenuation was first estimated with a centroid spectral shift method (Kuc et al. [1]). This means that a window of RF-data was taken to calculate a power spectrum. This power is calibrated with a spectrum from a phantom on equal depth to correct for the beam diffraction. The centre of mass of the resulting spectrum, is the estimate for the frequency on the depth in the tissue the RF-data are taken from. The spectra were calculated for RF time windows which overlapped by 50 percent. Due to the size of the tumour, it is not possible to guarantee that the RF-data were uncorrelated.

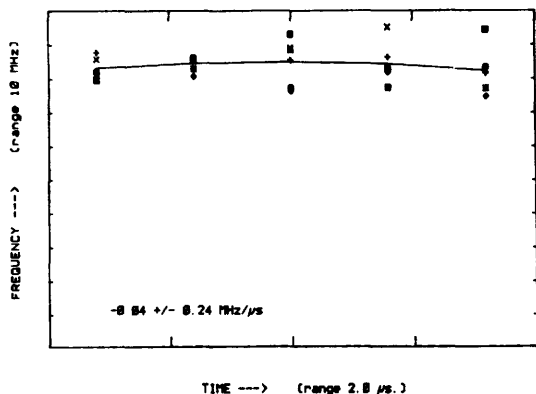


Fig.2 Estimates of the centroid spectral frequency, in tumour.

Before the calculation of the instantaneous frequency is performed, it is necessary to perform a diffraction correction. Figure 3 shows the diffraction power spectra recorded from a low attenuating silica phantom. It is obvious that the power in the focus is much larger than in the near- or far field. But also the centroid frequency of these power spectra is not a constant.

POWER SPECTRA  
silica gel phantom

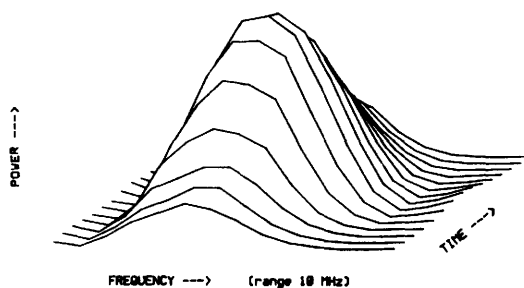


Fig.3 Diffraction effect of the transducer.

From the same figure it appears that the centre frequency changes with depth and is largest in focus. Because the central frequency in the focal point is not disturbed by the beam diffraction, it is possible to make a correction table for the frequency as function of depth. This kind of diffraction correction is needed for the instantaneous frequency method, as we have to correct the frequency estimation on every depth without use of the power spectra.

The next step in the calculations is the removal of data points which are not reliable. The logarithm of the envelope is calculated from the original RF-data (Cloostermans et al. [2]). A linear fit is made through these data and at times when the log-envelope differs more than one standard deviation from this fit the instantaneous frequency is supposed to be unreliable. High amplitude levels could indicate a specular reflector, that has no frequency dependence, where as at low amplitude levels the estimate of the instantaneous frequency is very unreliable

In Figure 2 frequency estimates are shown for six different rabbit eyes on the five different depths in the tumour. A straight line fit, results in a value for the frequency shift with a high standard deviation. Another method for estimating the frequency shift was found in the calculation of the instantaneous frequency.

because of the many destructive interferences of echoes. So the instantaneous frequency is calculated as function of depth with an envelope weighting. The empty signal samples are filled up if a number of RF-signals is averaged. This is because both specular reflections and interferences have a uniform random distribution.

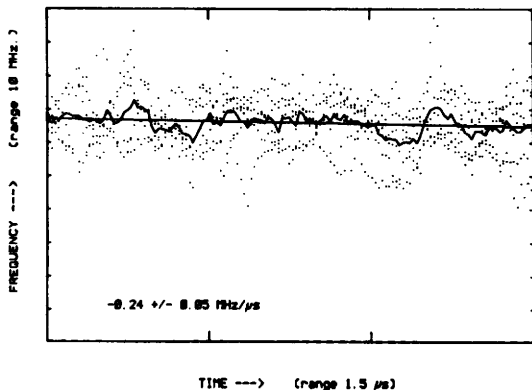


Fig.4 Estimates of the instantaneous frequency, in the tumour.

In Figure 4 the average was taken of all RF-data derived from the rabbit tumours. A linear fit through these data resulted in a value with a statistically sensible standard deviation. If the frequency shift ( $dF/dZ$ ) is known in the tumour, it is easy to calculate the attenuation coefficient ( $\mu$ ) with the formula.

$$dF = 2 \cdot \mu \cdot \sigma^2 \cdot dz \quad (1)$$

Implicitly it is assumed that the power spectrum of the transducer is Gaussian and that the attenuation coefficient is linear with frequency. And moreover that the standard deviation ( $\sigma$ ) of this spectrum is independent of depth ( $Z$ ) in the tissue. So a diffraction correction has to be applied (Verhoef et al. [3]).

The general behaviour of the logarithm of the envelope can be used as an extra parameter for discriminating tissue, since it is found to be very consistent.

The histogram showing the number of times the instantaneous frequency is estimated at each depth, exhibits a small increase with depth. This was to be expected since the logarithm is a non linear function, so the envelope weighting is slightly dependent on depth. Because the tumours were very thin, this effects needs no correction.

### Scattering

For a quantification of the relative backscatter a method is used as described by Feleppa et al. [4]. A relative amplitude spectrum is obtained through a calibration by an amplitude spectrum of the echo from a plane reflector in focus. Theoretical curves showing the relative amplitude of the spectrum versus frequency, as function of the scatterer diameter, were calculated by these authors. In these curves assumptions were made about the concentration of scatterers and the acoustic impedance of the scatterers. A linear fit through the curves yielded an intercept with zero frequency and a slope value. When this



procedure is reversed, it is possible to deduce from an intercept value and a slope value of a calibrated spectrum the diameter of the scatterers. This outcome is dependent on tissue and transducer characteristics.

Nice results have been presented by Feleppa et al. [4], although the theory does not cover all aspects of the scattering problem. For instance the beam diffraction correction which is incorporated is only correct in the small range of the focal zone. No attenuation correction is performed on the spectrum. Before reaching the region of interest this might not be a problem, as attenuation in vitreous is very low. But after penetration of the sound beam in the tumour, attenuation correction has to be performed, since it is apparent from the rabbit data that attenuation is not negligible and is certainly influencing the spectrum. Another point of doubt might be the linear fit through the relative backscattered spectra. And last but not least, the concentration of scatterers (number of scatterers per unit volume) is kept the same for all scatterer diameters. A more suitable parameter to keep constant might be the density of scatterers (mass of scatterers per unit volume) instead of the concentration. When doing so completely different values for the intercepts of the theoretical curves will be obtained, while the slope values remain unchanged. As the intercept is the most sensible parameter for the estimation of the scatterer diameter this is limiting the reliability of the estimate.

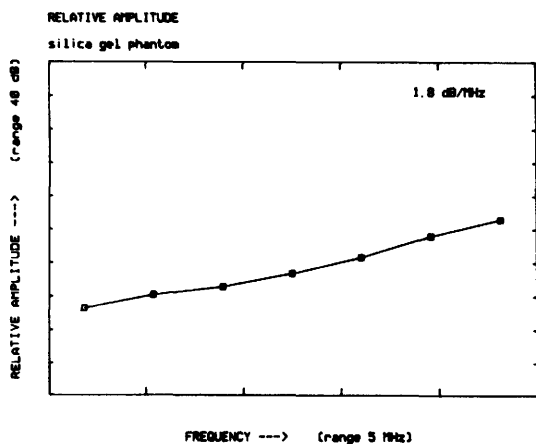


Fig.5 Calibrated power spectrum of a silica gel phantom.

The relative amplitude of the backscatter was measured for the low attenuating phantom and for the six intra-ocular rabbit tumours. Only the first window of RF-data in the region of interest was taken for backscatter analysis, thus preventing attenuation effects. The phantom consists of a low attenuating medium with a large number of silica gel scatterers. All scatterer diameters were smaller than 50 micro meters.

The linear fit through the calibrated spectrum, using all frequencies within the usable bandwidth of the transducer yielded a slope value which is equivalent to an average scatter diameter of 25 micro meter. The data derived from the tumours have a shallower slope value than the phantom.

The mean slope for all six tumours yielded a scatterer diameter of about 60 micro meters. The individual tumours had scatterer diameters varying from 57.5 to 65 micro meter. No histological data have been available till now. The slope and intercept values give good reason to hope that results can also be obtained from human tumours and that these results may lead to tumour characterization.

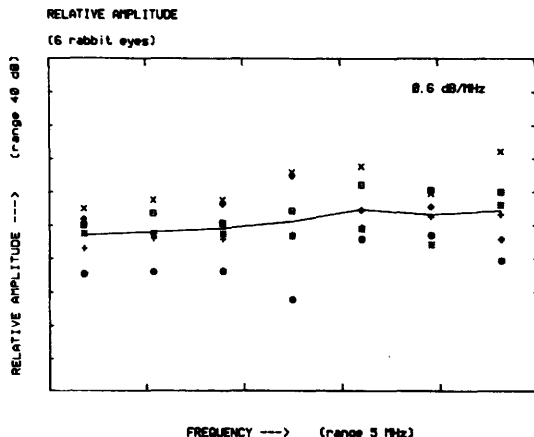


Fig.6 Calibrated power spectra of the tumours.

### Discussion

With a single element transducer it was not possible to collect enough uncorrelated RF-data for estimation of the attenuation in intra-ocular tumour within a single rabbit eye. But this is greatly due to the unfavourable shape of the tumour as compared to human intra-ocular tumours. By an improvement of the data acquisition system it has become possible now, to collect and process human data in vivo. (Kruimer et al. [5]). As it is already possible with a volume of six tumours. The ultrasonic front-end to be used in future is a Triscan echograph (type TR1), operating at 7.5 MHz centre frequency. The RF-data are digitized in a transient recorder (Bakker BE 256) at a sampling rate of 40 MHz. and send to a Professional 380 computer (Digital). In the computer the data are stored and displayed. From the computers screen it is possible to select a region of interest with a mouse. The RF-data in the region of interest are used to calculate the acoustic parameters.

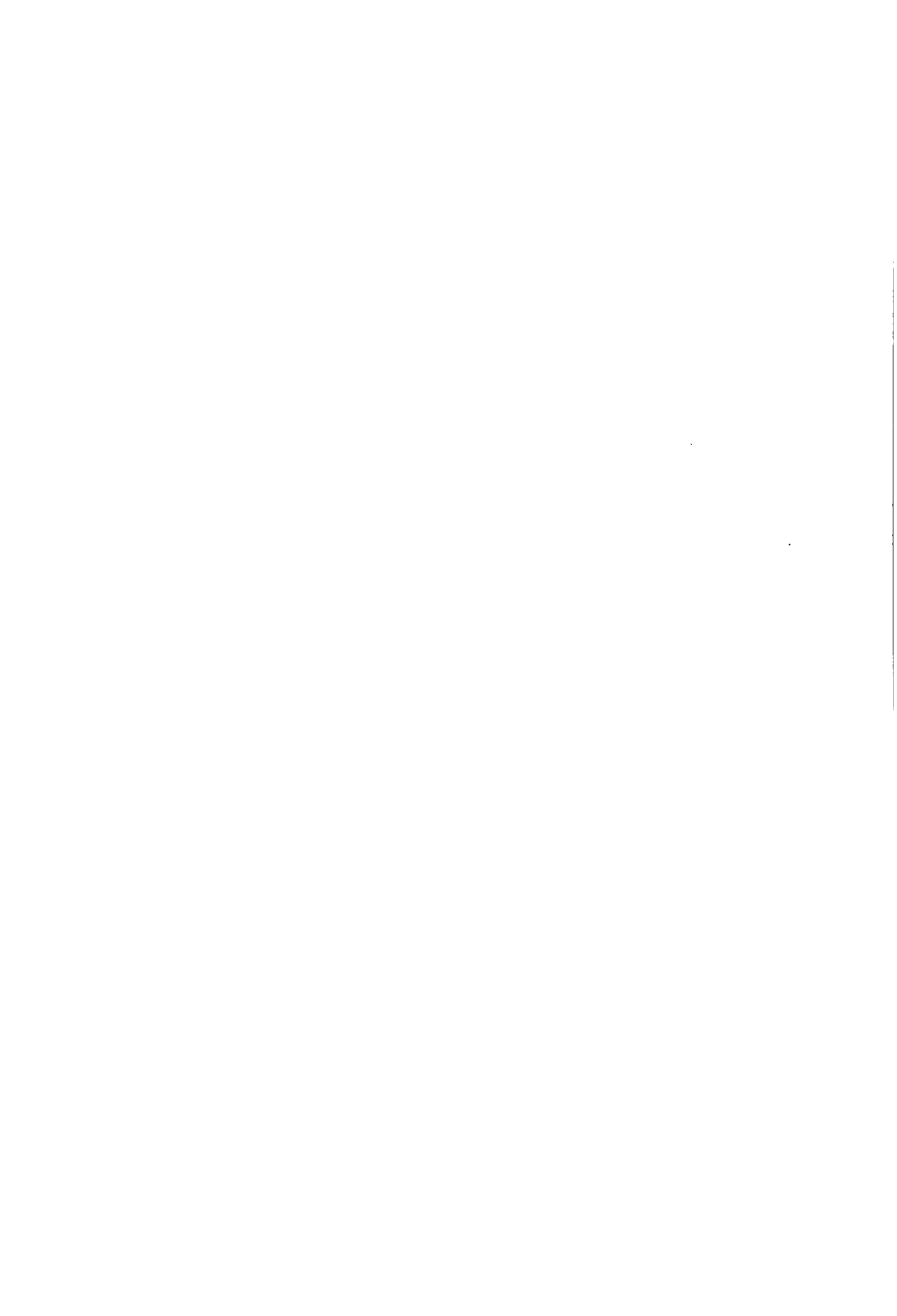
The scatterer diameter might in future prove to do what it now promises to do: characterization of the type of tumour, with only a very small amount of data. The attenuation coefficient can be reliably estimated as well. In conclusion: very promising techniques have been worked out for the estimation of two important acoustic parameters, of human intra-ocular tumours.

### Acknowledgements

This work is supported by the Netherlands' Cancer Foundation: Koningin Wilhelmina Fonds

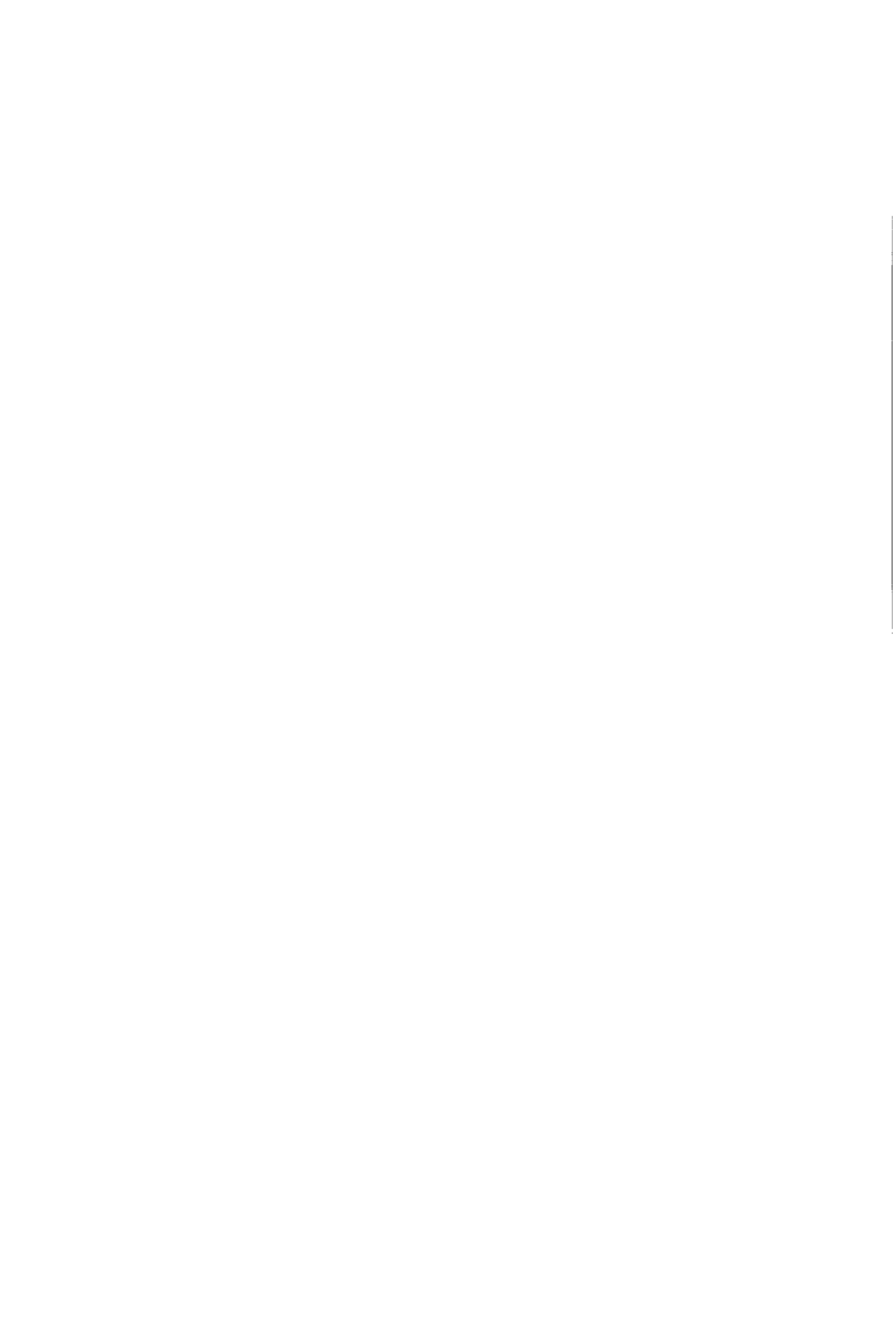
## Literature

1. Kuc, R., Schwartz, M., and von Micsy, L.  
Parametric estimation of the acoustic attenuation coefficient slope for soft tissue.  
IEEE Ultrasonics Symposium Roc. 76 CH 1120-5 SU,44-47, 1976
2. Cloostermans, M.J.T.M., Mol, H., Verhoef, W.A. and Thijssen, J.M.  
In vitro estimation of acoustic parameters of the liver and correlations with histology.  
Ultrasound in Med. and Biol. Vol. 12, No. 1, pp.39-51, 1986
3. Verhoef, W.A., Cloostermans, M.J.T.M. and Thijssen, J.M.  
Diffraction and dispersion effects on the estimation of ultrasound attenuation and velocity in biological tissues.  
IEEE Transactions on Biomedical Engineering Vol. 32, No. 7, 1985
4. Feleppa, E.J., Lizzi, F.L., Coleman, D.J. and Yaremko, M.M.  
Diagnostic spectrum analysis in ophthalmology : a physical perspective.  
Ultrasound in Med. and Biol. Vol. 12, No. 8, pp.623-631, 1986
5. Kruimer, W.H., Lammers, J.H.E. and Thijssen, J.M.  
Ultrasonic biopsy apparatus.  
Acoustical Imaging Vol. 14, A.J. Berkhout, J. Ridder and L.F. van der Wal, Eds., New York: Plenum, pp.665-667, 1985



Session 4 - ATTENUATION II

Chairmen : K.M. Irion, H.G. Trier



# THE RELATION OF COHERENT AND INCOHERENT SCATTERING TO MEASUREMENTS OF ATTENUATION AND SCATTERING IN TISSUE

R.C. Chivers

Physics Department, University of Surrey, Guildford GU2 5XH, U.K.

Two of the assumptions most commonly used in evaluating acoustic parameters of tissue are the 'plane wave' assumption, and the assumption that the scattering is only incoherent. The relation between and the significance of these assumptions is discussed in respect of measurements of attenuation and scattering. Experimental approaches to the investigation of the coherent and incoherent parts of the scattering are described and preliminary results on model systems and tissue are presented.

Key words: Coherent; incoherent; scattering; attenuation; phase

## 1. INTRODUCTION

In spite of the fact that the diagnostic ultrasonic pictures widely used in clinical practice are based on scattered signals, the biological identity of the scatterers appears to be, as yet, undetermined. One of the reasons for this is undoubtedly the fact that the scatterers are most probably very much smaller than the wavelengths used. However, there are a number of assumptions that are used - implicitly or explicitly - in converting the electrical measurements recorded into values of acoustic parameters such as attenuation coefficients or scattering cross-sections. The design of critical experiments to provide independent evidence for the validity of some of these assumptions is a challenging task, and one that is generally inglorious. It is made more complex by the fact that in many cases the extent to which a given assumption can be shown to be valid turns out to be one of numerical significance, and is thus determined primarily by the application under consideration at a particular time. Nevertheless, for the security of our scientific progress, and the development of its sophistication, these assumptions should be investigated if means can be devised to do it.

Although there may be more hidden away, two of the assumptions that occur most often are those of ultrasonic plane wave propagation and of incoherent scattering in soft tissues. The two are related in a relatively complex manner.

## 2. PLANE WAVES AND COHERENT SCATTERING

The 'plane wave assumption' is a shortened formulation describing the assumption that if a plane wave is incident normally onto a parallel sided specimen the emergent wave will also be a plane wave travelling in the same direction. This is essentially equivalent to the assumption of straight ray propagation. The assumption enters almost every area of ultrasonic tissue characterization. It is assumed in simple laboratory measurements of speed and attenuation. Disruption of the wavefronts may cause large systematic errors if phase sensitive receivers are used (see below). Measurements of speed and attenuation are prerequisites both for diffraction corrections on the measurements of velocity and attenuation, and for evaluation of scattering measurements. Of more significance is the fact that disruption of the wavefronts in general

precludes measurement of scatter in meaningful terms [1] because the effects of wavefront disruption in the tissue intervening between the transducer and the gated scattering volume cannot be distinguished from the scattered signal. In certain specific circumstances, the wavefront disruption may be sufficiently small to be negligible. For this to occur the gated scattering volume must either be relatively superficial, or the structure of the tissue must be such that the inhomogeneities appear as very weak scatterers.

Thus although the validity of the plane wave assumption over the depths from which scattering is to be measured in the tissue is a necessary condition, it would appear that it is not sufficient. Using the formulation of Foldy [2] we may write the total radiation density from an ensemble of scatterers as

$$\langle |\psi_0 + \psi_s|^2 \rangle = |\psi_0 + \langle \psi_s \rangle|^2 + \langle |\psi_s|^2 \rangle - |\langle \psi_s \rangle|^2 \quad (1)$$

where  $\psi_0$  is the irradiating wave and  $\psi_s$  is the scattered wave. This identity suggests that there is a part of the scattering,  $\langle \psi_s \rangle$ , which is added to the incident wave as a complex amplitude and may be called the 'coherent' part of the scattering. The remaining terms in  $\psi_s$ , namely  $\langle |\psi_s|^2 \rangle$  and  $- |\langle \psi_s \rangle|^2$ , add as intensities and are called the 'incoherent' part of the scattering. It should be noted that the terms coherent and incoherent scattering used by different authors sometimes vary in their physical interpretation. For the present discussion, Foldy's definition will be used, as given above.

In practical terms a plane wave incident upon a (parallel-sided) specimen may emerge with significant disruption. The mean values of the fluctuations in amplitude and phase give the amplitude and phase of the first term on the right hand side of Eq. (1), (i.e. of  $\psi_0 + \langle \psi_s \rangle$ ). Provided  $\psi_0$  is known, the coherent part of the scattering -  $\langle \psi_s \rangle$  - may be determined. The fluctuations about this mean value represent the incoherent part of the scattering, and give the last two terms on the right hand side of Eq. (1). From this simple picture it can be seen that the extent of the disruption of wavefronts that propagate through a specimen can only give information on the incoherent part of the scattering. The emergence of an essentially planar wavefront from the specimen may incorporate a significant degree of coherent scattering. Validity of the planar wave assumption can be consistent with a high degree of coherent scattering, which will generally occur if there is regularity in the spatial ordering of the scattering centres (in the extreme limit if they form a boundary), if they are sufficiently closely packed [3], or if they are strong enough scatterers for multiple scattering to be significant.

### 3. EXPERIMENTAL EVIDENCE FOR TISSUE

The situation regarding the validity of either of the assumptions mentioned in the first section, as far as ultrasonic wave propagation in soft biological tissue is concerned, appears to be unresolved at the present time. The information in the literature is extremely limited. Miller and his colleagues (e.g. [4]) published a number of papers in which attenuation measurements made with finite phase-sensitive piezoelectric receivers were compared with those made with smaller piezoelectric receivers, and with those made using phase insensitive acoustoelectric receivers. The measured attenuation decreased successively and the lowest value obtained was considered to be the 'right' one. These experiments



provide circumstantial evidence for significant wavefront disruption by soft tissues.

The only other - again circumstantial - evidence that has been available until recently comes from the enormous variation in the values of the backscattering cross-section per unit volume per unit solid angle. These, for fresh human liver, vary by over an order of magnitude [5]. This is consistent with the problem of making scattering measurements that would arise if the wavefronts were significantly disrupted, but such disruption is, of course, not the only mechanism that might lead to such an effect.

#### 4. EFFECT OF REALISTIC TRANSDUCERS ON MEASUREMENTS OF ATTENUATION AND SCATTERING

The most common approach to attenuation (and velocity) measurements in the laboratory is the replacement method in which a parallel-sided specimen of known thickness is interposed between two aligned transducers whose axes are perpendicular to the sides of the specimen. Measurements of the amplitude (and phase) of the received waves are compared to those obtained with a known fluid between the transducers. From these, the attenuation (and velocity) in the specimen are calculated. To a first approximation planar wave propagation is assumed. To a second approximation diffraction corrections are used to accommodate the finite size of the transducers. These rely on assuming ideal transducer performance. Frequency dependent effective dimensions (e.g. radius) for the transducers have been defined [6] and investigated in some detail [7] but their value in experimental situations has not yet been proven. No analysis appears to exist for corrections appropriate to the most common case of the medium between the transducers being piecewise discontinuous. The magnitude of diffraction corrections in homogeneous materials is, for attenuation measurements, of the order of a few percent, and for velocity measurements an order of magnitude lower. These corrections are of the same order of magnitude as the precision typically reported for the results of experiments on tissues.

The presence of inhomogeneities in the specimen which may cause wavefront fluctuations suggests that the one dimensional model for a plane wave at a distance  $x$  into the specimen,

$$\text{i.e. } p(x) = p(0)\exp(-\alpha x)\exp(i(\omega t - kx)) \quad (2)$$

needs very careful interpretation. In Eq. (2) the acoustic pressure wave has been used to define the so-called amplitude attenuation coefficient  $\alpha$ . With the validity of a plane-wave it is possible then to define an intensity attenuation coefficient  $\mu$ , where  $\mu=2\alpha$ . However if the wavefronts are disturbed by their propagation through the medium, the use of conventional amplitude detectors (e.g. piezoelectric transducers) and intensity detectors (e.g. cadmium sulphide transducers) will measure fundamentally different quantities. They may well be said to measure an amplitude attenuation coefficient,  $\alpha'$ , and an intensity attenuation coefficient,  $\mu'$ , but  $\mu'$  will not in general be equal to  $2\alpha'$ . The reason for this can be seen by reference to Eq. (1). The quantity measured by conventional piezoelectric phase-sensitive receivers is the integral of the complex

pressure over the surface of the transducer. If  $\psi_0$  is assumed to be a plane wave it is then simply  $\psi_0 + \langle \psi_s \rangle$ , i.e. the quantity inside the modulus on the first term on the right hand side of Eq. (1). In this case it can be seen that the attenuation (or velocity) measured will include the contribution to the attenuation (or velocity) of the coherent part of the scattering only. The quantity measured by cadmium sulphide transducers is the term on the left hand side of Eq. (1) which includes both coherent and incoherent parts of the scattering.

Thus the 'amplitude' attenuation coefficient includes the coherent scattering only, while the 'intensity' attenuation coefficient includes both coherent and incoherent scattering. In principle the difference between such measurements, appropriately manipulated will give the magnitude of the incoherent part of the scattering. In considering the implications of this approach it is important to recognise a fundamental difference between model systems which consist of known scatterers in a known matrix, the acoustic parameters of the scatterers being the same for all scatterers, and the situation for tissue. For tissue the scatterers are not a priori known. It is further not known whether they may be considered each to have the same acoustic parameter values. For this reason the definition of  $\psi_0$  in the above equations requires much more careful interpretation for tissue than it does for model systems.

When scattering measurements per se are attempted on tissue as a potential means of tissue characterization, it is necessary to use finite transducers - particularly if the angular dependence of the scattering is to be investigated [8]. The incorporation of the radiation characteristics of the probes into the analysis by which differential scattering cross-sections are calculated from the electronic measurements made, appears to be a relatively complex process. Most of the analyses that exist are related specifically to the problem of tissue characterization, attention being concentrated on backscattering measurements. Different authors have used the -3dB [9, 10] or the -6dB [11] measured beam profiles. Others have used an ideal piston source model [12, 13] or a Gaussian fit to measured beam patterns [14]. In general these different approaches will, with a given set of electronic measurements, lead to different numerical values for the differential scattering cross-sections. More recently an analysis has been described (Waag - private communication) in which arbitrary spatial distributions for both receiver and transmitter can be incorporated. The procedures for measuring these distributions, and their associated limitations, still require elaboration.

The penalty usually paid for the incorporation of a more complex approximation to reality as far as the behaviour of the transducers is concerned, is a simplification of the scattering situations that are covered. Specifically all the groups of authors cited in the preceding paragraph, with the exception of Madsen et al. [13] explicitly limit their analyses to uncorrelated scattering by weak scatterers. The Born approximation is used and the scattering is assumed to be only incoherent. Madsen et al. [13] discuss the part of the backscattering that may be coherent, and then use a measurement regime in which the only contributions to the coherent scattering arise from the edges of the gate used to define the scattering volume. They emphasise that their work is an extension of that of Glotov [15]. Machado et al. [16] have produced experimental results suggesting that multiple scattering becomes significant at 5MHz for concentrations of 0.6mm polystyrene spheres in a weak sugar solution above 100 per cubic centimetre. The interpretation of their results is based on Ishimaru's formulation [17].

The emphasis on scattering measurements - which is consistent with the

assumption that the scattering is only incoherent - is to take the mean square pressure amplitude as the appropriate parameter to measure. For some authors (e.g. [9] and [14]) there is an explicit requirement in the analytical formulation for the transducers to be far from the scattering volume. Others (e.g. [10]) introduce this as a means of reducing phase cancellation artefacts. Apart from this, the potential fluctuations in the scattered wavefronts and the resultant artefacts appear to be ignored, except for a model calculation by Shung and Drzewzianowski [18].

It is interesting to note in passing that the requirement that the scattering be only incoherent is potentially in conflict with the requirement that the wavefronts are not disrupted as they propagate through the tissue if sensible scattering measurements are to be made. The resolution of this conflict - at least at a numerical level - is an important area of work.

## 5. METHODS OF MEASURING COHERENT AND INCOHERENT SCATTERING

The experimental exploitation of the available experimental methods of looking at coherent and incoherent scattering are still at a very early stage of their development. Although there has been evidence from B-scan visualization of models that coherent scattering may play an important role in the imaging process [19], the majority of the work has been performed in the through-propagation situation appropriate to conventional attenuation measurements. Furthermore the approach mentioned above, of using the difference between measurements made with phase sensitive and phase insensitive receivers to determine the incoherent portion of the scattering does not appear to have been investigated experimentally. To some extent it is not useful if used alone. The majority of tissue characterization experiments have to date involved measurements using a single approach (which is, while based on assumptions that may have been appropriate for the model media on which the technique was based, may not be valid for tissue). The comparison of results from different or complementary techniques will be an important development in ultrasonic tissue characterization. In the particular context under discussion at present, it will be necessary for all the information available from the different approaches to be consistent before firm conclusions can be drawn.

The two approaches that have been most used are a novel technique employing focussed fields in penetrable media [20], and the measurement of phase and amplitude fluctuations of the waves propagating through a specimen in a plane perpendicular to the initial direction of the beam [21, 22].

The former technique is based on the analytical form of the axial pressure amplitude for a weakly focussed bowl transducer. Provided that the speed of sound in two media is quite closely the same, the logarithm of the ratio of the pressure amplitudes obtained in the two media is a straight line whose slope gives the difference of attenuation in the two media [20]. It is therefore relatively easy to measure the absorption of a homogeneous liquid such as castor oil using water, for example, as a reference. If scattering particles are included in the absorbing fluid, the axial pressure distribution is found to exhibit significant fluctuations. The magnitude of these fluctuations depends on the amount of stirring that is taking place. However it has been shown [23] that the mean level of the fluctuations measured without stirring gives the coherent contribution of the scattering by the particles to the overall attenuation in the suspension. The experiments were performed on 250 $\mu$ m diameter polystyrene beads in castor oil and the experimental results at volume concentrations of one

and two percent compared with the theory of Waterman and Truell [24]. The comparison showed good agreement between 1.0 and 2.5MHz.

The extension of the technique to tissue is technically difficult. However, studies have been carried out [25, 26] using miniature hydrophones inserted into intact tissues and these could be extended for exploitation in the focussed bowl technique. The major consideration in the analysis of the data concerns the distinction between the intrinsic absorption of the tissue (comparable to the absorption in the castor oil of the model system) and the coherent scattering contribution to the attenuation. This problem arises also with the measurement of phase and amplitude distributions.

The measurement of the phase and amplitude distributions of a beam impinging upon a specimen [7] and subsequently emerging from a specimen requires miniature hydrophones of known amplitude and phase directivities [27], and close attention to the precision of the timing circuits, the temperature control and the mechanical scanning arrangement. The precisions required increase significantly with increasing frequency. Measurements have been reported on a series of models of glass beads (50-500 $\mu$ m diameter, in four size bands) suspended in silicone rubber [22]. The preliminary results obtained on fresh beef liver in vitro [21, 29] have been extended [30]. In particular the potential effect of thickness variations in producing phase disruption (because of the difficulty of cutting soft tissues with plane parallel sides) has been removed by immersing the specimens in velocity matched saline solutions. The detection of the presence of airbubbles in the specimens is an unanswered question that is of considerable importance since even a few microbubbles could produce significant disruptive effects. The author is unaware of any reliable method for detecting such bubbles non-invasively. Selected results of these measurements are shown in the table.

It can be seen that the fluctuations observed in both tissue specimens were much less than those for the highest concentration of the largest scatterers (500-600 $\mu$ m diameter). The graphical form of the experimental results [22, 30] shows that the degree of phase disruption is, apart from the largest bead concentration and size, relatively small, suggesting that the plane wave assumption may well be valid to a good degree of approximation (particularly for specimen B). The analysis of the detailed results using equation 1 to extract the coherent and incoherent parts of the scattering is in progress. Preliminary results indicate that for the 7.5% concentration of 500 $\mu$ m diameter beads (selected because it is the model with fluctuations typical of those observed in the tissue specimens), the ratio of the coherent to incoherent scattering intensities is approximately 3:2. This high component of coherent scattering will have great significance if it is found to be present for tissues. As for the focussed bowl technique, however, it is probably necessary to obtain figures for the intrinsic absorption of the tissues - i.e. without the scatterers - from measurements made on homogenized specimens [31]. This is a procedure that needs care both in performance and in interpretation.

The major limitation that exists at present in the use of data obtained from fluctuation or finite transducer measurements concerns the lack of knowledge on the way in which the finite area over which such measurements have to be made influences the results of the calculations of the coherent and incoherent components of the scattering. In addition the effects of the finite hydrophone size (important at high frequencies), and the spatial sampling used need careful investigation.

6. SUMMARY

The development of the conceptual role of coherent and incoherent scattering in tissues is at a very early stage. It is clear that the plane wave assumption, needed for conventional attenuation studies, may still be valid but mask a high degree of coherent scattering. The use of phase sensitive and phase insensitive transducers in situations where the attenuation results from the two differ significantly indicates that fundamentally different quantities (both of which may be called an "attenuation coefficient") are being measured. The difference between the results obtained may give information on the incoherent part of the scattering.

Experimental evidence either for the validity of the plane wave model or for the ratio of coherent to incoherent scattering in tissue is very scarce at present. The focussed bowl technique for measuring the coherent scattering has not yet been extended to tissues, while the wave fluctuations approach has been used on only two specimens and considerable work needs to be done to analyse the data obtained, to define its limitations, and to obtain more data.

The main interest in the definition of the ratio of the coherent to incoherent scattering contributions in tissue is the basic conflict in the present analyses used to obtain differential scattering cross-sections that plane wave propagation is required (which allows coherent but not incoherent scattering, in general) but that the scattering is assumed explicitly to be incoherent in the analyses. This is clearly an important area to be clarified if scattering measurements are to be optimised as a means of tissue characterization.

ACKNOWLEDGEMENTS

The author gratefully acknowledges the contributions of Drs Adach, Aindow, Anson, Filmore and Sabino in this work.

Table of extreme variations in amplitude and phase observed on model systems and fresh beef liver

(The amplitude values are normalized to a nominal value of 1.)

Model Systems	Bead size ( $\mu\text{m}$ )	500	500	500	500	250	90
	Vol. concentration(%)	0	2	7.5	17.2	8	5
	Amplitude variations	0.16	0.34	0.90	1.22	0.60	0.16
	Phase variations ( $^{\circ}$ )	14	17	38	58	17	12
Tissue in velocity matched saline	Specimen (site)	A(i)	A(ii)	A(iii)	A(iv)	A(v)	
	Amplitude variations	0.20	0.36	0.36	0.51	0.43	
	Phase variations( $^{\circ}$ )	13.1	24.6	71.5	40.0	40.2	
	Specimen (site)	B(i)	B(ii)	B(iii)	B(iv)	B(v)	
	Amplitude variations	0.13	0.47	0.11	0.19	0.26	
	Phase variations( $^{\circ}$ )	19.5	35.9	25.2	43.7	41.3	

## REFERENCES

- [1] Chivers, R. C., Tissue characterization, *Ultrasound Med. Biol.*, **7**, 1-20 (1981).
- [2] Foldy, L. L., Multiple scattering theory of waves, *Phys. Rev.* **67**, 107-119 (1945).
- [3] Kur'yanov, B. F., Coherent and incoherent scattering by a set of point scatterers distributed randomly in space, *Soviet Phys. - Acoust.* **10**, 160-164 (1964).
- [4] Busse, L. J., Miller, J. G., Yuhas, D. E., Mimbs, J. W., Weiss, A. N. and Sobel, P. E., Phase Cancellation Effects : a Source of Attenuation Artefact Eliminated by a CdS Acoustoelectric Receiver, in *Ultrasound in Medicine Volume 3*, D. N. White, ed., pp. 1519-1535 (Plenum Press, New York, 1977).
- [5] Chivers, R. C., Ultrasonic Imaging and Analysis of Tissue Texture, in *Imaging with Non-Ionising Radiations*, D. F. Jackson, ed., pp. 50-84 (Blackie, Glasgow, 1983).
- [6] Chivers, R. C., Bosselaar, L., and Filmore, P.R., Effective area to be used in diffraction corrections, *J. Acoust. Soc. Am.* **68**, 80-84 (1980)
- [7] Aindow, J. D., Markiewicz, A., and Chivers, R. C., Quantitative investigation of disc ultrasonic sources, *J. Acoust. Soc. Am.* **78**, 1519-1529 (1985).
- [8] Zverev, V. A., The effect of the directionality of the receiving unit on the average intensity of the signal received due to scattering, *Soviet Phys. - Acoust.* **3**, 348-359 (1957).
- [9] Sigelmann, R. A., and Reid, J. M., Analysis of ultrasound backscattering from an ensemble of scatterers excited by sinewave bursts, *J. Acoust. Soc. Am.* **53**, 1351-1355 (1973).
- [10] O'Donnell, M. and Miller, J. G., Quantitative broadband ultrasonic backscatter: an approach to nondestructive evaluation in acoustically inhomogeneous materials, *J. Appl. Phys.* **52**, 1056-1065 (1981).
- [11] Nicholas, D., Hill, C. R., and Nassiri, D. K., Evaluation of backscattering coefficients for excised human tissues: principles and techniques, *Ultrasound Med. Biol.* **8**, 7-15 (1982).
- [12] Lizzi, F. L., Greenebaum, M., Felippa, E. J., and Gilbaum, M., Theoretical framework for spectrum analysis in ultrasonic tissue characterization, *J. Acoust. Soc. Am.* **73**, 1366-1373 (1983).
- [13] Madsen, E. L., Insana, M. F., and Zagzebski, J. A., Method of data reduction for accurate determination of acoustic backscatter coefficients, *J. Acoust. Soc. Am.* **76**, 913-923 (1984).
- [14] Campbell, J. A., and Waag, R. C., Normalization of ultrasonic scattering measurements to obtain average differential scattering cross-sections for tissues, *J. Acoust. Soc. Am.* **74**, 793-799 (1983).
- [15] Glotov, V. P., Coherent scattering of sound from clusters of discrete inhomogeneities in pulsed emission, *Soviet Phys. - Acoust.* **8**, 220-222 (1963).
- [16] Machado, J. C., Sigelmann, R. A., and Ishimaru, A., Acoustic wave propagation in randomly distributed spherical particles, *J. Acoust. Soc. Am.* **74**, 1529-1534 (1983).
- [17] Ishimaru, A., *Wave Propagation and Scattering in Random Media*, Volumes 1 and 2 (Academic Press, London/New York, 1978).
- [18] Shung, K. K., and Drzerzianowski, J. M., Effects of phase cancellation on scattering measurements, *Ultrasonic Imaging* **4**, 56-70 (1982).
- [19] Chivers, R. C., Uniqueness in ultrasonic grey-scale phantoms, *Ultrasound Med. Biol.* **7**, 91-95 (1981).

- [20] Adach, J., Anson, L. W., and Chivers, R. C., Coherent scattering measurement in penetrable inhomogeneous media, *J. Phys. E. - Sci. Instrum.* 19, 734-738 (1986).
- [21] Chivers, R. C., Phase distributions for characterization in vitro, in *Proc. III EURECH Workshop, Stuttgart*, pp. 117-120 (1983).
- [22] Chivers, R. C., and Aindow, J. D., Ultrasonic propagation studies in suspension systems, *J. Phys. D.* 16, 2093-2102 (1983).
- [23] Adach, J., *Focussed Ultrasonic Fields in Inhomogeneous Media*, Ph.D. Thesis (University of Surrey, Guildford 1986).
- [24] Waterman, P. C., and Truell, R. J., Multiple scattering of waves, *J. Math. Phys.* 2, 512-537 (1961).
- [25] Lewin, P. A., and Jensen, E. F., The use of miniature transducers for measurement in penetrable media, in *Proc. Ultrasonics International* 79, pp.279-284, (IPC Press, Guildford 1979).
- [26] Lewin, P. A., Focussed ultrasonic field distribution in tissue in vitro, in *Proc. Ultrasonics International* 81, pp.434-439, (IPC Press, Guildford 1981).
- [27] Aindow, J. D., and Chivers, R. C., Amplitude and phase directivity measurements on piezoelectric ceramic hydrophones in the low megahertz frequency range, *Acoust. Lett.* 5, 144-150 (1982).
- [28] Aindow, J. D., and Chivers, R. C., Measurement of the phase variation in an ultrasonic field, *J. Phys. E. - Sci. Instrum.* 15, 83-86 (1982).
- [29] Chivers, R. C., and Aindow, J. D., Wave propagation in biological tissue, in *Proc. Ultrasonics International* 83, pp.37-42, (Butterworths Scientific, Guildford 1983).
- [30] Aindow, J. D., and Chivers, R. C., Ultrasonic wave fluctuations through tissue - an experimental pilot study, *Phys. Med. Biol.* (submitted for publication).
- [31] Pauly, H., and Schwan, H. P., Mechanism of absorption of ultrasound in liver tissue, *J. Acoust. Soc. Am.* 50, 692-699.





## NON-LINEAR LOSSES IN THE MEASUREMENT OF ATTENUATION

F. A. Duck and H. C. Starritt

Department of Medical Physics,  
Royal United Hospital,  
Bath, BA1 3NG  
U.K.

The loss of energy from the fundamental frequency of a finite-amplitude ultrasonic wave has been measured. Transmission through water, excised liver tissue, and a combined path of liver and water have been investigated, in order to assess the importance of non-linear loss in the measurement of tissue attenuation in-vitro. It is concluded that non-linear effects, primarily in the water paths, cause losses which should be assessed and may be difficult to quantify. The losses are minimised by reducing waterpath length, source amplitude and focal gain.

Key Words: Acoustic shock; Attenuation measurement; Finite-amplitude loss; Focusing; Non-linear propagation.

### Introduction

The propagation of ultrasound through fluids and tissues is not a linear process. The non-linear acoustic effects in biomedical applications have been summarised by Muir and Carstensen [6]. A more complete general review of acoustic non-linearity is given, for instance, by Bjørnø [3]. One resultant effect of this non-linearity is that there is a greater loss of energy during the propagation of a high amplitude wave than would be predicted from simple considerations of low amplitude thermoviscous or relaxation losses. For plane waves, Blackstock [2] has given the term 'EXDB' to the excess dB ratio of the non-linear to ordinary small-signal losses,  $-20 \log (B_1 / \exp(-\alpha x))$  where  $B_1$  is the magnitude of the fundamental component in the wave and  $\alpha$  its amplitude attenuation coefficient for small amplitude waves. This additional loss can be associated with the harmonic components generated within the wave, and also with the losses once a pressure discontinuity, or 'shock' has been formed.

In this paper we present the results of experiments designed to investigate the magnitude and characteristics of these non-linear losses when measurement of tissue attenuation is being carried out. It is possible to consider these losses, broadly, in two ways. Firstly the loss from the fundamental frequency in the wave may be considered, ignoring whether this energy is still carried by higher harmonics in propagating wave, or is energy deposited in the medium. Secondly the total energy lost from the wave may be investigated. Here we consider only the former since loss from the fundamental frequency appears most

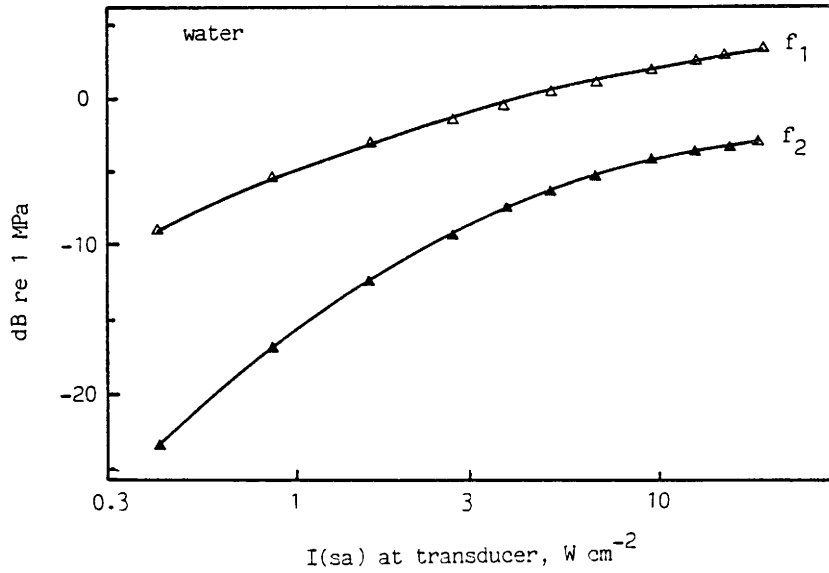


Figure 1 Variation of fundamental, 3.5 MHz ( $f_1$ ) and second harmonic, 7.0 MHz ( $f_2$ ) with spatial average intensity at the transducer  $I(sa)$ , measured at 5.0 cm in water.

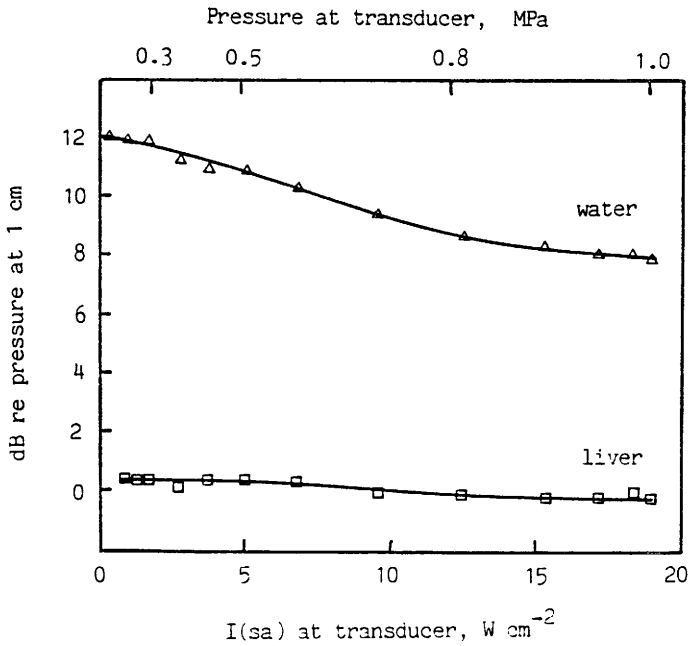


Figure 2 Variation of fundamental, 3.5 MHz, with  $I(sa)$  at 5.0 cm for water and ox-liver. 22°C. Referenced to  $f_1$  at 1 cm.

relevant to narrow-band attenuation measurements. For either fundamental frequency or total loss three different circumstances may be considered

- a) The transmission path is entirely coupling fluid (usually water). In this case the results are most relevant for calibration, and also in the interpretation of the 'mixed' behaviour (c).
- b) The transmission path is entirely tissue. In this case the results are primarily relevant in the interpretation of in-vivo attenuation estimation.
- c) The transmission path consists of both tissue and water. Here the behaviour of the wave is of most relevance in interpreting the results of in-vitro measurements of tissue attenuation.

### Experimental Apparatus and Methods

All measurements were carried out using a 3.5 MHz focused transducer, 13 mm diameter, focus 50 mm, focal gain 12.9 dB. The focal gain was calculated as the ratio of transducer radiating area to focal beam area, measured at  $1/e$  of the maximum pressure. The transducer was coupled via a thin polyethylene window to a small bath filled with tap water at room temperature (22°C). The drive was provided by an ENI 240L power amplifier. Tone bursts of controlled amplitude and of at least 10 cycles were used at a prf of 1 kHz. The ultrasonic wave was measured using a PVdF membrane hydrophone, which was located on-axis either at the beam focus or at 100 mm using a three dimensional micromanipulator assembly. The hydrophone was bilaminar 2 x 25  $\mu\text{m}$  thick with a 0.5 mm diameter poled sensitive area. The 5 cm hydrophone cable was connected to a unity gain amplifier, -3 dB band-width at 25 MHz, and to a HP54200A digitising oscilloscope. Hydrophone calibration at frequencies from 1 to 10 MHz was provided by the National Physical Laboratory, Teddington, England, and the overall sensitivity was 0.0465 mV/kPa at 3.5 MHz. The central two or three cycles of the pulse, averaged 64 times were captured and down-loaded to a HP216 microcomputer. The digitisation rate was 200 MHz. A DFT was carried out on the data points between the first and second positive-going zero crossings and power spectrum and phase values were calculated.

Ox-liver samples were obtained from the abattoir, refrigerated (not frozen) until used, and used within about 12 hours of death. Suitable thicknesses of liver were cut and held in polyethylene bags at 22°C in physiological saline, to be mounted at positions described below, between transducer and hydrophone. Slab thicknesses were not carefully controlled (50  $\pm$  2 mm and 20  $\pm$  5 mm) since the investigation primarily concerned the importance of non-linearity losses during attenuation measurements rather than absolute attenuation measurement itself.

Reference acoustic levels were obtained in two ways. Hydrophone measurements were made in water at about 1 cm from the transducer, slightly off axis. These measurements enabled reference to be made to the frequency content in the wave at a fixed (although arbitrary)

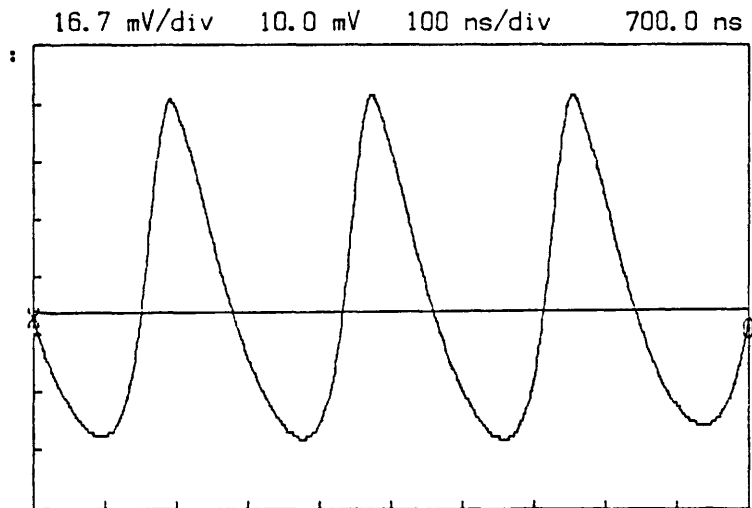


Figure 3 Measured waveform at  $I(sa) = 19 \text{ W cm}^{-2}$ , behind 5.0 cm ox liver. 0.0465 mV/kPa at 3.5 MHz.

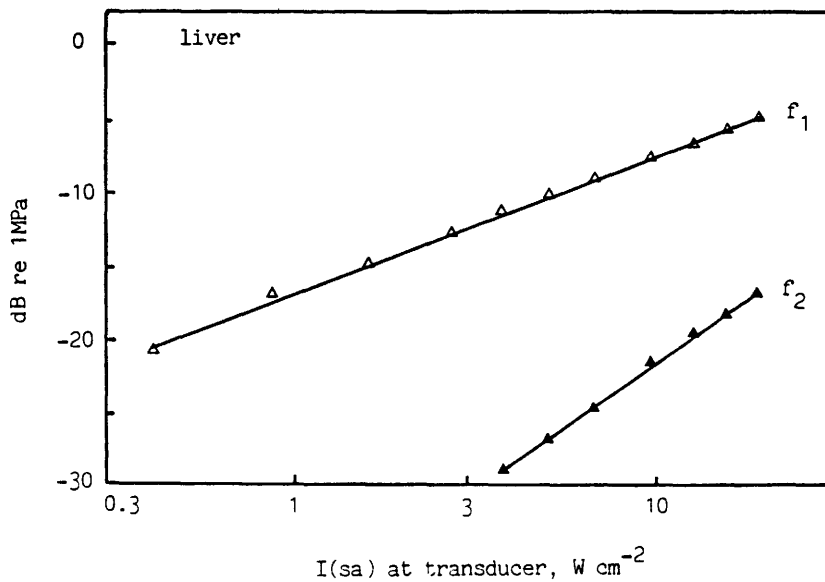


Figure 4 Variation of 3.5 MHz ( $f_1$ ) and 7.0 MHz ( $f_2$ ) at 5.0 cm following liver transmission.

location close to the transducer. The second harmonic level at this position was found to vary from 34 dB to 21 dB below the fundamental as the drive level to the transducer was varied from minimum to maximum. These levels were contributed in unknown proportions by transducer distortion, and propagation distortion. The second acoustic reference was provided by total acoustic power measurements using a radiation force balance [4]. Minor amplitude-dependent losses in the oil-filled chamber of the balance were estimated, and correction was applied. Spatial-average intensities during the pulse at the transducer,  $I(sa)$ , were calculated from the power measurement using knowledge of transducer radiating area, pulse duration and prf. Estimated overall accuracy for  $I(sa)$  was 10% above  $0.5 \text{ W cm}^{-2}$  and 15% below.

## Results

The variation of fundamental ( $f_1$ ) and second harmonic ( $f_2$ ) in water at 50 mm, as source intensity  $I(sa)$  was altered is shown in Fig. 1. Levels are referred to 1 MPa. The increase in  $f_1$  content is not linear with  $I(sa)$ .  $f_2$  content was measured to be 6.06 dB below  $f_1$  at the highest level ( $19 \text{ W cm}^{-2}$ ) and 7.92 dB below at  $I(sa) = 2.7 \text{ W cm}^{-2}$ . Parameter of non-linearity  $\sigma_m[1]$  calculated at these values were 2.7<sup>4</sup> and 1.25 respectively. Figure 2 shows the variation of  $f_1$  with  $I(sa)$  at 50 mm following transmission through water, and also through liver only (i.e. a 50 mm slab with transducer and hydrophone adjacent to the liver container bag).  $f_1$  is referred to the fundamental pressure amplitude at 1 cm. In water the pressure gain at low intensities of 12 dB compares well with the gain calculated from geometrical considerations. Above about  $I(sa) = 0.3 \text{ W cm}^{-2}$  ( $\sigma_m \sim 1.0$ ) the gain decreases, losing about 4 dB by  $I(sa) = 19 \text{ W cm}^{-2}$ . At low intensities, measurements through liver show a very slight gain (i.e. the focal gain is exactly balanced by attenuation loss at 5 cm). A slight additional loss was seen at highest intensities, increasing the low amplitude loss by about 0.5 dB. The measured waveform at  $I(sa) = 19 \text{ W cm}^{-2}$  is shown in Fig. 3 and the variation of  $f_1$  and  $f_2$  following transmission through 5 cm liver in Fig. 4. Second harmonic -11.8 dB re  $f_1$  is similar to results reported by us elsewhere for liver in-vitro using other experimental arrangements [7]. In comparison with the water results (Fig. 1) it is notable that the deviation from linearity over this intensity range for liver is slight.

The variation of fundamental with intensity was also investigated with the hydrophone located at 10 cm range, and with a liver slab about 2.0 cm thick interposed. Results are shown in Fig. 5. The additional non-linear loss in water reaches 6.4 dB at maximum intensity, and showed no plateau at the low amplitude end of the range of intensities used in this study. When the liver was placed immediately adjacent to the hydrophone (b) the variation of loss with intensity was similar in character to that in water alone, with a slightly reduced loss increment (5.7 dB). Locating the sample at 5.0 cm (a) gave a variation which was similar in form to that seen in water at 5.0 cm (Fig. 2).

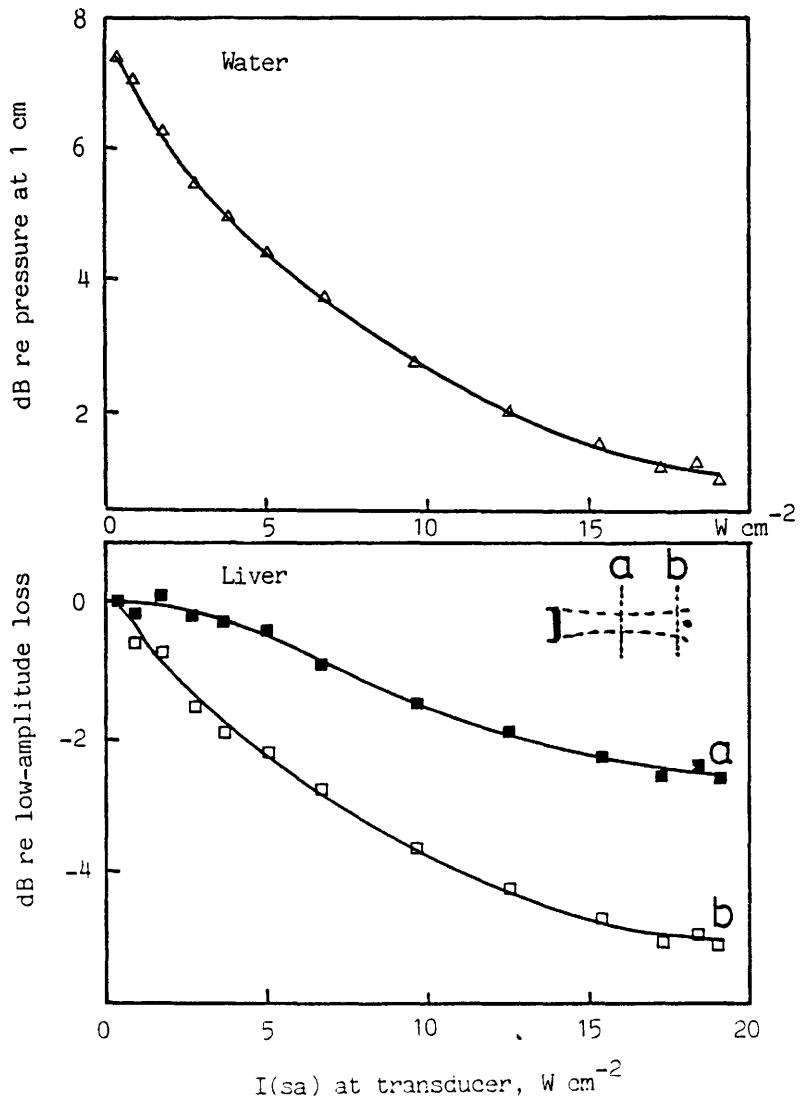


Figure 5 Variation of  $f_1$  at 10 cm (relative to  $f_1$  at 1 cm) following transmission through water only (upper) and water plus 2 cm (approx.) liver slab placed as indicated (lower).

## Discussion

The results from this particular set of experiments serve to illustrate the non-linearly generated losses which may occur during the propagation of ultrasound during attenuation measurements. The particular experimental arrangements used are sufficiently similar to commonly used arrangements to enable useful comparisons to be made. Intensities and pressures in the range used are exactly comparable with those generated by medical diagnostic equipment [4] and thus probably match well those used for attenuation measurements. The commonly-used broad-band pulse technique for attenuation measurement is especially likely to use high pressure amplitudes; the resulting losses and spectral alterations due to non-linear propagation in this case will be more difficult to quantify than in the monochromatic case considered here.

The finite-amplitude loss in water increases with distance, suggesting that experimental design should limit the water path to a minimum. Focusing of the beam serves to enhance the loss for a given source intensity (see [6, Fig. 8] for comparable 4 MHz plane wave values). Though not illustrated here the discontinuity length  $d$  (distance for shock formation with  $\sigma = 1$ ) decreases with increasing frequency, and thus non-linear losses occur sooner in the higher frequency beams. Liver, having a higher low-amplitude attenuation coefficient than water, has a larger  $d$  for otherwise similar conditions. Pressure amplitudes do not reach levels comparable with those reached in 'loss-less' liquids such as water, and thus comparable non-linear losses in liver are smaller.

The situation where water-paths occur both between the source and sample, and between the sample and detector is more complicated. Non-linear loss may occur in the first water space. Further loss in the tissue sample will result in the emerging wave being of lower amplitude than in the absence of the tissue, so decreasing the non-linear loss in the second water space. It cannot be assumed therefore that a reference measurement made through water alone is valid even in the presence of non-linear losses, and every effort must be made to minimise the circumstances where such losses may occur. The fact that harmonics in the wave incident on the tissue will be attenuated to a greater extent than the fundamental is not relevant since this energy has already been lost from the fundamental. The enhanced absorption noted by Goss and Fry [5] in tissue was attributed specifically to the attenuation of harmonics.

These observations highlight a particular problem in attenuation measurements using finite-amplitude beams. Non-linear effects in the water paths will cause losses which should be assessed, and may be difficult to quantify. The compromise chosen in any experimental design (including concerns for resolution, diffraction, S/N etc.) should include a recognition of this problem. Non-linear loss will be minimised by reducing water path length, source amplitude, and focal gain. Single frequency (tone-burst) methods are preferred to broad-band pulse techniques. In general it is important to measure the pressure amplitudes and waveforms used in order to assess the importance of

finite-amplitude effects in any particular experimental design.

### Acknowledgements

Grateful thanks are due to Mike Tysker and Steven Anderson for software development.

### References

- [1] Bacon, D. R., Finite amplitude distortion of the pulsed fields used in diagnostic ultrasound. *Ultrasound in Med. & Biol.*, 10, 189-195 (1984).
- [2] Blackstock, D. T., Thermoviscous attenuation of plane, periodic, finite-amplitude waves, *J. Acoust. Soc. Am.*, 36, 534-542 (1964).
- [3] Bjørnø, L., Non-linear Acoustics, in *Acoustics and Vibration Progress*, 2, Stevens and Leventhall (Eds.), pp. 101-203, Chapman and Hall, (1976).
- [4] Duck, F. A., Starritt, H. C., Aindow, J. D., Perkins, M. A. and Hawkins, A. J., The output of pulse-echo ultrasound equipment: a survey of powers, pressures and intensities, *Brit. J. Radiol.*, 58, 989-1001 (1985).
- [5] Goss, S. A. and Fry, F. J., Non-linear acoustic behaviour in focused ultrasonic fields: observations of intensity dependent absorption in biological tissue, *IEEE Trans. Sonics and Ultrason.*, SU-28, 21-26 (1981).
- [6] Muir, T. G. and Carstensen, E. L., Prediction of non-linear acoustic effects at biomedical frequencies and intensities, *Ultrasound in Med. & Biol.*, 6, 345-357 (1980).
- [7] Starritt, H. C., Duck, F. A., Hawkins, A. J. and Humphrey, V. F., The development of harmonic distortion in pulsed finite-amplitude ultrasound passing through liver, *Phys. Med. & Biol.*, 31, 1401-1409, (1986).



## ATTENUATION IN DOPPLER MEASUREMENT

T.J. Teo<sup>1-2</sup>, J.Y. Chapelon<sup>1</sup>, D. Cathignol<sup>1</sup> and J.M. Reid<sup>2</sup>

<sup>1</sup>Institut National de la Santé et de la Recherche Médicale  
Unité 281, Lyon, France.

<sup>2</sup>Drexel University, Biomedical Engineering and Science Institute,  
Philadelphia, U.S.A.

We present a theoretical study of the effect of attenuation in doppler measurement. Specifically, we study the effect on the signal-to-noise ratio when one uses a demodulating signal which takes into account the attenuation of the intervening tissue. We show that if we assume a gaussian spectrum, there is a closed form expression for the improvement in the SNR as compared with the conventional doppler processing where the demodulating signal has the same frequency as that of the transmitted signal and does not take into account the effect of attenuation. On the other hand, for a non-gaussian spectrum, no closed form expression has yet been obtained and a correcting factor is obtained by evaluating the integrals involved with the computer.

Key Words : Attenuation, Doppler measurement, Signal-to-noise ratio

### I. INTRODUCTION

The effect of attenuation due to tissue can cause error in the estimation of the centroid of a spectrum. This is particularly relevant in doppler measurement. In this paper we report some theoretical as well as computer simulation work that we have done. The main purpose of this paper is to show that if one uses a modified demodulating signal by taking into account the effect of attenuation, there is a substantial improvement in the signal-to-noise ratio over the conventional case where the demodulating signal has the same frequency as that of the transmitting signal.

The assumption that the transmitted signal has a gaussian spectrum is often used in the study of attenuation [1]. We show that a closed form expression can be obtained for the improvement in the signal-to-noise ratio. A computer simulation is performed to test this theoretical prediction and we find that the simulation results agree quite well with the theoretical prediction.

If the signal does not possess a gaussian spectrum, the discrepancy between the simulation and the previous theory is great. However, we were unable to evaluate the theoretical case for

a non-gaussian spectrum in closed form. If we evaluate the integrals involved with the computer, we can obtain a correcting factor which improves the agreement between the previous theory and simulation.

In section II, we describe briefly the relevant results on attenuation which are already well known in the literature on tissue characterization. We also describe the definition used for signal-to-noise ratio (SNR) in this paper. In section III, we describe the simulation and the several assumptions used in the simulation. The results are presented in section IV and the conclusion is presented in section V.

## II. THEORY

To simplify the theory, we first make the assumption that the spectrum of the transmitted signal is gaussian, and the attenuation of the tissue is linear in frequency. With these two assumptions, the effect of the attenuation is simply a down shift in the spectrum without change in the shape[1]. In other words, the spectrum after attenuation is again gaussian with the same variance. The amount by which the spectrum is down shifted can be evaluated easily and is given here as Eq.(1). In conventional doppler processing, this down shift in the centroid of the spectrum of the returned echo is not taken into account, and the same transmitted frequency is used in the demodulator. We wish to find out what improvement can be made in the SNR if one uses a demodulating signal which has a similarly down-shifted centroid.

$$S_2(f) = e^{-\frac{\Delta f(f_c - \frac{\Delta f}{2})^2}{\sigma^2}} e^{-\frac{(f-f_c+\Delta f)^2}{2\sigma^2}} \quad (1)$$

The signal-to-noise ratio (SNR) is defined as the ratio between the energy of the doppler output when there is only signal at the input and the energy of the doppler output when only white gaussian noise is applied to the input of the demodulator. We use SNR1 to denote the SNR when the demodulating signal is the same as the transmitted signal as in conventional doppler processing. We use SNR2 to denote the SNR when the demodulating signal is modified according to the attenuation of the intervening tissue between the transducer and the moving scatterer. SNR1/SNR2 is the parameter of interest in this present study.

In the appendix, we derive the theoretical improvement in terms of the ratio of the two SNR's as defined earlier. We find that the deterioration of SNR1 with respect to SNR2 is a function of the

depth. This is to be expected since the amount of the centroid down shift is proportional to the depth traversed by the signal. The closed form expression is simply that of a gaussian function with the centroid down shift as the independent variable and with a variance proportional to the variance of the gaussian spectrum.

### III. SIMULATION

To simulate doppler effect in a computer, we find that we need to approximate the real situation somewhat. For example, to be able to accomodate a spectral shift in the order of 2 KHz but a centre frequency of 5 MHz, one needs at least 5000 points with Nyquist sampling. We have approximated the situation with the assumption that the magnitude spectrum from pulse to pulse is basically the same and the doppler effect is only in the change of phase from pulse to pulse. This assumption is found to be good for low velocity doppler. In the time domain, this assumption is equivalent to the assumption that the return echo has the same shape from pulse to pulse but the repetition period is shortened by an amount related to the scatterer velocity.

In the computer simulations we have performed, the centre frequency is assumed to be 5 MHz and the sampling frequency is 25 MHz; the frequency dependence of the attenuation is assumed to be linear and the magnitude of the attenuation is assumed to be 1dB/cm/MHz. The pulse duration is 1 $\mu$ s and the pulse repetition period is 10 $\mu$ s. The depth varies from 0 to 15 cm and the two way travel distance is used as the independent variable for the ratio of the two SNR's. The range ambiguity is not a problem since in this simulation, there is only one scatterer whose position is known a priori.

For the case of SNR<sub>1</sub>, we use a demodulating signal which has the same frequency as the transmitted signal but without applying attenuation to the spectrum. For the case of SNR<sub>2</sub>, the same attenuation filter is applied to both the transmitted and demodulating signals. When the assumption of gaussian spectrum is made, we use  $6\sigma$  as the effective pulse duration where  $\sigma$  here is the variance of the gaussian envelope. When the assumption of gaussian spectrum is not made, we have gated sinusoids that are filtered by the transducer in both transmission and reception. The transducer transfer function is assumed to be gaussian. In all the simulation, the filtering is done on the power spectrum and the phase of the filter, be it that of transducer or attenuation, is assumed to be zero.

As mentioned earlier, the doppler effect is simulated by the phase change from pulse to pulse, hence, the two way attenuation effect on the spectrum is simulated independent of the doppler effect. The doppler effect is then simulated in the time domain

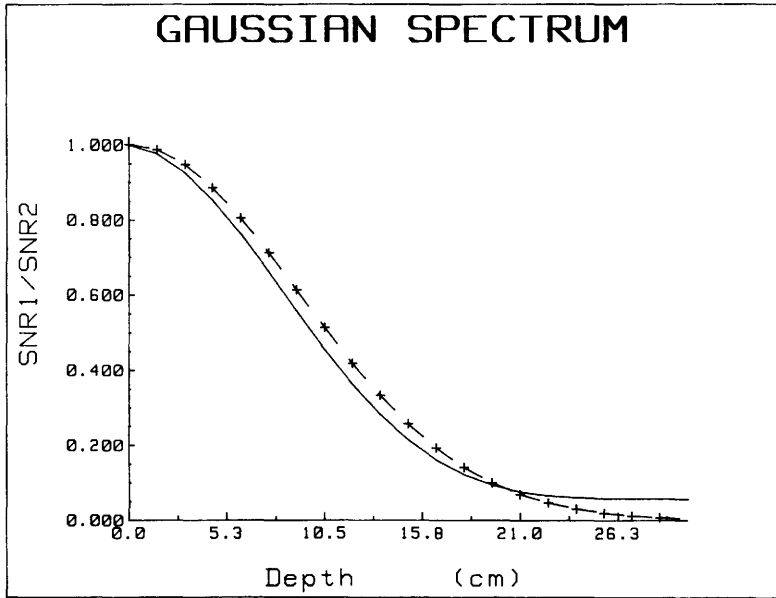


Fig. 1. Comparison between theoretical and simulation results. Gaussian spectrum is assumed. Solid line is used for the simulation results and dotted line with marker x is used for the theoretical results. Variance is 0.6 MHz.

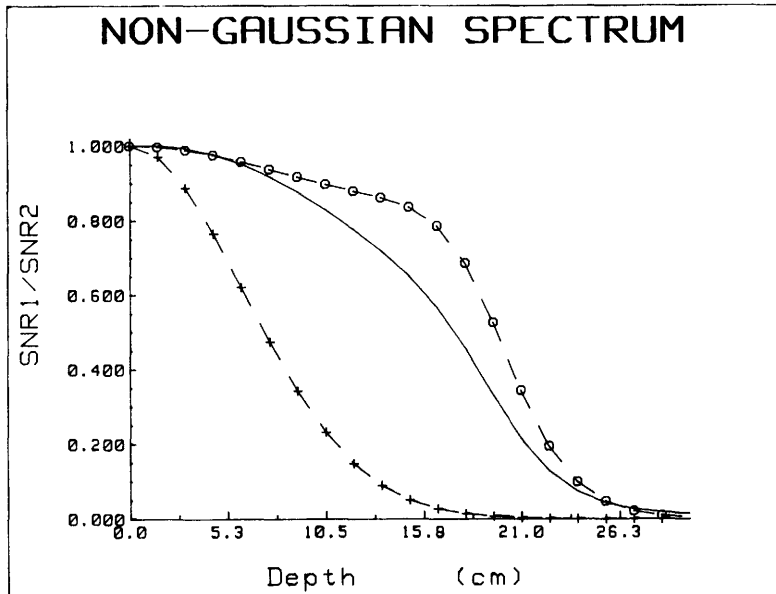


Fig. 2. Comparison between theoretical and simulation results. Non-gaussian spectrum is assumed. Solid line for the simulation results and dotted line with marker x for the theoretical results. Dotted line with marker o is used for the corrected theoretical results. Variance is 0.6 MHz.

after the spectrum has been appropriately modified by the transducer and/or the attenuation filter. After demodulation, an integrator is simulated which removes the sum frequency in the doppler signal and the output is then the desired doppler signal whose centroid can then be estimated.

#### IV. RESULTS

In figure 1, we have the  $SNR1/SNR2$  plotted as a function of depth. The continuous curve represents the results from simulation while the dotted curve with marker x represents the theoretical results. It is apparent that the agreement is good when we have gaussian spectrum. If the same theoretical result is used to predict the simulation using signal with non-gaussian spectrum, the discrepancy is significant. To account for the discrepancy, one needs an expression for the parameter  $SNR1/SNR2$  as a function of depth for the case of non-gaussian spectrum. Unfortunately, we have not been able to find a closed form expression for the case of non-gaussian spectrum. Nevertheless, if one evaluate the integrals involved with the computer, one can obtain a correcting factor which improves the agreement greatly.

In figure 2 and 3, we show the simulation results in solid curve, the theoretical results using gaussian spectrum in dotted curve with marker x and the corrected theoretical results in dotted curve with marker o. In figure 2, the variance of the transducer gaussian transfer function is 1 MHz and in figure 3, the corresponding value is about 0.6 MHz, the same as that of the gaussian power spectral density function used in figure 1.

#### V. CONCLUSION

We can see there is still some discrepancies between the theory and the simulation. Here we suggest some possible explanations for these differences between the theory and the simulation. In figure 1, the difference might be partially due to the fact that as the spectrum is down shifted, the bandwidth is really slightly reduced which in the time domain corresponds to a lengthening of the pulse. But in the simulation, this effect is not taken into consideration. Also, the theoretical derivation assumes that the gaussian function exists on the entire real line while this is obviously impossible with simulation. In the case of non-gaussian spectrum, the situation is even more complicated and the slight discrepancy between the simulation and the corrected theoretical prediction has not been resolved.

The modified demodulating signal which gives the reference  $SNR2$  used in this work may not be a practical one and we will continue to study the use of other demodulating signals in terms of their effect on the SNR.

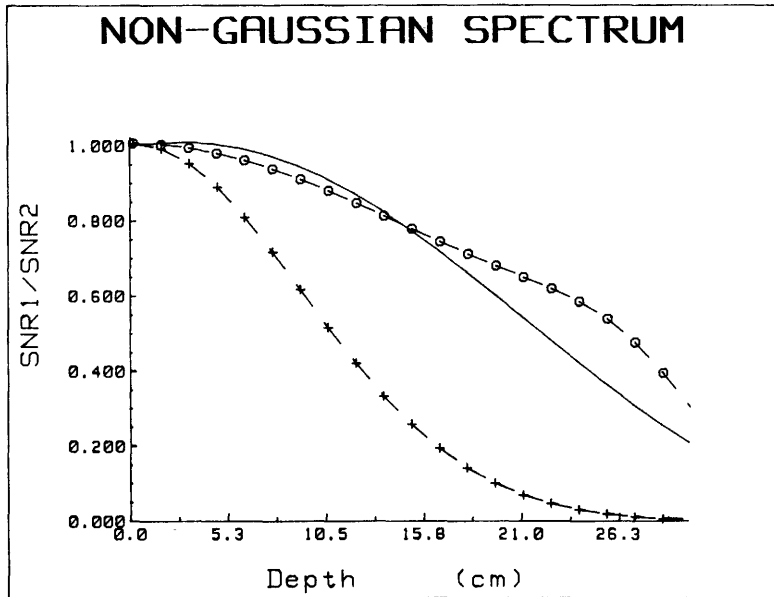


Fig. 3. Comparison between theoretical and simulation results. Non-gaussian spectrum is assumed. Solid line for the simulation results and dotted line with marker x for the theoretical results. Dotted line with marker o is used for the corrected theoretical results. Variance is 1.0 MHz.

## ACKNOWLEDGEMENTS

The first author would like to acknowledge the financial support from Institut National de la Santé et de la Recherche Médicale (INSERM), France and also grant from National Institutes of Health, USA, n°. HL 30045. Generous assistance from Jean-François Fady and Chantal Martin in preparing the manuscript is also much appreciated.

## REFERENCE

- [1] Kuc, R., Estimating acoustic attenuation from reflected ultrasound signals: comparison of spectral-shift and spectral difference approaches, *IEEE Trans. Acoustics, Speech and Signal Processing*, vol. ASSP-32, 1-6 (1984).

## APPENDIX

Let  $S_1(f)$  and  $S_2(f)$  be the gaussian power spectral density functions before and after attenuation respectively.  $A(f)$  be the transfer function of the attenuation filter. We have,

$$S_2(f) = S_1(f)A(f) = e^{-\frac{(f-f_c)^2}{2\sigma^2}} e^{-2\beta df} \quad (\text{A-1})$$

where  $f_c$  and  $\sigma$  are the centre frequency and the variance of the gaussian spectrum respectively.  $\beta$  is the coefficient of attenuation in neper/cm/MHz and  $d$  in cm is the distance traversed by the ultrasonic pulse in an attenuating medium. After some algebraic manipulations, we obtain,

$$S_2(f) = e^{-\frac{\Delta f(f_c - \frac{\Delta f}{2})^2}{\sigma^2}} e^{-\frac{(f-f_c+\Delta f)^2}{2\sigma^2}} \quad (\text{A-2})$$

where  $\Delta f = 2\sigma^2\beta d$ .

We see that apart for a scaling factor,  $S_2(f)$  is  $S_1(f)$  down shifted by  $\Delta f$ .

The demodulation of the return echo by a demodulating signal at the correlator can be viewed as the multiplication of the respective spectrum in the frequency domain. Using Parseval theorem, the energy of the doppler output is therefore the integral of the product of the two power spectral density functions. The same consideration applies to the case of noise input at the correlator. Hence, we have the following expressions for the signal energy and the noise energy as well as their ratio.

$$\text{Signal Energy} = \int_{-\infty}^{+\infty} S_2(f) S_1(f) df$$

$$\text{Noise Energy} = \int_{-\infty}^{+\infty} N(f) S_1(f) df$$

$$\text{SNR1} = \frac{\int_{-\infty}^{+\infty} S_2(f) S_1(f) df}{\int_{-\infty}^{+\infty} N(f) S_1(f) df} \quad (\text{A-3})$$

where  $N(f)$  is the noise power spectral density function.

If we assume a white noise spectrum, the expression for the SNR can be greatly simplified.

$$\text{SNR1} = \frac{e^{-\frac{\Delta f(f_c - \frac{\Delta f}{2})}{\sigma^2}} e^{-\frac{(\Delta f)^2}{4\sigma^2}} \int_{-\infty}^{+\infty} e^{-\frac{-(f-f_c + \frac{\Delta f}{2})^2}{\sigma^2}} df}{N \int_{-\infty}^{+\infty} e^{-\frac{-(f-f_c)^2}{2\sigma^2}} df}$$

Similarly, if we use a demodulating signal that has been



attenuated in the same way by the attenuating tissue, we obtain SNR2 as follows,

$$\text{SNR2} = \frac{e^{-\frac{\Delta f(f_c - \frac{\Delta f}{2})}{\sigma^2}} \int_{-\infty}^{+\infty} e^{-\frac{(f-f_c+\Delta f)^2}{\sigma^2}} df}{N \int_{-\infty}^{+\infty} e^{-\frac{(f-f_c+\Delta f)^2}{2\sigma^2}} df}$$

We see that the ratio between the two SNR's is simply another gaussian function if all the gaussian functions involved in the integral can be evaluated on the entire real line.

$$\frac{\text{SNR1}}{\text{SNR2}} = e^{-\frac{(\Delta f)^2}{4\sigma^2}} \tag{A-4}$$

In the case of non-gaussian spectrum, we have a gated sinusoid filtered by the transmitting transducer transfer function, the attenuation filter and then again by the the same transducer transfer function at reception. By using the same procedure, we arrive at the following expression for the ratio of the two SNR's for the case of non-gaussian spectrum.

$$\frac{\text{SNR1}}{\text{SNR2}} = e^{-\frac{(\Delta f)^2}{8\sigma^2}} \frac{\int_{-\infty}^{+\infty} \text{sinc}^4(fT) e^{-\frac{2(f+\frac{\Delta f}{4})^2}{\sigma^2}} df \int_{-\infty}^{+\infty} \text{sinc}^2(fT) e^{-\frac{(f+\frac{\Delta f}{2})^2}{\sigma^2}} df}{\int_{-\infty}^{+\infty} \text{sinc}^2(fT) e^{-\frac{f^2}{\sigma^2}} df \int_{-\infty}^{+\infty} \text{sinc}^4(fT) e^{-\frac{2(f+\frac{\Delta f}{2})^2}{\sigma^2}} df}$$

where T is the pulse duration and  $\text{sinc}(x) = \sin(\pi x)/\pi x$ .



## ATTENUATION WITHOUT DIFFRACTION CORRECTION ? EXPERIMENTAL RESULTS

E.T. COSTA, J.C. HODDINOTT and S. LEEMAN

Dept. of Medical Eng. & Physics, King's College School of Medicine and Dentistry, East Dulwich Grove, London SE22 8PT, U.K.

A new approach towards assessing attenuation by the substitution method is outlined, and contrasted against measurements by more conventional techniques, for both castor oil and glycerine samples. The results show that the method is indeed insensitive to diffraction effects, and can thus lay the basis for diffraction-free attenuation measurements.

Key words: artefact-free measurements; attenuation; diffraction.

### INTRODUCTION

Attempts to measure the acoustic properties of tissues are bedevilled by artefacts associated with the diffractive nature of the fields generated by transducers typical of those used for medical ultrasound applications. Many techniques have hitherto been proposed to overcome these diffraction effects, generally based on computational methods for diffraction correction [1]. Another alternative is to perform measurements only in the far field of the transducers: on occasions, this demands the use of unwieldy and cumbersome large water tanks.

In this paper we describe a measurement technique which ensures that diffraction artefacts are minimal in practice (and entirely absent in theory). The technique is based upon a purpose-built PVDF hydrophone [2], which has been used for measuring attenuation and its frequency dependence.

### THEORY

The main points of the theory are more clearly demonstrated in a simple example. Consider a one-dimensional (1-D) pulse  $p(x,t)$  propagating linearly in an ideal, lossless, uniform medium. This pulse can be written as a solution of the 1-D wave equation for example, such that:

$$\frac{\partial^2}{\partial x^2} p(x,t) - \frac{1}{c^2} \frac{\partial^2}{\partial t^2} p(x,t) = 0 \quad (1)$$

where:  $x$  = space coordinate  
 $t$  = time coordinate  
 $c$  = (constant) velocity of sound in that medium.

We consider only the case of a forward travelling pulse, i.e.  $p(x,t)$  is equal to  $p(x-ct)$ .

The representation of  $p(x-ct)$  in the Fourier domain can be written as:

$$p(x-ct) = \frac{1}{2\pi} \int P(\omega) e^{i(\omega t - kx)} d\omega \quad (2)$$

with:  $k = \omega/c$

$P(\omega) =$  Fourier Transform (FT) of  $p(x-ct)$

The 1-D pulse does not change its form or amplitude as it propagates, i.e. it does not show diffraction effects.

A three-dimensional (3-D) pulse  $p(x,y,z;t) [= p(\underline{r},t)]$  propagating linearly in the same ideal, lossless, uniform medium must satisfy the 3-D wave equation:

$$\nabla^2 p(\underline{r},t) - \frac{1}{c^2} \frac{\partial^2}{\partial t^2} p(\underline{r},t) = 0 \quad (3)$$

The equivalent representation of  $p(\underline{r},t)$  in the Fourier domain is written as:

$$p(\underline{r},t) = \frac{1}{(2\pi)^3} \int d^3\underline{k} P(\underline{k}) e^{i(\omega t - \underline{k} \cdot \underline{r})} \quad (4)$$

$$\text{where: } \omega = c|\underline{k}| = ck = c(k_x^2 + k_y^2 + k_z^2)^{\frac{1}{2}}$$

$\underline{k}$  = wave vector associated with the plane wave component of wavelength  $\lambda (=2\pi/k)$  and direction  $\underline{n}$ , where  $\underline{k} = nk$

$$P(\underline{k}) = P(k_x, k_y, k_z)$$

Consider a hypothetical, ideal, infinitely extended and coherently detecting planar hydrophone, located at  $x_0$  and intercepting this 3-D pulse orthogonally to its propagating ( $x$ -) direction. The output of such a device can be expressed as:

$$p_{df}(x_0, t) = \int dy \int dz p(x_0, y, z, t) \quad (5)$$

which can be written as:

$$p_{df}(x_0, t) = \frac{1}{(2\pi)^3} \int dy \int dz \left[ \int dk_x \int dk_y \int dk_z P(k_x, k_y, k_z) e^{i(\omega t - k_x x_0 - k_y y - k_z z)} \right] \quad (6)$$

Using the representation  $\delta(q) = 1/2\pi \int e^{ipq} dp$ , and integrating over the variables  $k_y$  and  $k_z$ , gives:

$$\begin{aligned} p_{df}(x_0, t) &= \frac{1}{2\pi} \int dk_x P(k_x, 0, 0) e^{i(\omega t - k_x x_0)} \\ &= \frac{1}{2\pi} \int dk F(k) e^{i(\omega t - kx_0)} \end{aligned} \quad (7)$$

where:  $\omega = ck$

$$F(k) = P(k, 0, 0)$$

Eq.(7) shows that  $p_{df}^o(x, t)$  is an equivalent, "true" 1-D pulse with Fourier Transform  $F(k)$ , that is invariant in shape and independent of location  $x$ , thus being free from diffraction artefacts. The spectrum of the output  $^o(1-D)$  pulse is identically equal to the values taken on by the three-dimensional pulse spectrum, along a line oriented in Fourier space in the same direction as the orthogonal to the hydrophone plane [see eqn.(7)]. The validity of this statement depends only on the ability to express the original field as a superposition of travelling plane waves, and does not require the field itself to have planar wavefronts. For example, even a spherically converging wavefront, as in a focused field, can be expressed as a superposition of plane waves, and, even in this case, the large planar hydrophone will give a distance invariant output as it moves through the focus, as experimentally confirmed below. For practical applications, we can mimic the effect of the ideal infinite receiver by using a planar hydrophone that is sufficiently large to intercept the bulk of the ultrasound field.

To emphasise the relative insensitivity of this measurement technique to diffraction artefacts, we show in Figure 1 the output of a receiver from stretched 110  $\mu$ m PVDF film, with a circular active surface of 75 mm diameter, that approximates to the large, planar, coherent receiver required by our technique. Compare these results with those obtained with a point hydrophone (Fig. 2), at the same three different (axial) locations in the pulsed ultrasound field generated by a 2.25 MHz, 19 mm diameter, focused transducer. The purpose-built hydrophone gives a remarkably invariant pulse (in shape and in amplitude), even through the focal region, as predicted by the theory, which is valid for any input field.

#### ATTENUATION MEASUREMENTS

In order to further verify the theoretical predictions, we carried out a series of measurements of the frequency dependence of attenuation, using the purpose-built PVDF hydrophone.

A substitution method was used to estimate the transmission loss of castor oil and glycerine samples relative to water, using a 19 mm diameter, 3.5 MHz (nominal), focused transducer as a transmitter, and the PVDF hydrophone as a receiver. For comparison, we carried out the same series of measurements using a 6 mm diameter, 5.0 MHz, focused transducer, and a point hydrophone as receivers.

The experimental set-up is shown in Figure 3. Measurements were performed in the 1 to 5 MHz frequency range, using sinusoidal tone-bursts of at least 20 cycles in duration. The transmitter was fixed and both the sample and the receiver could be translated axially. Experiments were performed in the following configurations: (1) sample at 3cm and receiver at 9cm from the transmitter; (2) sample at 6cm and receiver at 19cm from transmitter.

Figure 4 shows the variation of the transmission loss for castor oil and glycerine samples, as measured with the conventional, 6 mm diameter

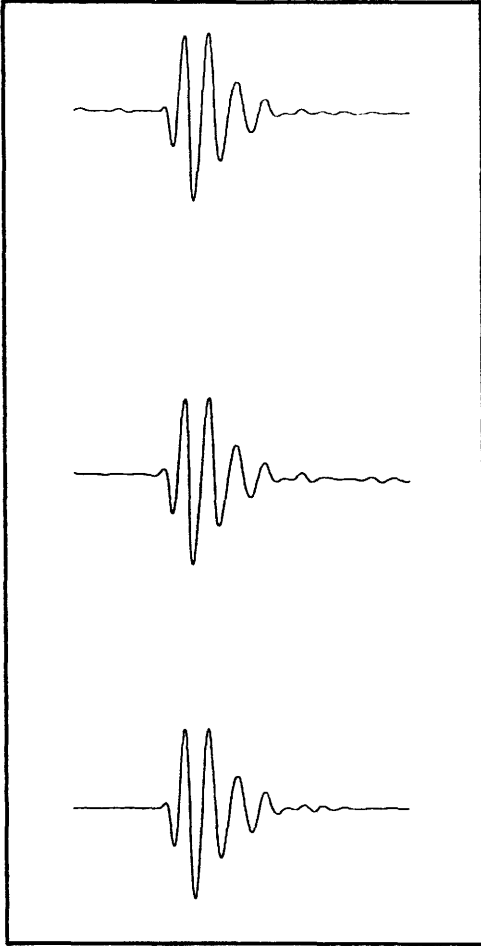


Fig.1. Output from the purpose-built PVDF hydrophone at three different locations (on-axis) of the pulsed ultrasound field generated by a 19 mm diameter, 2.25 MHz (nominal), focused transducer. Amplitude and time scales have not been altered for any of these waveforms. Top: at 4 cm from transmitter (before focus); centre: at 9 cm from the transmitter (nominal focus); bottom: at 14 cm from the transmitter (beyond focus).

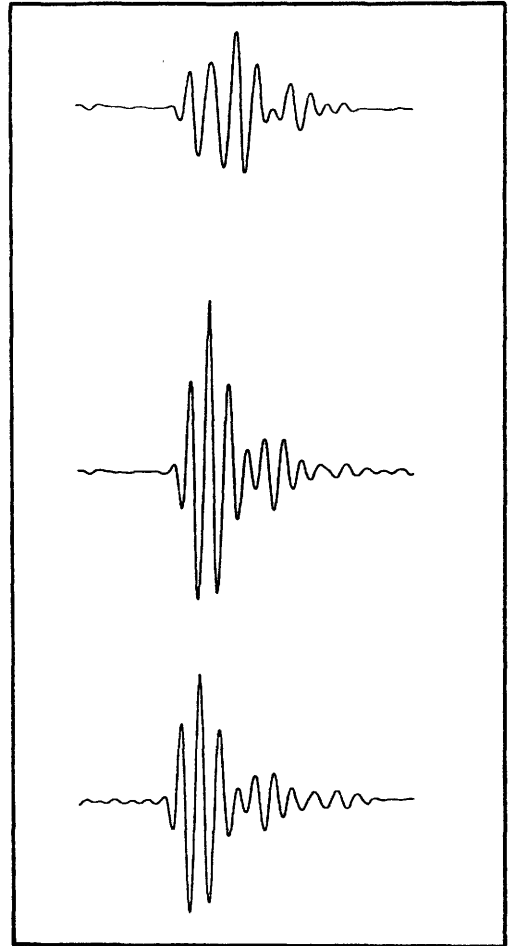


Fig.2. Output from a point hydrophone at the same locations and in the same field as explained in Figure 1. As before, time and amplitude scales have not been altered for any of these waveforms, although the overall gain is smaller than that used for the PVDF hydrophone, to compensate for the higher sensitivity of the point hydrophone.

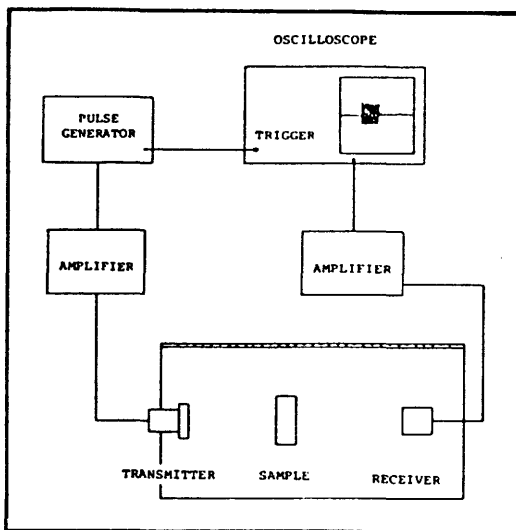


Fig.3. Schematic experimental arrangement for measuring frequency dependence of attenuation.

focused receiver. The erratic and unexpected frequency dependence shows clear evidence of diffraction artefacts. Unacceptably low and even negative, transmission loss values are obtained around 4 MHz. Clearly not much credibility can be attached to such measurements, as they are totally swamped by diffraction effects.

Another possibility is to use a "point" (0.3 mm diameter) receiver, which clearly removes the problems associated with possible phase-cancellation effects. Results for the same samples, as in Figure 4, are shown in Figure 5. Clearly, a much more acceptable frequency dependence of the transmission loss is obtained. However, there are quite significant differences between the results obtained in the two experimental configurations. Moreover, occasionally, zero, or negative, transmission losses can still be obtained. We conclude that diffraction artefacts are still present. For each sample, we have attempted to indicate the best fit (by eye) to all the data by a simple curve. Given the differences obtained in the two experimental configurations, it is questionable whether too much significance should be attached to such an interpolation. However, the scatter about the smooth curve may be interpreted as giving some indication of the severity of the diffraction effects.

Results obtained with the PVDF "diffraction-free" hydrophone are shown in Figure 6. For both samples, there is a quite good overlap between measurements obtained in the two different configurations. A simple curve can, quite readily, be fitted to the pooled data in each case. No unexpected frequency dependence emerges, and no unacceptable zero or negative transmission losses are seen.

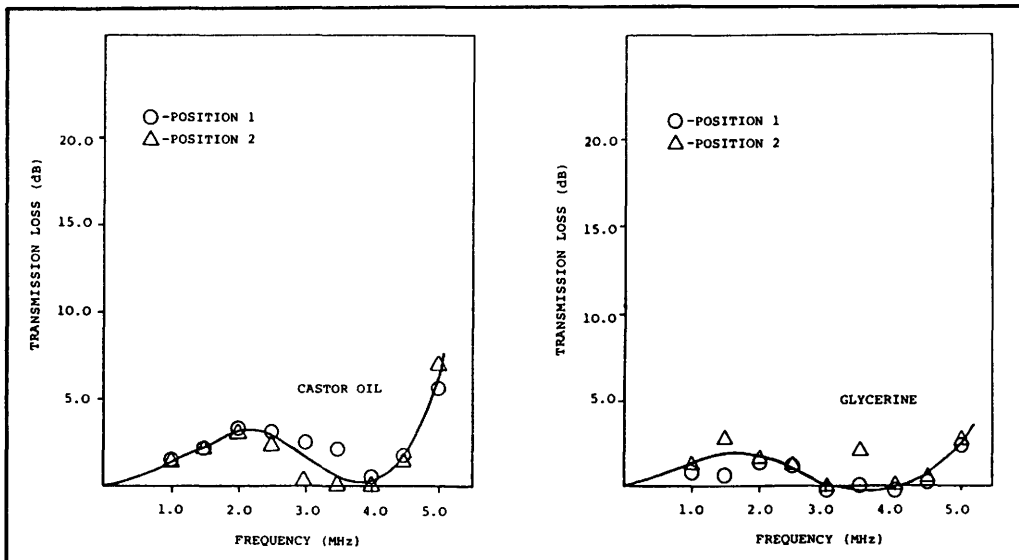


Fig.4. Frequency dependence of the transmission loss of castor oil and glycerine samples, relative to that of an identical water sample, as measured with a 6 mm diameter focused PZT receiver for two different experimental configurations: position 1 - sample at 3 cm and receiver at 9 cm from transmitter; position 2 - sample at 6 cm and receiver at 19 cm from transmitter.

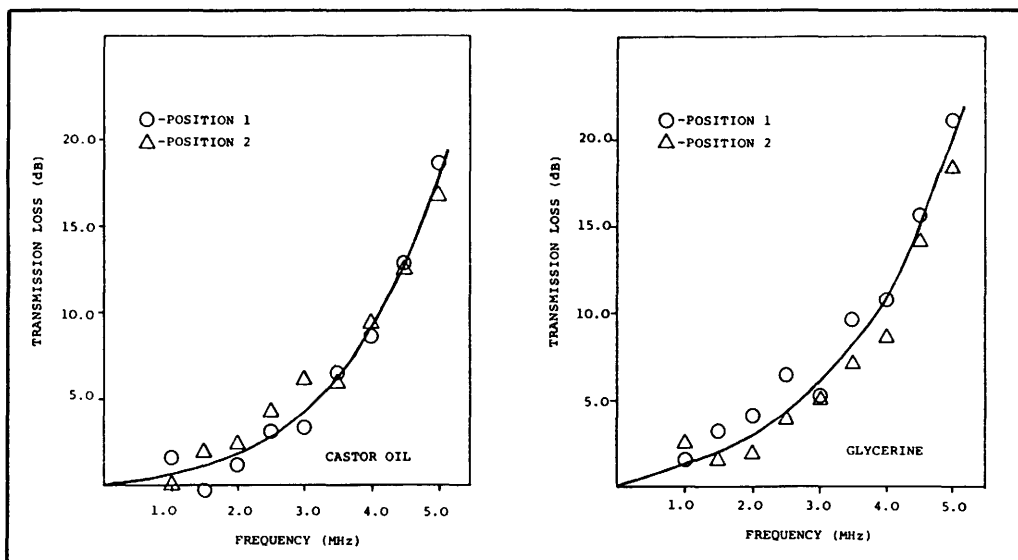


Fig.5. Frequency dependence of the transmission loss of castor oil and glycerine samples, relative to that of an identical water sample, as measured with a point (0.3 mm diameter) hydrophone for the same positions as for figure 4.



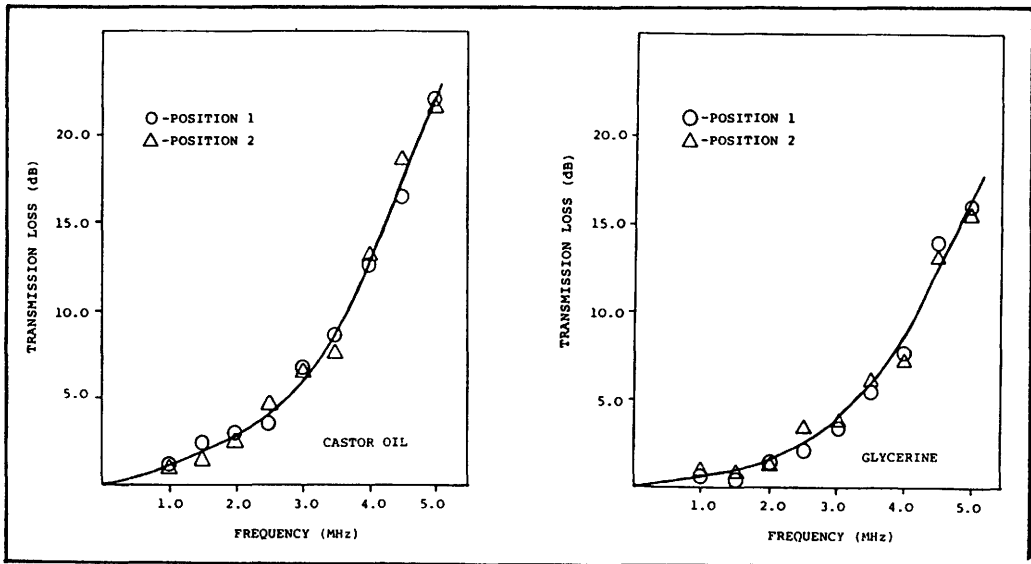


Fig.6. Frequency dependence of the transmission loss of castor oil and glycerine samples, relative to that of an identical water sample, as measured with the purpose-built PVDF hydrophone for the same positions as for Figure 4.

As opposed to the demands of measuring with conventional transducers, our technique did not present setting-up difficulties, as the relative locations of the transmitter, sample and receiver did not significantly affect the results. Measurements may be carried out in the near or the far field, with focused or unfocused transmitters, as the circumstances dictate.

#### CONCLUSION

We have presented provisional measurements of the transmission loss of castor oil and glycerine samples, relative to that of a water sample, using the substitution method with a purpose-built PVDF hydrophone as receiver. We have compared the results against those obtained with a point hydrophone and with a conventional medical ultrasound (focused) transducer as receivers. Our measurements show that our purpose-built hydrophone assesses attenuation with minimal diffraction artefacts, and its use avoids the great care needed in setting-up the experimental configurations when using conventional transducers. There is also no need to perform measurements in the far field.

We have attempted here only to illustrate the feasibility and ease of application of our technique, and have not therefore attempted to provide absolute attenuation values. A much more careful and dedicated programme towards that end is now under way.

#### REFERENCES

- [1] Fink, M. and Hottier, F., Short Time Fourier Analysis and Diffraction Effect in Biological Tissue Characterization, *Acoustical Imaging* 12, 493-503 (1982).
- [2] Costa, E.T., Leeman, S., Richardson, P.A.C., and Seggie, D., Measurement and Calibration of Transducer Fields, in *Proceedings of the Institute of Acoustics, Ultrasound in Medicine*, Vol. 8, Part 2 (1986).

## Attenuation and Frequency Imaging

P.Nauth, H.Schmidt, E.-G.Loch, W.v.Seelen

Deutsche Klinik für Diagnostik, Aukammallee 33, D-6200 Wiesbaden

### Abstract

A system to reconstruct frequency-images was developed representing the mean frequency of the backscattered power spectrum. These images can improve tissue characterization as exemplified by mamma tissue. To use the information of both, B- and frequency-images, we implemented an image combination system computing parameters from each image. These parameters are comprehended in one vector which is classified by a linear algorithm.

### Keywords

frequency image, attenuation coefficient, characteristic frequency, pattern recognition, image combination.

### Introduction

Nowadays a physician examining patients by ultrasonics makes use of the B-image technique. B-images contain the local distribution of the reflected and backscattered energy. Because local structures, representing information about shape and expansion of ill tissues, are very important for the diagnosis, ultrasonography was more and more applied during the last years. Nevertheless in many cases a tissue characterization is not possible by ultrasonics. The reason is that frequency- and scatterinformation describing the structure of tissues are neglected in B-images. Additional parameters like the attenuation coefficient have been computed by several groups from the RF-signal, but so far a reconstruction of the local information is not usual.

Because both, tissue characterizing parameters and their local representation in an image, are helpful solving questions of

tissue characterization, we developed a method to reconstruct frequency images from in-vitro measurements. These images then can be used to compute additional parameters like the attenuation coefficient.

Reconstruction of frequency images

The principles of our measurement equipment can be seen in fig.1. A tissue probe placed in the middle of a cylindric water tank can be displaced perpendicular to the incident sound impulse, which is emitted from a piezoceramic transducer fixed at one side of the water tank. A center frequency of 2.4 MHz and a bandwidth of 0.9 MHz resulted from a Measurement with a point reflector. The received signal is digitized by a Biomation 8100 A/D converter with a sample frequency of 20 MHz and stored in a PDP 11/34 computer. Displacing the tissue probe in steps of 1 mm the backscattered signal can be measured in various lines of the tissue.

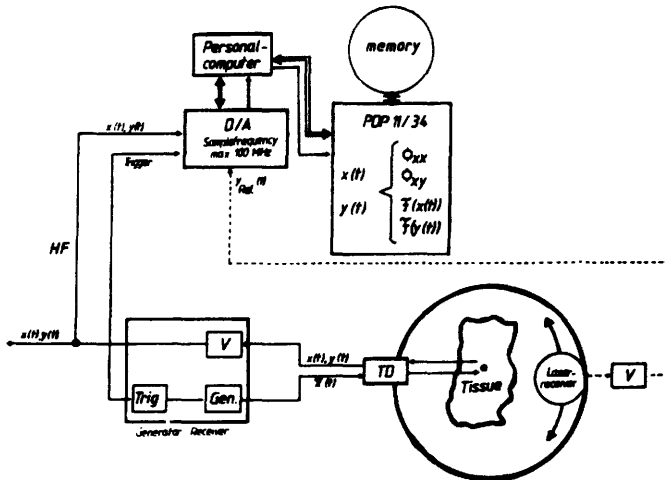


fig.1: Measurement equipment for the reconstruction of frequency- and scatter-images

The sampled RF-signals, the displacement intervals and the time of flight are used for reconstructing B- and frequency-images. B-images are computed from the demodulated data, whereas the center frequency of the frequency power spectrum is represented in frequency images. The Fourier Transformation is computed from a window of 100 sample points and a displacement width of 21 sample points which corresponds to 0,77 mm depth in tissue,

if the sample interval is  $0,05 \mu\text{m}$  and the sound velocity  $1470\text{m/sec}$ . The disproportion of the displacement intervals in lateral ( $1\text{mm}$ ) and axial ( $0,77\text{mm}$ ) direction can be corrected expanding the F-image lateral by a factor of three and axial by a factor of four. The demodulated data are comprehended by a factor of seven to get a depth interval of  $0,26 \text{ mm}$ . A post processing with a median filter is added to this procedure.

The reconstruction of scattering images is also possible with our measurement equipment. For that purpose the scattered waves are measured by a second transducer - in general we use a laser receiver - and analyzed for the number of maxima per 100 degree scatter angle. This parameter is shown in scattering images, which, representing the angle dependence of the scattered signal, contain information about the mean scatterer distance.

Fig.2 shows a part of a B-image of mamma tissue reconstructed with our measurement equipment. The pattern can be divided in two low amplitude zones and one of high amplitude, but there was no correlation of these patterns with the histological structure.

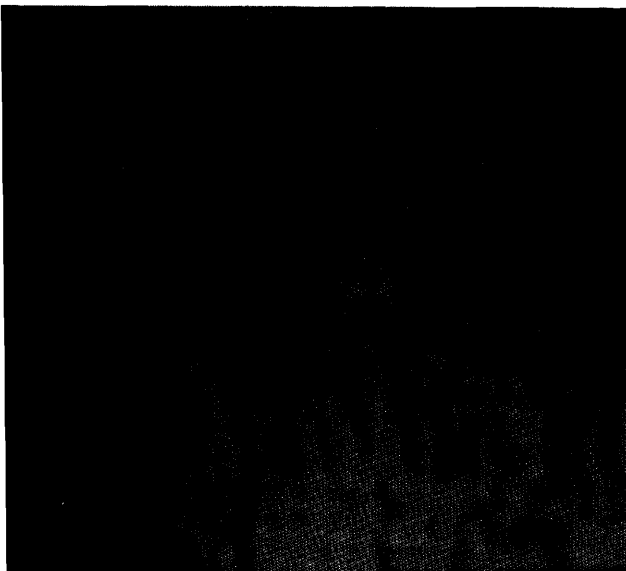


fig.2: B-image of mamma tissue with a carcinoma



fig.3: Frequency image of mamma tissue with a carcinoma

On the contrary one can see in the frequency image (fig.3) of the same tissue probe a homogeneous pattern except an area of lower frequency on the right side. The histological findings confirmed that this zone corresponded to a carcinoma. Therefore in this example the frequency image renders a better tissue characterization possible than the B-image.

It is also possible to compute quantitative parameters from a Region-of-Interest of an frequency image. The attenuation coefficient is estimated by the frequency shift method. After correcting B- and frequency images for attenuation by this coefficient, the mean value of the center frequency in this region is computed named "characteristic frequency".

The two parameters of frequency images from uterus tissue allow a good decision between normal uterus, uterus myoma and -sarcoma. The myoma has a lower characteristic frequency than normal uterus while sarcoma can be distinguished from those two groups by it's lower attenuation coefficient.

#### Combined evaluation of B- and frequency images

In spite of the advantages of frequency images and the parameters computed from, we do not expect that frequency images will resplace B-images. Both types of images contain information for tissue characterization which is supplementary to each other. Therefore a diagnosis should be done by a combined evaluation based an amplitude and spectral data.

The system is similar to that we used to evaluate 60l in-vivo B-images of the prostate. We got a detection rate of 90% with the pattern recognition system differentiating carcinoma from

adenoma whereas visually only 74% of all cases could be classified correctly. The histological finding was used as reference in all cases. Similar good results we got by pattern recognition used for images of the thyroid.

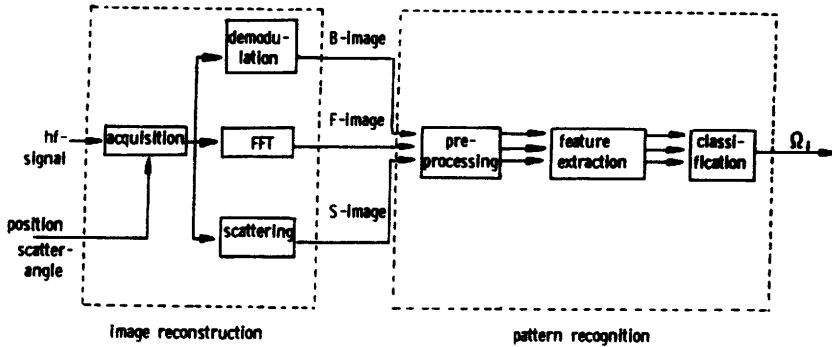


fig.4: Image combination system

The principles of image combination system are demonstrated in fig.4: First, B-, frequency- and, if necessary, scattering images are computed. Preprocessing includes improving the signal-to-noise-ratio and marking off the Region-of-Interest (ROI). Feature extraction means computing the attenuation coefficient and the characteristic frequency from frequency image. Also first and second order statistical parameters are extracted from the ROI of the B-image and from the scattering image. In a last step the parameters of all image types are comprehended in a parameter vector which is classified by a linear classifier.

We use a geometric algorithm which can be adapted on various decision problems and which is independent of the statistical distribution of the features.

So far we used this method to combine B- and frequency-images of uterus. For that the physician marks off ROI's in the B-image. Then parameters from these ROI's of the B-image and from the equivalent areas of the frequency image are computed. The classification result can be visualized in the B-images characterizing the decision classes in different colours.

## References

Nauth,P., P.Pfannenstiel, E.-G.Loch, W.v.Seelen: Improved Tissue Characterization Using Scattering Images. In: Acoustical Imaging 15. Plenum Press, New York, 1986 in print

Negoita,C.V.: Expert Systems and Fuzzy Systems. Benjamin Cummings, London-Amsterdam 1985

Zielke,Th., P.Nauth, N.Stein, W.v.Seelen, E.-G.Loch, A.Gaca, P.Pfannenstiel: Quantitative Verfahren bei der Ultraschall-diagnostik. Radiologe 25 (1983) 468-473



**Session 5 - BACKSCATTERING**

**Chairman : G. Berger**



# IMMEDIATE EFFECT OF MYOCARDIAL INFARCTION ON THE HISTOGRAM OF THE ULTRASONIC ECHO AMPLITUDE

A. Vieli, S. Basler and P.P. Lunkenheimer\*

Institut für Biomedizinische Technik, ETH und Universität, CH-8092 Zürich, Schweiz

\* Experimentelle Thorax-, Herz-, und Gefässchirurgie, Universität, Münster, BRD

Histograms of ultrasonic echo amplitude from canine myocardium have been evaluated with respect to variations during the first 10 cardiac cycles after coronary artery occlusion. It has been found that a high amplitude tail appears almost immediately after ligation. The ratio between the mean and the standard deviation of the amplitude distribution was slightly reduced during this period but showed a tendency to recover around the 10th cycle after occlusion.

**Key words:** Acute ischemia; Amplitude statistics; Tissue characterization; Ultrasonics

## Introduction

It has been proposed to utilize the deviation of the first order ultrasonic echo statistics from a Rayleigh distribution as a parameter for tissue characterization [1]. This modality offers itself to cardiac applications because relatively small areas of interest are sufficient for investigation and because it is insensitive to filtering by the intervening chest wall. The method has been successfully applied to differentiate an intracardiac thrombus from an artefact in humans[2] and was refined [3] to a degree that allowed the detection of early ischemia in canine models [4]. However, a sound basis of understanding the relation between the biological tissue state and the measured parameters has not been established yet. This is in contrast to second order statistics, which are related more easily to biological parameters [5]. An interesting argument has been brought up recently [6] suggesting that temporal decorrelation of spatially coherent structures may be responsible for some of the effects observed in the infarction model.

The present study addresses the question whether the histogram of the echo amplitude changes within the first ten cardiac cycles after coronary artery occlusion.

## Theoretical Background

The underlying theoretical model is to a large extent borrowed from laser speckle studies. In the classical statistics of speckle the results obtained in connection with the extensively studied random walk problem are applied to the summation of the randomly phased contributions of a large number of scatterers [7].

According to this theory the amplitude of the resulting sum follows a Rayleigh distribution under the following assumptions:

1) The amplitudes of the individual scattered waves must be independent of each other and of their phases. (Thus, the ultrasonic attenuation must be compensated well enough to make depth dependence negligible within a range of one wavelength.)

2) The phases of the individual contributions must be equally distributed within an interval of a length of  $2\pi$ . (Random allocation of the scatterers in a total depth range of several wavelengths)

3) The number of scatterers per sampling volume must be large and must not fluctuate from one scattering volume to another within the region of interest. (Homogeneous regions of interest should be interrogated with sufficiently large sample volumes of spatially invariant dimensions.)

In the case of pulsed echography the classical theory applies to the individual frequency components and their respective sample volumes. The resulting amplitude at a given location can be found by adding the respective sum phasors of all spectral components. If each of these phasors is Rayleigh distributed the resulting amplitude does show these characteristics as well. An analogous result can be applied to scatterers grouped into subsets exhibiting Rayleigh statistics each. Other deviations from the ideal assumptions mentioned above are difficult to take into account analytically in a general case [8].

For computational simplicity the ratio between mean and standard deviation (MSR) was utilized in the present study to quantify the discrepancy between the measured echo amplitude distribution and Rayleigh statistics ( $MSR_{Rayleigh}=1.91$  [9]).

#### **Data Acquisition and Evaluation**

The equipment utilized for data acquisition and evaluation consisted of a prototype 15 MHz echography system, a commercial dual channel Digitizer<sup>1</sup> and an IBM PC AT running a statistical software package<sup>2</sup> (Fig. 1).

The piezoelectric transducer utilized was built in house. Its active element, a disc with a diameter of 4 mm, was encapsulated in a cylindrical block 20 mm in diameter and 5 mm thick. It was excited by bursts consisting of 15 periods of a 15 MHz sine wave. The receiver amplified the echo linearly without any time gain compensation, demodulated it orthogonally to the baseband and limited its bandwidth to 1.5 MHz. The pair of orthogonal signals was then digitized simultaneously at a rate of 18 MHz and a resolution of nine bits each and subsequently transferred to the computer.

One data set consisted of 10 consecutive pulse echoes obtained in intervals of 20 microseconds. In each tracing the computer calculated the echo amplitude from the two orthogonal components and extracted a region of interest 150 samples long by selecting a depth range starting at 2 and ending at 8 mm from the transducer surface.

---

<sup>1</sup> Data 6000 with D630 plug-in digitizer (Analogic, Danvers, Ma.)

<sup>2</sup> Statgraphics (STSC, Rockville, Md.)

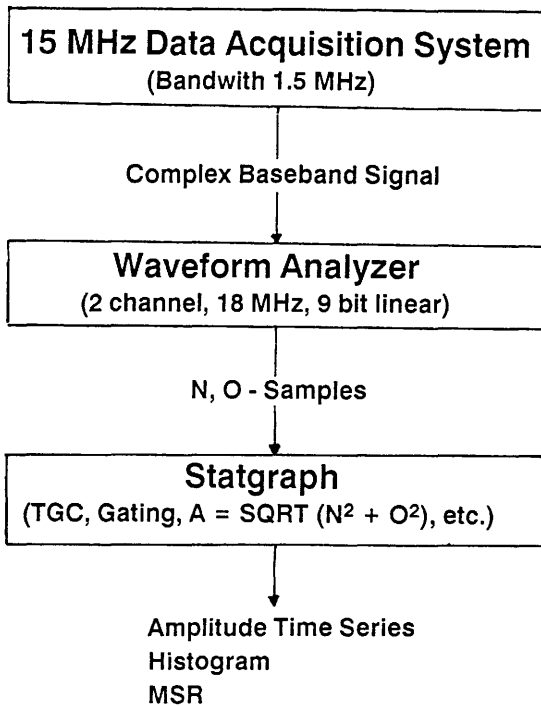


**Fig. 1. Data acquisition and evaluation.**

The Ultrasonic echography system operates in pulsed mode at 15 MHz. It provides the lowpass filtered (1.5 MHz) complex echo amplitude demodulated into the baseband. A commercial waveform Analyzer (Data 6000) is utilized to linearly digitize each of two orthogonal components of the complex echo envelope with a rate of 18 MHz and a resolution of 9 bits. By means of the statgraph software package running on an IBM PC AT the data are time gain compensated, gated to select the range of 2 to 8 mm from the transducer, and transformed into an amplitude values.

The apparent attenuation was determined by summing up all the 60 data sets available and fitting a negative exponential to the resulting sum (Fig. 2). It was compensated for by multiplying the individual pulse echoes by the inverse of this exponential. From the resulting data sets the histograms as well as the corresponding MSRs were computed.

Two different open chested dogs were investigated. They were anesthetized but not paced. After the left anterior descending coronary artery was prepared for ligation the transducer was sutured onto the epicardium such that the center of the ischemic area could be investigated. As the pericardium was kept as intact as possible, it helped keeping the transducer tightly in place. Data sets were taken every second heart cycle in late diastole. Five of these sets correspond to one measurement covering 10 cardiac cycles.

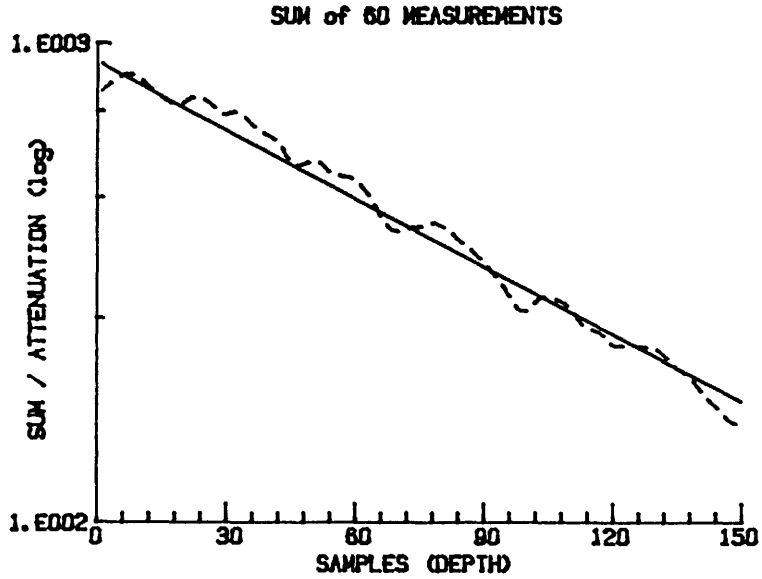


**Fig. 2. Average attenuation used for time gain compensation**

The horizontal coordinate represents depth into the myocardium, the vertical one the logarithm of the echo amplitude. The dashed curve corresponds to the sum of all echo tracings recorded, whereas the solid line gives the exponential fit to these data which is the inverse of the time gain function.

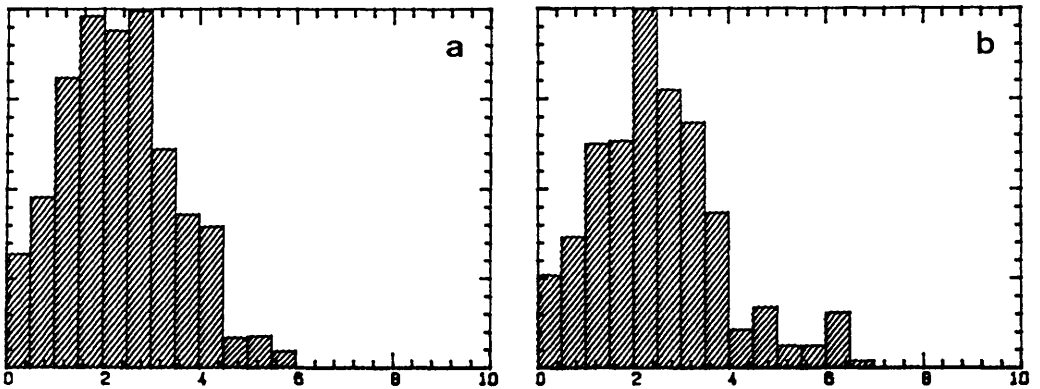


**Fig. 3. Baseline histograms**

The figure depicts two baseline histograms of the echo amplitude. They were taken from cardiac cycles number -3 (a) and -1 (b) before coronary artery occlusion. Horizontally the echo amplitude is plotted, whereas the height of the bars indicates the number of occurrences.

Measurements were made for baseline results before ligation and for transient results immediately after ligation. To allow for a second transient measurement the occlusion was removed in one dog for a recovery period of 30 Minutes after the first ischemic period of 30 seconds.

## Results

In spite of some beat to beat variations the baseline results taken every second heart cycle before ligation show a common overall pattern fairly close to a Rayleigh distribution (Fig. 3). The first cardiac cycle after coronary artery occlusion still fits into this pattern (Fig. 4), whereas cycles number 3,5 and 9 contain an additional tail of high amplitude echoes. Surprisingly, cycle number 7 does not match this general pattern. The MSR results computed from these distributions are given in Figure 5 together with the MSRs obtained from the second dog.

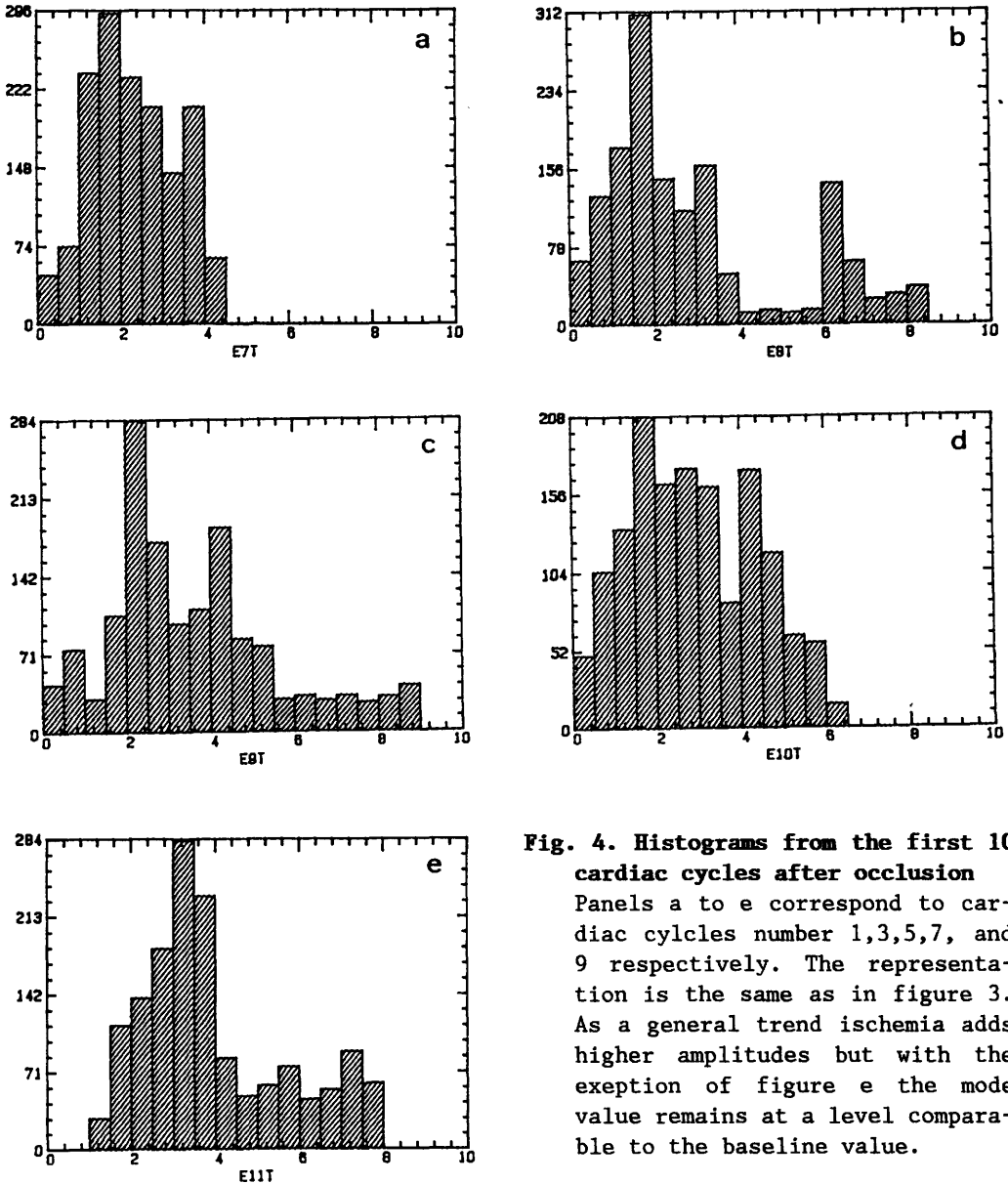


**Fig. 4. Histograms from the first 10 cardiac cycles after occlusion**

Panels a to e correspond to cardiac cycles number 1,3,5,7, and 9 respectively. The representation is the same as in figure 3. As a general trend ischemia adds higher amplitudes but with the exception of figure e the mode value remains at a level comparable to the baseline value.

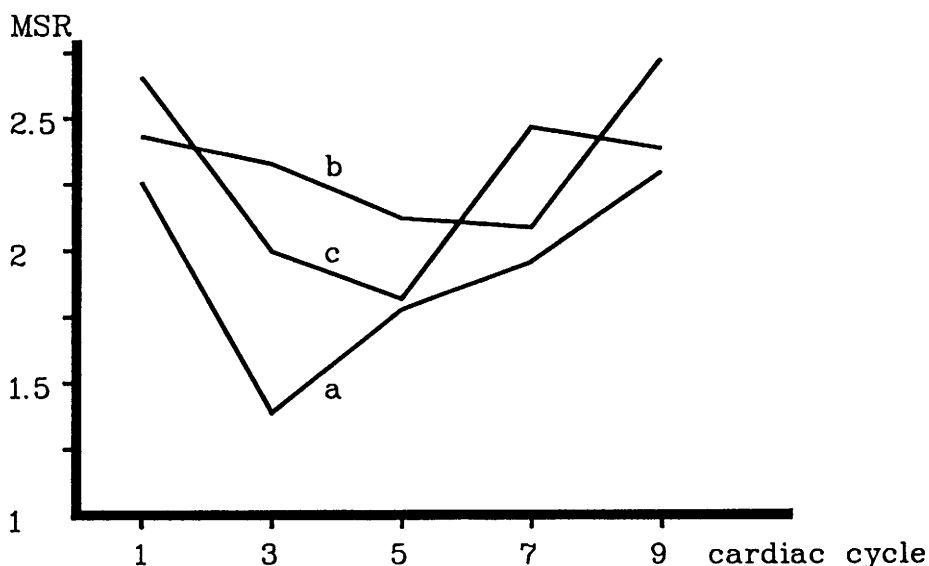


**Fig. 5. MSRs of 3 acute ischemias in 2 dogs**

The horizontal coordinate represents cardiac cycles number 1 to 9 after ligation, the vertical one the corresponding MSRs (see text). Tracing a was obtained from dog number 1 and tracings b and c from dog number 2. In the second dog the initial ischemia experiment yielded curve b and the repetition curve c.

### Discussion

The results presented are obviously preliminary. Nevertheless, it is surprising that in all three cases of ischemia the MSR has a tendency to drop instead of the expected rise. The end of the curves seem to indicate that a longer period of observation might have shown a reversal of this tendency, though. The fact that cycle number seven after ischemia does not match the characteristic of its neighbours may be attributed to a possible arrhythmia because the dog was not paced.

This study differs in several respects from the one reported in [4]. First, the ultrasound frequency has been considerably higher yielding wavelengths on the order of 100 microns, which corresponds to only about ten fiber diameters. This fact may be responsible for the higher MSR values obtained from the present investigation. Second, the pulse repetition frequency has been chosen such that an entire data set was recorded within a mere 200 microseconds. Third, there are some modifications in data processing: a) The data sets were not inspected individually in order to set the region of interest for each one of them. b) Time gain compensation was realized digitally thereby sacrificing about 2 of the nine bits dynamic range. c) The analytical magnitude of the complex echo signal was evaluated instead of its sampled real component. These differences hamper a detailed comparison and suggest that further studies should include measurements both immediately after ligation and during at least the first hour of ischemia.



The small number of observations makes it highly speculative to draw any specific conclusions other than the one that Figures 3 and 4 do show a change in the echo amplitude statistics during the first 10 cardiac cycles after ischemia. Further investigations will have to substantiate this finding and to clarify which biological process it may correspond to.

#### **Acknowledgement**

This work was supported by the Swiss National Science Foundation under grant number 4.890-0.85.18 (NFP 18)

#### **References**

- [1] Fellingham-Joynt L., A Stochastic Approach to Ultrasonic Tissue Characterization, Ph.D. thesis, Stanford University, Technical Report No. G557-4 (1979)
- [2] Green S., Joynt L., Fitzgerald P., Rubenson D., and Popp R.L., In vivo ultrasonic tissue characterization of human intracardiac masses, *Am. J. Cardiol.* 51, 231-236 (1983)
- [3] Vieli A., Heiserman J., Schnittger I., and Popp R.L., An improved stochastic approach to RF amplitude analysis in ultrasonic cardiac tissue characterization, *Ultrasonic Imaging* 6, 139-151 (1984)
- [4] Schnittger I., Vieli A., Heiserman J., Director B., Billingham M., Ellis S., Kernoff R., Takamoto T., and Popp R.L., Ultrasonic tissue characterization: Detection of acute myocardial ischemia in dogs, *Circulation* 72, 193-199 (1985)
- [5] Insana M.F., Wagner R.F., Garra B.S., Brown D.G., Shawker T.H., Analysis of ultrasound image texture via generalized Rician statistics, *Optical Engineering* 25, 743-748 (1986)
- [6] Wear K.A., and Popp R.L., Characterization of myocardium contraction from temporal correlation of ultrasonic echoes, to be published in *IEEE Trans. Ultrason. Ferro. Freq. Control*
- [7] Goodman J.W., Statistical Properties of Laser Speckle Patterns, in *Laser Speckle and Related Phenomena*, Dainty J.C., ed., pp 9-75, Springer Verlag, Berlin (1975)
- [8] Goodman J.W., A random walk through the field of speckle, *Optical Engineering* 25, 610-612 (1986)
- [9] Burckhardt C.B., Speckle in ultrasound B-mode scans, *IEEE Trans. Sonics Ultrasonics* 25,1-6 (1978)



## INTRODUCTION TO SIGNAL RESTORATION FOR FIBROUS TISSUE CHARACTERIZATION

S. Cherif, A. Herment, Ph. Dumée and P. Péronneau.  
INSERM U. 256, Hôpital Broussais, 96 rue Didot, 75674 Paris cedex 14,  
France.

### ABSTRACT

Most studies achieved in ultrasonic tissue characterization are concerning the definition of bulk parameters such as attenuation or velocity. Indeed, these are important parameters since they represent fundamental values in the acoustical phenomenon, but they do not allow for an early diagnosis, which would be very useful for clinicians. The present study is an introduction to tissue characterization of muscular structures. Since we consider the muscle mainly as a fibrous tissue, we aim to determine the fiber size and the space between fibers. In order to reach a resolution in the range of micrometers, it seems indispensable to deconvolve the R.F. signal so as to translate the problem from the resolution of the probe frequency to the sampling frequency. An acoustical study allows comparisons between theoretical results and measurement ones. The results obtained on nylon threads are very encouraging, but, of course, we need to look very cautiously at them, since propagation in tissues is much more complex and problematical.

Key words : muscle, wire, scattering, resolution, deconvolution, echoe, spectrum.

## INTRODUCTION

Scattering of ultrasound in biological tissues still remains one of the most important problems in tissue characterization since it impacts on the quality of ultrasonic imaging and on the measurement of quantitative parameters.

Theory of scattering is commonly used for the definition of bulk characteristics of the medium, then, instead of taking scatterers into consideration, it is usual to deal with a unit volume of scatterers. As a typical example, many authors try to define backscattering cross-section for measurement of attenuation.

Another study of interest is the diffractive behaviour of tissue scattering achieved by Nicholas [1], where he showed some diffraction patterns at fixed frequency provided by the convolution of a pulse with a 5  $\mu$ s time gate. He found some correlations between theory and experiments on models of wires and tissues, but for a spacing of the scatterers within the range of 0.5 mm to 0.2 mm, while the frequency used was 1 MHz ; hence, we have a ratio : size versus wave-length, between 0.1 and 0.3. Hunter [2] and Koch [3] worked on scattering, using also sizes neighbouring the wavelength. All these interesting works help us define the macrostructure of tissues (about 1 mm and greater) ; it means that, if a tumour is big enough, it will then be possible to detect it. But, if we have a tumour at its beginning (microscopic scale), then we will observe very small changes in the macrostructure of tissues, while we will have important ones from a microscopic viewpoint.

As a consequence, it will be very useful for clinicians to get some information on the microstructure of tissues, and then to deal with sizes much more small than the wavelength.

### I. PROBLEM FORMULATION

Let us consider microscopic photographs of the myocardium. In the normal case, the mean size  $D$  of the fiber is about 13  $\mu$ m ; we can note important changes from this case in hypertrophic myocardium, where  $D = 40 \mu$ m, and in atrophic myocardium,  $D = 6 \mu$ m. Hence, we can set up a kind of modelization to define two interesting parameters which are helpful in diagnostic, the mean size of fibers and the mean space.

In this paper, we are only dealing with the most simple case of single scattering and we compare quantitative information between theory and experiments. Since it is not easy to perform experiments in the range of sizes encountered in tissues (6  $\mu$ m to 40  $\mu$ m), we made a translation of the problem in a numeric viewpoint, in order to keep the same ratio : size versus wavelength.

Tissues : D [6  $\mu\text{m}$ , 40  $\mu\text{m}$ ]  
 Transducer : 5 MHz  $\lambda = 300 \mu\text{m}$

D	10 $\mu\text{m}$	15 $\mu\text{m}$	30 $\mu\text{m}$
D/ $\lambda$	1/30	1/20	1/10

Wires : D = 0.1 mm ; D = 0.3 mm ; D = 0.5 mm  
 Transducer : 0.5 MHz  $\lambda = 3 \text{ mm}$

D	0.1 mm	0.3 mm	0.5 mm
D/ $\lambda$	1/30	1/10	1/6

We are, of course, speaking of a wavelength associated with the central frequency of the transducer.

## II. SINGLE SCATTERING FROM A WIRE

Let us remember the major points of the theory of scattering from a wire developed by Morse and Ingard [4].

Assuming a plane wave propagating along the x positive axis normal to the z axis of the cylinder, we can write the classical expression of the plane wave in rectangular coordinates (x, y, z) as follows :

$$P_i = P_0 e^{ik(x-ct)} \quad (1)$$

where  $k = 2 \pi / \lambda$   
 $\lambda$  is the wavelength  
 $c$  is the velocity of sound

In terms of cylindrical coordinates (r,  $\theta$ , z), we have :

$$P_i = P_0 e^{ik(r \cos \theta - ct)} = P_0 e^{ikr \cos \theta} e^{-i\omega t} \quad (2)$$

which can be developed in the series form :

$$P_i = P_0 \left[ \sum \epsilon_m i^m \cos(m\theta) J_m(kr) \right] e^{-i\omega t} \quad (3)$$

where  $J_m$  is the Bessel function of the first kind of the nth order,  
 and  $\epsilon_m = 1$   $m = 0$   
 $\epsilon_m = 2$   $m > 1$   
 $m : 0 \rightarrow \infty$

As a solution of the general equation of wave propagation, the outgoing scattered wave is of the following form :

$$P_s = \left[ \sum A_m \cos(m\theta) H_m(kr) \right] e^{-i\omega t} \quad (4)$$

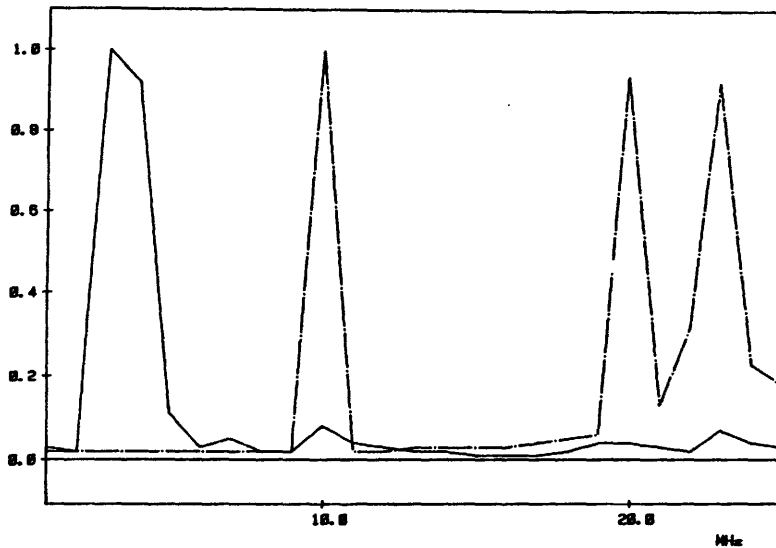


Fig. 1. Spectrum of the output signal  $z$  of the filter, with the spectrum of the input signal  $x$  in dashed lines.

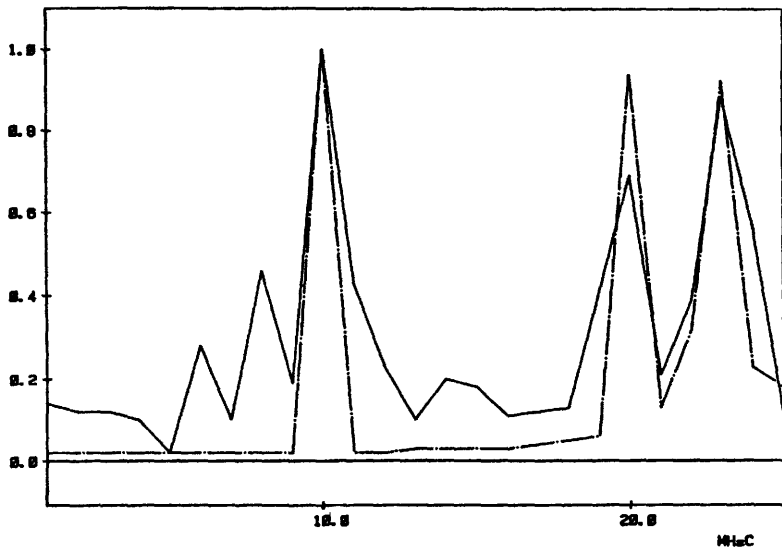


Fig. 2. Spectrum of the deconvolved signal in continuous line, with the real spectrum of the input signal  $x$  in dashed line.

where  $H_m(kr)$  is the Hankel function of the first kind,  $A_m$  being a coefficient such that the total radial velocity  $U_{tr}$  equal to 0 at the surface of the cylinder :

$$U_{tr} = U_{ir} + U_{sr} = 0 \text{ at } r = a$$

$U_{ir}$  = radial velocity of the incident wave  
 $U_{sr}$  = radial velocity of the scattered wave  
 Then :

$$A_m = \epsilon_m P_0 i^{m+1} e^{-i\gamma_m} \sin \gamma_m \quad (5)$$

with :

$$\text{tang } \gamma_0 = \frac{-J_1(ka)}{N_1(ka)} ; \quad \text{tang } \gamma_m = \frac{J_{m-1}(ka) - J_{m+1}(ka)}{N_{m+1}(ka) - N_{m-1}(ka)}$$

where  $N_m$  is the Neumann function.

When the distance becomes much greater than the wavelength,  $r \gg \lambda$   
 $kr \gg 1$

The Hankel function tends to the limit form :

$$H_m(kr) \rightarrow \sqrt{\frac{2}{\pi kr}} e^{ikr}$$

Then, we can write the scattered outgoing wave as :

$$P_S(r, a, \theta, \lambda) = \frac{1}{\pi} \sqrt{\frac{\lambda}{r}} P_0 [\Gamma - \epsilon_m i^{m+1} e^{-i\gamma_m} \sin \gamma_m \cos m\theta] e^{ik(r-ct)} \quad (6)$$

Since we are interested in the backscattering, we have fixed :

$$\theta = \pi$$

$$r = r_0$$

$a = a_0$  as a parameter,

We will see in the following that, in order to obtain noticeable changes in the curve with different diameters, we have to go far outside the bandwidth of the transducer, and, hence, to apply a deconvolution filter.

### III. DECONVOLUTION FILTER

We can modelize the system by using convolution with an additive noise, and so we have :

$$z = h * x + n \quad (7)$$

In matrix form, we can write :

$$Z = H X + n$$

$Z$  is the vector representing the measurement,  $H$  is the matrix representing the impulse response of the system on a rigid plane,  $n$  is the noise vector,  $X$  is the vector representing the reflectivity of the medium.

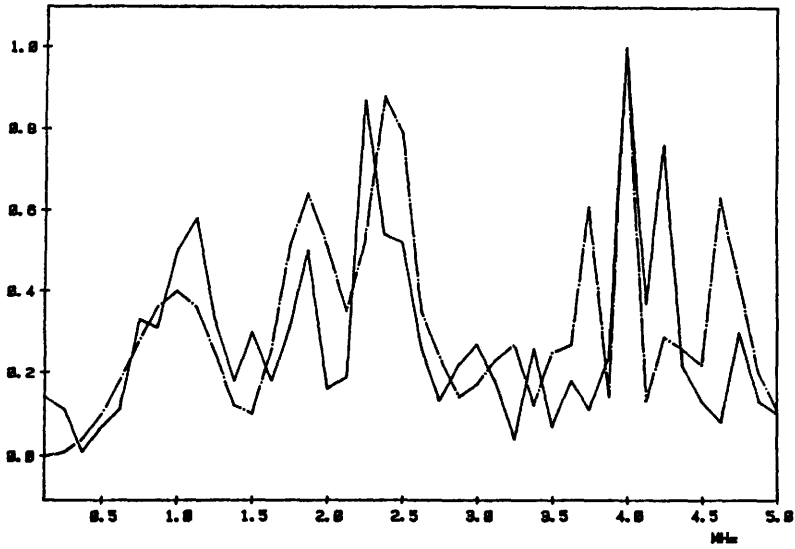


Fig.3. Spectrum of the deconvolved echo of the 0.5 mm diameter wire in continuous line, with, in dashed line : theory for 0.44 mm.

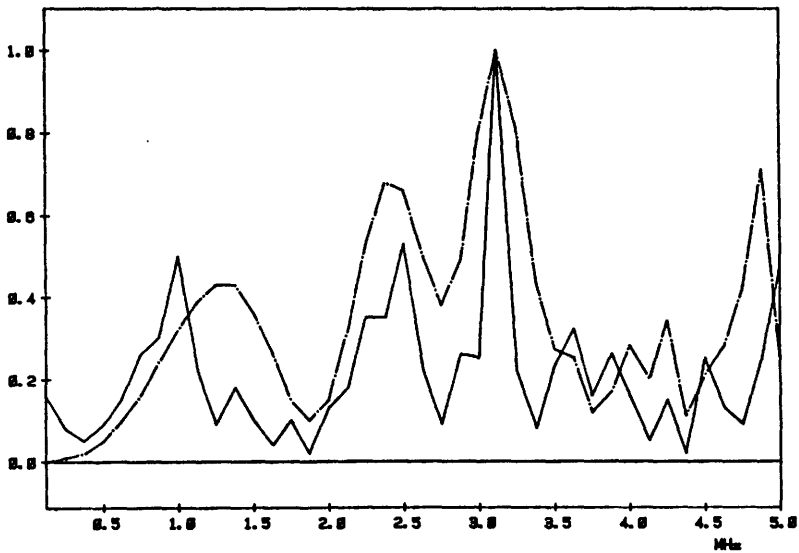


Fig.4. Spectrum of the deconvolved echo of the 0.3 mm diameter wire in continuous line, with, in dashed lines : theory for 0.34 mm.



We used the minimum linear variance estimator [5] defined as :

$$\underline{x} = E \left\{ \underline{x} \underline{z}^t \right\} \left[ E \left\{ \underline{z} \underline{z}^t \right\} \right]^{-1} \underline{z} \quad (9)$$

If we make the following assumptions about the statistics of signal and noise :

$$\begin{aligned} E \left\{ \underline{x} \underline{x}^t \right\} &= CI \\ E \left\{ \underline{n} \underline{n}^t \right\} &= RI \\ E \left\{ \underline{x} \underline{n}^t \right\} &= 0 \end{aligned} \quad \begin{aligned} E \left\{ \underline{x} \right\} &= 0 \\ E \left\{ \underline{n} \right\} &= 0 \end{aligned}$$

where I is the identity matrix.

It means that we have uncorrelated, white, zero-mean signal and noise.

Then, we have :

$$\underline{x} = \underline{C} \underline{H}^t \left[ \underline{H} \underline{H}^t + \underline{R} \underline{I} \right]^{-1} \underline{z} \quad (10)$$

and we reach the classical form :

$$\underline{x} = \underline{H}^t \left[ \underline{H} \underline{H}^t + (\underline{R}/\underline{C}) \underline{I} \right]^{-1} \underline{z} \quad (11)$$

#### Simulation for deconvolution

In order to show the results of deconvolution, we have simulated a signal  $x$  which is the sum of three sinusoids at 10 MHz, 20 MHz and 23 MHz. Then, we apply this signal to a filter with a 3.75 MHz impulse response of a transducer, with additional noise, in order to obtain the output signal  $z$ .

We can see in Figure 1 the spectrum of the signal  $z$  in continuous line, with the spectrum of the signal  $x$  superimposed in dashed lines. The filtering effect of the transducer is so strong that it seems that there is no information outside the bandwidth. But, in fact, we can say that the modulus is much more small outside than in the bandwidth itself, but it is not a zero one, and then we have information. Afterwards, the major problem is that of noise, and this is the reason why the deconvolution method must be employed very carefully and be optimal. Until now, the best estimator we had is that of Eq. (11) computed in the time-domain and realized in a recursive form to reduce the computation time. The result of the simulation is shown in Figure 2 where we obtain again the three sinusoids and, unavoidably, some other peaks of noise.

#### IV. EXPERIMENTS AND RESULTS

We used a 0.5 MHz, 25 mm-diameter, unfocused transducer positioned at 80.0 mm of the wire.

We have compared the spectrum obtained after deconvolution to the nearest theoretical results (Eq. 6) superimposed in dashed lines in Figures 3, 4, 5.

#### V. CONCLUSION

Despite the problem involved in the noise inherent in acquisition and the acoustic noise caused by the presence of microbubbles and micro-objects in water, we have obtained a rather good agreement between theory and experiments. It is therefore obvious that deconvolution is mandatory when we

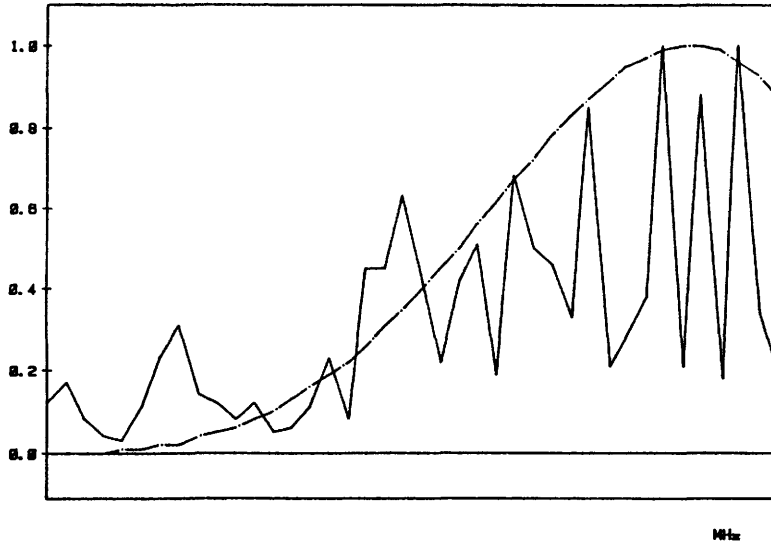


Fig.5. Spectrum of the deconvolved echo of the 0.1 mm diameter wire in continuous line, with the theory for 0.1 mm in dashed lines.

want to get interesting information on scattering, due to the limited bandwidth of the transducer.

Another important point is the impulse response that we used for deconvolution. The radiation point or line response, as defined in [6], may improve the result of deconvolution, if, and only if we have exact information on the geometry of the medium, and if we define a good theoretical result of scattering.

In the other case, it is more advisable to start deconvolution with the impulse response on a plane, since we broaden the spectrum of the echo without favoring certain frequencies with respect to other ones.

#### REFERENCES

- [1] Nicholas, D., Recent advances in ultrasound in biomedicine, Frequency dependence of backscattered energy and its clinical application, vol. 1, Chap. 2, pp. 29-52 (1977).
- [2] Hunter, L.P., Lee, P.P., and Waag, R.C., Forward sound scattering by small nylon cylinders in water, J. Acoust. Soc. Am. 68 (1), pp. 314-319 (1980).
- [3] Koch, I., Classification of scattering objects by regular arrays of scatterers using Fourier analysis, Ultrasonic Imaging 5, pp. 346-360 (1983).
- [4] Morse, Ph.M., and Ingard, K.U., Theoretical Acoustics, Mc Graw Hill, chap. 7, pp. 356-366, chap. 8, pp. 400-403 (1968).
- [5] Chong-Hung, C., and Mendel, J.M., Performance of minimum variance deconvolution filter, IEEE Trans. ASSP 32, n° 6, pp. 1145-1153 (1984).
- [6] Fatemi, M., and Kak, A.C., Ultrasonic B-scan imaging : theory of image formation and a technique for restoration, Ultrasonic Imaging 2, pp. 1-47 (1980).

**A COMPARISON BETWEEN THE RESULTS OF TISSUE ANALYSIS BY MEANS OF POWER SPECTRA  
AND THE HISTOLOGICAL STRUCTURE OF CHOROICAL MELANOMAS**

Vincenzina Mazzeo, Gualtiero Golfetto, Luca Ravalli, Paolo Perri, Gloria Galli, Antonio Rossi.

**University Eye Clinic, Ferrara, Italy.**

Abstract

Ultrasound tissue characterization by means of power spectra analysis was attempted in 19 cases of choroidal melanomas and in one case of choroidal metastasis from a thymoma. All the pathological specimens have then been reviewed by the same pathologist in order to achieve a uniform answer. An a posteriori comparison between the obtained power spectra, subdivided according to their more or less homogenous trend, and the various types of malignant melanomas (i.e. spindle B, mixed and epithelioid) revealed that at this moment the kind of analysis adopted has not a predictive value even if an almost complete correlation exists between the structural tissue organization and the power spectra response and that a close correlation exists between the highly positive values of the angular coefficient of the regression lines and tissue homogeneity.

Key words: Best fit approximation, Choroidal melanoma, Comparison, Computerized analysis, Hystology, Power spectra, Ultrasound.

Introduction

The study of tissue characterization, with the method followed in these last years at the Eye Clinic of the University of Ferrara, whose basic principles and results have already been published (1,2,3,4) has recently been integrated with the comparison between echographic data and histological characteristics of the intraocular lesions. It is of course an inductive analysis which regards almost only eyes enucleated for choroidal melanomas. In this way we tried to assess the presence and the extent of a correlation between echographic data and histological structure and to find out the

anatomic elements responsible for the echographic modifications.

### Subjects and methods

All the data about the acquisition of signals and their analysis have already been widely described ( 1,2,3,4, ).

In this study the eyes of patients, who underwent enucleation since suffering from choroidal malignant melanoma, have all been examined by the same pathologist in order to achieve a homogenous assessment. The Callender modified classification ( 5 ) has been adopted which distinguishes:

- spindle A and B malignant melanomas,
- mixed malignant melanomas,
- epithelioid malignant melanomas.

19 patients were examined, with 24 echographic acquisitions, in this study also a single patient was introduced who was suffering from an ocular thymoma metastasis which had hughely grown in a short lapse of time, thus occupying almost all the eye and who underwent enucleation.

### Results

The results of the echographic characterization of choroidal malignant melanomas ( MM ) in particular, have already been described ( 1,2,3,4, ). We can therefore only remind that, at a simple visual inspection of the spectral curves, the first relevant aspect was the rather homogeneous behaviour of a group of cases. Particularly the highest-frequency sector of the curve is reasonably approximable to a straight line while other power spectra have a very irregular trend. This sector ( from the frequency of 7.8 to 15 MHz ) has been chosen as representative also because, at the above mentioned visual inspection, the behaviour of the power spectra of the low-frequency sector is absolutely irregular, with no correlation among the various groups of pathologies and within the same.

The linear behaviour of this group of MM has been expressed by calculating the regression line of the curve representing the power spectrum, by taking in account, however, that such an approximation is reasonably significant only if the relative standard error ( SE ) is comprised

between  $\pm 0.1$  folds the value of the line, i.e. of 10 percent. It is clear that the higher the SE, the less representative the straight line.

Eight out of thirteen power spectra of the spindle B MM showed a very regular trend, whose regression line produces a high positive angular coefficient, SE between  $\pm 0.1$ , a mean P/P ratio of 16 dB at 15 MHz (fig.1). Five out of these eight cases, after a histological examination, showed a rather homogeneous structure, with dense cells placed in an ordinate way (fig.2), sometimes grouped in nests through a very subtle net of fibers, too subtle to be echographically revealed as an interface or to alter the homogeneous structure. The vessels are usually small and spread, more often grouped in a certain sector of the tumour (in its section under examination). Two out of these five cases showed a cell growing nest which peripherally compresses another tumoural area, thus suggesting that a cellular line has developed and grown within the tumour itself. A second echographic assessment classified one of the two above mentioned cases as belonging to the group of the spindle B MM, with higher SE (i.e. irregular).

Another case of this group, which underwent two echographic assessments, differentiates itself as less homogeneous in its histological structure. The cells have in fact a storiform distribution which should cause some discontinuity, i.e. echographically relevant interfaces. The only consideration that can be made about this particular distribution regards the size of the cellular bundles which are very small, much smaller than a wavelength unit and whose main borderlines have a roughly perpendicular trend to the tumoral surface (obviously when referring to the examined histological section). This trend could have therefore been parallel to the investigating ultrasound beam.

As far as the last case is concerned, only one histological section could be defined which, being roughly storiform, has been classified as belonging to the group with higher SE. Furthermore, the conventional echography revealed two different areas which are likely to have caused different power spectra, the one with a regular, the other with a less regular trend. Among the five power spectra of the spindle B MM which showed a less regular pattern with SE between  $\pm 0.1$  and  $\pm 1$  (fig.3) two are assessments made

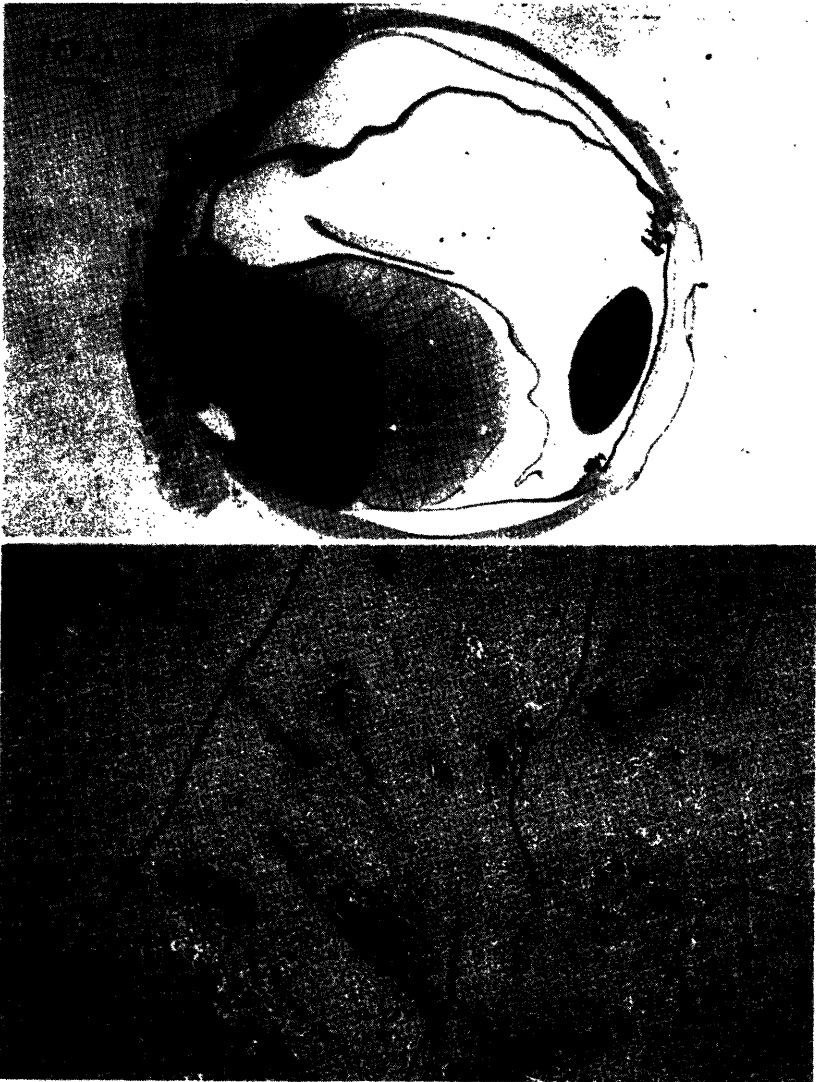
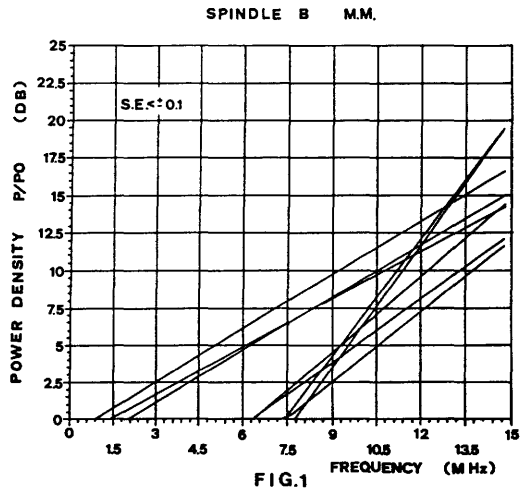
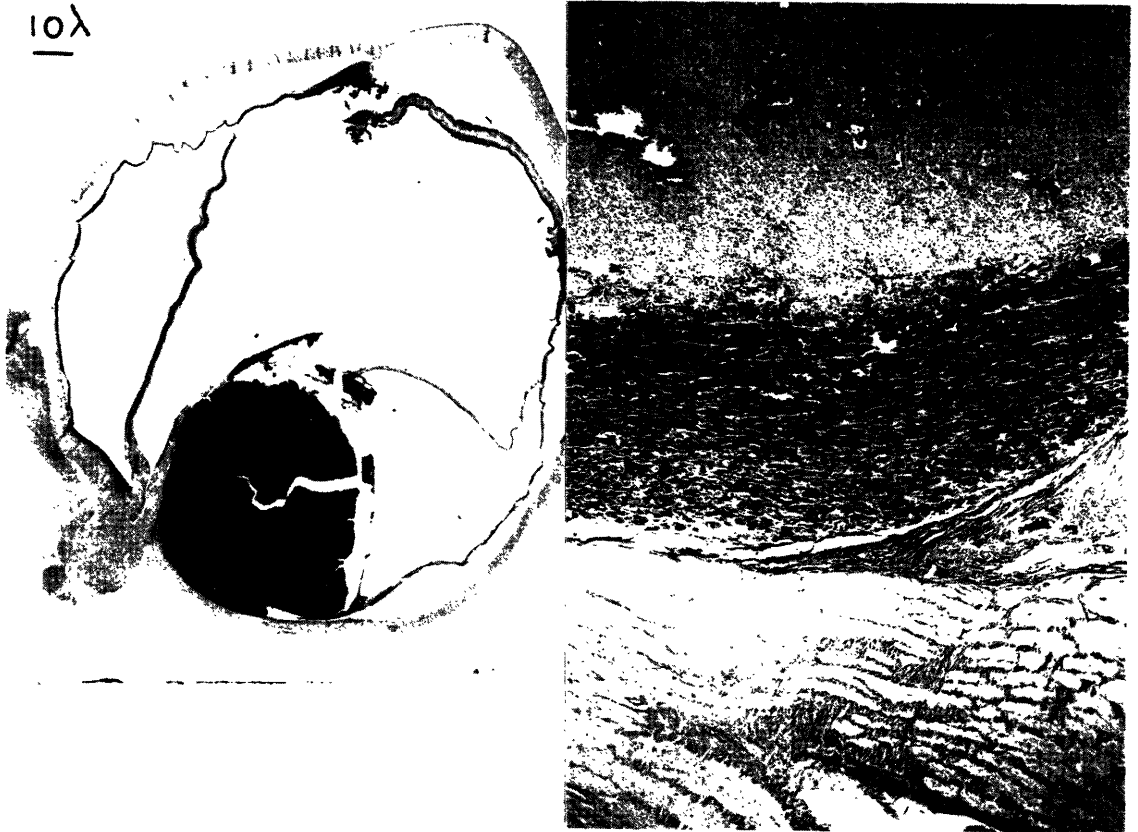
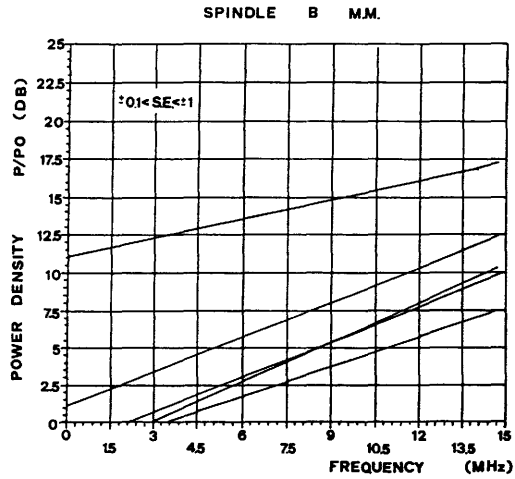


Fig.2: Choroidal MM with a homogeneous histological structure.

Top: magnification 3.5: I; Bottom: microscope picture.

On the left of each picture we report the hawe lenth ( $\lambda = 0.14$ ).



**Fig.4:** Mixed MM with predominant spindle component, which shows a very large growing nodule with a marked peripheral compression of some other neoplastic tissue. The phenomenon is clearly visible even in the section with a small magnification.

on the last of the patients described in the previous group, another one refers to one of the cases previously described, characterized by an inner nodule of homogeneous cell growth, with a peripheral compression of neoplastic tissue.

The fourth case has the same characteristics as the previous one, while the last one shows a quite heterogeneous histological appearance, not rather for its cellular distribution but for existence of areas of discontinuity originated by a rich vessels' net.

Within the group of the five mixed tumours with a predominant spindle component and more or less frequent nests of epithelioid cells, for produce a regular power spectrum, i.e. with SE between  $\pm 0.1$ , a regression line with a high positive slope and a mean P/P<sub>0</sub> ratio of 15.8 MHz. One case, on the contrary, shows a very irregular trend, with SE  $\gg 1$ .

Unfortunately it was impossible to find the histological preparation referring to this last case. All the other cases have a very homogeneous histological structure, and one of them shows a very large growing nodule which peripherally compresses other neoplastic tissue (fig. 4).

Among the remaining four mixed tumours, characterized by SE between  $\pm 0.5$  and  $\pm 1$ , a much slighter slope of the regression lines, and a mean P/P<sub>0</sub> ratio of 8.2 dB at 15 MHz, two show a characteristic similar to others, already described, i.e. a richly cellulate growing nodule with a peripheral area of tissue compression. In one of these cases the neoplastic nodule shows a storiform appearance in its cellular distribution, even if not as marked as in other cases. The third case is histologically very heterogeneous with a rotation of cellular islets and large necrotic areas. The last case shows some areas with a high concentration of vessels, hence roughly heterogeneous, as well as regular ones (fig. 5).

As regards the histological aspects of the only two epithelioid melanomas of this series, while the case with SE  $\pm 0.1$  is densely cellulate with a sometimes homogeneous and sometimes slightly fasciculate cellular distribution, the one with SE  $\pm 1$  is very heterogeneous with homogeneous areas and large necrotic zones.

Among the enucleated eyeballs, finally, one shows a thymoma metastasis.



10λ



**Fig.5:** Heterogeneous mixed MM with large areas at high concentration of vessels.

This case showed an extremely regular power spectrum in comparison with the other metastasis we have examined (all from mammae or lung carcinomas). In this last case two echographic assessments have been made at intervals. The first showed a small tumour mass (hence likely formed by homogeneous lymphocyte layers) and the echographic report had a regular plot. The second showed a hughely grown mass and at the hystological analysis (the patient was infact enucleated, being the eyeball aching because of a secondary glaucoma) a strong recent hemorrhage became evident within a homogeneous tumour.

#### Analysis of the results

When examining the spectral responses of MM, it was found that most MM showing a so-called "regular" behaviour belong to spindle B MM and mixed MM with predominant spindle component. This fact can be explained by reminding the acquisition method. Since an average of all measurements is run, a homogeneous tissue where, potentially, all the RF signals are the same in all the examined areas, will produce a power spectrum with a regular trend. This statement can be extended to all homogeneous tissues. The ever positive and sometimes high angular coefficient trend of the regression lines of the MM is due to the fact that the cells act as scatterers, which spread the sound increasingly at the highest frequencies. The more homogeneous the tumour, the more evident this phenomenon.

When a certain acoustic discontinuity, due to larger scatterers and/or to reflecting surfaces, is present, the homogeneity of the acoustic response decreases, thus producing higly irregular spectra.

This hypotesis seems to be supported by the study of the histological analysis, infact most MM with a regular power spectrum seem to have a homogeneous histological structure, while the ones with an irregular spectrum tend to be heterogeneous either for a storiform distribution, with large bundles of interlaced cells, or for the presence of vessels and necrotic areas.

The only histological forms which belong both to the group of tumours with a regular power spectrum (  $SE \leq \pm 0.1$  ) and to the one with an irregular spectrum are those MM characterized by a large homogeneous growing nodule which peripherally compresses other tumoural tissue.

Supposing that, in this first stage of the study, the retrospective analysis of the histological preparation has not influenced its "echographic reading", this ambiguous behaviour might be explained through a different structure of the various areas, depending both on the size of the nodule and on the extent of the compression it exerts on the surrounding tissue, with a consequent difference of site between acoustic and anatomical specimen.

This does not mean that these structural differences cannot exist for the other case too. Infact the changeability of the tissues and of their behaviour is always enormous. Moreover, both the acoustic and the anatomical drawings are performed at random, though one tries, in both cases, to examine the thickest areas of the tumour.

Probably, a homogeneous tumour with no growing nodules is more likely to be alike in all its zones, while a highly disorganized tumour is more likely to have more than one disorganized area. In both case, therefore, the random specimens are more reliable, as far as structure is concerned.

In those forms with a central nodule, different power spectra may arise, according to the acquisition site, the incidence of the ultrasonic beam towards the growing line of the neoplastic nodule and therefore the line of compression of the surrounding tissue.

The phenomenon of a certain tissue discontinuity which determines an irregular appearance of the power spectra becomes quite obvious when examining those tissues with a histological structure mostly made up by reflecting surfaces rather than scattering centres, as for instance choroidal haemangiomas.

As far irregular spindle B MM are concerned, their amount decreases from 5 to 3, if we consider that in two cases the SE is comprised between  $\pm 0.18$  and  $\pm 0.21$ , hence very close to 0.1, defined as significant for the linear approximation of the power spectrum curve.

The first of these cases is the one were a roughly storiform cellular distribution became histologically evident and were three echographic assessments were performed: the first belongs to the regular spindle B MM, the second has a very slight SE, while the third (probably belonging to the area which was already different for the conventional echography) has a definitely irregular trend.

The second case is a tumour characterized by a growing nodule and, as we have previously underlined, such tumours can belong both to the regular and irregular group.

If we still consider irregular spindle B MM, the other two cases, with a SE between  $\pm 0.26$  are respectively represented by another neoplasia with a growing nodule. Infact one echographic assessment was regular and by the last case described in this group with large homogeneous zones in spite of the vessels. By following this method and through the above described reports, it is impossible to distinguish the spindle B, the mixed and the epithelioid MM as other kinds of tumours, too.

If a comparison with the histology can still be valid, from the few examined cases we should be able to state that a certain correlation exists between regular or irregular echographic report and structural cell organization within the tissue.

When the cells are very dense, therefore, with no separating surface to share them as in the monotonic forms (like spindle B and regular MM, fresh haemorrhages, lymphomas) they act as scattering centres. It is known, for example, that groups of erythrocytes act as scatterers rather than as reflecting surfaces; while when the cells assume a certain organization (such as a distribution in variously directed cell bundles, or in nodules compressing other peripheral cells rotation of necrotic areas and vascular gaps) they instead act as reflecting surfaces.

Moreover it seems that the farther we go from homogeneous structures, the weaker the response of the lesion in the high frequency range (hence the lower part of the curve).

### Conclusions

This study is preliminary and retrospective, based on a small amount of cases, hence with no statistical significance. The collation of a larger amount of patients will be necessary for each histological type, to be able to state that some spectral differences do exist among them and to find out tissue properties which determine them.

The comparison between the MM histological preparations and the trend of the

lines of approximation to the spectral curves makes us suppose that:

- an almost total correlation exists between structural tissue organization and echographic plot;
- a close correlation exists between the highly positive value of the angular coefficient of the approximation lines and tissue homogeneity. The homogeneous tissues give a stronger response at high frequencies ( 7.5 to 15MHz ).

According to Coleman and Coll. ( 6,7 ) a total correspondance ( degree of reliability 98.4 percent ) exists with the "acoustic biopsy" performed with their system for differentiating spindle and mixed-epithelioid MM. The histological classification these scientists followed is not clear, but we have to underline that their system draws an "acoustic sample" of 7.5 by 3 mm within the tissue hence a large amount of tissue ( it is however a local specimen that can be repeated even in different areas, according to the size of the tumour ). When analyzing echographic results collected through our method, on the other hand, we always must take in account some significant aspects.

First of all the acquisition of the signals is unfortunately limited to a window of 2 microseconds only, owing to the characteristics of the instruments at our disposal.

Moreover, when comparing this study with the ones of other research groups, in particular of the New York Group (6,7,8), remarkable differences emerge, both about technics ( larger acquisition windows, opportunity to isolate the scanning lines ) and results. Infact, the power spectra obtained with our technique shows a distribution of the received spectra which is shifted with respect to the central output frequency of the transducer, with two peaks of energy towards the maximum and minimum frequencies. According to the American authors, on the contrary, the power spectra show a slowly increasing trend towards the central output frequency of the probe and beyond it.

Probably, larger windows could make the spectrum change, but even this possible variation can't explain the reason why we observe a different distribution of the return frequencies to the probe, as shown in this series of cases.

Moreover, the investigations which gave our present results underlined the power spectra characteristics in the highest frequency range, i.e. over 7.5 MHz. It would be desirable to fully understand the importance of the power

spectrum behaviour in the low frequency range, as well as to find the elements which influence the different behaviour between the power spectra obtained by Coleman's group and ours.

An enlightenment of all these doubtful aspects could also arise from a direct confrontation among the various groups, to verify and compare their own methods.

Once achieved this goal, the last step forward for these investigations could be based upon a modified reference echo. This new reference echo should be developed starting from an "in vivo" acoustic structure within the complex retina-choroid-sclera. The power spectra of the different lesions should then be reprocessed by starting from this signal regarding normal tissues rather than from a glass plate reflector, as it has been done since now. In this way the variables caused by sound diffusion and dispersion in healthy tissues.

## References.

- 1) Mazzeo V., Golfetto G., Rossi A., Ravalli L.: Early results in ocular tissue characterization by means of the power spectral analysis. In: Ultrasonic tissue characterization 4. Thjissen J.M. and Smith M. eds. University of Nijmegen Press. 123-129, (1985).
- 2) Mazzeo V., Golfetto G., Rossi A., Ravalli L., Perri P., Galli G.: Ultrasonic tissue characterization in eye diseases (choroidal melanomas and metastatic lesions). In: Ultrasonic tissue characterization 5. Thjissen J.M. and Mazzeo V. eds. University of Nijmegen Press. 85-90, (1986).
- 3) Mazzeo V., Golfetto G., Ravalli L., Scorrano R., Galli G., Perri P., Rossi A.: Primi risultati di analisi tessutale mediante spettro di potenza. Clinica Oculistica e Patologia Oculare, VIII/1, 31-35, (1987).
- 4) Mazzeo V., Golfetto G., Ravalli L., Perri P., Galli G., Rossi A.: Ultrasound tissue characterization of Choroidal diseases by means of computerized spectral analysis. Acta of the XXV International Congress of Ophthalmology, Rome (1986) (In press).
- 5) Spencer W.H.: Ophthalmic Pathology. An Atlas and Textbook. (Saunders Co., Philadelphia 1985).
- 6) Coleman D.J., Lizzi F.L., Silverman R.H., Rondeau M.J., Smith M.E., Torpey J.H.: Acoustic biopsy as a means for characterization of intraocular tumours In: Acta XXIV International Congress of Ophthalmology. Henkind P. ed. Lippincot Co. Philadelphia, 115-118, (1982).
- 7) Coleman D.J., Lizzi F.L., Silverman R.H., Rondeau M.J., Smith M.E., Torpey J.H., Greenall P.: Acoustic tissue typing with computerized methods. In: Abstract Book of X SIDUO Congress. (1984).
- 8) Lizzi F.L., Coleman D.J., Feleppa E., Herbst J., Jaremko N.: Digital processing and imaging modes for clinical ultrasound. In: Ultrasonography in Ophthalmology. Thjissen J.M. and Verbeek A.M. eds. Junk W. Publishers, The Hague, 405-410, (1981).





**INDEX of KEYWORDS**



Acquisition system	73
Acoustic shock	137
Acoustic ischemia	171
Amplitude statistics	171
Aperture synthesis	23
Artefact-free measurements	155
Atherosclerosis	51
Attenuation	43, 101, 113, 117, 127, 137, 145, 155, 163
Backscatter imaging	15
Best fit approximation	187
B-scan	61
Carrier (Duchenne Muscular Dystrophy)	101
Cirrhosis	43
Characteristic frequency	163
Choroidal melanoma	187
Coherent-incoherent	127
Computerized analysis	187
Correction	43
Deconvolution	15, 179
Diffraction effect	43, 113, 155
Diffuse disease	61
Discriminant analysis	61
Doppler	3, 145
Echo	179
Echocardiography	51
Echography	15
Finite amplitude loss	137
Focussing	23, 137
Focussing effect	43, 137
Frequency image	163
Front end equipment	73
Histology	187
Image analysis	35, 51
Image combination	163
Image restoration	67
Instantaneous frequency	117

Integrated backscatter	51
In-vivo	113
Liver	35, 43, 61, 113
Muscle	101, 179
Non-linear propagation	137
Ophthalmology	73
Pattern recognition	35, 163
Phase	127
Reconstruction	3, 15
Resolution	179
Resolution enhancement	67
RF signal analysis	35
Scanning acoustic microscope	23
Scatterer size	117
Scattering	113, 117, 127, 179
Signal processing	73
Signal to noise ratio	145
Speckle	43
Spectrum	179, 187
Statistical classification	51
Texture	43, 61
Thyroid disease	35
Transmission	3
Tumours	113, 117
Ultrasonic tissue characterization	35, 51, 67, 73, 171
Ultrasonic tomography	3
Ultrasound	35, 89, 175
Wire	179

European Communities — Commission

**EUR 10931 — Ultrasonic tissue characterization and echographic imaging 6  
— Proceedings of the sixth European Communities workshop**

Edited by: *J.M. Thyssen, G. Berger*

Luxembourg: Office for Official Publications of the European Communities

1987 — XIV, 204 pp., 12 tab., 95 fig. — 17.6 × 25.0 cm

Medicine series

EN

ISBN 92-825-7623-X

Catalogue number: CD-NA-10931-EN-C

Price (excluding VAT) in Luxembourg

ECU 15.10    BFR 650    IRL 12    UKL 10.60    USD 17.20

The state of the art in the entitled field is highlighted.

Progress within the European Community is greatly enhanced by the stimulation through the running concerted action programme. The topic in this volume is 'ultrasound computerized tomography'. The full profits of employing ultrasound for CT are becoming realized in various techniques of transmission tomography and reflection tomography. Parametric images from back-scattering, attenuation and velocity are currently obtained with excellent resolution. The estimation of attenuation and back-scattering parameters with more conventional echographic techniques has recently reached a level of sophistication allowing for clinical studies to be performed at several centres. Theoretical work on the analysis of the texture of echographic images has brought about a breakthrough for the purpose of tissue characterization and useful clinical information is already obtained. The potentials of the analysis of tissue movements for clinical diagnosis are explored. Technological developments, like ultrasound transducers, on-line processing and analysis systems and specialized hardware are outlined.

**Venta y suscripciones · Salg og abonnement · Verkauf und Abonnement · Πωλήσεις και συνδρομές  
Sales and subscriptions · Vente et abonnements · Vendita e abbonamenti  
Verkoop en abonnementen · Venda e assinaturas**

**BELGIQUE/BELGIE**

**Moniteur belge/Belgisch Staatsblad**  
Rue de Louvain 40-42/Leuvensestraat 40-42  
1000 Bruxelles/1000 Brussel  
Tél 512 00 26  
CCP/Postrekening 000-2005502-27

Sous-dépôts/Agentschappen

**Librairie européenne/  
Europese Boekhandel**

Rue de la Loi 244/Wetstraat 244  
1040 Bruxelles/1040 Brussel

**CREDOC**

Rue de la Montagne 34/Bergstraat 34  
Bte 11/Bus 11  
1000 Bruxelles/1000 Brussel

**DANMARK**

**Schultz EF-publikationer**

Møntergade 19  
1116 København K  
Tlf (01) 14 11 95  
Telecopier: (01) 32 75 11

**BR DEUTSCHLAND**

**Bundesanzeiger Verlag**

Breite Straße  
Postfach 10 80 06  
5000 Köln 1  
Tel (02 21) 20 29-0  
Fernschreiber: ANZEIGER BONN 8 882 595  
Telecopierer: 20 29 278

**GREECE**

**G.C. Eleftheroudakis SA**

International Bookstore  
4 Nikis Street  
105 63 Athens  
Tel 322 22 55  
Telex 219410 ELEF

Sub-agent for Northern Greece

**Molho's Bookstore**

The Business Bookshop  
10 Tsimiski Street  
Thessaloniki  
Tel 275 271  
Telex 412885 LIMO

**ESPAÑA**

**Boletín Oficial del Estado**

Trafalgar 27  
28010 Madrid  
Tel (91) 446 60 00

**Mundi-Prensa Libros, S.A.**

Castelló 37  
28001 Madrid  
Tel (91) 431 33 99 (Libros)  
431 32 22 (Suscripciones)  
435 36 37 (Dirección)  
Télex 49370-MPLI-E

**FRANCE**

**Journal officiel**  
**Service des publications  
des Communautés européennes**  
26, rue Desaix  
75727 Paris Cedex 15  
Tél (1) 45 78 61 39

**IRELAND**

**Government Publications Sales Office**

Sun Alliance House  
Molesworth Street  
Dublin 2  
Tel 71 03 09

or by post

**Government Stationery Office**

**Publications Section**

6th floor  
Bishop Street  
Dublin 8  
Tel 78 16 66

**ITALIA**

**Licosa Spa**

Via Lamarmora, 45  
Casella postale 552  
50 121 Firenze  
Tel 57 97 51  
Telex 570466 LICOSA I  
CCP 343 509

Subagenti

**Libreria scientifica Lucio de Biasio - AEIOU**

Via Meravigli, 16  
20 123 Milano  
Tel 80 76 79

**Libreria Tassi**

Via A. Farnese, 28  
00 192 Roma  
Tel 31 05 90

**Libreria giuridica**

Via 12 Ottobre, 172/R  
16 121 Genova  
Tel 59 56 93

**GRAND-DUCHÉ DE LUXEMBOURG  
et autres pays/and other countries**

**Office des publications officielles  
des Communautés européennes**

2, rue Mercier  
L-2985 Luxembourg  
Tél 49 92 81  
Télex PUBOF LU 1324 b  
CCP 19190-81  
CC bancaire BIL 8-109/6003/200

Abonnements/Subscriptions

**Messageries Paul Kraus**

11, rue Christophe Plantin  
L-2339 Luxembourg  
Tél 49 98 888  
Télex 2515  
CCP 49242-63

**NEDERLAND**

**Staatsdrukkerij- en uitgeverijbedrijf**

Christoffel Plantijnstraat  
Postbus 20014  
2500 EA 's-Gravenhage  
Tel. (070) 78 98 80 (bestellingen)

**PORTUGAL**

**Imprensa Nacional  
Casa da Moeda, E. P.**

Rua D. Francisco Manuel de Melo, 5  
1092 Lisboa Codex  
Tel 69 34 14  
Telex 15328 INCM

**Distribuidora Livros Bertrand Lda.**

**Grupo Bertrand, SARL**

Rua das Terras dos Vales, 4-A  
Apart 37  
2700 Amadora CODEX  
Tel 493 90 50 - 494 87 88  
Telex 15798 BERDIS

**UNITED KINGDOM**

**HM Stationery Office**

HMSO Publications Centre  
51 Nine Elms Lane  
London SW8 5DR  
Tel (01) 211 56 56

Sub-agent

**Alan Armstrong & Associates Ltd**

72 Park Road  
London NW1 4SH  
Tel (01) 723 39 02  
Telex 297635 AAALTD G

**UNITED STATES OF AMERICA**

**European Community Information  
Service**

2100 M Street, NW  
Suite 707  
Washington, DC 20037  
Tel (202) 862 9500

**CANADA**

**Renouf Publishing Co., Ltd**

61 Sparks Street  
Ottawa  
Ontario K1P 5R1  
Tel Toll Free 1 (800) 267 4164  
Ottawa Region (613) 238 8985-6  
Telex 053-4936

**JAPAN**

**Kinokuniya Company Ltd**

17-7 Shinjuku 3-Chome  
Shinjuku-ku  
Tokyo 160-91  
Tel (03) 354 0131

**Journal Department**

PO Box 55 Chitose  
Tokyo 156  
Tel (03) 439 0124

## NOTICE TO THE READER

All scientific and technical reports published by the Commission of the European Communities are announced in the monthly periodical '**euro abstracts**'. For subscription (1 year: BFR 3 300) please write to the address below.

Price (excluding VAT) in Luxembourg  
ECU 15.10 BFR 650 IRL 12 UKL 10.60 USD 17.20



OFFICE FOR OFFICIAL PUBLICATIONS  
OF THE EUROPEAN COMMUNITIES

L-2985 Luxembourg

ISBN 92-825-7623-X



9 789282 576236